# THE DEVELOPMENT OF MULTI-AXIS REAL-TIME SUBSTRUCTURE TESTING

Paul A. Bonnet

A thesis submitted to the degree of

Doctor of Philosophy

University of Oxford

Trinity 2006

# ABSTRACT


## THE DEVELOPMENT OF MULTI-AXIS REAL-TIME SUSBTRUCTURE TESTING

A thesis submitted to the degree of doctor of philosophy at the University of Oxford
Paul A. Bonnet – St Catherine's College – Trinity 2006

Real-time substructure is a novel hybrid method for the dynamic testing of structures. During an experiment, the structure of interest is divided into two entities. The crucial parts for the project undertaken are physically replicated and loaded dynamically through powerful actuators while the rest is numerically modelled and solved via real-time software. The dynamics of both substructures must be accurately reproduced, as well as their mutual interaction. The applications are multiple but that of earthquake engineering is primarily considered in this research.

Beyond the accurate modelling of both substructures, three main issues are crucial to the validity of a real-time hybrid simulation. Firstly, the loading equipment must be capable of imposing large loads and accurate displacements on the laboratory specimen. The behaviour of this loading system must be consistent and predictable over a wide range of frequencies and velocities. Secondly, the computational solver employed to emulate the numerical model dynamics requires stability, computational efficiency and accuracy. It must be able to deal with non-linear multi-degree of freedom systems. Thirdly, the interaction between the two substructures must be reliably emulated by a set of communication devices. The reciprocal boundary conditions must be imposed on the interface of each substructure. This notably implies quasi-instantaneous measurement and application of physical forces and displacements. The two substructures have to be solved simultaneously and in real-time.

The three areas mentioned above have been investigated in this research. Initially, the laboratory installations of the hardware and software were focussed on. The servo-controlled hydraulic actuation system was optimised and a development rig was designed and constructed. It was found that hardware settings could greatly improve the general actuator performance, even though some particular situations could compromise it. This work was then complemented by an extensive study of the necessary actuation compensation. Numerous algorithms – either previously published or developed in the course of this research – were implemented and formally compared through a set of real-time experiments. Particularly, some challenging multi-axis experiments with a high level of actuator coupling were conducted. Direct extrapolation coupled with adaptive delay estimation was found to be the most effective approach to ensure synchronisation of the substructures. Attention was then given to the integration algorithms used to solve the numerical substructure problem and output the actuator demand on a real-time basis. Both explicit and implicit schemes were considered, even though an explicit formulation is required for this hybrid application. Computationally simple schemes are more suitable and several were shown to satisfy the necessary accuracy and stability requirements. Successful real-time hybrid tests were carried out with fifty degrees of freedom in the numerical substructure, including non-linear force/displacement relationships and using integration time-steps proving unconditional stability of the algorithms used. Finally, a realistic earthquake engineering application of the real-time substructure method was conducted. A steel column was tested physically as part of 20-storey building structure subject to the 1940 El Centro earthquake. To further display the usefulness of the method, an energy dissipative device was also integrated in the numerical model and its effect on the building response was shown.

# ACKNOWLEDGEMENTS

This DPhil research has been a very stimulating experience. I am delighted to have undertaken it and I will undoubtedly encourage many people to carry out a research degree. I have received tremendous help and support since starting in January 2003, especially from my supervisors Dr Martin Williams and Dr Anthony Blakeborough. I take this opportunity to formally thank them both for their invaluable guidance. It is obvious but nevertheless important to remember that this research would not have been possible without them.

This research has benefited from the financial support of the EPSRC under grant number GR/S03720/01. Much of the experimental results presented herein could not have been obtained without this support and I am grateful to the EPSRC for their support.

This research was also much facilitated by the Civil Engineering research group and I am grateful to all the academic members of the group as well as to Alison May for their assistance. I have also greatly benefited from support staff at departmental level and I would like to thank Heather Burrage, Guy Edwards, Karen James, Geoffrey Jones, Maurice Keeble-Smith, John Mooney, Eric Peasley, Robert Sawala and Debbie Wyatt to name but a few.

I have also enjoyed a lot of support from many people around me. I would like to thank Delphine for her backing and advice in the difficult and busy times, Clive for putting up with me in the laboratory, Mobin for proof reading this report and Andreas, Anthony, Bin, Edmund, Felipe, Giang, Jackie, Jens, Kaori, Ken, Lam, Miguel, Oliver, Philip, Richard, Thanasis and Xiaowei for their friendship both in and out of the office. Lastly, I am grateful to my family and friends for their unconditional encouragement.

# TABLE OF CONTENTS

# CHAPTER 1

# INTRODUCTION

## 1.1- PRESENTATION OF THE METHOD AND APPLICATION CONSIDERED

Structural dynamics has become more and more important as lighter, cheaper, higher and larger structures continue to be built. As structures become lighter, for the same forces, the deflections increase due to higher accelerations. Also, with more efficient use of materials, this lightness also reduces the robustness of the designs and effects that would not in the past have been important take on a larger significance. Consequently, static testing and analysis have increasing limitations when applied to structures failing due to wind, earthquakes or traffic from vehicles or pedestrians.

Dynamic analysis can be efficiently computed. Much software is available and the cost of computing power continuously reduces and now very complicated and detailed numerical simulations are possible. However, for many components, failure modes or materials are still not well understood. In such cases, numerical analyses and simulations lose some of their validity, as more detailed realistic properties are obviously needed for the critical components in order to obtain meaningful results. Physical testing therefore still has an important role to play and it is broadly accepted that this role will remain for a long time.

Laboratory testing of large structures has given rise to various test methods. For the analysis of structural response to complex dynamic loading, such as earthquake records, two basic experimental methods have co-existed for some time: the shaking table method, which is a fully dynamic experimental approach, and the pseudo-dynamic scheme. However, they both have inherent limitations and are evolving to cope. As explained in the following sections, some of these evolutions lead them in a similar direction, the very direction of interest for this research.

The test method presented and developed herein is based on combining the advantages of computer simulations with those of physical testing. It involves sharing a complex model between a computer and a test rig. The structure of interest can be divided into two parts:

- On one hand, the parts and regions that can easily be numerically modelled, either because they have a simple behaviour or because they are not considered to be critical for the analysis conducted.
- On the other hand, the parts and regions of most interest, which should be physically replicated, either because they are critical to the safety and performance of the structure or where perhaps a high degree of non-linearity is expected.

Those two categories are exactly complementary and their combination would form a good model of the complete structure of interest. The combination and interaction of the two parts is the emulated structure. The first category is entirely numerically simulated – typically through spatial and time discretisation – and its dynamics are solved through time integration. This is the numerical substructure. The second category is physically modelled and subject to dynamic loading with hydraulic actuators. This is the physical substructure. Since both substructures are connected together in the emulated structure, they need to interact with each other during the hybrid experiment. Thus, their loading can only be applied simultaneously. Moreover, if the physical substructure has significant velocity or acceleration dependent properties such as inertia, damping or strain-rate effects, the test has to be carried out in real-time. An important benefit of this new testing method lies in this real-time character. Critical regions that would be difficult to study computationally – for reasons mentioned above – can be modelled physically. The rest is modelled numerically, ensuring the laboratory installations remain manageable in terms of size and cost.

The real-time substructure (RTS) method combines various concepts developed independently, so it is not clear where the idea first originated. The substructuring concept has been used in finite element analysis for a number of years (see for example Craig & Bampton 1968). In this work, this concept will be applied to hybrid testing of physical and numerical models. This technique has also been used in several industries, including aerospace and automotive. Control engineers have also developed rapid control prototyping, which involves the real-time testing of a controller unit against a computer simulation of the controlled unit. The application of the RTS method to civil engineering, and more specifically to seismic loading, has also been developed for a few years now and the concept can be tracked down to Hakuno in 1969 (Takanashi & Nakashima 1987) although the application was not very successful, for understandable hardware reasons.

As mentioned above, the RTS technique has many possible applications; this research will most particularly focus on the field of earthquake engineering. This application presents some notable challenges especially due to the size and weight of the physical tests to be conducted, inducing large forces which need to be reproduced. This leads to the use of hydraulic actuation, which also brings its own limitations.

## 1.2- TERMINOLOGY

It is important here to define precisely some aspects of the experiments included in this research, primarily to avoid confusion and mark both the differences and the similarities with the work conducted in other research centres:

- Experiment – Test – Simulation: the real-time substructure method enables laboratory hybrid experiments to be conducted, involving both physical and computational components. Such experiments can also be described as tests or as simulations (the word simulation in itself does not imply a fully computational nature). All three words have previously been employed by other researchers, and all three are used herein.

- Real-time: in the real-time hybrid earthquake experiments mentioned in this report, the dynamic loading is applied at a time scale of one. So if, typically, the earthquake record signal has a duration of 30s, the experiment will last 30s. All inherent aspects of the physical substructure – like strain-rate effects, inertial loads, damping, friction, hysteresis, etc. – can be reproduced accurately and measured as part of the interface feedback signal.

- Multi-degree of freedom (MDOF) system: in the hybrid tests considered, a general system (the emulated structure) is split into two distinct and complementary parts: the substructures. The physical substructure, by definition, contains an infinite number of degrees of freedom (even though it may be approximated to a system with discrete degrees of freedom for presentation and verification purposes). The numerical substructure, typically spatially discretised, may possess any number of degrees of freedom. When using the MDOF phrase, the system concerned will need to be explicitly named, whether it is the numerical substructure, an approximation of the physical substructure or the emulated system.

- Multi-axis or multi-variate interface: in a hybrid simulation, the boundary between the substructures may extend over several degrees of freedom of the numerical substructure. It may also not be continuous, for example if one substructure contains several separate entities, each linked to the other substructure via an interface. In all these cases, the emulation interface may be described as multi-axis or multi-variate. Note that a multi-axis interface will necessarily require at least the same numbers of actuators as there are axes.

## 1.3- OBJECTIVES OF THE RESEARCH

The RTS test method is promising and is an important research area for several reasons. First of all, it reduces the limitations brought by conventional computational and experimental structural dynamics methods when they are used separately. This is achieved thanks to the hybrid character of the process. In particular, the cost of an experiment can be reduced dramatically if only a small part of the structure is needed physically. It follows that a real-time hybrid test could typically be achieved without scaling factors, thereby allowing a better representation of the problem considered. Another benefit of the RTS method is that it can be used as a design verification tool for an isolated physical substructure entity with effective infinite repeatability of the surrounding numerical substructure – several potential designs of a key component could be tested and compared in real-life loading conditions within a relatively small laboratory installation. The structural part of interest can be focussed on while its environment is fully accounted for in the procedure.

With these benefits in mind, the objectives for the present research are as follows. Several numerical integration schemes will be implemented and tested for solving the numerical substructure. Evaluating their individual merits and their optimal implementations with the hardware available will be carried out according to the results obtained on various test configurations. Similarly, direct delay compensation schemes and outer-loop controllers will be implemented and evaluated against their results and guidelines derived as to their best use. Another major objective of this research is to conduct multi-axis RTS simulations successfully with a high level of coupling between the various actuators. This problem was raised by previous researchers, especially from Oxford, and solving it would significantly increase the applicability of the method. The RTS method will also be used for the testing of non-linear systems – the non-linearity being included in the numerical and/or the physical substructures – and of systems with numerous DOFs. Most of this work has taken place on a simple "proof of concept" development rig. Following this, the final objective of this research is performing RTS experiments on a more realistic earthquake engineering problem.

Although the field of civil earthquake engineering is that targeted by this research, it is felt that reaching these objectives will represent an important step towards making the RTS method a standard procedure that can be applied to different disciplines in the future. It follows that an additional objective of this research is the development of best-practice guidelines in order to make the method more readily available and easier to implement on a large number of problems in different fields of engineering or science.

## 1.4- STRUCTURE OF THE THESIS

This thesis presents the research conducted by the author on the development of multi-axis real-time substructure testing during the DPhil program that started in January 2003. This research has been sponsored by the EPSRC.

The second chapter reviews the previous work accomplished by other researchers, their findings and the problems they have encountered. It first discusses the various experimental options currently offered to earthquake engineers and introduces the RTS method in more detail. The issue of actuator dynamics compensation is then reviewed, followed by that of numerical time integration schemes. It finally draws up a more precise definition of the challenges ahead for the development of the RTS method.

Chapter 3 presents a description of the environment in which the research was conducted. The Oxford University Structural Dynamics Laboratory is introduced and the design and implementation of the purpose-built development test rig is described in detail. Finally, the real-time substructure commissioning tests of the development rig and the results are described.

In Chapter 4, the quality of the hydraulic actuation is discussed in the context of real-time hybrid testing. A technique is introduced to measure this quality in terms that are easy to relate to the complexity of performing an RTS experiment. This topic is taken one step further in Chapter 5 with the introduction and implementation of several actuation compensation schemes and the implementation of various types of real-time hybrid simulations.

The issue of time integration is then dealt with in Chapter 6. Several numerical schemes are considered. Due to the high number of existing schemes, a selection is made and algorithmic and implementation details are then presented. These schemes are then used to conduct evaluation tests and recommendations are finally drawn regarding which method to use.

After the specific issues studied in Chapters 4, 5 and 6 using the development rig, a more realistic application of real-time substructure testing is conducted in Chapter 7. This builds on the knowledge acquired from the more simple experiments and serves as a final verification of the recommendations produced in the previous chapters.

Finally, conclusions of this research are presented in Chapter 8. Future prospects for the RTS method are also assessed.

# CHAPTER 2

# BACKGROUND

This chapter presents a review of relevant previous research. It first assesses the role of RTS as a method of structural dynamics testing. Then, the second section focuses on the integration methods used for solving the numerical substructure model in real-time. The third section focuses on the particular delay limitation imposed by the use of hydraulic actuation and details the various ways this has been directly compensated for so far. The fourth section presents work conducted on control algorithms dedicated to RTS testing applications. Finally, in the light of what is established in the first four sections, the fifth presents more precise challenges for the development of the method.

## 2.1- INTRODUCTION – RTS TESTING WITHIN THE DYNAMIC LABORATORY TESTING OF STRUCTURES

Records from past earthquakes have led to the conclusion that the rate of loading is typically contained between 0 and 10Hz. Many civil engineering structures have their lowest natural frequency within this range. Their response may therefore be largely dependent not only on their stiffness, but also on their inertial and damping characteristics. Various techniques have been investigated to affect and control the dynamics of structures, generally classified as passive, active or semi-active devices. For an introductory review on this and examples of how semi-active devices can best be used, see, for example, Spencer & Nagarajaiah (2003). To assess earthquake resistance, a test method that emulates the full dynamics of a structure is needed. Many civil engineering buildings are based on reinforced concrete (RC), a material that is made of diverse constituents and that is highly non-linear when subject to high loads and near failure. The need for a test method that can accommodate non-linearity is therefore equally crucial (Booth 1998).

This section first gives a brief overview of two more well-established testing methods used in earthquake engineering. Relative advantages are discussed. The following sections present more recent developments and, finally, the real-time substructure method is presented and key challenges ahead are detailed.

### 2.1.1- Shaking table method

The most natural experimental technique used for earthquake engineering is shaking table testing. Here, a specimen representing the structure – either scaled down for practical reasons or ideally at full scale – is anchored on top of a rigid platform, which is vibrated to replicate a ground motion. Any input motion may be applied, but, for earthquake engineering purposes, genuine earthquake accelerograms are often used.

The main specifications for shaking table facilities are the table surface area, the mass of the specimen that may be tested and the number of degrees of freedom. The largest facilities can feature testing areas of 15×15m, capacities as high as 1200t and provide translations and rotations in all three orthogonal axes (Williams & Blakeborough 2001).

### 2.1.2- Pseudo-dynamic (PsD) method

A PsD test setup very much resembles that of a classic static loading test. The structure to be analysed is spatially discretised according to a lumped mass approximation and actuators are located at these points to provide the loading. This experimental concept originated in Japan in 1974 (Takanashi & Nakashima 1987) following failed attempts to realise real-time hybrid tests.

During a PsD test, the dynamic equations of motion of the idealised structure are solved in the time domain by numerical integration. The inertia and damping properties are numerical inputs, as well as the external loading the structure is subject to (typically the particular earthquake record considered). However, the displacement at each node of the idealised structure, worked out from the time integration process, is physically applied by an actuator in a quasi-static manner. When the displacement command has been imposed, the restoring force is measured and used in the numerical model as the missing stiffness term to carry on the test with the next time step. Slow loading of the structure is important so as not to excite its inertial and damping properties, which are already accounted for computationally (Mahin *et al.* 1989; Shing *et al.* 1996; Molina *et al.* 2002). If non-linear hysteretic behaviour occurs in the specimen, the energy dissipation is automatically taken into account and the amount of viscous damping – typically difficult to estimate with accuracy – chosen in the numerical model becomes less critical (Mahin *et al.* 1989).

In simple terms, a PsD test can be thought of as a computational structural dynamics analysis in which the stiffness term is measured from a corresponding physical specimen. Note that during a conventional PsD test, a pause is often made after each displacement step in order to inspect the specimen for failures. Careful monitoring of failure propagation is therefore possible. The PsD method is also referred to as “online” testing.

In the case of PsD testing, the facilities usually have specifications in terms of load capabilities (both in shear force and bending moment) of the reaction wall and of the actuators. The actual size of the reaction wall is also important to accommodate large scale structures (Williams & Blakeborough 2001). For instance, the reaction wall at the European Laboratory for Structural Assessment (ELSA – Pegon & Pinto 2000) is 16m high, 20m long and 4m thick.

### 2.1.3- Pros and cons of shaking table and PsD testing methods

The two test methods presented above can be considered as forming the basis of the dynamic laboratory testing of structures. A critical analysis of shaking table testing compared with PsD testing raises the following comments.

While shaking table testing better represents live earthquake experience inside a laboratory, it is also more expensive and involves more hardware, as well as control issues to realise the correct motions in real-time (Williams & Blakeborough 2001). Due to the cost of the facilities, shaking table testing is often conducted with reduced scale specimens. The advantages are that large structures can be modelled in normal size laboratories and that it reduces the magnitude of the testing loads. But scaling introduces errors. Similitude analysis shows that the slightest scaling factor cannot conserve all properties and therefore introduces discrepancies (Nakashima 2001), notably in the fidelity of ductility and yielding properties of materials such as RC. As soon as the full size cannot be modelled, shaking table testing is compromised by the scaling extrapolation of the results. Therefore, considerable facilities to test at large scales are needed, such as the newly completed and unique 6-axis E-Defense table at Miki City, Japan. It should be noted, however, that in shaking table testing only base vibration is introduced and loads due to wind for example cannot be modelled (Darby *et al.* 2001).

On the other hand, PsD testing allows better inspection of the failure mode of the structure and is conducted with simpler static hydraulic actuators. Such equipment can produce higher forces than dynamically rated equipment for a given cost, making it possible to avoid scaling. The relevance for civil engineering applications is therefore high (Nakashima 2001; Molina *et al.* 2002). But due to PsD testing being conducted on an extended time-scale, it cannot represent properly the dynamics of the specimen – like strain-rate effects or resonance amplifications (Williams *et al.* 1998; Williams & Blakeborough 2001). Moreover, a PsD test is based on the assumption that the structure can be approximated by a lumped mass system. This is a limitation of pseudo-dynamic testing as not all structures can be accurately regarded as such (Mahin *et al.* 1989; Darby *et al.* 2001).

The problem of asynchronous testing should also be mentioned here as a shortcoming for both the shaking table and PsD methods. Indeed, in the case of the first one, a separate table is needed for each input, making the experiment very expensive for equipment and laboratory layout requirements. In the case of the PsD method, asynchronous testing can only be carried out in conjunction with substructuring and if each physical substructure is only directly loaded by one external input at the most. This, for instance, allows the PsD experiment of a bridge with different inputs at each pier where the whole deck constitutes the numerical substructure (Pegon & Pinto 2000) but would not allow one section of the deck between two piers to be included physically. Both methods have fundamental pros and cons and it should be noted that some laboratories progress towards combining shaking tables with PsD facilities.

### 2.1.4- Effective force testing

Another basic method for the seismic testing of structures is also under development. In the effective force testing (EFT) method, the test setup is very similar to that of the PsD method. However, the actuators used are dynamically rated and force controlled.

The load applied onto the physical specimen in real-time by the actuators is calculated as the earthquake acceleration record multiplied by the lumped masses of the structure. The loading can be determined in advance of the test and no numerical integration is needed, unlike in a PsD test (Dimig *et al.* 1999; Williams & Blakeborough 2001). For this reason, the EFT principle is very appealing. It requires a fairly simple test setup allowing testing of large structures.

However, as for PsD testing, the EFT method is only valid for structures that can be represented as lumped mass systems. Moreover, because the inertial properties are physically excited, the whole structural mass is needed to conduct an EFT test. But the major limitation of EFT lies in the inability of hydraulic actuators to produce a force at the natural frequency of a lightly damped structure. By fully understanding the hydraulic actuation system characteristics, some compensating solutions based on the introduction of an additional velocity feedback loop within the control system were proposed (Dimig *et al.* 1999; Zhao *et al.* 2003, 2005).

Recently, Yu *et al.* (2005) have adapted the principle of the EFT method to conceptualise the so-called linear shaker seismic simulation (LSSS) test method. It uses a linear shaker to input inertial forces directly onto the structure so as to replicate the earthquake loading at the most critical points.

### 2.1.5- PsD with substructuring

The PsD method has been implemented with the concept of substructuring (Pegon & Pinto 2000). This concept is based on splitting the structure considered into two or more substructures and conducting separate analyses on each part, while making sure the interface constraints are continuously verified both in terms of displacements and forces. The idea behind applying this to structural testing is to subject a sensitive part of the structure to the physical quasi-static loading while the rest of the structure is numerically simulated, along with the inertial and damping characteristics of the sensitive part.

The technique has been applied to studying bridges (Buchet & Pegon 1994). In this experiment, the deck is the numerical substructure, while the four piers are physically tested for their stiffness components. Therefore, the largest part of the bridge, assumed to behave linearly, does not have to be physically present, while the piers can be accommodated in the laboratory for non-linear testing. This also allowed an earthquake asynchronous motion to be applied.

It was also used to study base isolated buildings (Molina *et al.* 2002). However, in this experiment, the physical substructure (the base isolators) exhibited coupled stiffness and damping behaviour. In order to perform the quasi-static PsD test, a series of characterisation tests was first undertaken so the full behaviour of the base isolating devices could be empirically worked out. Using these results, the restoring force was constantly corrected during the test according to the velocity difference. This illustrates the limits of the slow PsD method, requiring to pre-characterise the component of interest beforehand because it cannot be accurately excited at low velocities.

A major advantage of the substructuring technique is that it allows only the part of main interest to be physically tested, thereby providing infinite repeatability of the remainder. The creation of the substructure interface makes the experiment more difficult to realise, by typically having to control a larger number of statically rated actuators.

### 2.1.6- Real-time substructure testing

#### 2.1.6.1- New convergence towards RTS

A further development was to conduct a substructure PsD test on less extended time scales. The inspection pause can easily be removed from the algorithm, but this is not enough as the actuator still has to stop and remain in position while the numerical model works out the next step command (Nakashima *et al.* 1992). This shortcoming has been addressed in several ways. The same authors have used a twin time integration system and a memory buffer in order to always keep the following set of command signals until they are needed. Another system was later developed with the use of extrapolations and interpolations governed by multi-tasking routines (Nakashima & Masaoka 1999; Nakashima 2001). Magonette (2001) has presented a similar sub-stepping routine for continuous PsD tests. More importantly, the loading rate needs to be increased through the use of dynamically rated actuators. Fast-online tests have also been carried out on shorter – but still extended – time-scales. Note that the damping and inertial forces generated from the physical specimen can then neither be ignored nor regarded as exact since the loading rate is scaled and the real-time scale becomes a necessary target. When such a real-time experiment is conducted, the damping and inertial properties of the specimen are no longer computed but are fully accounted for through the measured force feedback. Therefore, the PsD description is not accurate and the term RTS ought to be used instead. Following the original inception of the PsD method in the 1970s as an easier way to realise dynamic experiments than the RTS method (Takanashi & Nakashima 1987), the maturity of the hardware has again enabled engineers to perform dynamic tests.

Shaking table testing can also use the substructuring technique to conduct RTS tests. This can be achieved with additional actuators where the shaking table accommodates the bottom part of a structure and the actuators impose the interface conditions computed by the top part in real-time (Kobayashi & Tamura 2000). It can also be done by using the shaking table itself as the transfer system between the numerical and physical substructures (Horiuchi *et al.* 2000; Igarashi *et al.* 2002; Stoten *et al.* 2002; Neild *et al.* 2002, 2005). These methods are regarded by many shaking table laboratory researchers as the way forward to encompass the limitations of pure shaking table testing and important investments towards state of the art facilities are being made (Reinhorn *et al.* 2002).

An RTS test is therefore a hybrid method involving a physically tested part and a numerically modelled part, the two substructures being complementary to form the complete emulated structure. During the real-time dynamic test, both substructures send and receive data from each other, because they need to know the state of the other to work out their own. The interface between the substructures is realised with fast communication and dynamic hydraulic actuation. A simplistic view of an RTS test is shown in Figure 2.1. Practically, this is usually achieved by the numerical substructure generating a strain state of a physical substructure, this strain state being applied and the reaction force being sent back to the numerical model to carry on the real-time simulation.

RTS testing is especially convenient to study the behaviour of structures that contain highly non-linear and/or rate-dependent parts within them, those regions being subjected to physical testing (Williams *et al.* 1998; Horiuchi *et al.* 1999). As the testing is in real-time, the full properties can be excited and measured. This allows one to concentrate on the behaviour and performance of a specific part of interest, while having the rest of the structure modelled separately with infinite repeatability. Bespoke RTS tests have already been performed, proving that the technique is viable (Darby *et al.* 1999; Horiuchi *et al.* 1999; Nakashima & Masaoka 1999; Blakeborough *et al.* 2001; Williams & Blakeborough 2002).

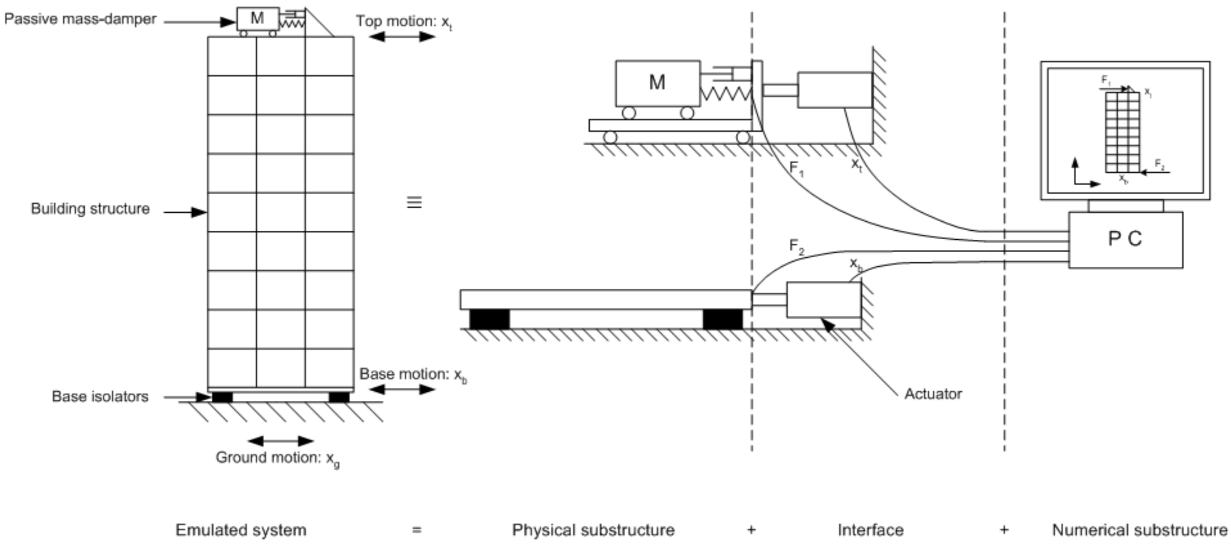


Figure 2.1: Conceptual view of an RTS test

2.1.6.2- Actuator control strategy

Theoretically, dynamic actuators can either be controlled in displacement or in force. However, the vast majority of RTS tests conducted so far have been realised in displacement control. This is more directly applicable, as most numerical methods work out displacement variables from knowledge of the forces. Such a choice is also safer in the case of a catastrophic failure in the physical substructure. Finally, for physical substructures that contain a significant level of inertial forces, force control can be more arduous.

On the other hand, force control has potential advantages. Since civil engineering structures only experience small displacements which produce high forces, controlling on force could be easier than controlling on displacement. Also, when several actuators interact, a hybrid control method where some actuators are displacement controlled and some are force controlled may prove advantageous. Blakeborough has implemented such a strategy in real-time for dissipative devices (Molina *et al.* 2006). Recently, Pan *et al.* (2005*a*) have presented two mixed-control strategies for the application to PsD testing. However, the use of hydraulic dynamic actuators has shown that important limitations exist in dynamic force control (Dimig *et al.* 1999; Zhao *et al.* 2003) and work is needed for force control to be reliable in real-time. To circumvent these problems, Reinhorn *et al.* (2004) have devised a concept where, through the use of a compliant element, the hybrid test outer-loop control would be realised with a force feedback while the inner-loop control of the actuator would be conducted under displacement feedback. In the rest of this thesis, displacement is assumed to be the chosen control mode.

## 2.2- TIME-INTEGRATION NUMERICAL METHODS

### 2.2.1- Introduction – Two types of method

The aim of this section is to review the various numerical methods that could be used for time integration during an RTS test. Many of the references in this section treat the application of time integration to conventional PsD testing. However, the numerical problem is similar to that posed during an RTS test. Instead of being measured, the restoring force is numerically computed (the stiffness behaviour is known) and the outside forces include an additional term representing the interface with the physical substructure.

During an RTS test, the numerical substructure needs to contribute its response "continuously". For a MDOF system, this consists of solving the set of differential equations of motion:

$$\mathbf{M}\,\mathbf{a} + \mathbf{C}\,\mathbf{v} + \mathbf{K}\,\mathbf{d} = \mathbf{f} + \mathbf{F} \tag{2.1}$$

where **M**, **C** and **K** are respectively the mass, damping and stiffness matrices, **a, v** and **d** are respectively the vectors of nodal accelerations, velocities and displacements for the degrees of freedom, and **f** and **F** are respectively the vectors of substructure interface and outside forces. Initially, **M**, **C**, **K** and **F** are known entities. Note however that **K** and **C** may change during the analysis. **M** will be regarded as a constant, assuming mass conservation even during failures.

With a dynamic system, the response depends not only on the system itself and on the external input but also on its time history. (For a thorough reference on structural dynamics, see Clough & Penzien (1995) or Battini (2003)). The response of the numerical substructure depends on the physical substructure response over time, which is not known in advance. Therefore, the problem cannot be solved analytically. Instead, time is discretised and the integration of the equation of motion is done numerically, assuming idealised properties over small time steps. These properties, depending on the scheme considered, are obtained through difference equations, which can be written in the form:

$$\mathbf{d}_{n+1} = g\,(\,\mathbf{d}_n\,,\,\mathbf{v}_n\,,\,\mathbf{a}_n\,,\,\mathbf{d}_{n-1}\,,\,\mathbf{v}_{n-1}\,,\,\mathbf{a}_{n-1}\,,\,\ldots\,) \tag{2.2}$$

or

$$\mathbf{d}_{n+1} = h\,(\,\mathbf{v}_{n+1}\,,\,\mathbf{a}_{n+1}\,,\,\mathbf{d}_n\,,\,\mathbf{v}_n\,,\,\mathbf{a}_n\,,\,\mathbf{d}_{n-1}\,,\,\mathbf{v}_{n-1}\,,\,\mathbf{a}_{n-1}\,,\,\ldots\,) \tag{2.3}$$

where the subscripts denote the incremental time steps considered.

The various numerical schemes can be classified in two types: explicit or implicit. An explicit scheme yields the left hand term in (2.2) for the time-step ($n$+1) based exclusively on values from time-step ($n$) or earlier, while an implicit scheme also exhibits a dependency on one or several values from step ($n$+1) as in (2.3). An implicit scheme, because of its causality, involves a more complex implementation than an explicit one, often comprising an iterative process or a predictor/corrector algorithm.

Because the numerical integration has to be very fast in a real-time test for stability reasons, it can be argued that the scheme should preferably be explicit (Blakeborough *et al.* 2001). Moreover, iterations can be undesirable for substructure testing as they might anticipate failure and therefore cause non-realistic stiffness measurements for the rest of the test (Algaard 2001). Iterations may also cause partial unloading within a step and produce errors in physical substructure force reading, affecting overall accuracy.

However, the fact that an implicit scheme relies on a future term makes it more stable, regardless of the chosen time-step length. In fact, there is a generally shared consensus that explicit schemes are always conditionally stable and that most implicit schemes are unconditionally stable (Shing *et al.* 1996). In other words, an explicit scheme will need a time step short enough to ensure the stability of the scheme, while the stability of an implicit scheme will not depend on the time step chosen because it is partially based on a term from the end of the step considered.

For earthquake engineering applications, the interesting response of structures is in the 0 to 10Hz range, since this is where the ground motion might excite the fundamental resonance. For accuracy reasons, it is generally considered that ten steps are needed per cycle of the shortest period *of interest* (which may not be the shortest period of the structure) (Algaard 2001). Thus, a time step in the order of 10ms can be regarded as necessary (Nakashima & Masaoka 1999). However, for stability reasons when using conditionally stable schemes, the time step should not be larger than the shortest natural period of the structure – which may be of little significance for MDOF systems – divided by $\pi$ (Algaard 2001). Depending on the highest natural frequency of the structure considered, the stability criterion will either be more stringent or more flexible than the accuracy criterion.

The number of DOFs in the structure has a major importance here, as it will largely influence the stability criterion. The more DOFs that are present, the higher the maximum natural frequency is likely to be. And therefore the more severe the stability criterion for a conditionally stable scheme is. Thus, conditionally stable schemes are often used for single degree of freedom (SDOF) numerical substructures, but can become difficult to implement for MDOF ones, unless a very fine step can be used (Shing *et al.* 1996; Chang 2002*b*). On a similar note, an unconditionally stable integration scheme is essential when the structure has rotational degrees of freedom with no inertia.

Being based on a feedback loop, the RTS method is subject to experimental errors, which have two major causes (Bursi & Shing 1996):

- A displacement control error occurs when the actuator displacement achieved is different from the target set by the numerical scheme.
- A force measurement error occurs when reading the load from the specimen, due to imperfections of sensor technology, electrical noise and possible oscillations.

For a real-time test using hydraulic actuation, provided good quality force transducers are used, the second point is typically negligible and the term *experimental errors* will be used to denote actuation control errors. Experimental errors can be of systematic types like undershooting (actuator movement regularly falling short of the required displacement) or overshooting (the opposite) (Algaard 2001). Such systematic errors need to be monitored as they can propagate and accumulate during an RTS test (Shing and Mahin 1990) and potentially cause spurious higher structural mode excitation (Shing and Mahin 1987*a*). This problem can be increased by using very fine time steps as a large number of steps will increase the likelihood of accumulation.

If non-linear MDOF numerical substructures are to be modelled, the computation of the stiffness matrix will increase the CPU time needed at each step. This is another major limitation of conditionally stable schemes.

However, using a long time step also introduces shortcomings. In such a case, the real dynamics of the system might not be continuously reproduced, but rather suddenly executed at the start of the time step and then the system may remain “static” for the rest of the time step until the next input is being sent. This can be solved by having the input into the actuators quadratically interpolated between two main time-steps (Darby *et al.* 2001), making the actuator move continuously from one main time step to the next.

The following sections present the most common numerical schemes used for structural analysis. For each scheme, the stability and accuracy properties are discussed. As discussed previously, stability is linked to the explicit or implicit type of scheme chosen, to the time step used and to the sensitivity to propagation of errors. The stability can also be affected by the numerical dissipation produced by the difference equations of the scheme itself. Numerical dissipation is often a necessary evil in time-domain discretisation, adding both stability and error to the finite difference schemes. The schemes are also considered in terms of the amount of computation involved and their suitability to RTS testing. Another important criterion is the ability of the schemes to handle non-linear numerical substructures.

### 2.2.2- Central difference method

The central difference method (CDM) is probably the most popular time integration scheme for PsD and RTS testing (Nakashima *et al.* 1992; Shing *et al.* 1996; Horiuchi *et al.* 1999; Nakashima & Masaoka 1999; Kobayashi & Tamura 2000; Algaard 2001 Darby *et al.* 2001, 2002; Horiuchi & Konno 2001; Zhao *et al.* 2003). It can be mathematically described with Equations (2.4).

$$\begin{aligned}
&\mathbf{Ma}_n + \mathbf{Cv}_n + \mathbf{Kd}_n = \mathbf{f}_n + \mathbf{F}_n \\
&\mathbf{a}_n = \frac{1}{T^2}(\mathbf{d}_{n+1} - 2\mathbf{d}_n + \mathbf{d}_{n-1}) \\
&\mathbf{v}_n = \frac{1}{2T}(\mathbf{d}_{n+1} - \mathbf{d}_{n-1})
\end{aligned} \tag{2.4}$$

where $T$ is the integration time step chosen.

The CDM is explicit. By substituting the acceleration and velocity terms from the difference equations into the equation of motion, the next step displacement vector $\mathbf{d}_{n+1}$ can be isolated and expressed as a function of terms known from the two previous time steps (Darby *et al.* 2001). It is very simple to implement and fast to compute (Kobayashi & Tamura 2000). Time steps as short as 0.5ms have been used (Horiuchi *et al.* 1999). Moreover, this scheme allows the easy introduction of a non-linear stiffness. Indeed, with the displacement being worked out from previous steps only, the stiffness matrix can be updated accordingly for the next calculation to take the non-linearity into account. Non-linear damping can also be introduced, but because the velocity is only determined with a one step delay, only a fairly simple non-linear damping behaviour could be accommodated without an iterative process. Alternatively, Wu *et al.* (2004, 2005) have proposed a modified CDM formulation to be used with non-linear damping.

The CDM exhibits no numerical dissipation (energy stable scheme) and generates no amplitude error. However, it produces a periodicity error (period shortening) increasing with the time step (Algaard 2001). For error propagation purposes, when using the CDM, it is better to use the computed displacements rather than the experimentally measured ones to compute the next step displacement (Shing *et al.* 1996).

This method is only conditionally stable. For a structure with a maximum circular natural frequency $\omega_{max}$, the time step $T$ must satisfy the condition:

$$\omega_{max} T < 2 \tag{2.5}$$

which can also be written:

$$T < \frac{\tau_{min}}{\pi} \tag{2.6}$$

where $\tau_{min}$ is the shortest natural period.

During an RTS test, at the end of a time step, the actuator force is measured before the next step command signal can be generated and sent out. So a potential time delay exists that can prevent the real-time character of the test method. To get around this problem, Nakashima *et al.* (1992) have used two integration schemes running in parallel, each based on the central difference method. The method is called the “staggered integration method”. In this numerical setup, $\mathbf{d}_{n+2}$ is worked out from $\mathbf{d}_n$, $\mathbf{d}_{n-2}$ and $\mathbf{f}_n$. It is sent to the actuator as soon as computed, shortly after the start of step ($n$), well before reaching ($n$+1), and is applied as a ramp function over the whole step length. When reaching ($n$+1), $\mathbf{d}_{n+3}$ is worked out with $\mathbf{d}_{n+1}$, $\mathbf{d}_{n-1}$ and $\mathbf{f}_{n+1}$. As soon as this is done, this new command signal is sent to the actuator and replaces the previous one before it is finished, thereby eliminating the pause effect. Although the two integrations seem to run in parallel, they only take a fraction of the step to compute, so one is always finished well before the other one starts. This setup, however, doubles the effective integration step, which may cause instability, especially for MDOF systems.

## 2.2.3- Newmark implicit scheme

Newmark (1959) proposed a numerical integration scheme that was to become the basis of a whole family of successful methods. It is mathematically described by:

$$\begin{aligned}
&\mathbf{Ma}_{n+1} + \mathbf{Cv}_{n+1} + \mathbf{Kd}_{n+1} = \mathbf{f}_{n+1} + \mathbf{F}_{n+1} \\
&\mathbf{d}_{n+1} = \mathbf{d}_n + T\mathbf{v}_n + T^2\left(\frac{1}{2}-\beta\right)\mathbf{a}_n + T^2\beta\mathbf{a}_{n+1} \\
&\mathbf{v}_{n+1} = \mathbf{v}_n + (1-\gamma)T\mathbf{a}_n + \gamma T\mathbf{a}_{n+1}
\end{aligned} \tag{2.7}$$

The choice of $\beta$ and $\gamma$ in the two finite difference equations shifts the position of the equilibrium within the step by weighting the acceleration terms. Numerical damping can be introduced in the scheme (with $\gamma > 0.5$), but this reduces the order of accuracy to 1.

For better numerical properties, Hilber (Hilber 1976; Hilber *et al.* 1977) coupled the $\beta$ and $\gamma$ parameters by a third parameter, $\alpha$, which is also used to shift the equilibrium point of the equation of motion. The following scheme results, also referred to as the $\alpha$-method:

$$\begin{aligned}
&\mathbf{Ma}_{n+1} + (1+\alpha)\mathbf{Cv}_{n+1} - \alpha\mathbf{Cv}_n + (1+\alpha)\mathbf{Kd}_{n+1} - \alpha\mathbf{Kd}_n = (1+\alpha)\mathbf{f}_{n+1} + (1+\alpha)\mathbf{F}_{n+1} - \alpha\mathbf{f}_n - \alpha\mathbf{F}_n \\
&\mathbf{d}_{n+1} = \mathbf{d}_n + T\mathbf{v}_n + T^2\left(\frac{1}{2}-\beta\right)\mathbf{a}_n + T^2\beta\mathbf{a}_{n+1} \\
&\mathbf{v}_{n+1} = \mathbf{v}_n + (1-\gamma)T\mathbf{a}_n + \gamma T\mathbf{a}_{n+1} \\
&\gamma = \frac{1}{2} - \alpha \\
&\beta = \frac{(1-\alpha)^2}{4}
\end{aligned} \tag{2.8}$$

For most values of $\alpha$, $\beta$ and $\gamma$ this method is implicit, as the displacement vector $\mathbf{d}_{n+1}$ can only be defined in terms of the acceleration at ($n$+1). When $\alpha < 0$ (or $\gamma > 0.5$), the method produces some numerical dissipation while still featuring second order accuracy (Hughes 1983). This numerical damping is typically advantageous because it grows with the square of the frequency considered. Therefore, such dissipation opposes the accumulation of experimental errors at high frequencies while not affecting the response of interest in the low modes.

When -1/3 < $\alpha \leq 0$, the scheme is also unconditionally stable. Therefore, this scheme offers very good stability and dissipation properties, making it attractive, especially for solving systems with many DOFs and/or high frequencies of interest.

Due to its implicit character, the general Newmark scheme has so far only been used for PsD. For a non-linear numerical substructure, a modified Newton iteration procedure is used based on a stiffness predictor term that should always remain higher than or equal to the actual tangent stiffness of the structure for unconditional stability (Shing *et al.* 1991). To start the iterations, the stiffness predictor is set to the initial stiffness of the system. A convergence tolerance is needed and usually set as a percentage of the expected maximum displacement of the structure. The tolerance should be tightened according to the importance of non-linearity in the structure (Bursi & Shing 1996). Note that this method applied to RTS is still implicit even with a linear numerical substructure since the interface force is not known. Moreover, the iterations can imply unnecessary loading/unloading that would render a real-time test very inaccurate. To solve this problem, the adoption of a small reduction factor is proposed (Shing *et al.* 1991).

Thewalt & Mahin (1995) have described an alternative experimental method to solve the Newmark implicit scheme during a PsD test. The iterative process for calculation of the implicit terms is replaced by a direct analogue feedback of the measured restoring force into the command signal. This is physically realised by using a summing amplifier. The explicit part of the displacement is implemented and the corresponding restoring force voltage from the specimen is multiplied by a conversion matrix to produce the implicit part of the displacement command signal. This signal is then added to the explicit part of the displacement command signal using the same summing amplifier. This procedure allows the implicit scheme to be performed without iteration. A slow PsD test was conducted with this method and produced good results.

Other schemes have been derived from the original Newmark implicit method. Interested readers can refer to Garcia de Jalon & Bayo (1994) and Bajer (2002).

## 2.2.4- Constant average acceleration method

The constant average acceleration method (CAAM) can be derived from the Newmark implicit scheme by introducing $\alpha = 0$ (hence $\beta = 0.25$ and $\gamma = 0.5$). The equations therefore become:

$$\begin{aligned} &\mathbf{Ma}_{n+1} + \mathbf{Cv}_{n+1} + \mathbf{Kd}_{n+1} = \mathbf{f}_{n+1} + \mathbf{F}_{n+1} \\ &\mathbf{d}_{n+1} = \mathbf{d}_n + T\mathbf{v}_n + \frac{T^2}{4}(\mathbf{a}_n + \mathbf{a}_{n+1}) \\ &\mathbf{v}_{n+1} = \mathbf{v}_n + \frac{T}{2}(\mathbf{a}_n + \mathbf{a}_{n+1}) \end{aligned} \tag{2.9}$$

The CAAM is implicit and has the lowest frequency distortion of all the unconditionally stable second order accurate schemes (Bursi & Shing 1996). It does not produce any numerical damping, which can be regarded as ideal from an accuracy point of view, but means that it is prone to instabilities due to experimental errors. This is the main limitation of this scheme compared to the general Newmark implicit scheme.

The error propagation properties of the CAAM for PsD tests of linear and non-linear systems have been studied by Chang (2005). Also, Shing *et al.* (1996) have used this method for a slow PsD test with a modified Newton iterative algorithm. The residual errors are limited by the use of a correcting method where the difference between the target displacement and the achieved displacement is multiplied by the initial stiffness of the structure and added to the restoring force.

Bayer *et al.* (2000, 2002, 2005) developed a digital version of the algorithm proposed by Thewalt & Mahin (1995) and used it for conducting RTS tests with linear numerical substructure models for aerospace engineering applications, using a small capacity electro-dynamic shaker. A sub-step algorithm was developed so as to replicate the analogue feedback. Again, this succeeds in avoiding iterations within each step. The explicit part of the control signal is computed at the beginning of the time step and applied as a ramp over the whole of the time step. The implicit part varies within the time step. It is evaluated and applied at each sub-step by addition over the explicit ramp. The sub-step algorithm proposed is shown to produce good experimental results, even though stability beyond the common limit was not proven. The application presented by Bayer *et al.* is one of the very few where an implicit scheme was effectively used to conduct an RTS test.

## 2.2.5- Newmark explicit scheme

The Newmark explicit scheme is derived from the Newmark implicit scheme by introducing $\beta = 0$ and $\gamma = 0.5$:

$$\begin{aligned}
&\mathbf{Ma}_{n+1} + \mathbf{Cv}_{n+1} + \mathbf{Kd}_{n+1} = \mathbf{f}_{n+1} + \mathbf{F}_{n+1} \\
&\mathbf{d}_{n+1} = \mathbf{d}_n + T\mathbf{v}_n + \frac{T^2}{2}\mathbf{a}_n \\
&\mathbf{v}_{n+1} = \mathbf{v}_n + \frac{T}{2}(\mathbf{a}_n + \mathbf{a}_{n+1})
\end{aligned} \tag{2.10}$$

The first difference equation is used to work out explicitly the command signal for step ($n$+1) to be imposed on the specimen. The force vector $\mathbf{f}_{n+1}$ is measured and the combination of the equation of motion and of the second difference equation is used to work out $\mathbf{a}_{n+1}$ and $\mathbf{v}_{n+1}$, necessary to carry on the scheme for ($n$+2).

Similarly to the CDM, the vector $\mathbf{d}_{n+1}$ is worked out explicitly, thus allowing non-linear stiffness to be introduced in the numerical substructure without any need for iterations. Note however that the velocity vector expression is implicit, so the damping property is ideally linear for an efficient use of this scheme.

Unlike the CDM, the Newmark explicit scheme has the minor advantage that it does not require any start up procedure as it does not need information from the ($n$-1) time step (Algaard 2001). Like the CDM, it is only stable on the condition that $T < \tau_{\min} / \pi$ (Thewalt & Mahin 1995), so is not always suitable for MDOF systems. It has no numerical dissipation and very low frequency distortion provided a fine time-step is used. The frequency distortion has been shown to be even lower than that of the CAAM provided that $T < 0.3\ \tau_{\min}$ (Chang 2002*b*). Note that the Newmark explicit scheme can be made dissipative but this is not advantageous as response to the lower modes would be affected too (Algaard 2001). The error propagation properties of the Newmark explicit scheme have been shown by Shing & Mahin

(1990) to be more favourable than those of the CDM. More recently, Chang (2003) analysed those properties for non-linear PsD experiments.

An interesting development from the Newmark explicit scheme was proposed by Chang (2002*b*). Two parameters $\boldsymbol{\beta}_1$ and $\boldsymbol{\beta}_2$ are introduced in the displacement difference equation. The defining equations for the scheme are:

$$\begin{aligned}
&\mathbf{M}\mathbf{a}_{n+1} + \mathbf{C}\mathbf{v}_{n+1} + \mathbf{K}\mathbf{d}_{n+1} = \mathbf{f}_{n+1} + \mathbf{F}_{n+1} \\
&\mathbf{d}_{n+1} = \mathbf{d}_n + \boldsymbol{\beta}_1 T\mathbf{v}_n + \boldsymbol{\beta}_2 T^2 \mathbf{a}_n \\
&\mathbf{v}_{n+1} = \mathbf{v}_n + \frac{T}{2}(\mathbf{a}_n + \mathbf{a}_{n+1})
\end{aligned} \tag{2.11}$$

The careful choice of $\boldsymbol{\beta}_1$ and $\boldsymbol{\beta}_2$ allows remarkable properties to be achieved by this explicit scheme. Their definitions are:

$$\begin{aligned}
&\boldsymbol{\beta}_1 = [\mathbf{I} + \frac{1}{2}T\mathbf{M}^{-1}\mathbf{C} + \frac{1}{4}T^2\mathbf{M}^{-1}\mathbf{K}_0]^{-1} \times [\mathbf{I} + \frac{1}{2}T\mathbf{M}^{-1}\mathbf{C}] \\
&\boldsymbol{\beta}_2 = \frac{1}{2}[\mathbf{I} + \frac{1}{2}T\mathbf{M}^{-1}\mathbf{C} + \frac{1}{4}T^2\mathbf{M}^{-1}\mathbf{K}_0]^{-1}
\end{aligned} \tag{2.12}$$

Note that $\boldsymbol{\beta}_1$ and $\boldsymbol{\beta}_2$ are determined from the initial stiffness matrix of the structure $\mathbf{K}_0$, and are therefore constant during the test.

Chang (2002*b*) conducted some analytical work on this proposed explicit method, which shows that its numerical properties are similar to those of the constant average acceleration method. The scheme is said to be unconditionally stable, to exhibit no numerical dissipation and to have no overshooting effect. However, this is only demonstrated for a linear structure, where $\mathbf{K}_0$ represents the constant stiffness.

Both simulation work and PsD tests show the proposed method is indeed stable for large steps, well beyond the limit for conditionally stable explicit schemes. This work also shows that the proposed method offers little error propagation and more importantly, unlike the Newmark explicit and the CDM, the error propagation does not increase dramatically when $\omega_{\max} T > 1.5$, which further confirms the unconditional stability of the scheme. The method was also shown to behave accurately for a non-linear PsD specimen with forced experimental error.

This method seems to break through the usual assumption that an explicit scheme cannot be unconditionally stable, which makes it a very good candidate for RTS testing. However, the method was only compared to other explicit methods, so more challenging comparisons should be undertaken.

### 2.2.6- Operator-splitting method

The operator-splitting method (OSM) is defined by the following equations:

$$
\begin{aligned}
&\mathbf{M}\mathbf{a}_{n+1} + \mathbf{C}\mathbf{v}_{n+1} + \mathbf{K}\mathbf{d}_{n+1} = \mathbf{f}_{n+1} + \mathbf{F}_{n+1} \\
&\mathbf{d}_{n+1} = \tilde{\mathbf{d}}_{n+1} + \frac{T^2}{4}\mathbf{a}_{n+1} \\
&\tilde{\mathbf{d}}_{n+1} = \mathbf{d}_n + T\mathbf{v}_n + \frac{T^2}{4}\mathbf{a}_n \\
&\mathbf{v}_{n+1} = \mathbf{v}_n + \frac{T}{2}\left(\mathbf{a}_n + \mathbf{a}_{n+1}\right)
\end{aligned}
\tag{2.13}
$$

The mathematical formulation of this scheme is equivalent to that of the CAAM. However, the displacement difference equation is rearranged to form a predictor term from the explicit parts and a correcting term from the implicit part. The scheme is implemented for slow PsD testing without iterations through the application of the predictor displacement $\tilde{\mathbf{d}}_{n+1}$. The corresponding predictor restoring force $\tilde{\mathbf{f}}_{n+1}$ is measured and the remaining implicit terms are expressed by the supplementary Equation (2.14) using the predictor stiffness matrix $\tilde{\mathbf{K}}$.

$$
\tilde{\mathbf{K}} \cdot \tilde{\mathbf{d}}_{n+1} - \tilde{\mathbf{f}}_{n+1} = \tilde{\mathbf{K}} \cdot \mathbf{d}_{n+1} - \mathbf{f}_{n+1} \tag{2.14}
$$

The application of the OSM to PsD testing is rendered possible by Equation (2.14), assuming the force measured from the specimen for the predictor displacement provides a good indication of how the specimen would react to the full displacement.

For this method to be unconditionally stable during a PsD test, the predictor stiffness must be higher than or equal to the tangent stiffness. If the tangent stiffness is not known, an estimate based on the initial stiffness can be used for elements with strain hardening properties. This scheme is suitable for working with non-linear numerical substructures. However, highly variable stiffness can add noticeable inaccuracies to the predictor-corrector process.

Similarly to developments of the Newmark implicit scheme, the introduction of $\alpha$-damping has been proposed for the OSM. The $\alpha$-operator-splitting method ($\alpha$-OSM) is mathematically expressed by:

$$
\begin{aligned}
&\mathbf{M}\mathbf{a}_{n+1} + (1+\alpha)\mathbf{C}\mathbf{v}_{n+1} - \alpha\mathbf{C}\mathbf{v}_n + (1+\alpha)\mathbf{K}\mathbf{d}_{n+1} - \alpha\mathbf{K}\mathbf{d}_n = (1+\alpha)(\mathbf{f}_{n+1} + \mathbf{F}_{n+1}) - \alpha(\mathbf{f}_n + \mathbf{F}_n) \\
&\mathbf{d}_{n+1} = \tilde{\mathbf{d}}_{n+1} + T^2\beta\mathbf{a}_{n+1} \\
&\tilde{\mathbf{d}}_{n+1} = \mathbf{d}_n + T\mathbf{v}_n + T^2\left(\frac{1}{2} - \beta\right)\mathbf{a}_n \\
&\mathbf{v}_{n+1} = \mathbf{v}_n + (1-\gamma)T\mathbf{a}_n + \gamma T\mathbf{a}_{n+1} \\
&\gamma = \frac{1}{2} - \alpha \\
&\beta = \frac{(1-\alpha)^2}{4}
\end{aligned}
\tag{2.15}
$$

Similarly to the implicit Newmark scheme, the $\alpha$ parameter is chosen to produce advantageous numerical damping varying with the square of the frequency to damp out the part of the response due to experimental errors. This ability to adjust the numerical damping easily is very attractive. The $\alpha = 0$ choice implies no numerical damping and a response that may be affected by higher mode contributions.

The $\alpha$-OSM is relatively sensitive to experimental errors. So, in a PsD test, an I-modification algorithm is often used with the $\alpha$-OSM to correct the displacement control errors (Bursi & Shing 1996). This algorithm simply amends the restoring force vector according to the known displacement error and to the predictor stiffness.

Bursi & Shing (1996) and Combescure & Pegon (1997) have extensively compared the Newmark implicit method (used with a Newton iterative correction procedure) and the $\alpha$-OSM in comparable simulations and slow PsD tests of linear or non-linear systems. Both methods showed good results, but in the majority of the tests, the benefit of the Newmark implicit method over the $\alpha$–OSM was noticeable. As a summary of these comparisons, one can say that the Newmark implicit scheme with an iterative process may require slightly longer computations than the $\alpha$-OSM but is shown to have similar stability properties and to be more accurate, especially for highly non-linear systems.

More recently, Bonelli & Bursi (2004) have presented developments of generalised-$\alpha$ predictor-corrector methods for PsD testing and Zhang *et al.* (2005) have developed a predictor-corrector scheme that is explicit thanks to the use of polynomial extrapolation techniques. Finally, Wu *et al.* (2006) have studied the application of the OSM to systems with non-linear damping and have proposed an updated formulation of the OSM to render the scheme explicit for such systems.

## 2.2.7- Integral form

All the methods discussed so far were presented with the original second order form of the equation of motion. However, a lot of work has been conducted using an integrated first order form of the equation (Chang 1998, 2001; Chang *et al.* 1998; Algaard 2001). The integral form of the Newmark explicit scheme is expressed by:

$$\begin{aligned}
&\mathbf{Mv}_{n+1} + \mathbf{Cd}_{n+1} + \mathbf{Ks}_{n+1} = \bar{\mathbf{f}}_{n+1} + \bar{\mathbf{F}}_{n+1} \\
&\mathbf{s}_{n+1} = \mathbf{s}_n + T\mathbf{d}_n + \frac{T^2}{2}\mathbf{v}_n \\
&\mathbf{d}_{n+1} = \mathbf{d}_n + \frac{T}{2}(\mathbf{v}_n + \mathbf{v}_{n+1})
\end{aligned} \tag{2.16}$$

where $\mathbf{s}$ represents the integral of the displacement vector, $\bar{\mathbf{f}}$ is the integral of the substructure interface force vector and $\bar{\mathbf{F}}$ is the integral of the external force vector.

The main motivation behind this approach lies in the fact that non-linearity can occur in the physical substructure within a time step and may not be fully captured by only evaluating equilibrium at the end of the step. If the force feedback is measured more frequently, the physical substructure response within a time step can be fully described and integrated, so that rapid changes in stiffness and load can be picked up and influence the following step calculations. Similarly, the effect of noise in the force transducer signal can be minimised.

Chang *et al.* (1998) have applied the integral form to the Newmark explicit scheme to perform some PsD experiments and conducted extensive comparisons with the non-integral scheme applied to the same tests. The time integration procedure for the Newmark explicit scheme with the integral form of the equation of motion is slightly different. The second equation in (2.16) is multiplied by the tangent structural stiffness matrix. This allows the restoring force to appear in the equation, based on the assumption that the tangent stiffness is constant over the time step. Both difference equations are then expressed as functions of known values and of the displacement vector $\mathbf{d}_{n+1}$, which is computed and implemented by the actuator.

The linearization error in a PsD test of a non-linear structure is due to the feedback force at the start of a time step being used over the entire step. Using the integral form of the equation of motion, the feedback force can be measured several times or even "continuously" over the time step and trapezoidal integration can be used to produce the required integral of the restoring force. The integral form was shown to reduce the linearization error for a PsD test. Finally, the integral form is shown to capture better the rapid loading changes during a PsD test. The integral form of the Newmark explicit scheme also has less error propagation effect than the standard form (Chang *et al.* 1998). It also allows the smoothing out of potential noise from the force transducer.

A development of the integral form similar to that proposed for the Newmark explicit scheme was proposed by the same author more recently (Chang 2002*a*). Using supplementary matrix parameters defined as in (2.12), the scheme is rendered unconditionally stable for linear systems.

As mentioned above, the scheme requires the multiplication of a difference equation by the tangent stiffness matrix, assuming it is constant over the time step, in order to solve the system. This has limitations for non-linear structures. As the tangent stiffness is not available for non-linear structures in a PsD test, the initial structure stiffness is often used instead. Again, the validity of this approximation depends on the degree of non-linearity of the structure considered. Therefore, applying this method to highly non-linear numerical substructures may prove inaccurate.

The application of this scheme to RTS testing is not as straightforward as it is to PsD testing as the interface force $\bar{\mathbf{f}}_{n+1}$ is a supplementary unknown in the RTS method – an unknown which, moreover, cannot be approximated as proportional to $\mathbf{d}_{n+1}$. Strictly speaking, this scheme should therefore be described as implicit for RTS simulations.

### 2.2.8- Sub-stepping and multi-tasking

For a real-time substructure experiment to take place and produce accurate results, some care has to be given so that the physical substructure is continuously loaded, as opposed to receiving incremental steps of displacements and producing steps of force response. Nakashima *et al.* (1992) have presented a method of smoothing the input signal received by the specimen during real-time PsD tests by eliminating the pause effect.

The same authors later developed an interesting sub-stepping technique (Nakashima & Masaoka 1999; Nakashima 2001) to provide a smooth transition between successive integration time steps. The computation of the numerical substructure is executed at each main integration time step while a smooth command signal generation task is also executed at each sub-step. The two tasks are computationally independent and separated. Multi tasking is used for the two to compute in turns whenever they need to. The authors have presented results with ten sub-steps for each main time step.

After the main step command is calculated and sent to the actuator, the signal generating task extrapolates a new command signal at every sub-step. A third order polynomial approximation is used for this extrapolation. This process carries on as long as the next main step command signal has not been worked out by the time integration scheme. At that time, the signal generation task switches from extrapolation to interpolation towards the next main step command for the remaining sub-steps. For simple numerical models, the authors show that only one extrapolation is needed. By the end of the first sub-step, the next main step command has been worked out and interpolations are used. A non-linear analysis with a bi-linear force-displacement curve was conducted and still one extrapolation only was needed. By artificially rendering the non-linear analysis more complex, the number of extrapolations reached five and the displacement time history matched that of the same model with no added complexity.

This sub-stepping technique, combined with the use of priority based multi-tasking, was shown to be beneficial in order to produce a smooth command signal for the physical substructure. Such a device provides more flexibility for the choice of the time step. It also ensures a smooth command signal is generated even while the next step computation is not finished. So the complexity of the numerical model can vary without implying any pause or high discontinuity in the generated command signal. In other words, the time requirement for solving the numerical problem is less stringent.

### 2.2.9- Modal form – modal reduction / augmentation

The standard form of the equation of motion was used so far. However, for linear systems, the modal form of the equation may be advantageous (Blakeborough *et al.* 2001; Williams & Blakeborough 2002). Using modal superposition, provided the damping matrix can be expressed as a diagonal matrix or as a Rayleigh approximation, the equations for an MDOF system become uncoupled and the calculation time can be reduced. Moreover, the higher modes may be neglected if they do not participate in the overall response of the structure to the earthquake loading. Such an approximation reduces the calculation time further and increases the critical time-step beyond which an explicit algorithm may become unstable. This can be very important for real-time considerations. This technique has also been used in a more extreme way at Aichi (Japan) for hybrid tests by Iemura *et al.* (2005) and Igarashi *et al.* (2002) where all modes but the first were suppressed to prevent spurious higher mode response.

Another technique to reduce the size of the dynamic analysis problem is based on generating a reduced set of pseudo-modal vectors and coordinates, depending on the known spatial distribution of the loading (Léger & Wilson 1987). The reduced set is able to emulate the dynamic behaviour of the linear structure as if all its modes were represented. Then, the equation of motion can be replaced by another one of smaller dimension. The secret behind this efficiency lies in the fact that the reduced set of modes is worked out depending on the known loading applied to the structure to be studied, thereby eliminating the eigen-modes that are not excited.

The transformation matrix used to produce the reduced set is formed by a set of Ritz vectors. More efficiency is gained by a careful choice of the Ritz vectors (Léger & Wilson 1987). The reduced mass, stiffness and damping matrices are indeed generated with a smaller bandwidth than the original ones. An alternative to the transformation proposed would be to choose the reduced set from amongst the original set of eigenvectors. However, this has major limitations:

- The choice of eigenvectors to keep cannot be accurately made *a priori*.
- The generation of the complete system of eigenvectors is a time-consuming task.

Through simulation work, the authors conclude that the proposed reduction of the problem is useful for problems where the spatial distribution of the loading remains fixed.

The methods proposed above reach their limitation when non-linearity is needed in the numerical substructure. Indeed, the computation of the mode shapes for a structure is based on the mass and stiffness matrices. If these do not remain constant during the whole experiment, new mode shapes would need to be computed at every step, which may be too time-consuming for complex structures. To get around this problem, a new method was developed in Oxford (Williams 2000; Blakeborough *et al.* 2001; Williams & Blakeborough 2002). Based on a non-linear numerical analysis of the numerical substructure conducted prior to testing, a set of orthogonalised deformed shape vectors is computed and added to the set of linear mode shapes found assuming the structure was linear, to form a new basis which can finally be used in the real-time test to model non-linearity in the numerical substructure. Some RTS tests were conducted using this technique with non-linear numerical and physical substructures. The numerical substructure had fifty DOFs and using the reduced Ritz basis meant that only three elastic mode shapes and six plastic mode shapes were used (Blakeborough *et al.* 2001; Williams & Blakeborough 2002). The authors conclude that the method is encouraging, though more work is needed.

### 2.2.10- Note on using hold equivalence techniques

Several numerical methods have been studied above in order to find a discrete equivalent to the continuous differential equations modelling the numerical substructure. Extensive literature has been found on the subject of applying such schemes to experimental structural analysis. However, it is also possible to generate a discrete equivalent using the hold equivalence techniques widely used in control engineering (Franklin *et al.* 1998).

Darby *et al.* (2001) have investigated these techniques and implemented the first order hold (FOH) equivalent for RTS testing. The central difference method was also implemented, both methods using a time step of 20ms. The results from both methods were compared to a finite element method solution and the data obtained with the FOH were significantly closer than those with the CDM. However, the 20ms step chosen was close to the stability limit of the CDM (24ms) given the shortest natural period of the numerical substructure. Moreover, the FOH was implemented together with an integral form of the equation of motion whereas the CDM was not, making it difficult to identify the exact source of the improvement observed.

## 2.3- ACTUATION DELAY AND COMPENSATION TECHNIQUES

### 2.3.1- Presentation of the actuator delay and of its importance

For earthquake engineering applications, the high level of load is usually provided by dynamically rated servo-hydraulic actuators. Rapidly imposing high loads or accurate displacements over a range of frequencies is obviously a difficult task which hydraulic actuators cannot execute exactly. The discrepancies are typically minor and rightly neglected for open-loop tests. However, due to the RTS method being based on the physical substructure feedback, the slightest inaccuracies translate into a feedback error and in turn propagate into an actuator command signal error on the following time-step.

When analysed over a wide frequency range, actuator dynamics are shown to be complex (Plummer 2006). Moreover, they are not just a function of command signal frequency but also vary with the type and behaviour of the specimen and of the command signal (more on this is presented below and in Chapter 4). To characterise such complex dynamics in terms that can be analysed and acted upon during a real-time test, a pragmatic approach is to define a time delay and an amplitude error, assumed to vary continuously (see Chapter 4 for more details). The time delay approach of actuator dynamics has been used by numerous researchers in the field of RTS testing.

For the hardware used in this research, the delay is of the order of 5-10ms. It is therefore not negligible compared to the integration time step considered. The total time delay for an RTS setup has various causes. The main ones are (Darby *et al.* 2002):

- The dynamics of the actuator, servo-valve and hydraulic fluid.
- The processing by the actuator controller.
- The communication time for the information to reach the controller and actuator.

The delay is also affected by the specimen (Clarke & Hinton 1997; Zhao *et al.* 2003); a stiff structure opposes the actuator more, resulting in longer delays (Darby *et al.* 2002). Finally the frequency and amplitude of the input signal affect the delay (Horiuchi *et al.* 1999).

If the delay is not accounted for, the displacement actually achieved on the physical substructure may be smaller than the numerical integration required, because not enough time was left for the actuator to reach the target. In turn, the force measured on the physical substructure will be somewhat overestimated by the numerical substructure, as it corresponds to a smaller displacement than that required by the numerical model. Considering a SDOF emulated system with the spring as physical substructure, the delay is equivalent to extra energy being injected into the system (Horiuchi *et al.* 1996). This added energy can be thought of as a virtual negative damping, proportional to the physical substructure stiffness. It makes the test less stable and if the negative damping provided is larger in absolute value than the structural damping, then instability is inevitable. More recently, the influence of the actuator delay has been studied analytically through the use of delay differential equations and similar conclusions have been found (Wallace *et al.* 2005*a*; Kyrychko *et al.* 2006). Wallace *et al.* also state that, for MDOF systems, the delay may not necessarily be equivalent to the addition of negative damping on higher modes, and may actually increase the effective damping.

### 2.3.2- Delay compensation implementation

Implementing a delay compensation algorithm is often crucial to avoid instability during an RTS experiment. Horiuchi *et al.* (1996, 1999) have developed one based on the forward extrapolation of the command signal by a time equal to the expected actuator delay (i.e. the command signal sent to the actuator is in advance of what is really asked by a time equal to the delay). The extrapolation is obtained by an exact third order polynomial fitting. This simple and efficient method has since been used by many researchers (Darby *et al.* 1999, 2001; Nakashima & Masaoka 1999; Blakeborough *et al.* 2001; Williams & Blakeborough 2002). Its popularity lies in the fact that no knowledge of the structure tested is needed in advance. It can therefore be used on a large variety of tests.

A theoretical criterion was developed where the frequency of the command signal (assumed to follow a sine wave) multiplied by the actuator delay should be kept below 1.5 for stable calculations and below 0.5 for accurate representations of the stiffness and damping by the polynomial extrapolation algorithm (Horiuchi *et al.* 1996). The implementation of the polynomial extrapolation can be quite different depending on the relative importance of the time step and the actuator delay. If the time step is much smaller than the actuator delay, the polynomial equation can be directly expressed at delay-spaced points using the existing step-spaced points without much error (Horiuchi *et al.* 1999). An outline of the method is shown in Figure 2.2.

On the other hand, if the time step is not much smaller or even greater than the actuator delay, one cannot expect that the step-spaced points can be used to directly extrapolate for one delay ahead. Instead, a forward extrapolation by one or two time-steps ahead is first conducted and a backward interpolation is then needed to the target time with the known delay (Darby *et al.* 2001). This method has proved to work well for algorithms with large time-steps. The integration time-step is chosen based on many other constraints and modifying it to suit the actuator delay compensation is not often an option.

An evolved approach for the polynomial extrapolation has been proposed by Wallace *et al.* (2005a). Instead of exactly fitting a third order polynomial through the last four data points from the numerical model, a best-fit third order polynomial is produced around, for instance, the last eight data points. This scheme recognises the possibility that noise in the feedback loop can produce undesired oscillations in the numerical substructure output. The idea is quite appealing, although substantially more complex algebra is required at each time step. It is advised to keep the polynomial order fairly low especially if large variations of the delay are expected during the experiment, for instance due to a poor initial estimate.

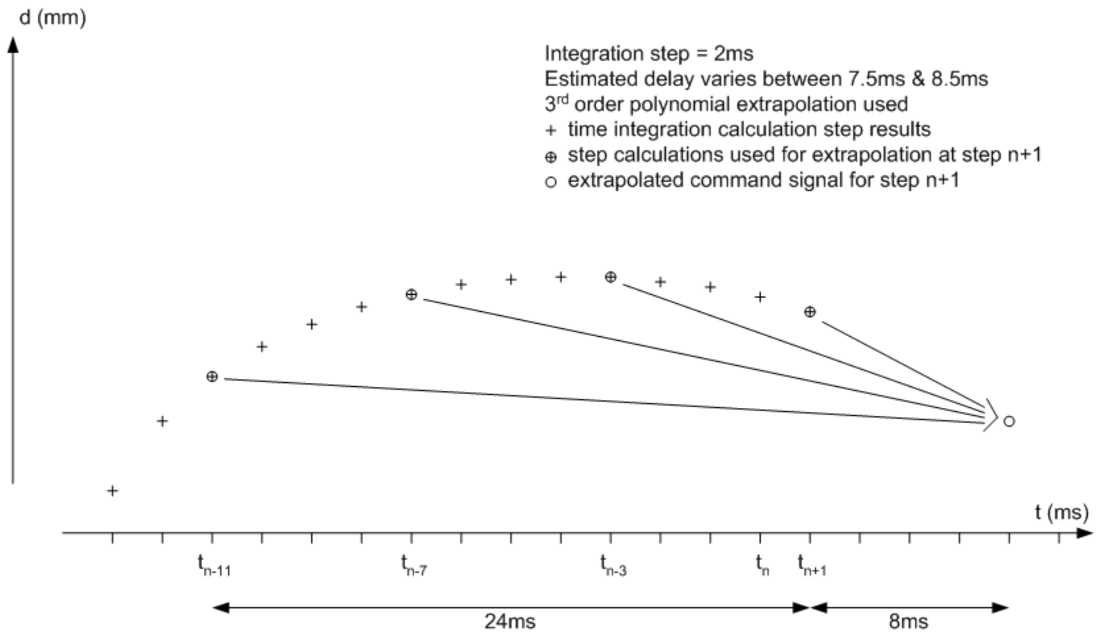


Figure 2.2: Actuator delay extrapolation when time step << delay

## 2.3.3- Adaptive delay estimation

The early tests conducted in Oxford and elsewhere assumed the actuator delay was constant during a test. The delay was estimated by the researcher before a test was conducted and this value was used for the duration of the test. The estimation itself was based on experience and empirical results.

But as mentioned earlier, the delay is due to factors that vary during a test. The strategy therefore needs to be adaptive – i.e. the delay should be continuously estimated during the test according to live data. More realistic actuator delay compensation algorithms were implemented based on more accurate time-delay estimation (Horiuchi *et al.* 1999; Nakashima & Masaoka 1999; Horiuchi & Konno 2001; Darby *et al.* 2002).

Darby *et al.* (2002) based their adaptive estimation on the actuator displacement error and its velocity. However, the model is also based on constant gains that are empirically set after an iterative preliminary testing process. This seems to be the major drawback of this method, which is otherwise powerful in reducing potential instability of the system. It was also shown that this adaptive compensation significantly reduced the experimental error in the test.

Recently, Wallace *et al.* (2005*b*) have presented an adaptive method based on the measurement of the real-time control error at zero-crossings. Due to being published too recently, this scheme could not be taken into account in the comparative analysis conducted in Chapter 5. However, it seems that some of the limitations found for the zero-crossing and original Darby schemes would also apply to it.

### 2.3.4- Linear acceleration based extrapolation

Horiuchi & Konno (2001) have proposed a new compensation scheme. The idea is still to produce a displacement signal extrapolated forward by a time equal to the actuator delay. But instead of conducting a polynomial extrapolation on command displacement points, the approximation is based on a linear expression of the command signal acceleration and by successive integrations the extrapolated displacement can be expressed. However, to use this compensation method, one needs to know the displacement, velocity and acceleration at the current time step. If using the CDM, only the current displacement is known, so the prediction has to be done with values from previous time steps. Then, all variables are known and the algorithm is carried out over a longer period comprising one time step and the actuator delay. This drawback is not too restrictive if the time step is a lot smaller than the actuator delay, as used by the Horiuchi.

An analytical study of the proposed method was conducted (Horiuchi & Konno 2001) and two criteria were developed in order to evaluate in advance the stability of various delay compensation methods. The criteria are based on ideal substructure models where either a single stiffness or a single mass compose the physical substructure. Note that the criterion with respect to stiffness is the same as that previously described by the same author and presented in paragraph 2 above (Horiuchi *et al.* 1999). The criterion with respect to mass gives a ratio of the physical substructure mass to the numerical substructure mass above which the delay compensation process will introduce instability. The new method is shown, theoretically, to reach larger values for these criteria, implying that the stability is improved. Unfortunately, no RTS testing results are presented.

## 2.4- CONTROL ENGINEERING ISSUES – IMPLEMENTATION OF ADAPTIVE CONTROL

### 2.4.1- Inner loop problem

The actuators generally receive the command signal from a bespoke linear controller unit, of the proportional-integral-derivative (PID) type. In the Oxford laboratory, this is the 8800 Labtronic provided by Instron, which also includes a lag component and an anti-integral windup procedure to limit a potential high response of the integral term to large variations of the error signals (Williams *et al.* 2001). The control loop update rate is 5kHz (0.2ms steps).

In an RTS test, the actuators and their controller unit form a so-called inner loop, allowing the efficient application of the command signal by the actuator at every time step. In practice, the settings of the inner loop controller need to be adapted according to the actuator used, the control mode chosen and also to some extent to the tested specimen (Williams 2000). They can be set by an auto-tuning process or manually and the user can verify the behaviour in advance with checking routines. More details on this controller are given in the next chapter of this report.

Because the inner-loop system cannot respond instantaneously, it is seen as the source of the synchronisation problem (Gawthrop *et al.* 2005). In this section, the actuator, the inner loop controller and the physical substructure are grouped into a system called the plant. In most RTS tests conducted so far, the numerical substructure and the plant exchange information directly. The numerical model output (after delay compensation) is the command signal for the plant and the plant outputs are sent back to the numerical model to continue the test. In control engineering terms, the actuator response is characterised by a phase lag (a frequency dependent delay) and most previous tests have been conducted using compensation techniques to make the interface displacements match (Neild *et al.* 2005).

### 2.4.2- Control engineering view of the RTS problem

A different approach to the problem is given by control engineering considerations, where an outer loop controller is used in place of the compensation algorithm to impose the matching of the interface conditions between the numerical substructure and the plant. The outer loop controller effectively works around the numerical substructure and the plant. Instead of trying to compensate explicitly for the actuator delay, this approach considers the synchronisation error as a whole and minimises it. This is done by including in the plant a model of the transfer system (e.g. actuator). Figure 2.3 shows a diagram outlining how an outer loop controls an RTS test.

With an outer loop controller, there is no longer direct flow between the two substructures apart from the interface force feedback (note that this signal can also be taken into account by the controller). All information goes through the controller, which computes the transfer system command signal accordingly. Cutting direct influence from the numerical substructure onto the physical one is the aim of the outer loop controller (Neild *et al.* 2002, 2005).

This concept has been implemented for simple RTS tests at Bristol University using the shaking table as the transfer system for the physical substructure. Both numerical model and controller were modelled using continuous time transfer functions with 1ms steps and a zero-order-hold discrete equivalent was used for the discretisation (Neild *et al.* 2005). The controller can also be modelled in a discrete way (Neild *et al.* 2002).

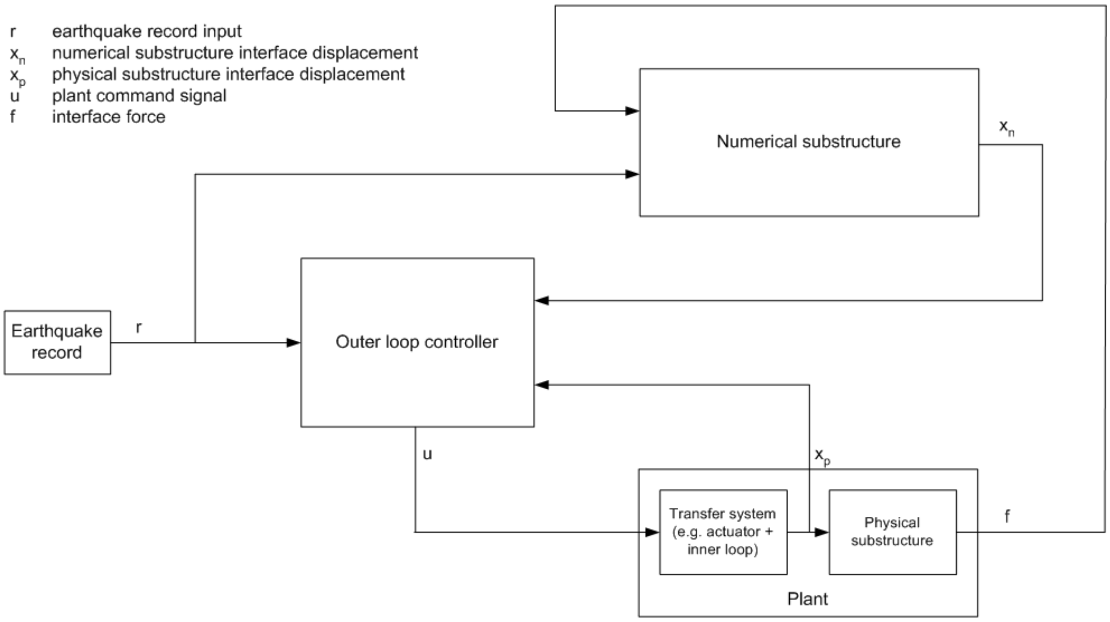


Figure 2.3: Outer loop controller concept diagram

Several researchers also propose adopting an adaptive control algorithm (Bayer *et al.* 2002; Neild *et al.* 2002, 2005; Stoten *et al.* 2002). Adaptive control techniques provide a mechanism to continuously update the controller parameters in the light of the changing process dynamics. Therefore, a change in a substructure would not necessarily imply re-tuning the control system. This way, an application engineer would be able to test several systems and compare them more easily, without having to conduct tedious calibration work on the controller every time. Such a possibility is quite appealing for the future development of the RTS method. Researchers from Bristol University have worked on the minimal control synthesis (MCS) family of adaptive controllers (Stoten 1993) towards their use in RTS testing (Wagg & Stoten 2001; Drury *et al.* 2002; Neild *et al.* 2002, 2005; Stoten *et al.* 2002).

## 2.4.3- Implementation and potential of adaptive outer loop controllers

Both adaptive control routines (based on MCS) and classic ones (based on PID types) have been tested and extensively compared when used for RTS testing or with computational simulations (Neild *et al.* 2002, 2005; Stoten *et al.* 2002). The Bristol shaking table was used as the transfer system and a SDOF spring-mass-damper system was simply substructured by considering part of its mass (or all of it) as the physical specimen. The main criterion for evaluating the controllers tested was the agreement between the measured transfer system displacement and the displacement produced by a computer simulation of the complete system. The adaptive character was also tested by changing the physical and/or numerical substructure properties without any change in the initial controller settings.

The linear controller developed for the application to RTS testing was of a PID type with error feedback (Neild *et al.* 2005; Stoten *et al.* 2002). A difficulty encountered was due to the control signal being partially based on a velocity term, since discretising such a term using simple differentiation of the displacement signal can produce significant noise. Instead, a composite filter was used to compute the velocity from displacement and acceleration signals.

The linear controller was based on a first order approximation of the shaking table and showed good results only when implemented with an error feedback. However, an excessively high feedback gain caused instability. The controller showed good results without needing filters to be introduced. It also proved to be fairly robust for slight changes in the structure parameters. However, simulations with significant changes showed its limits and became unstable (Stoten *et al.* 2002).

The implementation of adaptive algorithms proved to reach its best results with the use of filters. However, filters introduce an additional lag, so the same filter must be used for the force and displacement signals (Neild *et al.* 2002). The controller uses a parameter $\alpha$ which the user sets to the maximum value before reaching instability (Stoten *et al.* 2002). Both the standard MCS algorithm and a modified one, the error-based minimal control synthesis with integral action (Er-MCSI – Stoten & Neild 2003), have been implemented. An error feedback also proved beneficial for both algorithms (Neild *et al.* 2005).

Results obtained from the MCS algorithm were reasonable but somewhat inferior to those from the Er-MCSI controller because of unwanted drift and oscillations. Setting the $\alpha$ value was also easier with the Er-MCSI than with the MCS (Neild *et al.* 2005) for the same reason. Simulations with significant parameter changes or the introduction of non-linear damping proved the good adaptive character of the Er-MCSI algorithm, without needing any initialisation process (Stoten *et al.* 2002).

However, with the MCS and Er-MCSI algorithms, the adaptivity of the gains is limited in speed, and when the gains are initialised to zero at the start of the experiment, large errors are needed to produce the adaptation required. Instead, some previous knowledge of the transfer system can be used to initialise the gains to typical values, and avoid periods of large errors at the start. This required *a priori* knowledge of the transfer system goes against one of the previously stated advantages of adaptive control, but is now regarded as an inevitable prerequisite (Lim *et al.* 2005). Moreover, an updated structure of the MCS algorithm was proposed recently, featuring an inverse of the reference model applied to the external demand before the application of the controller gains. The resulting algorithm, MCS with modified demand (MCSmd), was shown to feature improved characteristics (Lim *et al.* 2005). The application of MCS-based algorithms still has to be shown to work for a variety of conditions, such as low damping systems, frequency sweep tests or multi-variate systems. More details on the application of MCS algorithms to substructuring are given in Chapter 5 of this report.

## 2.5- SUMMARY - MAIN CHALLENGES AHEAD FOR THE RTS METHOD

Many of the RTS tests conducted so far have had very simple numerical substructures. Few degrees of freedom were modelled; non-linearity was rarely introduced. This often allowed the use of conditionally stable numerical algorithms. Such schemes are typically based on an explicit formulation, allowing a solution to be produced more quickly. However, an unconditionally stable method may be needed in order to compute more complex numerical substructures within a larger chosen time step. However, as discussed in section 2.2.1, it should be noted that iterative schemes are not appropriate for RTS testing.

Another present limitation in the majority of the tests conducted so far is that of conducting a test with only one DOF present at the interface between two substructures (Nakashima 2001). This is very restrictive for potential applications of this method and testing with several degrees of freedom at the interface needs to be proven for RTS to become more widely used. It would also allow studying asynchronous base excitation.

The technique has been applied to very small vibrating structures using an electrodynamic shaker to provide the excitation (Bayer *et al.* 2000, 2002). The results were promising but only very small forces were involved compared to what is needed for civil engineering applications. Other simple tests with more realistic forces have been conducted by Darby *et al.* (1999) using hydraulic actuators. A more complicated test was conducted and showed that care is needed for crucial points like the actuator delay estimation and compensation, the limitations of lumped-mass modelling and also damping estimation. Other tests were conducted with high forces and high displacements – of earthquake engineering standards – but were only valid for low frequency response up to 3Hz (Nakashima 2001). Combining all the objectives for earthquake engineering representative loads and frequencies is also an important challenge ahead for RTS testing. The limitations of hydraulic actuation equipment have to be compensated, either directly or with the use of outer loop control.

RTS also requires every process to be quick. The computer model, the communications and the actuator all have to be fast enough for the feedback loop to be closed in a time step providing good coherence (Williams *et al.* 2001). If this is not the case, the computer model parameters are out of date compared to the feedback force and the whole process loses accuracy, and may become unstable. Again, the time integration scheme used for solving the numerical substructure has to be chosen very carefully and specially adapted for the RTS method.

The long term prospects for RTS testing are towards state-of-the-art earthquake engineering applications. From the review presented above, it is clear that the RTS experiments conducted so far have showed promising results but have also highlighted various shortcomings. There is therefore still a clear need for deep investigations to be carried out, ideally through the use of simple test rigs that can introduce the above mentioned levels of difficulty one at a time. This approach has been used for the research presented in this thesis, as demonstrated by the test rig presented in the following chapter. The specific objectives of this thesis are to perform detailed analyses of the available and potential solutions to the problems of actuation compensation, time-integration of the numerical substructure and real-time implementation strategy. This will involve bespoke implementation and testing programmes. The realisation of this initial set of objectives will lead to the subsequent objectives of:

- Implementing successfully some real-time hybrid experiments with an unconditionally stable numerical scheme.
- Enabling non-linear elements to be computed in the numerical scheme without significantly limiting the computational power of the hardware.
- Increasing the number of degrees of freedom solved in the numerical substructure from what was managed in earlier experiments.
- Performing multi-axis experiments and extending the workability limit of multi-axis tests.
- Performing real-time hybrid experiments with ranges of excitation frequency and load that are relevant to the use of hydraulic actuators for earthquake engineering applications.

# CHAPTER 3

# RTS TESTING IN OXFORD

Beside reviewing the literature and defining the general aims of the project, the preliminary work conducted for this research consisted of getting familiar with the experimental equipment and testing procedures as well as designing and building a development test rig. Accordingly, the first section of this chapter presents a review of the Oxford University Structural Dynamics Laboratory (OUSDL), focussing on the equipment used for this research. It also gives more specific details about what is involved in performing an RTS test. The second section is dedicated to the design and construction of the development test rig. Finally, the third section presents the description and results from an initial RTS test as a preliminary activity for the research detailed in the following chapters.

## 3.1- THE LABORATORY AND THE EQUIPMENT

### 3.1.1- The Oxford University Structural Dynamics Laboratory

The structural dynamics laboratory, in which the testing for this thesis took place, is a small laboratory compared with many structural laboratories. It is, however, well equipped. Figure 3.1 gives an overview of the laboratory.

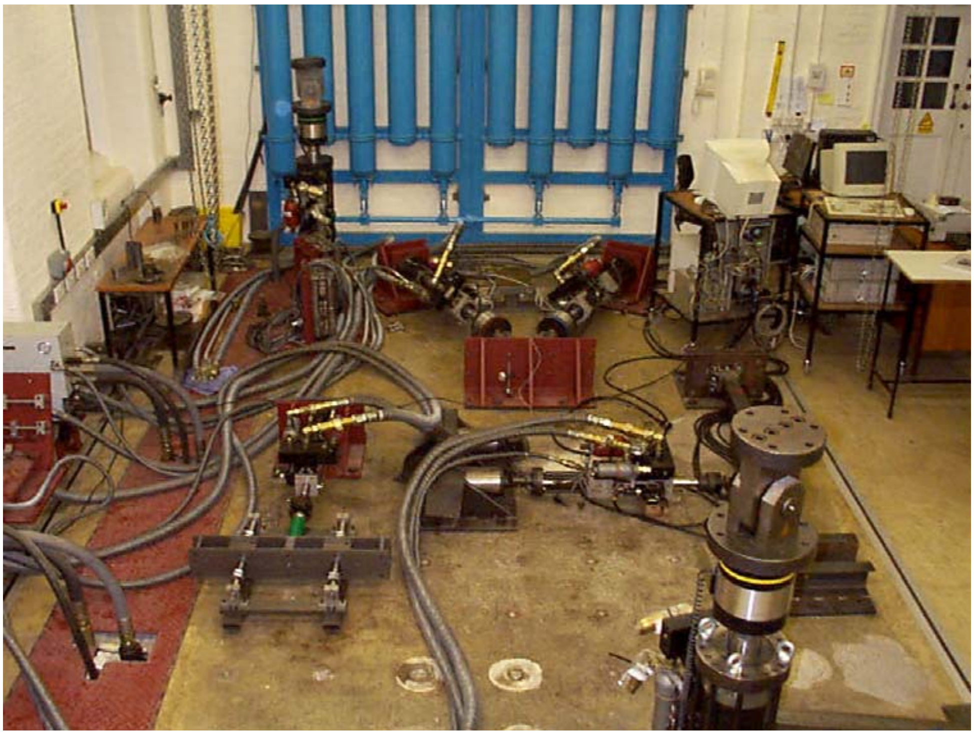

Figure 3.1: Overview of the Oxford University Structural Dynamics Laboratory

The core equipment in the laboratory is the set of six Instron made servo-hydraulic actuators. In other words, most of the laboratory equipment is based on the proper exploitation of these actuators. The main actuator properties are summarised in the following table.

| Denomination (dynamic rating) | Number | Piston Stroke (mm) | Maximum stall rating (kN) |
|---|---|---|---|
| 10kN actuator | 2 | ±75 | ±13 |
| 100kN actuator | 2 | ±125 | ±124 |
| 250kN actuator | 2 | ±125 | ±311 |

Table 3.1: Displacement and load capabilities of the actuators

In Figure 3.1, both 10kN actuators can be seen occupying floor space in the middle of the laboratory on two separate rigs. Both 100kN actuators are at the back of the laboratory (used in a V shape setup at the top of the picture), and the 250kN actuators can be seen in an upright position, one in the bottom right corner, the other in the opposite corner.

The two 10kN actuators were used for this project. It can be seen from Table 3.1 that they are the smallest in the range available. To gain a better idea of their size and performance, here are a few more specific physical details:

- Piston rod diameter: 44.5mm.
- Maximum piston velocity: 1.67m/s.
- Oil volume within actuator: 115cm3 (0.1L).
- Complete actuator weight: 31kg.
- Piston weight (without load cell): 7kg.
- Body height: 690mm.

Further details of the actuator are shown in Figure 3.2. The actuators receive their power via pressurised oil through Moog servo valves. The valve controls the piston movements by directing the oil to one side of it and connecting the other side to the return line. The servo valves used here have an oil flow capacity of 40L/min. The natural frequency of the actuation system (actuator & pressurised oil column) to be used obviously depends on the mass attached to the piston. The piston fitted with the load cell has a mass of about 11kg. For an additional mass of about 120kg, the natural frequency is 38Hz (Williams 2000). When the additional mass is only 9kg, the natural frequency is as high as 99Hz. For no additional mass, it is expected that the frequency would be about 130Hz.

The pressurised oil is distributed to the servo valves by a substation. The laboratory currently has two substations, each having the capacity to provide oil flow to two actuators. The substations are installed directly on the main hydraulic high pressure line, operating at 210bar. The high pressure line runs all along the laboratory from the Dartec power pack (containing three pumps) to the accumulators. This power pack can provide a peak flow of 180L/min and individual pumps may be switched off when low consumption is needed. The accumulators are able to store highly pressurised oil to be used at peak consumption when the instantaneous supply from the pumps is not enough. They can approximately double the oil flow to the substations during a short period of time. The substations are also connected to the return line to the oil reservoir.

All the hydraulic equipment is installed on a large concrete block. The block is 9.1m by 4.2m in surface area, 1.6m deep and weighs 166 tonnes. The foundations of the block are designed to let the testing induced vibrations to be transmitted to the ground well below the foundations of the host building. The area of the floor dedicated to testing is 7.5x3.5m. A 2 tonne capacity crane covers this area with a 3.5m clearance.

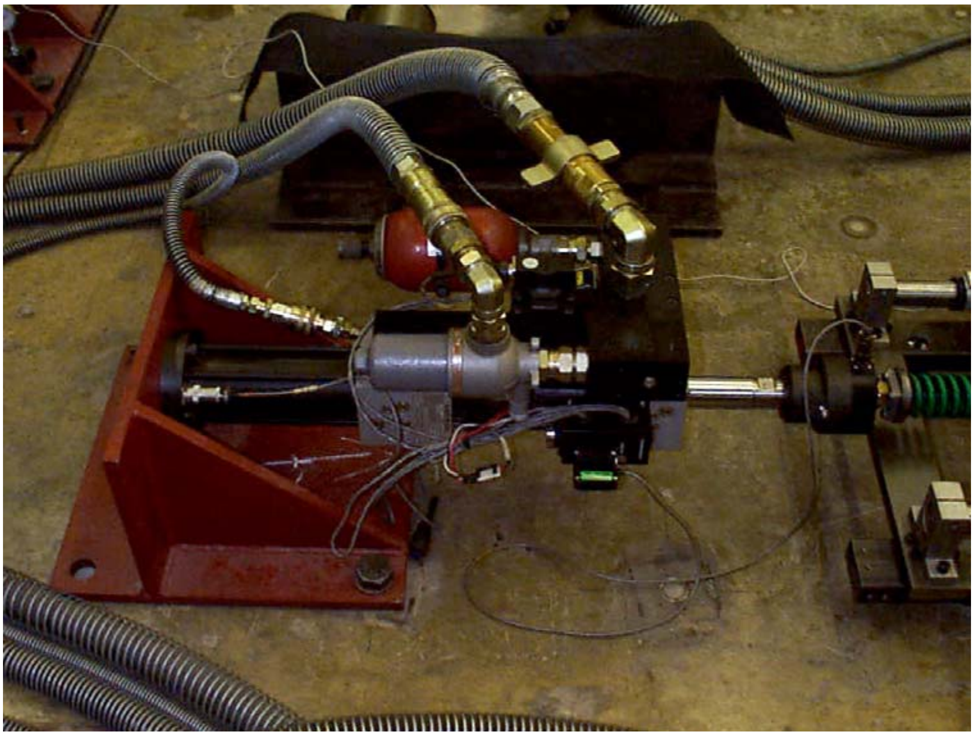

Figure 3.2: Detailed view of a 10kN actuator

The closed loop control of the substation and the actuator is conducted by an Instron Labtronic 8800 controller. This unit provides four channels of position or force control, allowing the control of four actuators simultaneously. This number is limited both by the 8800 four-axis controller and by the number of substations currently installed. The controller parameters are accessible through the Instron proprietary program RS+. The PC running RS+ communicates with the 8800 controller through a GPIB/IEEE interface. The 8800 is based on a proportional-integral-derivative-lag controller, with its parameters set either by an auto-tuning process or by hand.

In addition to the hydraulic apparatus, the laboratory is also equipped with two digital signal processing (DSP) boards (a dSpace 1104 R&D and a Microstar DAP 3200a), a 32 channel data acquisition system, various load, acceleration and displacement transducers and an oscilloscope. The dSpace DSP board is described further later in this section.

### 3.1.2- Using the hydraulic actuators and the 8800 controller

Some simple physical tests on an existing cantilever rig have been conducted for familiarisation with the use of the actuators and the controller. The RS+ software is provided by Instron and is fully integrated with the hydraulic equipment of the laboratory. When switching the system on, RS+ automatically detects what the valid and operating connections are and displays which actuators may be used.

Each actuator is fitted with two transducers. A load cell, fitted externally, connects the end of the piston to the tested specimen, and a linear variable differential transformer (LVDT) is fitted inside the actuator body and outputs the effective piston displacement relative to the actuator body. An initial process of calibration of the load cell is usually conducted before any testing. The signals from both transducers are sent to the controller, and in turn to the PC hosting the RS+ software. The signals can be monitored, acquired, stored and exported for post-processing.

The 8800 unit allows the actuator to be used either in force or displacement control. In each case, the corresponding transducer provides the signal for the unit to close the control loop, by comparing the command signal (sent to the actuator) to the effectively achieved one (coming back from the transducer) and reacting accordingly. This is where the PIDL settings mentioned previously take their full role. Depending on various testing conditions and depending on the control mode chosen (force or displacement), the control loop parameters will allow the actuator to reach the required state in a fast and smooth manner, with little or no overshoot. The control loop is completed every 0.2ms.

As mentioned before, there are two ways to change these parameters, but both involve the use of the PC connected to the 8800 unit through the GPIB interface. They can be set using an auto-tuning procedure provided with the RS+ software. If the result is not satisfactory, or if a set of specific parameters are required, it is possible to access and modify them by hand through RS+. The simple procedure for obtaining accurate control parameter settings by hand is the following. A square wave command signal is sent to the actuator. The control mode transducer provides the measured signal to the controller and in turn to the RS+ software. By plotting simultaneously on the live data acquisition system the command and the measured signals, the error achieved by the control system can be monitored. The PIDL parameters can be adjusted by hand as the equipment runs until the error eventually reduces to a level considered to be acceptable by the user.

### 3.1.3- RTS testing procedure and description of the dSpace DSP board

This section describes the usual hardware procedure to conduct an RTS test and presents the reasons for the setup chosen. The 8800 controller unit has some programming capabilities. With suitable software, they could be used to program the controller to react to the physical model response so as to reproduce the behaviour of the numerical substructure. However, the version of the RS+ software in the laboratory does not give access to these programming capabilities. Discussions with Instron for updating the software version have taken place, but no solution was available in the time frame of this research.

Communication between the RS+ PC and the 8800 controller are achieved through a GPIB interface (IEEE HS488). This interface is fast in principle, but effectively operates using batches of data, which makes the overall transmission slower and in fact too slow for accurate real-time control. This means that the bus cannot be used for the fast exchange of data between the two substructures necessary during an RTS test. However, this interface is used for software monitoring of the actuators and controller.

Another way to send a customised input to the controller is provided, using a BNC connector located on the front panel of the 8800 unit. The signal provided through this connection can become the active command signal for the controller once the test is set up and ready to be conducted. From the RS+ software, the user can select the command signal to be either generated by the controller itself (which is the case for a normal cyclic or ramp input) or received from the "External Auxiliary" analogue input connector. This is the access route into the controller that is used for the command signal in the RTS tests.

In addition to the feedback loop formed by the actuators and the controller, a second outer control loop is created in order to perform a real-time test. This is physically achieved via a second PC. In order to make sure the real-time command signal is sent to the controller in due time at every time-step, the operating PC system tasks should not interfere with the RTS related tasks. This is done through the use of a bespoke digital signal processing board installed within the computer central unit via a PCI slot. For this project, the dSpace® DS1104 R&D board was used.

This DS1104 board is based on a 250MHz PowerPC unit (dSpace 2002). It provides digital input and output facilities (although these cannot be used for signal transmissions) as well as analogue channels through 16 bit and 12 bit ADC and DAC units. The board is equipped with an external connector panel allowing connections via BNC leads. Generally speaking, the performance of the DSP board dictates the limit to the complexity of the numerical substructure the board can host for a given integration time step.

Before conducting an RTS experiment, the PC hosting the dSpace board downloads the numerical substructure model onto the DSP. This is done using bespoke dSpace software called ControlDesk®. An operational advantage of the dSpace hardware is its full compatibility with Matlab® and Simulink®. Once a Simulink model of the numerical substructure is compiled, it can be downloaded to the DSP for execution. During the execution, the user can monitor the experiment via ControlDesk and alter the simulation parameters. However, the DSP works with an independent timer and is not slowed down by processes the user may run on the host PC. The actuator load and displacement signals and the real-time command signal are connected to the 8800 controller through the BNC connection box. A schematic of the overall setup is shown in Figure 3.3.

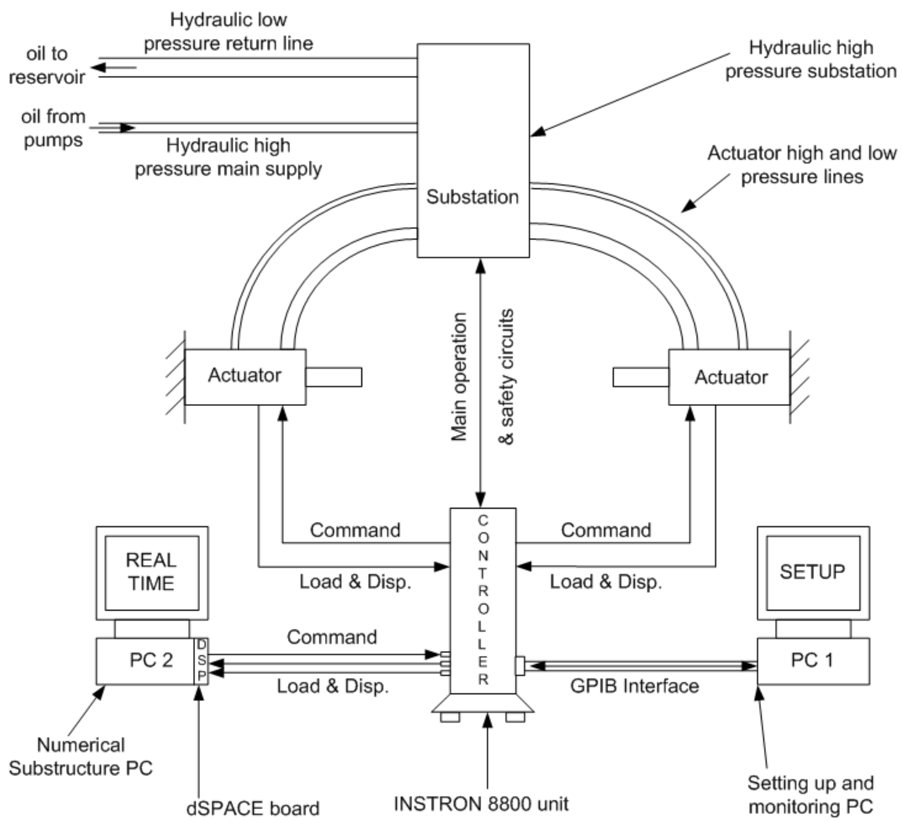


Figure 3.3: Connections for an RTS test

As mentioned in the previous chapter, when conducting an RTS simulation, the delay in both the inner and outer loops should be minimised and its variation should be reduced. Much work, which is described in Chapter 4, was devoted to measuring the delay for various test conditions. Three key hardware and software parameters for the laboratory setup were identified as having important effects on the overall delay:

- The time-step of the command signal output on the DSP board: due to the time discretisation, a delay equal to this time-step will always be present. It should therefore be minimised. In the experiments carried out in this research program, the default strategy has been to set this time-step to be the same as the sampling period of the actuator controller. See Chapter 6 for more details.
- The proportional gain ($P$) in the actuator controller should be maximised. See Chapter 4 for more details.
- In the 8800 unit, a low-pass filter is present with the analogue to digital converter to improve the quality of the acquired command signal. This filter generates a delay that increases as the cut-off frequency of the filter decreases. To avoid aliasing (Smith 1997), the cut-off frequency should not be lower than twice the upper bound of the expected frequency content (i.e. around 20Hz). However, such a cut-off frequency would induce an effective filter delay of about 10ms. Testing showed that a cut-off frequency of 1000Hz could be used to minimise the filtering delay to about 1.5ms without altering the quality of the transmitted signal.

Using these guidelines, the actuator delay, as measured at the DSP board and including both the inner and outer loops, could be reduced to about 4.5 to 6ms for most of the experiments carried out in this research.

## 3.2- DESIGN AND CONSTRUCTION OF THE DEVELOPMENT RIG

### 3.2.1- Overall requirements and design principles

The previous chapter identified some important challenges for the RTS test method. This thesis has focussed on some of those challenges. Trying to develop methods to overcome and solve these challenges involved much testing work using a variety of techniques, and a versatile test rig was essential. This section describes the design of this test rig. The initial purpose of the rig was to provide a simple but robust test base for the RTS test method using a model with several DOFs, before trying to implement the method on more realistic and complex applications.

The specification of the rig was to allow testing of a linear system, either a simple (SDOF) or more complex (two or three DOFs) one. It should enable testing of pure stiffness components (springs) or inertia components (masses) or a combination of them. It should also allow a physical system to be excited by either one or two external sources in order to test multi-variate systems with opposing actuators. Finally, the rig should be laid out so that damping devices may be easily added. This short specification for the rig highlights the need for a high degree of flexibility and versatility. The rig should be easy to update when a change in one of the parameters is needed.

Another major requirement is that the whole system containing the rig needs to be simple to model numerically. In order to make advances in the RTS test method, it is important to have a full understanding of the physical substructure, the control loop and the actuator behaviour. To achieve this, the physical specimen was required to behave in an easily predictable way, with minimal non-linearity. Nonetheless, the rig needs to provide some complexity in the form of three interacting degrees of freedom.

Finally, a major requirement for the rig was to be cheap. The available budget for the mechanical parts was approximately £2,000.

The general layout of the rig is a system of springs and masses connected in series, moving inline and connected to two actuators, one at each end. A schematic view is given in Figure 3.4. Such a layout fulfils the DOF requirements stipulated above. The use of linear coil springs, low friction bearings and rigid masses allows a straightforward prediction of the theoretical behaviour. The RTS test method can be implemented in a variety of ways by replacing a combination of spring(s) and mass(es) by the corresponding numerical substructure.

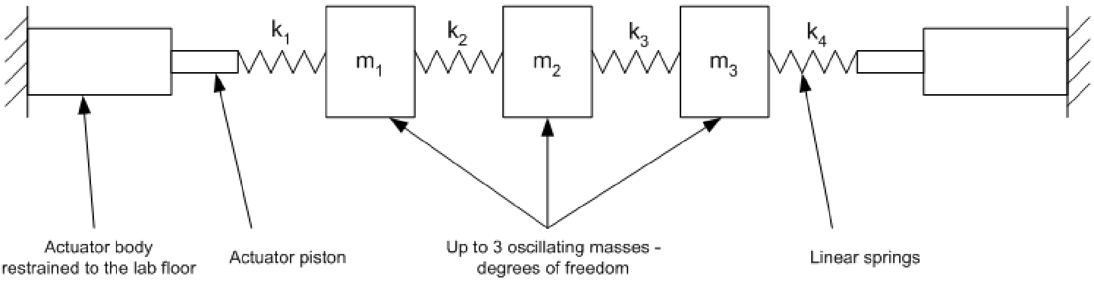

Figure 3.4: Conceptual view of the rig to be designed

The masses should move with low friction, requiring the use of bespoke linear bearings. The orientation of the rig is not indicated in the sketch above. Either a horizontal or a vertical orientation could be chosen. On one hand, a vertical orientation would mean that no bending would be introduced by the masses on the support system. An obvious difference between the horizontal and vertical orientations is that the gravity would have an effect on the spring compressions. However, this is considered to be neither an advantage nor a drawback in itself, although it means changing a spring would be more difficult in the vertical orientation. The clear advantage of a horizontal system is the ease of implementation and use in the laboratory, especially due to the layout of the floor and to the fact that no versatile facility for vertically restrained structures existed, implying the design and construction of a new fixture frame. The vertical option was not chosen because of its implications in terms of cost and work involved.

As shown in Figure 3.4, it was decided to design the rig for a maximum capacity of three masses (three physical degrees of freedom), four springs and two actuators. This would allow sufficiently complex systems to be tested. The actuators available for these tests had a stroke of ±75mm and a load capacity of ±10kN. In the RTS tests, the substructuring would take place with one or both actuators replacing a combination of spring(s) and mass(es). One aim for this rig, as mentioned above, was to allow testing on physical systems with a range of natural frequencies. This required the ability to change the masses of the moving carriages and/or the stiffnesses of the springs used.

Another feature which would allow the rig to be easily reconfigurable was to have each mass on its own separate support which could then be installed or removed from the test setup as and when required.

In terms of target masses and spring rates, the main requirements were:

- Significant displacements of the masses, of around ±50mm from the rest position.

- Ability to handle the various weights.
- The oscillation frequencies should cover the significant range, i.e. up to 10-15Hz.

### 3.2.2- Example of a similar rig developed at Bristol University

A similar rig already existed at Bristol University. A general view of the rig is shown in Figure 3.5. The masses are adjustable, from a minimum carriage weight of 80kg up to a maximum of 200kg by adding additional plates on the above and below the carriage. The natural damping ratio of the rig is estimated to be in the region of 2%.

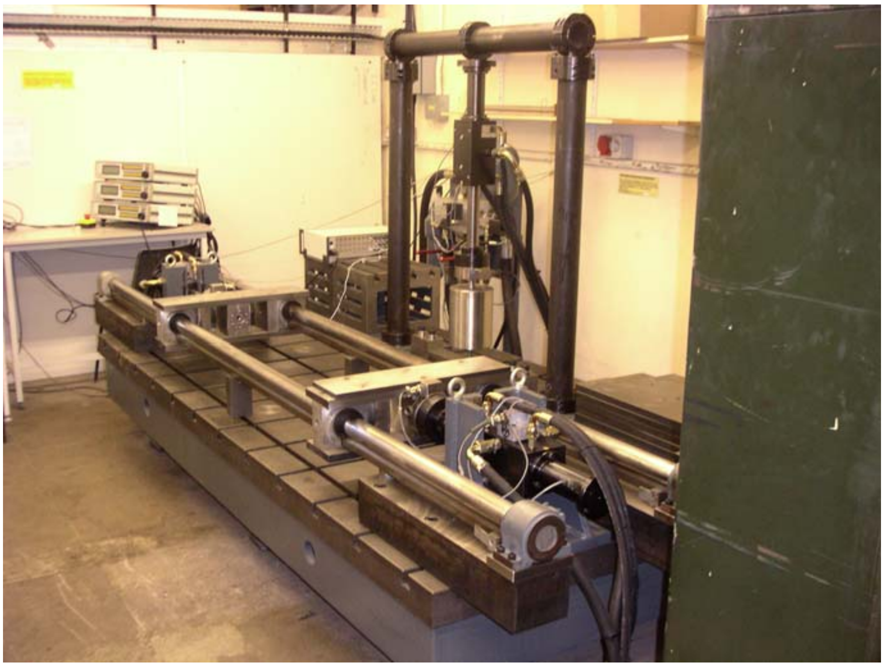

Figure 3.5: Overall view of the rig in Bristol

The rig is based on two shafts supporting two carriages. The masses are linked at both or either end to one or two actuators mounted horizontally (parallel and in-between the two rails). Each carriage is supported on the rails by a pair of open linear bearings. Note in Figure 3.5 that the rail bending is also controlled by an additional support at the rail midpoint.

The springs (not present in Figure 3.5) are of the compression type with a spring rate of 15.8kN/m, wire diameter of 9.52mm, outer diameter of 85mm and a free length of 400mm (of which 300mm is compressible, the remaining 100mm being held in the clamps). With the empty carriage mass of 80kg, such a spring produces oscillations at a natural frequency of 2.2Hz.

The major points from this rig that needed improvement were:

- Increasing the flexibility in use, by separating the physical dependency of the various masses with each other.
- Decreasing the bending of the support system significantly.
- Using stiffer springs and lighter masses to produce higher natural frequencies. The target maximum mass for the Oxford rig was 100kg. The minimum mass would be set by the weight of the empty carriage (i.e. without any ballast).

## 3.2.3- Detailed requirements and design issues

### 3.2.3.1- Overall target

The target of providing the three 100kg masses with natural oscillations at 15Hz with 100mm peak to peak displacements was impossibly expensive to achieve. The springs necessary would not only have needed to be very stiff (~90kN/m) but also be very strong, as they need to remain linear for 100mm peak to peak displacements. The stiffer the springs are, the larger they need to be to achieve a given elastic range, and such springs become very expensive.

Instead, use of the empty carriages was assumed and the response that could be produced with standard stiff commercially available springs was worked out. A Matlab model was created to assess the oscillatory behaviour of the rig. Figure 3.6 shows the results obtained from a model of the form shown in Figure 3.4. It displays the free undamped oscillations of three 35kg masses linked in series to fixed ground supports. The masses are linked to each other and to the supports through four springs as shown in Figure 3.4. The springs stiffnesses used were all 73kN/m. The initial condition is a 25mm deflection of the first mass whilst keeping the other two in their rest position. The time-scale on the X axis of the graph shows the first second only. There is no damping in the model, hence the deflections do not decay.

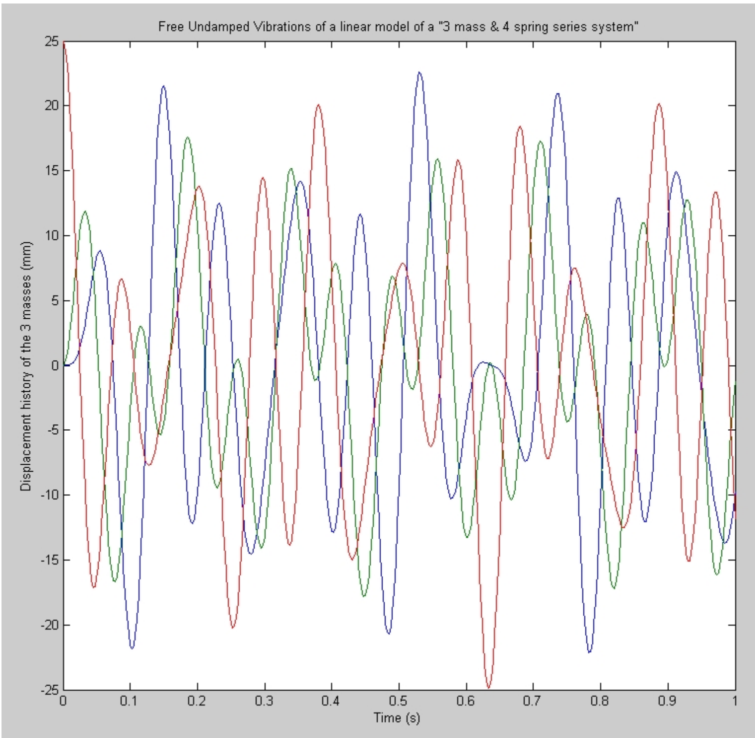

Figure 3.6: Free oscillations of 3 masses and 4 springs in series

The natural frequencies of the 3DOF system produced in this model are 5.6, 10.3 and 13.4Hz, which was regarded as an acceptable target. Springs were available commercially, to allow for ±50mm deflections and did not have a prohibitive cost (they were around £25 each). This solution was therefore pursued. Should higher frequencies be needed, it would be possible to install stiffer springs and compromise on displacement, or use stiffer and longer springs and compromise on cost. The rig must be versatile enough to allow for different spring sizes to be fitted.

#### 3.2.3.2- Typical spring specifications and spring attachment

The previous section gives approximate values for the spring rates needed. It is also known that they needed an elastic range of ±50mm. Springs satisfying these requirements from the “Bordignon” die spring supplier were selected with nominal rates of 23, 44 and 62N/mm. Die springs have rectangular wire sections and are significantly shorter than round wire springs for a given spring rate and working deflection; their use ensures the rig remains compact. Moreover, they are relatively cheap, in part because of their compactness.

All springs provide the same maximum working deflection of 81.2mm. This is well above the required range of 50mm but it was found to be necessary to ensure the extension elasticity. All the springs have the same free length, which is particularly useful when changing a spring on the rig. The variation in stiffness results purely from the different wire section used.

A problem still to be considered is the attachment of the springs to the rig. The springs are required to work in both compression and extension with very similar rates in each direction. Compression springs are usually sold with ends ground flat in order to have good support on the contacting platform. This is good for making the spring work in compression, but a secure fixing is needed on the spring to make it work in extension. This was most easily achieved by welding the rig fixings to the ends of the spring. According to the manufacturer, the springs can be welded, but this is not advised as it reduces the material strength obtained through heat treatment. The welded joint would also be particularly subject to stress concentration and fatigue loading, so reliability was likely to be an issue in the day to day operation of the rig. However, spring failure is unlikely to cause significant damage to other parts of the rig. In the eventuality of a failure, repair or at worst purchase of a new spring is possible. Another important problem is that the manufacturers specify spring rates in compression but not in extension. Spring calibration was therefore needed to check the validity of the choices so far. Calibration results are shown in Figure 3.7.

These results show that the stiffest spring selected is linear in compression and extension, both before and after welding, across the required range of 50mm. The average measured spring rate was 65.2N/mm.

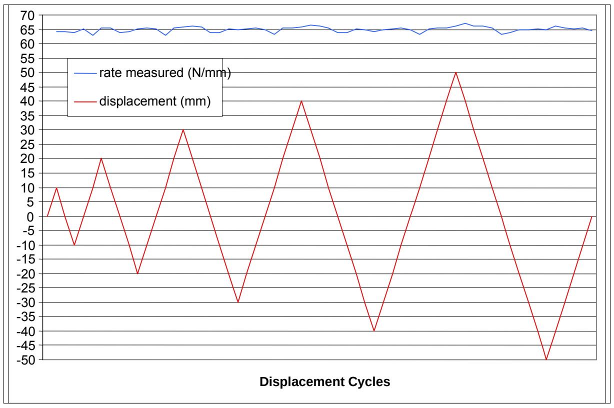


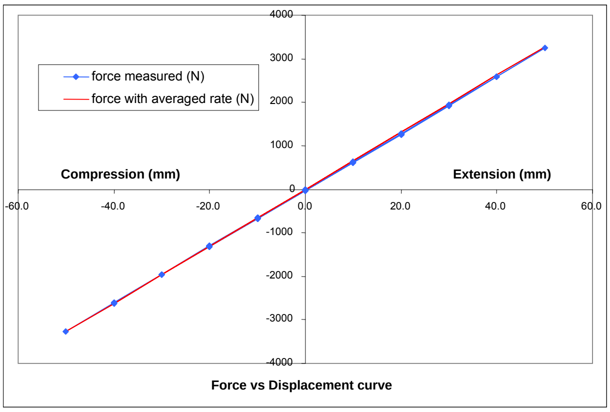


Figure 3.7: Welded spring calibration results

3.2.3.3- Ballast material and volume

Assuming an empty carriage mass of around 35kg, to reach the 100kg target, 65kg of ballast was needed for each carriage. For all the carriages, this totalled to 195kg of ballast. Such a mass requires a large volume of material. It was important to know this volume at an early stage to design the rig appropriately.

The two materials considered to provide the extra mass are lead and steel. Their respective densities are 11,300 and 7,900kg/m$^3$, so lead is 43% denser than steel, making it more attractive in terms of volume. However, cost estimations revealed that the use of lead would be far too expensive given the available budget. Steel was therefore selected. Note that 65kg of steel would occupy a volume of 0.0082m$^3$ on each carriage.

3.2.3.4- Shaft and bearing system choice

Two main options exist for the linear bearings in the support and guiding system. One is to use plain round shafts supported by clamps at the ends. The other is to support the shafts all along their length and use “open linear bearings”. These bearings do not slide around the whole periphery of the shaft, but just two thirds of it, the bottom third being freed for the support and therefore needing to be cleared by the bearing and the whole carriage system.

This second solution is appealing because it prevents bending in the shafts almost completely. On the other hand, it would mean that some parts of the rig would be difficult to access. This would also mean that the centre of gravity of the carriage assembly would have different locations as ballast is added to it. Then, if the centre of gravity is not at the same height as the shafts, an overturning moment is created around the shafts, which is not a good characteristic for the rig. This option was therefore dropped and the plain shaft system with normal bearings used instead. This also reduced the overall cost of the rig.

As mentioned before, to increase flexibility in use it was required to be able to separate each degree of freedom completely by having three units that can be added or removed without affecting the others. This meant that each carriage would be moving on two short shafts, which, in turn, meant that the shaft bending would be very limited. From calculations, a shaft 40mm diameter 600mm long with clamped ends submitted to a 50kg load at its centre would only deflect by 0.015mm.

On the other hand, by increasing the number of shafts, problems would be introduced with a more difficult alignment setup for the bearings to operate smoothly. However, whilst the alignment of the two shafts in each unit would need to be good, the alignment of the units with each other would not be so crucial, since the coil springs linking the adjacent carriages allow for some misalignment in the system.

#### 3.2.3.5- Linear bearings

In order to select the linear bearings, the maximum carriage speed and accelerations were first estimated. For a motion of displacement amplitude $A$ at a frequency $f$:

- Displacement: $$u = A \cdot \sin(2 \cdot \pi \cdot f \cdot t) \quad (3.1)$$
- Velocity: $$\dot{u} = 2 \cdot \pi \cdot f \cdot A \cdot \cos(2 \cdot \pi \cdot f \cdot t) \quad (3.2)$$
- Acceleration: $$\ddot{u} = -4 \cdot \pi^2 \cdot f^2 \cdot A \cdot \sin(2 \cdot \pi \cdot f \cdot t) \quad (3.3)$$

Assuming maximum values of $A$ = 50mm and $f$ = 12Hz, the maximum velocity and acceleration are 3.8m/s and 284m/s$^2$ respectively.

No manufacturer will guarantee their bearings for such high velocity and acceleration values. INA Ltd state their bearings can work at velocities up to 5m/s, but the maximum recommended operating acceleration is 50m/s$^2$. However, the specified operating limits vary significantly depending on the load applied to the bearings and on the way this load is applied. The loads envisaged are very low compared to the bearing capacity. Moreover, the maximum velocity would only be reached when the acceleration was reduced to zero and vice versa. So the bearings would not experience high velocities and high accelerations simultaneously. INA also point out that higher levels of performance can be obtained when the load is carried close to the bearing and the ideal is directly above, which is the case here. The operating limits stated are for cases were the layout is not so advantageous. Finally, these operating limits are stated to optimise bearing life, which is not a critical issue for this research compared with industrial applications where the bearings would be used extensively and repeatedly for long periods of time.

Another point worth mentioning regarding the velocity and acceleration operating limits of the bearings is that the actuators to be used to excite the test rig have a maximum velocity specification of 1.67m/s. This is less than half the maximum velocity specified above. This means that, to produce those velocities, natural frequencies of the specimen will have to be excited. This would probably be commonly the case, but with more moderate target displacements than with the maximum allowable amplitude of ±50mm.

#### 3.2.3.6- Rig base and SDL floor occupation

As previously stated, the 3 DOF rig will comprise three separate self-contained and removable units. The cheapest and easiest solution for an adjustable and stiff assembly is to base it on steel box sections.

The floor contains anchors placed on a 400x400mm grid within the concrete matrix. These floor anchors provide the ground attachments for the rig. Unfortunately, the grid is not accurately centred and allowances of ±5mm all around theoretical locations need to be provided. Moreover, the floor surface is not perfectly level and horizontal. Here again, elevation can vary by about ±5mm. Therefore, the support units need provision for easy adjustment in order to align the units horizontally and axially.

### 3.2.4- CAD design, detailed drawings, manufacturing and assembly

According to all the requirements and choices discussed above, the detailed rig design was developed using the computer aided design package I-DEAS Master Series provided on the departmental UNIX network. Figure 3.8 shows overall isometric, side and plan views of the system produced.

The CAD system being a 3D one, the use of solid modelling was fully exploited and masses and centres of gravity were monitored as the design developed to make sure suitable properties were obtained. The mass of the empty carriage achieved is 43kg. Ballast units can be added to bring the weight of a carriage to 80kg and then to 100kg per carriage with virtually no displacement of the centre of gravity.

Because of the flexibility and versatility requirements, processes like gluing and welding were proscribed wherever possible. The extensive use of bolts was preferred in order to make things changeable if new needs arise. The only welded joints are the ones used for the spring attachments.

To allow for an easy shaft alignment procedure, the plinth, composed of 4 beams forming a square, was designed with a vertical setting device at each corner to take up any misalignment induced by the imperfect floor of the lab. This was provided simply by a leadscrew nut system.

Again, to reduce costs, none of the components contains particularly complex features. For this reason and also for ease of access and speed in production, the detailed drawings were produced with Microsoft Visio.

Many provisions for alternative fixing holes were made wherever a potential need might arise. Also, the system linking the springs to the carriages provided for many adjustment possibilities, and different springs could easily be used.

After the rig components were manufactured and the proprietary parts obtained, one carriage of the rig was assembled in the laboratory. The assembly was particularly straightforward. It only took a few hours to have the actuator, the first carriage and the shaft unit assembled and lined up. The alignment of the two shafts was quite easy to obtain thanks to the leadscrew-nut arrangement.

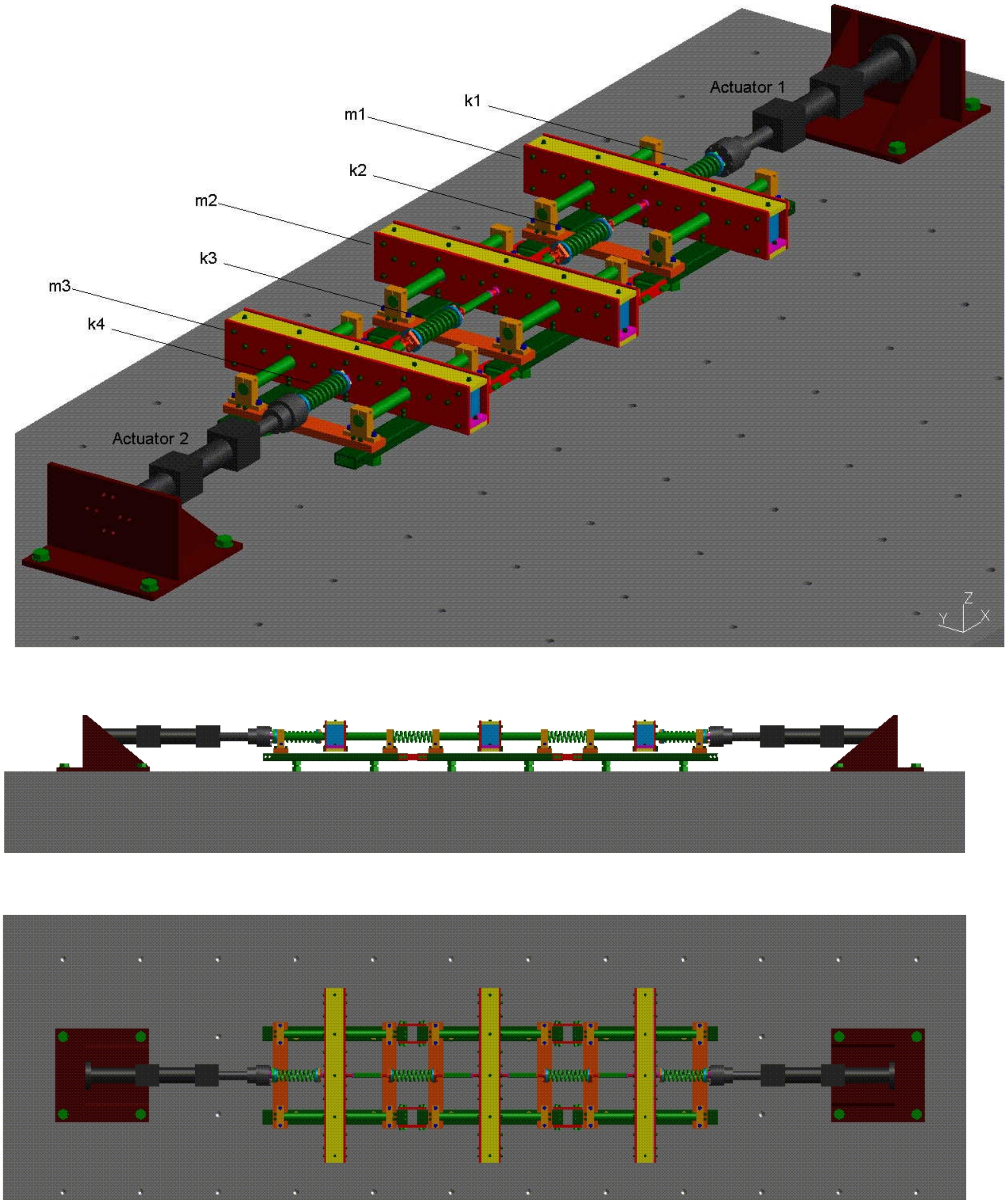


Figure 3.8: Isometric, side and plan view of the rig from the CAD software

## 3.2.5- Final modifications, instrumentation and property measurements

After assembly of the rig, it was obvious that the linear bearings provided significantly more play than had been expected and each carriage could develop cyclic angular displacements around the vertical axis. Although this would be very unlikely to have any structural impact on the rig, it could potentially affect the linear dynamics of the system, of interest here. An extra shaft/bearing arrangement was therefore added to the design of each carriage. This extra guiding system was designed with no load carrying capacity and could therefore provide a significant amount of guiding stiffness within a compact assembly, featuring only a small amount of friction. Ground shafts 25mm in diameter were attached underneath each carriage and plain low friction bronze bearings fixed to the transverse beams. The guidance provided was very good and obtained only at the cost of some setting up time to ensure the alignment of the additional shaft.

The rig was also equipped with instrumentation consisting of an accelerometer and an LVDT on each carriage. These sensors measure absolute values, i.e. relative to the stationary floor, and are logged directly onto the real-time PC via the DSP board. Thanks to the actuator displacement signals provided by the controller, all spring deflections can be obtained simply by subtracting the appropriate channels.

Then, important work was carried out to measure the final mechanical properties of the rig. These properties were used to build simple models of the rig to check the accuracy level of the RTS tests completed. The properties required were the masses of the moving carriages, the spring stiffnesses and the damping and friction values. Note that damping has two main sources in this system: the springs and the linear bearings. The springs provide damping from the relative motion of the masses whilst for the bearings it is from the absolute motion.

The moving assemblies and components were all weighed and the individual masses were recorded. The main results to note are those of the total moving masses in their main three configurations: 45, 85 and 105kg. These numbers include the mass of all the connected components.

Then, each spring was individually tested to extract stiffness and damping information. In these tests, the carriage was fixed in place so that the actuator displacement was also the spring compression. The actuator was made to perform a 25mm sine sweep from 0 to 6Hz over 50s and the load was recorded. An initial test with no spring was first carried out in order to estimate the dynamically reacting mass of the actuator load cell (found to be 0.23kg). For each spring, the inertial load – from the load cell reacting mass, the spring attachment and one half of the spring mass – was subtracted from the actuator load signal. The resulting spring load is assumed to be made up of elastic and viscous components. By linear regression of the load against actuator displacement, the average spring stiffness was worked out. The elastic load was then recreated by multiplying the stiffness by the actuator displacement and subtracted from the spring load found earlier. This new load was assumed to have a viscous origin and a new linear regression could be conducted of residual force against the actuator velocity to obtain the viscous damping for the spring.

Damping and friction in the rig also arise from the linear bearings. To measure this, a carriage was directly attached to the actuator via a rigid link and some constant velocity displacement strokes (i.e. saw-tooth shape) were conducted. Since the acceleration was negligible, no inertial force should be involved and the overall forces measured should be purely damping and friction dependent. Runs were conducted for each carriage mass configuration (45, 85 and 105kg) and for velocities of: 5mm/s, 50mm/s, then every 50mm/s up to 400mm/s (0.4m/s). The load signal was then averaged over each constant velocity period. The results were then plotted against velocity for each mass configuration. Two different models were fitted to these graphs: a purely linear viscous damping model and a non-linear Coulomb friction/viscous damping model. The former is a crude approximation but has the advantage of being linear but the latter was found to be a better fit to the measured data.

The results obtained from these tests are presented in Figure 3.9. In the masses section, a simple calculator can be seen on the right hand side to work out the total mass of the assembly considered out of the individual sub-assembly and component masses.

**1- Moving Masses**

| | | Mass | | Calculator |
|---|---|---|---|---|
| Carriage | | 45.25 | kg | 1 |
| (empty carriage) | 42.79 | | | |
| (LVDT + extra shaft) | 2.40 | | | |
| (accelerometer) | 0.06 | | | |
| Ballast 1 | | 37.01 | kg | 1 |
| Ballast 2 | | 19.97 | kg | 1 |
| 1/2 soft spring | | 0.67 | kg | 0 |
| 1/2 medium spring | | 0.79 | kg | 2 |
| 1/2 stiff spring | | 0.90 | kg | 0 |
| 1/2 super stiff spring | | 1.14 | kg | 0 |
| 1/2 dummy spring | | 0.96 | kg | 0 |
| 1/2 rigid link | | 0.16 | kg | 0 |
| Attachment actuator | | 0.41 | kg | 0 |
| Attachment short | | 0.34 | kg | 1 |
| Attachment long | | 0.48 | kg | 0 |
| Attachment turnbuckle | | 0.89 | kg | 0 |
| Attachment turnbuckle rotafree | | 1.55 | kg | 1 |
| Load cell reacting mass | | 0.23 | kg | 0 |
| | | | **Setup mass:** | 105.68 kg |

**2- Spring stiffness & damping**

| Spring number | Stiffness (N/mm) | Damping (N.s/m) |
|---|---|---|
| 2 | 61.8 | 12 |
| 3 | 66.0 | 12 |
| 4 | 66.0 | 13 |
| 5 | 66.4 | 11 |
| 6 | 44.0 | 20 |
| 7 | 47.4 | 16 |
| 8 | 47.8 | 18 |
| 9 | 47.2 | 17 |
| 10 | 25.0 | 22 |

**3- Carriage damping & friction**

| Linear Model | | Non-linear Model | | |
|---|---|---|---|---|
| Carriage mass (kg) | Damping (N.s/m) | Carriage mass (kg) | Damping (N.s/m) | Friction (N) |
| 45 | 73 | 45 | 38 | 10 |
| 85 | 86 | 85 | 38 | 12 |
| 105 | 109 | 105 | 38 | 16 |

Figure 3.9: Results of the rig property measurement tests

## 3.3- PRELIMINARY RTS EXPERIMENT

This section describes the simple RTS experiment devised to commission the test rig. The schematic arrangements are shown in Figure 3.10. The emulated structure is a two DOF system excited by an actuator. The system undergoes a simple test whereby the actuator imposes a 2.5mm constant amplitude sinusoidal frequency sweep from 0 to 10Hz (this range covers typical earthquake excitation frequencies). Both natural frequencies of the system are below 10Hz (3.3 and 7.9Hz) and are excited during the test. For the RTS test, this structure is divided into two parts:

- The spring and mass adjacent to the actuator in the emulated system become the numerical substructure and are simulated computationally together with the external loading provided by the actuator in the emulated test.
- The second "spring and DOF" unit is the physical substructure and is connected to an actuator to replicate the interface boundary condition.

Note that the damping is modelled as coming from both the spring and the linear bearings. As seen on Figure 3.10, the testing of the emulated structure and that of the substructured system can be conducted simultaneously (although this is of course not necessary for an RTS test). The results can then be observed as the experiment progresses.

The numerical scheme used for this experiment is the Newmark explicit scheme, with a time step of 5ms. Its explicit nature makes it straightforward to implement for a real-time experiment. The delay compensation scheme is a time-step independent third order polynomial extrapolation of a constant delay estimate of 5.3ms. The principle was originally presented in Horiuchi *et al.* (1996) (see Chapter 5). Finally, the real-time code uses multi-tasking to conduct the various tasks at two different sampling times. The integration of the numerical substructure equations of motion and the delay compensation are conducted at “base-steps” of 5ms, while the command signal generation as well as the data acquisition are conducted at 0.2ms steps.

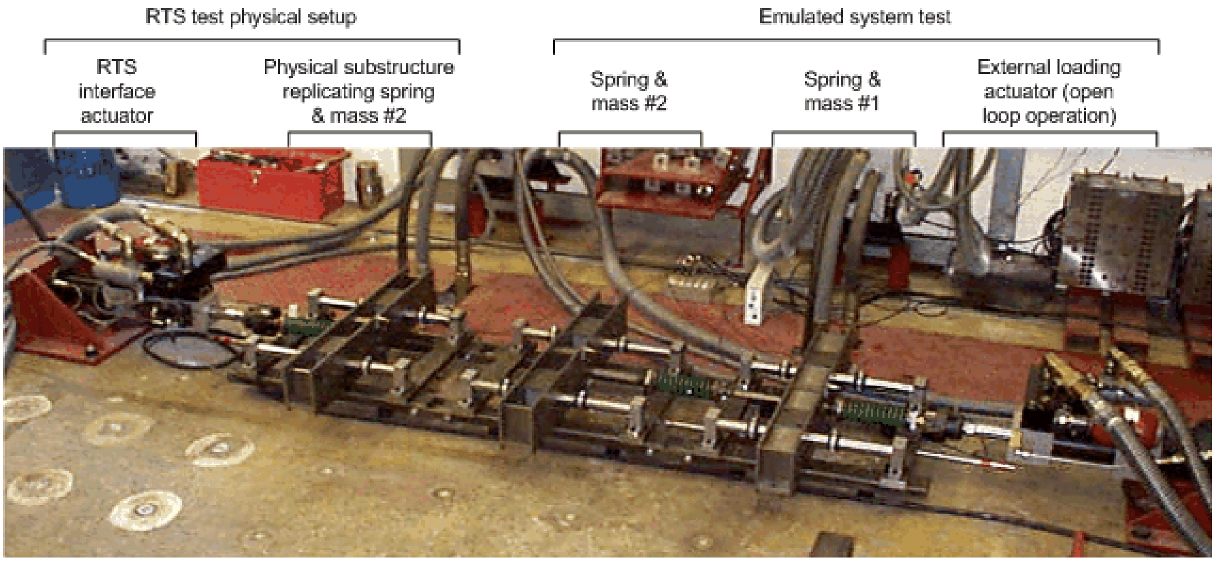


Figure 3.10: RTS demo test setup

Figure 3.11 presents the results of the experiment regarding the quality of the interface emulation. The top graph shows the interface displacement desired in the RTS test (i.e. before delay compensation); the second graph shows the displacement recorded from the actuator and the third one shows the difference between the two, namely the synchronisation error. The error is at its worst at the two natural frequencies of the structure, but only reaches 0.1 & 0.2mm (0.4 & 1.5% of the required displacement respectively). Away from the natural frequencies, the error is minimal and increases with the excitation frequency: from 20μm near 0Hz up to 40 μm at 10Hz. These very small errors confirm that the interface loading is correctly applied in real-time. Figure 3.12 presents the response plots for the emulated and RTS tests. The first graph shows the frequency content of the emulated system response (second DOF displacement) and of the RTS test response (physical substructure). The second graph shows the time domain responses in the form of their positive envelopes, as well as the error between the two. The frequency domain graph shows good agreement. The first resonance occurs slightly earlier in the emulated system than in the substructured one. This is confirmed in the time domain with the error curve showing a positive peak just after the first resonance. The graph also shows slight amplitude discrepancies between the emulated and substructured response envelopes. These discrepancies are mostly due to the stiffness and damping differences between the springs and carriage setups. On the whole, the response is well reproduced and the test is validated.

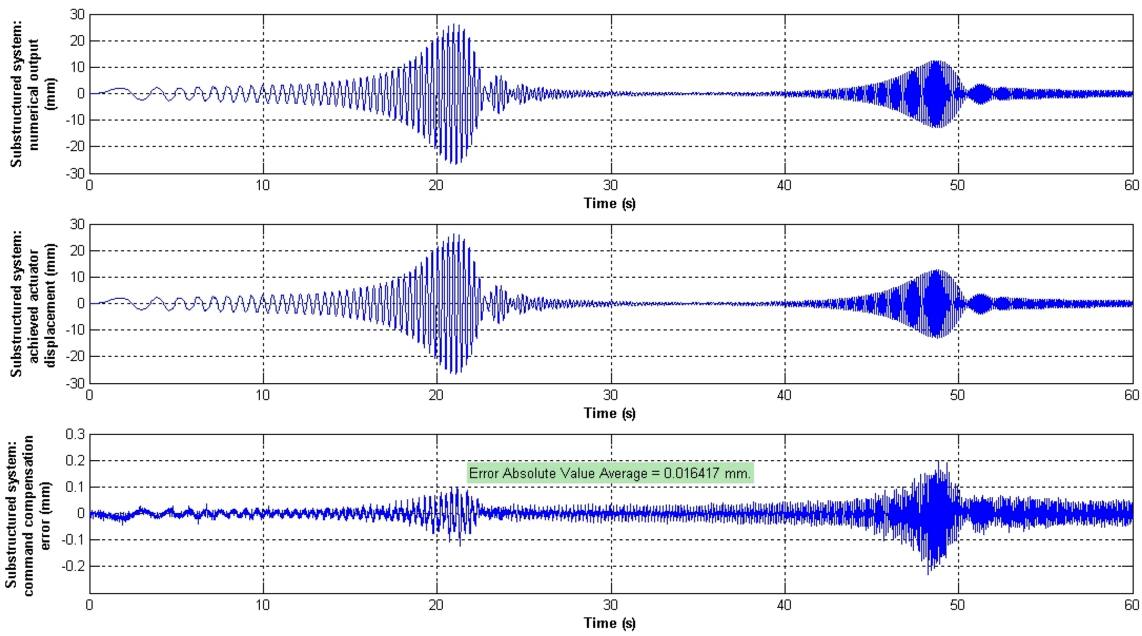


Figure 3.11: Substructure interface plots

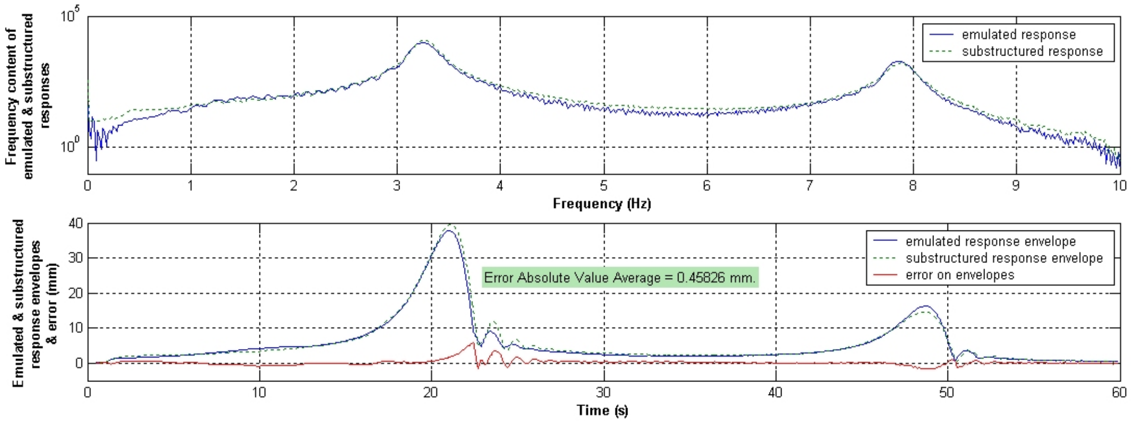


Figure 3.12: System response plots

## 3.4- SUMMARY OF THE HARDWARE AVAILABLE

Following the review in Chapter 2, this chapter focussed on the hardware and described the equipment that was used to conduct the research. The laboratory environment was described in detail, followed by the work on the design, construction and commissioning of the development test rig. The rig produced is a very versatile MDOF arrangement, with masses and springs that can be adjusted to obtain the desired natural frequencies. The dynamic properties – including mass, spring rates, relative and absolute damping and Coulomb friction – of the rig were also measured accurately for modelling purposes. Finally, preliminary real-time hybrid simulations were presented. The results of these substructure experiments were good with a low level of control error and only slight discrepancies with the fully experimental test results. With this work, the basis of the research was established and more fundamental issues could be investigated.

# CHAPTER 4

# THE ISSUE OF ACTUATION QUALITY FOR REAL TIME TESTING

## 4.1- INTRODUCTION

The use of servo-hydraulic actuators is widespread in the field of experimental testing of structures under dynamic loading. Many types of experiments exist, among which cyclic fatigue testing, pseudo-dynamic experiments or large scale real-time shaking table substructure tests can be cited (Williams and Blakeborough, 2001).

Some of these methods use the actuators in an open loop (i.e. the loading history is known before the test is carried out); others require a closed loop and calculate the load signal for the actuator input as the test progresses using a feedback signal and a numerical process. Amongst the closed loop methods, some operate in real-time (Nakashima and Masaoka, 1999) while others are conducted on an elongated time scale (Molina *et al.*, 2002). The majority of the closed loop tests operate with displacement controlled actuators.

In all of these tests, poor actuation performance (e.g. undershooting, response time, etc.) leads to a lack of accuracy for the measured response. However, in the case of closed loop tests, the lack of accuracy propagates from one loop to the next and is therefore likely to be amplified. For real-time closed loop experiments, poor actuation also often leads to a more severe issue: instability.

The main point of interest in this chapter is the realisation of closed loop tests involving servo-hydraulic actuators, with a focus on the real-time substructure method. This method is the focus of a lot of attention at the moment and many large scale investments are being made towards state of the art facilities around the world (see for example Reinhorn *et al.*, 2002).

Some authors presenting results of such tests have mentioned cases of instability due to poor actuation performance (Blakeborough *et al.* 2001). It is widely accepted that high-quality actuation is crucial for the execution of hybrid tests such as RTS experiments. Other researchers have also shown analytically that systematic errors are particularly known as problematic (Shing & Mahin 1990). Others have developed actuator mathematical models to investigate performance effects (Williams *et al.* 2001; Zhao *et al.* 2004). However, to the knowledge of the author, no dedicated literature has shown first-hand experimental evidence quantifying the actuation performance and detailing the simple situations that make it vary substantially. This is what this chapter focuses on.

Although displacement controlled actuators are directly dealt with in this chapter, the techniques used are believed to be transferable to load controlled actuation.

## 4.2- TYPICAL CONSEQUENCES OF THE PROBLEM

This section explains the importance of actuator performance in an experiment where an actuator is used in closed loop control. In an RTS experiment, the structure of interest is divided into two entities:

- On one hand, parts that can easily be numerically modelled and therefore do not need to be tested physically.
- On the other hand, the more crucial parts, physically replicated, for example exhibiting high non-linearity.

The two categories are complementary and their combination forms the structure of interest. The dynamics of the numerical substructure are solved computationally through time integration, while the physical substructure is subject to experimental dynamic loading through hydraulic actuators. Both substructures interact with each other in real-time at their interface to represent the emulated structure.

In a real-time substructure test, the stiffness, damping and inertial properties of the physical substructure are accounted for through the measured force feedback. The substructures send and receive data from each other and the interface between the substructures is realised with dynamic hydraulic actuation. The numerical substructure generates a strain state of the physical substructure and the actuator reaction force is fed back to the numerical model to carry on the real-time emulation. The integration step is typically a few milliseconds.

In the system used for this research, the closed loop control of the actuator is conducted by a proprietary digital controller unit, using a proportional-integral-derivative-lag algorithm operating at 5kHz. A second loop operates between the controller and a digital signal processing board. The DSP board's communications with the controller and the actuator itself realise the boundary conditions between the substructures.

The DSP board implements the integration scheme to solve the numerical substructure discretised equations of motion and compute the next step interface displacement to be applied to the physical substructure. A compensation scheme is also run on the DSP board, extrapolating the actuator command in advance of a time equal to the delay estimate (Horiuchi *et al.*, 1996). Indeed, hydraulic actuators are known not to respond instantaneously. Their response can be fully characterised in the frequency domain (Plummer 2006), but for the realisation of RTS simulations the characterisation of the actuator dynamics in the form of delay and amplitude error time histories is more practical for compensation algorithms, as shown in the next chapter. Please note that the term *delay* will be used throughout this chapter, while other terms may also be used.

An example is presented here, conducted with a 10kN actuator (±75mm piston stroke). The emulated structure is composed of two SDOF oscillators mounted in series and to the actuator through coil springs. For the RTS test, the spring and DOF adjacent to the actuator become the numerical substructure. The second "spring and DOF" unit becomes the physical substructure which is connected to the actuator, replicating the interface boundary condition. The numerical scheme used is the Newmark explicit scheme, with a time step of 10ms (please see Chapter 6 for details on numerical schemes). It is straightforward to implement for a real-time experiment. The delay compensation scheme is a time-step independent third order polynomial extrapolation of a constant delay estimate. The real-time code uses multi-tasking to conduct the various tasks at two different sampling times. The delay compensation – like the integration of the numerical substructure – is conducted at 10ms steps. The command signal generation is conducted at 0.2ms steps (i.e. the same sampling frequency as the actuator controller).

The system undergoes a simple test with the external excitation being a 2mm constant amplitude sinusoidal frequency sweep from 0 to 10Hz. Both natural frequencies of the system are below 10Hz and are excited during the test. The emulated system is tested first, and then the RTS test as described above. The actuator delay is estimated to be 4.7ms, so this estimate is used. Then a second RTS experiment is conducted with a delay estimate deliberately chosen too small at 3.1ms. Note that the delay estimate is only used for the delay compensation algorithm. Figure 4.1 presents the response plots for the emulated test and for both these RTS tests.

While the response obtained with the 4.7ms estimate matches well that obtained for the emulated system (despite a slight resonance frequency discrepancy for the second mode), the response obtained with the 3.1ms estimate is highly inaccurate after the second mode. Note also that the response to the first mode is less accurate in amplitude. Another test was conducted with a 3.0ms compensation. Instability occurred at the second mode excitation and led to the actuator safety limits being reached, provoking the immediate end of the test.

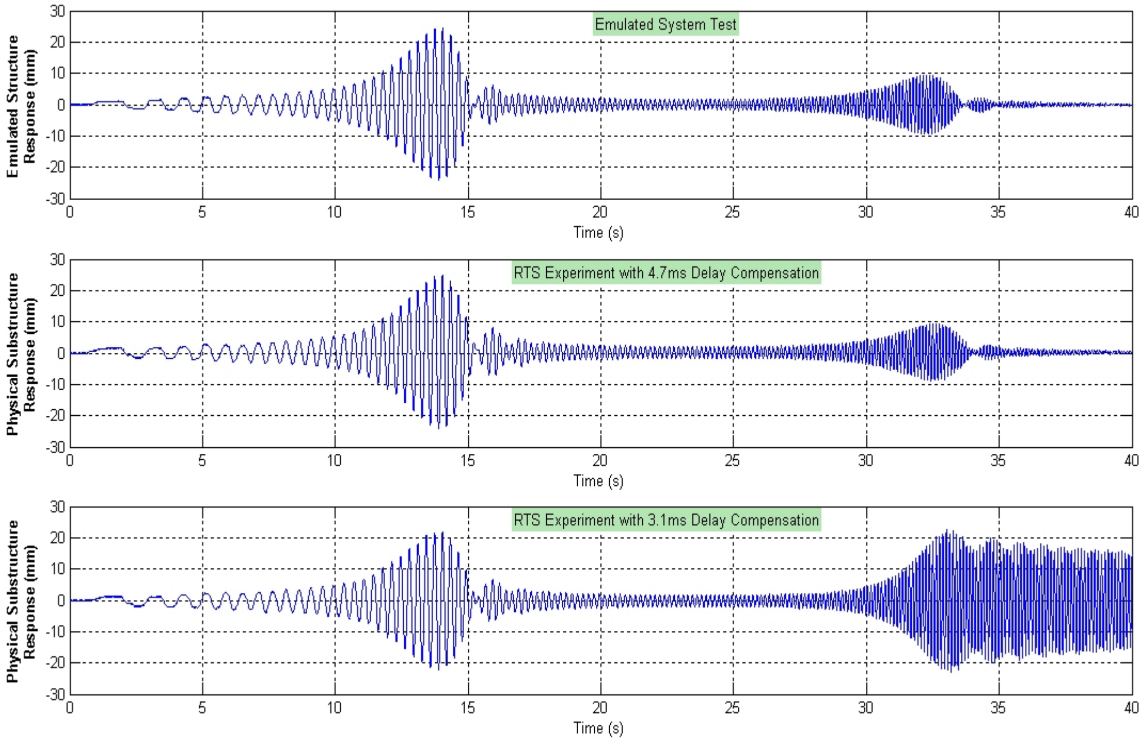


Figure 4.1: Example of RTS experiment results & importance of the delay estimation

In this section, the RTS method was described and shown to work on a simple demonstration test. But it was also shown that the method is very sensitive to the delay estimate used and the actuator performance must be relatively well known in advance for the test to be accurate and stable. Previous literature provides examples of similar tests becoming unstable for more complex reasons, like non-linearities in the specimen or high levels of interaction between several actuators (such as two independent actuators used to provide a translation and a rotation at the same structural point). It is also implied that delay variations within a test can potentially render it unstable if they are not properly taken into account. As a result, to perform complex RTS experiments, it is important to know better why, how and by how much the actuator performance may vary during a test.

## 4.3- STEPPING BACK: ON HOW TO QUANTIFY ACTUATOR PERFORMANCE

Figure 4.2 shows schematically the time histories of a displacement command signal and the actuator response to it. The real-time command error is defined by the difference between the response displacement and the command at any moment in time. It can also be called the synchronisation error. The delay can be defined as the time difference from a given command point to its execution by the actuator (e.g. points A and A’ respectively) and the amplitude error as the displacement difference between the same points.

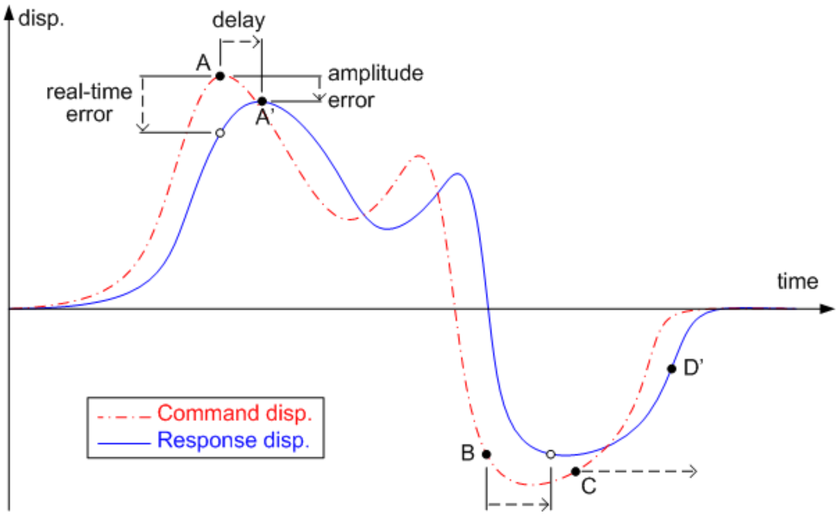


Figure 4.2: Schematic of time histories of displacement command and actuator response

The real-time command error has the great benefit of being very easy to measure. However, an undershooting behaviour, for instance, as shown in Figure 4.2, does not necessarily imply the actual displacement will always be less than the command in absolute value, because some delay is also present that makes the two signals cross. So no simple relationship can be established between a purely undershooting response (as shown in Figure 4.2) and the real-time response error. The same applies for an overshooting behaviour.

Moreover, the real-time command error is very much dependent on the excitation frequency. Indeed, if a frequency sweep is input and the actuator response is purely delayed by a constant, the real-time error will vary substantially. Finally, trying to quantify the delay without taking any amplitude error into account can lead to poor results. For instance, point B on Figure 4.2 would be associated with an artificially high delay and, for point C, no solution would be found at all.

On the other hand, the amplitude error and its sign, as defined above, can simply characterise the nature of a response, because some account of the delay is taken: if the sign of the amplitude error is opposite to that of the command signal at the point considered, undershooting is identified (and vice versa for overshooting). And if the error can always be taken into account in the delay calculation, much better quality delay results will be obtained. The problem of actuation performance can therefore be described by those two simple variables, which will be used in the rest of this chapter. Note that for this enterprise, it is not intended to measure the delay and amplitude error in real-time during the test; only a simple post-processing approach is required.

But if the aim is to measure the delay and amplitude error, it is important to realise that they can partly "hide" each other. In fact, the only places where they can be easily measured are the local peaks (e.g. point A). Away from these places, if the command signal is as defined in Figure 4.2, if one starts with the response point D' and tries to find the corresponding point D from the command signal so as to find a measure of the delay and amplitude error, there is an infinite number of solutions. Unless an assumption is given about one of the two unknowns (or possibly an additional relationship between the two) the problem cannot be solved.

From previous literature and experience, the delay is more crucial than the amplitude error since it is more likely to lead to instability. So it is natural at this stage to formulate an assumption about the amplitude error as follows. The amplitude error can be measured at the local peaks and assumed to vary linearly with time between consecutive local peaks. The amplitude error measured and calculated this way then allows the measurement of the delay at any point of the response signal. Provided the amplitude error does not show substantial changes and always remains fairly small, the assumption will lead to a good enough approximation and therefore to a good estimate of the delay. Note that this method obviously ensures the right solution at the local peaks.

The method described in the previous paragraph allows comparison of any pair of command and actual displacement signals obtained experimentally and analysis of the performance of the actuator through its delay and amplitude error. Various situations and conditions of use have been tested in the laboratory and are analysed in the following section, using the same 10kN dynamic actuators as mentioned in the previous section. The rest of this chapter is mainly concerned with a pragmatic presentation of experimental results, and a discussion of the potential causes behind the results observed is not always made. However, when analysing the data, it will be important to bear in mind the assumption made about the variations of the amplitude error between local peaks.

Because various tests have been conducted for different displacement amplitudes, instead of analysing the amplitude error in absolute terms, the amplitude factor will be analysed, as defined in Equation (4.1):

$$amplitude\_factor = \frac{response}{command} = 1 + \frac{amplitude\_error}{command} \tag{4.1}$$

This simple transformation ensures fair relative comparisons can be made between values obtained in tests where different amplitudes were required.

## 4.4- ANALYSIS OF ACTUATOR PERFORMANCE FOR VARIOUS PARAMETERS

### <u>4.4.1- Command frequency & local peak behaviour</u>

A constant amplitude sinusoidal frequency sweep from 0 to 15Hz was conducted on the bare actuator. The amplitude (13mm) was chosen so that the maximum piston velocity at the end of the sweep reached 75% of the maximum piston velocity specified by the actuator manufacturer. The results are shown in Figure 4.3.

The delay variations are very important at low frequencies. When trying to describe sine waves at low piston velocities, the hydraulic actuator produces large delays at the peaks immediately followed by very low delays (or even negative delays although not accounted for in the data processing) just after a peak. This typical behaviour is shown in the third graph of Figure 4.3 with a local peak time history of the normalised command and response displacements. This effect decreases vastly at higher frequencies but always remains present to some extent (making the task of measuring the delay at all times worthwhile). Friction within the actuator body may be one of the causes of this phenomenon. This is also the moment when the real-time error changes sign. This behaviour is typical of the hardware used in this research and can also be detected from Figure 4.4 and 4.7.

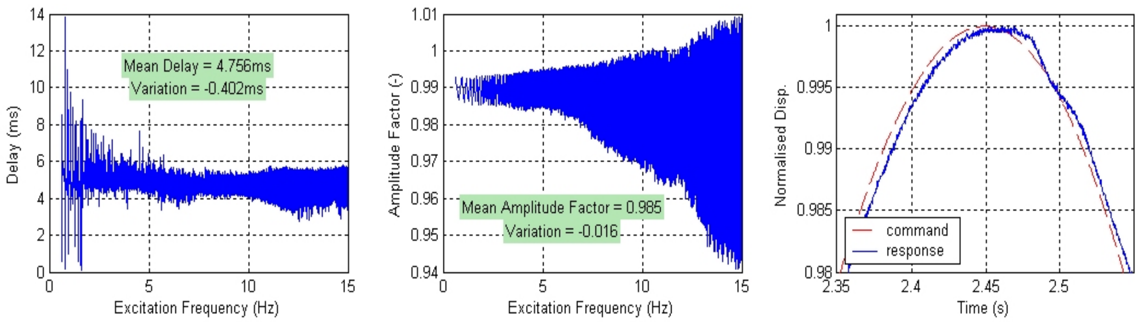


Figure 4.3: Actuator performance as a function of excitation frequency

The delay variations are then fairly low between 5 and 10Hz, and pick up again above 10Hz. The trend seen above 10Hz is probably due to the piston velocity reaching the highest values.

The amplitude factor (slightly decreasing with frequency on average in this example) is also seen to vary much more when the frequency and the piston velocity increase.

## 4.4.2- Actuator controller proportional gain settings

Tests on bare actuators were conducted with a constant amplitude sine sweep from 0 to 15Hz. Several proportional gain *P* settings were tested and the results, presented in Figure 4.4, show that the actuator delay depends largely on the setting chosen. The amplitude factor and its variations are also affected, to a lesser extent. In summary, a high *P* setting implies a lower delay average and better delay consistency. This is therefore the preferred choice.

Note that the *P* setting has an upper limit above which the actuator inner-loop control becomes unstable. This maximum setting is related to the oil column resonance of the hydraulic system and therefore depends on the mass directly attached to the actuator piston. The settings used to compile the results presented here allow stable control of various specimens.

The inner-loop controller used in the OUSDL operates with a PID-lag architecture. The control parameters are routinely set through the use of an automatic proprietary optimisation process based on the achievement of a target square wave response overshoot (Instron 1998).

From the results of this optimisation, it was found that the process can be seen as very conservative and substantial gains could be obtained by further increasing the *P* gain. This is probably due to the optimisation process being based on square wave response, which is inadequate for the application to dynamic real-time loading, where the discretised input into the inner-loop ought to make the actuator describe a smooth continuous loading path, as opposed to a series of step inputs. Therefore, different optimisation strategies may be better suited to RTS applications, even though the issue was not investigated in this research.

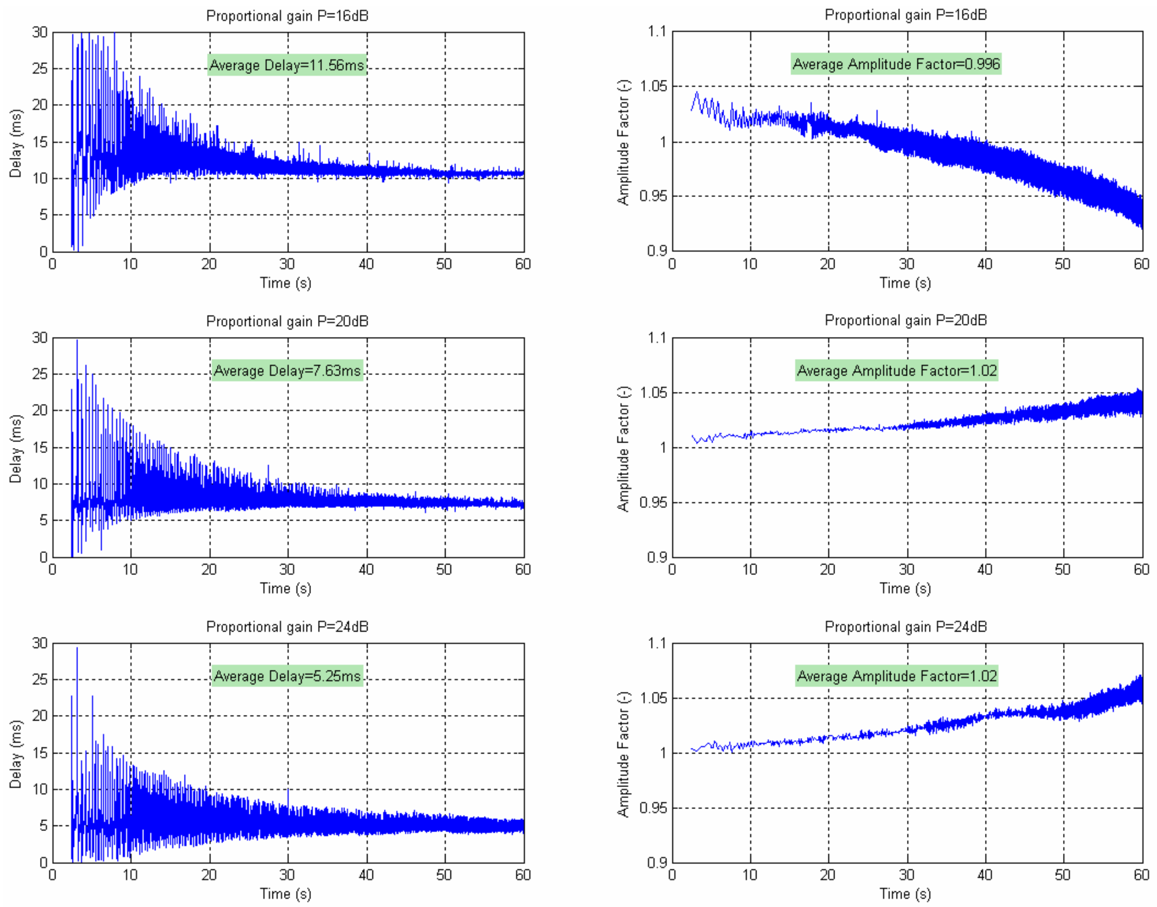

Figure 4.4: Actuator performance as a function of controller setting

## 4.4.3- Piston position within the actuator body & amplitude of displacement

Similar tests were conducted on a bare actuator with constant amplitude sine sweeps from 0 to 15Hz for various starting positions of the piston within the actuator body. No significant effect was noted on the average delay and its variations. However, the amplitude factor results were not as consistent. A few typical results are shown in Table 4.1. For the central position of the piston within the body, the amplitude factor is about 1.02 and shows an increase of about 5% across the frequency range. For all other positions (i.e. for positive or negative offsets), it is about 0.99 and displays no measurable variation across the frequency range. This result, possibly caused by a higher level of wear near the central position, should not be forgotten and, as a consequence of it, comparisons between a test conducted around the central position and another conducted with an offset will be avoided.

Another interesting result was found during these tests. The actuator performs better on delay, both in average value and in standard deviation, when the amplitude of the oscillations required is higher. No similar trend is found with the amplitude factor. An example of this is shown in Table 4.1 and illustrated in Figure 4.5. Again, any future comparison will need to account for this result.

| | Starting Offset (mm) | Oscillations amplitude (mm) | Mean Delay (ms) | Delay Stand. dev. (ms) | Mean Ampl. fac. (-) | Ampl. fac. Variation (-) |
|---|---|---|---|---|---|---|
| Central position | 0 | 5 | 4.71 | 0.49 | 1.02 | 0.05 |
| 20mm Offset Inwards | -20 | 5 | 4.75 | 0.57 | 0.99 | 0.00 |
| 40mm Offset Outwards | 40 | 5 | 4.75 | 0.56 | 0.99 | 0.00 |
| 40mm Offset Outwards & 1mm Oscillations | 40 | 1 | 5.05 | 1.30 | 0.99 | 0.00 |

Table 4.1: Actuator performance for various piston positions & required amplitudes

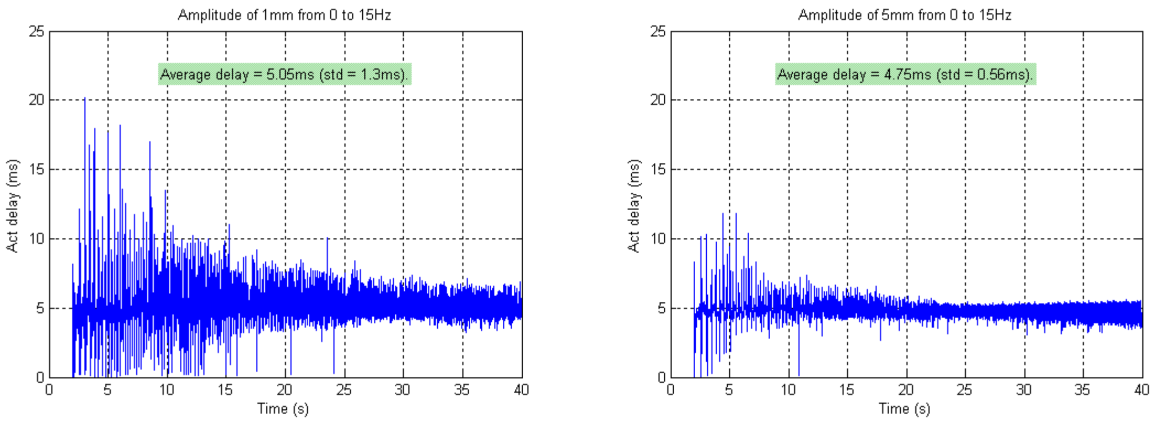


Figure 4.5: Live actuator delay with different oscillation amplitudes

## 4.4.4- Specimen stiffness

Testing was also conducted to monitor the performance of the actuator attached to a specimen with high stiffness, low mass and low damping, depending on the value of the stiffness. Five springs were tested with one end attached to the floor and the other to the actuator. The actuator was then required to conduct a 3mm sine sweep from 0 to 3Hz, around the central piston position. The bare actuator was also subject to the same test in order to obtain a measurement for no specimen stiffness. From these various runs, it was seen that the amplitude factor and its variations do not depend noticeably on the specimen stiffness. The results obtained for the delay and its variations, however, are notable. The results are presented in Figure 4.6.

It is found that the actuator responds faster for a lower stiffness specimen, but also with less consistency. The influence of the stiffness on the average delay is found to be about 1.2ms/(kN.mm$^{-1}$). The specimen stiffnesses investigated here are lower than for the corresponding results published earlier (Darby *et al.*, 2002), but a similar trend is found, even though Darby's result is approximately twice as large. Darby was only measuring the delay at zero-crossings, but this different method is not believed to be the reason for the discrepancy in the ratio of the delay increase with stiffness, since the zero-crossing method applied to the present data gives roughly the same slope of dependency as observed with the more comprehensive method. The present data were collected with the same displacement oscillations required at the actuator for various specimens, hence increasing the maximum actuator load with the stiffness tested. The approach chosen by Darby *et al.* is not known, which means the data points presented may have been gathered with different amplitudes, different loads, or both.

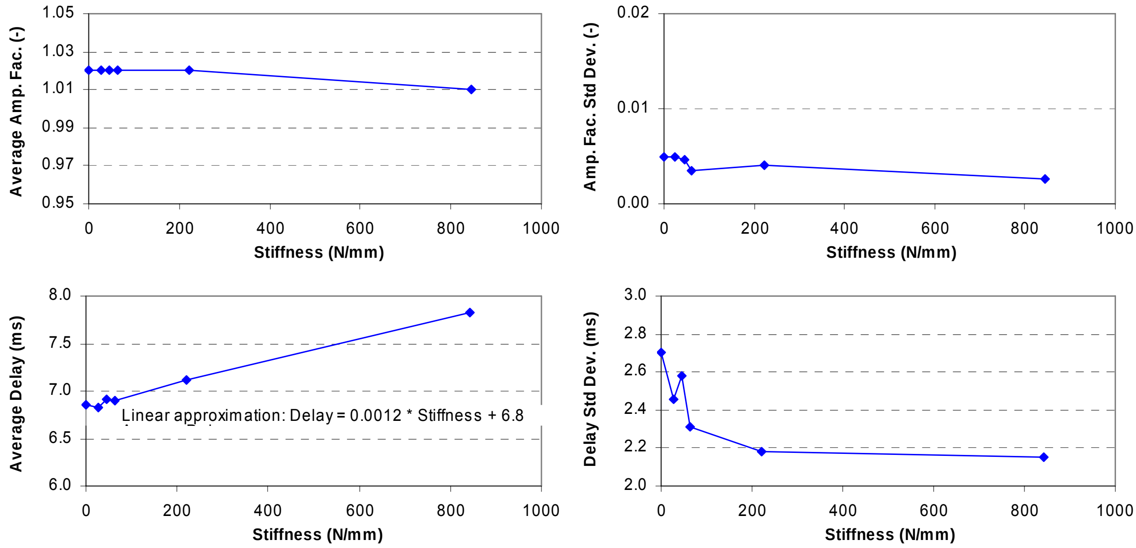


Figure 4.6: Delay performance as a function of specimen stiffness

## 4.4.5- High loads

Similar tests were conducted with a stiff specimen in order to check the influence of the high mean loads required on the actuator performance. Knowing the specimen stiffness and displacement amplitudes affect the performance, a test is devised where the actuator deflects a linear spring from a preloaded situation in order to create substantial loads. Tests with increasing amounts of preload are compared to discover if higher loads affect the actuator performance. Note that the various preload settings tested did not require any actuator movement. Instead, they were achieved by displacing the stationary end of the spring, hence validating the comparisons made.

From each starting position, the actuator is required to follow 1mm sinusoidal oscillations sweeping from 0 to 10Hz. The results are shown in Figure 4.7. Clearly, higher loads make the actuator perform less well in average delay. The increase is just under 1ms when the mean load required goes from 17% to 76% of the actuator dynamic rating.

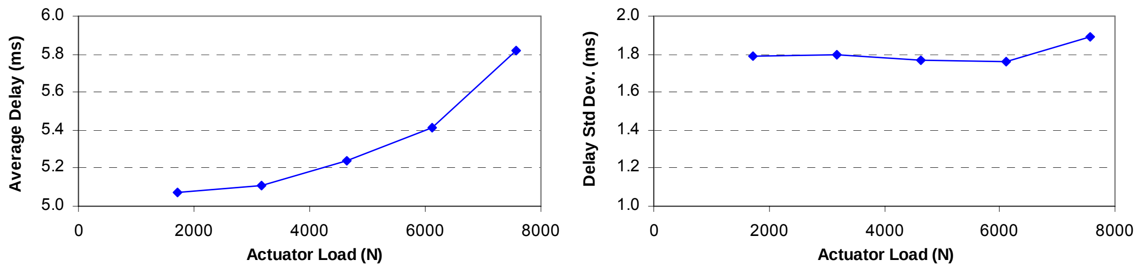


Figure 4.7: Delay performance as a function of mean actuator load

The average delay increase with mean load is greater for high loads and may be negligible for low loads (i.e. exponential effect across the range tested). However, the higher loads do not make this performance less consistent during each test. No significant trend can be found between the higher loads and the amplitude factor or its variations.

## 4.4.6- Non-linear specimen

Tests were conducted where the actuator was connected to a fairly soft (~70N/mm) coil spring, set to preload the spring by 40mm, and then required to describe a 20mm sine sweep from 0 to 4Hz. The specimen was also preloaded by 30mm from its other end. The specimen linearity was checked for this baseline run. Some rubber coating was then added on the spring to make it behave non-linearly and the same test was conducted. The specimen exhibited a stiffening behaviour as the deflection increased. The load-displacement curves obtained are shown in Figure 4.8 and measurements of the stiffness changes are presented in Table 4.2. The effect on the actuator performance of the addition of non-linearity to the specimen was analysed. The same process was then repeated for a stiffer spring (~300N/mm) with 10mm oscillations and a smaller initial deflection. The results are presented in Table 4.2.

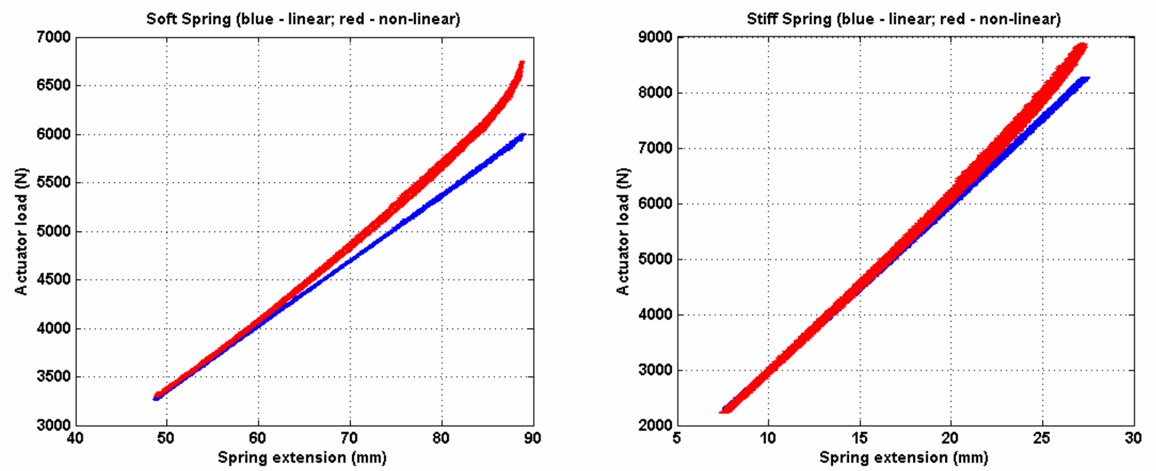


Figure 4.8: Load-displacement curves for linear and non-linear specimen

| | Mean Load (N) | Lowest Stiffness (N/mm) | Highest Stiffness (N/mm) | Mean Stiffness (N/mm) | Mean Delay (ms) | Delay Stand. dev. (ms) | Mean Ampl. fac. (-) | Ampl. Fac. Stand. dev. (-) |
|---|---|---|---|---|---|---|---|---|
| Linear soft spring | 4656 | 67 | 72 | 68 | 4.89 | 0.82 | 0.99 | 0.00 |
| Non-linear soft spring | 4880 | 69 | 161 | 87 | 4.93 | 0.87 | 0.99 | 0.00 |
| Linear stiff spring | 5337 | 300 | 314 | 306 | 5.09 | 1.01 | 0.99 | 0.00 |
| Non-linear stiff spring | 5521 | 311 | 415 | 339 | 5.18 | 1.15 | 0.99 | 0.00 |

Table 4.2: Actuator performance for linear and non-linear specimen

For both springs, the addition of rubber brings an increase in the mean load required at the actuator (by about 200N), an increase in the highest stiffness measured coupled with a more moderate increase in mean stiffness over the range tested. During the two tests with the non-linear specimen, the actuator performance in average delay is slightly poorer than for the respective baseline tests. Also, the increase in average delay is coupled with a decrease in consistency shown by a slightly higher standard deviation. However, once the results are adjusted for the higher mean load and for the higher mean stiffness (according to the sensitivities found in the previous two analyses), the increase in average delay becomes nil for the soft spring test and reduces from 0.09ms to 0.03ms for the stiff spring. Moreover, no effect can clearly be seen from the results regarding the influence of the non-linearity on its amplitude performance. So overall, the influence of non-linearity on the performance of the actuator could only be explained in terms of stiffness and load level changes. In other words, a non-linear behaviour makes the actuator vary more in delay performance but achieve similar average results.

## 4.4.7- SDOF specimen properties

Following on from the investigations conducted above with a stiff specimen, the actuation performance has also been analysed for a SDOF specimen consisting of a mass attached to the actuator through a spring. The actuator was required to input 2mm sinusoidal waves from 0 to 15Hz. The stiffness and the mass were varied, and the resulting natural frequency ranged between 2.4 and 5.9Hz. The damping was low and could be approximated as linear (~100N.s/m). The bare actuator was also tested with the same input. The results are shown in Table 4.3.

| Mass kg | Stiffness N/mm | Calc. f Hz | Ave. del. ms | Amp. fac. ave. |
|---|---|---|---|---|
| 104 | 65 | 4.0 | 5.28 | 1.02 |
| 104 | 44 | 3.3 | 5.28 | 1.02 |
| 104 | 24 | 2.4 | 5.27 | 1.02 |
| 84 | 24 | 2.7 | 5.27 | 1.02 |
| 84 | 44 | 3.6 | 5.27 | 1.02 |
| 84 | 65 | 4.4 | 5.27 | 1.02 |
| 47 | 65 | 5.9 | 5.24 | 1.02 |
| 47 | 44 | 4.9 | 5.23 | 1.02 |
| 47 | 24 | 3.6 | 5.24 | 1.02 |
| 0 | 0 | - | 5.21 | 1.02 |

Table 4.3: Actuator performance for various SDOF properties

These results show very little dependency of the actuator performance on the SDOF system parameters. The moderate average delay increase with stiffer specimen noted earlier is also found here.

## 4.4.8- Linear SDOF specimen resonance

The actuator performance was also observed whilst exciting a SDOF system through resonance. The data plotted in Figure 4.9 were obtained with the actuator describing a 2mm sine sweep through the resonance of a 47kg and 65N/mm SDOF oscillator (5.9Hz natural frequency). Each plot shows about two seconds' worth of data either collected just before, during or just after the specimen resonance.

From Figure 4.9, the effect of going through the resonance is obvious for both performance criteria. While the average values are roughly conserved, the consistency is notably worse during the specimen resonance. This effect is quite different from what was observed with the higher loads, although it is also coupled with it to some extent. Presumably, the transient character of the actuator load / displacement relationship during resonance is key to the variations observed. The amplitude factor variations are greater than for any other situation analysed.

Note that the delay plots against actuator displacement also show the more extreme values found at local peaks. This is the same phenomenon as shown in the third graph of Figure 4.3 and discussed with the command frequency sensitivity.

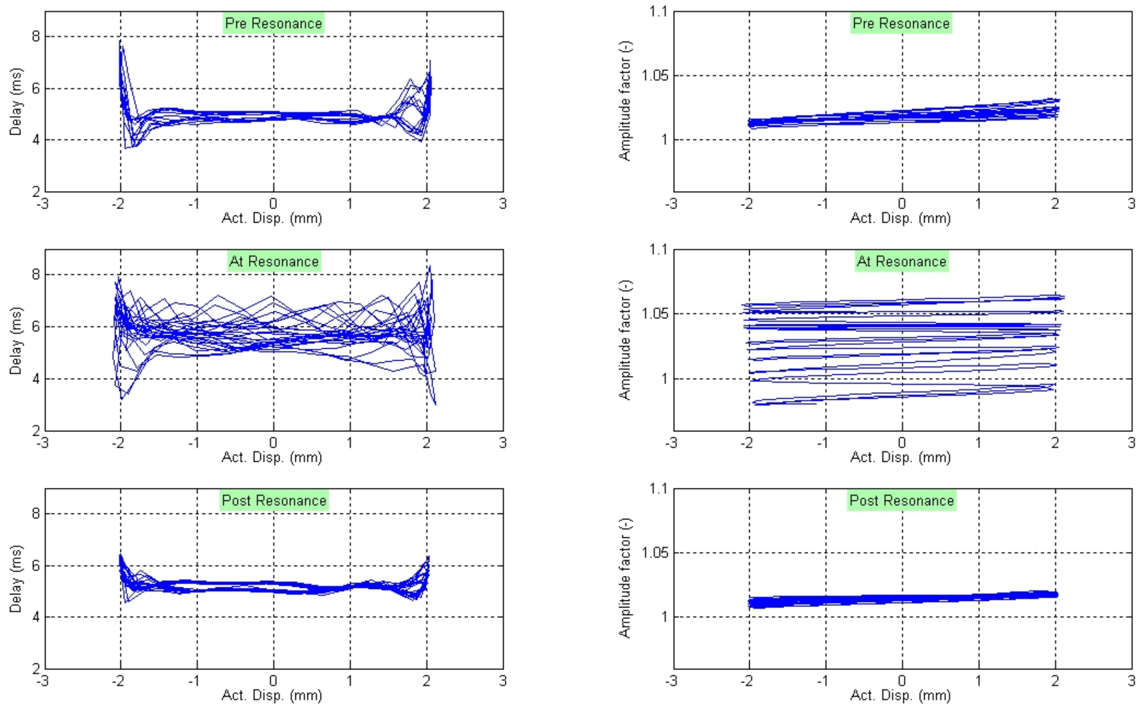


Figure 4.9: Actuator performance through a SDOF specimen resonance

## 4.4.9- Active opposition to the actuator – multi-axis system with linear specimen

In this experiment, an actuator is required to produce 6mm & 2Hz triangle waves. The actuator is attached to a SDOF system through a spring. The other end of the SDOF system is also attached through a spring to a second actuator. In the baseline run, the second actuator is stationary. The test is then repeated with the second actuator describing a 6mm sinusoidal sweep from 0 to 8Hz, hence providing an active opposition to the first actuator. The performance of the actuator conducting the triangle waves is shown in Figure 4.10 for both tests.

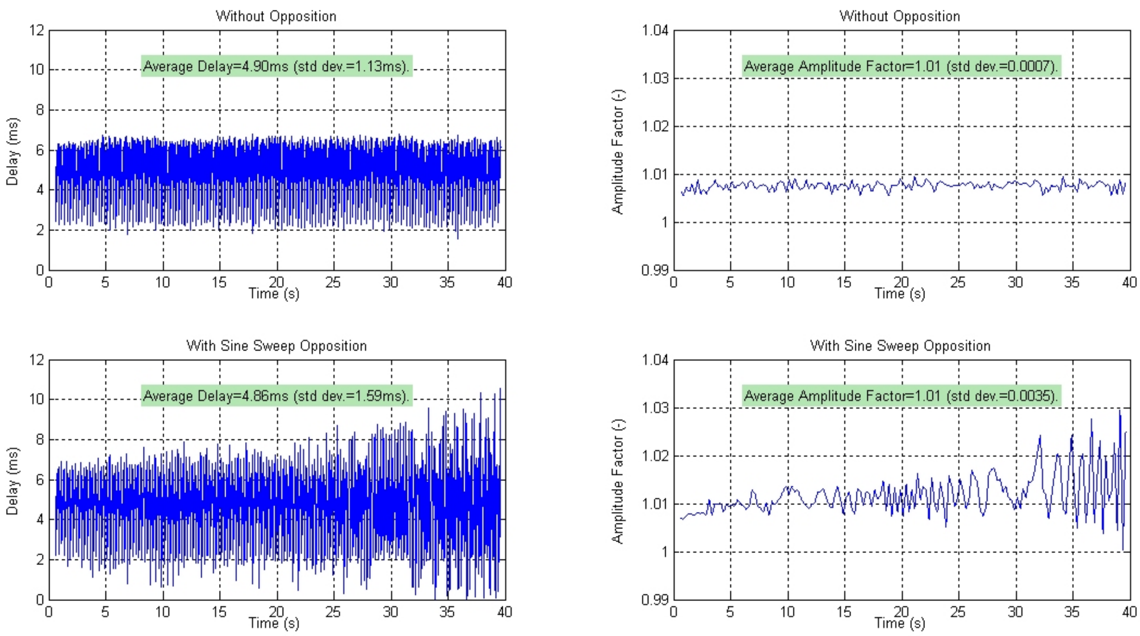


Figure 4.10: Actuator performance without & with active opposition

Due to the design of the experiment, there was no specimen stiffness change between the two runs, and the SDOF resonance frequency was not approached. The conclusions can be clearly drawn from the data plots. The active opposition seen by the actuator – although filtered by the SDOF system before reaching it – makes it significantly less consistent in performance, whilst the average values are conserved. This is quite different from the effects observed for the higher loads.

## 4.5- CONCLUSIONS

The issue of hydraulic actuation performance was presented and discussed in the context of conducting real-time closed loop experiments for structural dynamics. A method to quantify the performance with two measurable criteria was described and applied to various simple experiments. The effects of many parameters and situations were analysed.

The following points can be noted:

- The amplitude factor measured at local peaks is on the whole fairly constant and the measurements taken from the various tests were repeatable. The assumption made about its variations is therefore justified.
- The delay typically gets higher at local peaks and low frequency. However, over the frequency range of interest, the variations in delay are quite small, justifying the decision to treat the actuator dynamics as a delay and amplitude factor rather than a frequency response.
- More generally, there are higher delay variations at low frequencies, and higher amplitude factor variations at high frequencies.
- A high controller proportional gain helps in keeping the average delay and its variations small, while not implying poor amplitude behaviour.
- The amplitude factor can be affected by the position of the piston within the actuator body. The central position was seen to lead to a more frequency dependent result than when any offset is present.
- The average delay and its variations are higher when the amplitude of the oscillations required decreases.
- The average delay is higher when the specimen stiffness increases.
- The average delay is higher when the required actuator loads increase. The trend is exponential across the dynamic rating of the actuator.
- Potentially large variations of delay and/or amplitude error may occur within a test if a transient behaviour is involved (e.g. resonance, high stiffness change, active actuator opposition). Such situations should be carefully considered when conducting closed loop dynamic tests involving servo-hydraulic actuators to ensure stability and a good level of accuracy. The use of dedicated algorithms may be required (e.g. an adaptive delay compensation algorithm or an adaptive controller).

# CHAPTER 5

# ACTUATION COMPENSATION FOR MULTI-AXIS RTS TESTING

## 5.1- INTRODUCTION

The real-time substructure test method is based on splitting the structure of interest into two distinct and complementary entities. There are five main issues to address in order to conduct successful RTS experiments. They can be expressed from the most "physical" to the most "numerical" as follows:

1. The level of fidelity for the physical substructure model needs to be high.
2. The dynamic actuation hardware and its inner-loop control system need to perform well.
3. The outer-loop control problem needs to ensure the boundary conditions at the interface of both substructures are properly applied and measured.
4. The level of fidelity for the numerical substructure model needs to be high.
5. The computational method employed to solve the numerical substructure in real-time needs to be fast and accurate.

Of all these, points 1 and 4 are crucial "starting points", assuming the engineer is able to model the system of interest, partly physically and partly numerically. These modelling problems may be complex to deal with but, for this work, they have been respectively avoided and solved by building an arbitrary and simple rig whose properties have been easily measured with adequate instrumentation. The second point obviously assumes access to some actuation system, able to dynamically apply a load or a displacement. It will be assumed that this equipment is of servo-hydraulic nature, by far the most commonly used type in the field of earthquake engineering. Points 3 and 5 represent, in the view of the author, the main challenges inherent to the RTS method. In other words, these two issues are "created" by the RTS method and are central to its future as a widely available test method for structures under dynamic loading. Point 3 only is of primary interest in this chapter.

A high-quality actuation system comprises sophisticated dynamically rated servo-hydraulic actuators and an inner-loop digital control system. Besides the crucial load and displacement signal calibrations, work conducted on the tuning of the system showed that the performance could be optimised by the maximisation of the inner-loop proportional gain, the maximisation of the inner-loop A/D converter filter cut-off frequency to reduce the delay induced on the command signal and the minimisation of the outer-loop signal generation time-step on the DSP. However, a well-tuned system can still not realise perfect real-time actuation and can be characterised by a delay and an amplitude error (Bonnet *et al.* 2005). The delay is at most times positive and means the actuator response lags behind its command signal. The amplitude error can be of either sign. Those two criteria have different consequences for the project of conducting RTS experiments. Essentially, the delay can easily render an RTS experiment unstable by constantly injecting more energy into the structure than the amount it can dissipate (Horiuchi *et al.* 1996). On the other hand, the amplitude error is only likely to affect the accuracy of the experiment.

Post-processing the delay and amplitude error is not a straightforward task as they can be seen as interconnected (Bonnet *et al.* 2005). Consequently, the delay and amplitude error can be measured at local peaks and it can then be assumed that the amplitude error varies linearly between local peaks. The resulting amplitude error history is then used to work out the delay history data.

Besides the tuning of the actuation system itself, several types of situations have been identified that can affect the performance of servo-hydraulic dynamic actuators (Bonnet *et al.* 2005). The stiffness of the physical system connected to the actuator, as well as the level of loads required of the actuator, are known to affect the delay. Also, transient situations, such as going through resonance, experiencing non-linear behaviour or testing with opposing actuators (such as in multi-axis experiments), have been shown to affect the performance of the actuation system, and especially its consistency. All these situations can potentially render an RTS experiment inaccurate and/or unstable if not or poorly compensated for. Delay compensation is a commonly known process (see for example Horiuchi *et al.* 1996 or Blakeborough *et al.* 2001). Its natural counterpart, the amplitude error compensation, although less critical, should also be implemented for accuracy reasons.

In this work, the framework considered is that of displacement controlled RTS tests, which so far represent the vast majority of conducted experiments. It is believed that the content of this work still applies to force controlled or mixed controlled experiments. The RTS tests presented are conducted using a bespoke explicit integration scheme to solve the numerical substructure problem. Note that the integration scheme outputs the displacements of the numerical substructure relative to the base (e.g. the ground for an earthquake engineering experiment), which, once added to the reference displacement, produce the absolute displacements desired at the interfaces. Moreover, multi-tasking is used to divide the real-time computational work into tasks that need to be computed frequently (e.g. production of the final actuator command signal) and tasks that can be carried out less frequently (e.g. numerical model integration and actuation compensation). The real-time code is programmed in MATLAB Simulink and downloaded onto a compatible DSP board. More details about this procedure and its implementation at the Oxford University Structural Dynamics Laboratory can be found in Bonnet (2005). The main idea behind the multi-tasking strategy is that complex numerical substructure models can still be solved, even if the solving time exceeds the control algorithm time-step. This strategy is very similar to that already published by Nakashima (Nakashima & Masaoka 1999). This said, the numerical models actually used for this work were very simple and could be solved very fast, thereby simplifying the problem of task priorities, which is not the issue of concern here.

Much research work has been published in the past using existing compensation schemes and/or developing new ones. However, no work seems to have been devoted to an experimental comparative study regarding the relative merits of the schemes proposed. This is precisely what this work aims at addressing.

It is important at this stage to define properly the three main signals involved in the actuation compensation problem:

- The *desired output* ($d_{des}$) is the displacement signal produced by the numerical substructure model. It represents what the actuator would ideally apply to the physical substructure.
- The *actuator command* ($d_{com}$) is the displacement signal sent to the actuator controller (before application of the electric signal conversion).
- The *actual output* ($d_{act}$) is the displacement actually produced at the actuator, measured experimentally.

The purpose of the actuation compensation schemes detailed in the rest of this chapter is to produce an **actuator command** signal that will force the **actual output** to mimic the **desired output**.

## 5.2- PRESENTATION OF THE VARIOUS SCHEMES AND OF THEIR IMPLEMENTATION

### 5.2.1- Classification of the various schemes

The compensation methods tested and presented in this chapter can be classified into several categories. The first distinction can be made between:

- The schemes that, from known, assumed or calculated delay and amplitude error estimates, aim at directly correcting the command signal accordingly. They will be referred to as "direct compensation schemes".
- Those that correct the command signal from the knowledge of the real-time error to the desired output using more standard control engineering techniques, referred to as "outer-loop controllers".

Within the former category, for the amplitude error compensation, with the assumptions made in the previous section about the amplitude error variations, there is only one significant issue: the amount of amplitude correction that needs to be applied. The way to apply it is trivial: the command before correction is divided by the amplitude factor specified (the amplitude factor is defined as the actual output divided by the corresponding actuator command). However, for the delay compensation, two issues are of concern. The amount of delay that needs to be compensated for is unknown and the way to compensate for it is not trivial, as some kind of forward extrapolation of the desired output is necessary. The direct compensation methods can therefore be further classified as:

- Those that aim at calculating the delay and amplitude factor more precisely along a test, starting from rough estimates provided by the user, referred to as "performance estimation" schemes.
- Those that aim at more precise corrections, assuming the delay and amplitude factor estimates are known and accurate. The challenge here lies in the delay correction method where extrapolation techniques are used. These schemes will be referred to as "forward prediction" schemes.

The forward prediction schemes can be used on their own, with constant delay and amplitude factor estimates. In the 0-30Hz range, and hence for earthquake engineering applications (0-10Hz), a pure frequency analysis such as the one shown in Plummer *et al.* 2006 suggests that such a strategy can be a reasonable approximation. However, as shown in the previous chapter, higher real-time synchronisation can be obtained with variable delay and amplitude estimates through the use of a performance estimation scheme.

It should be noted here that, due to the use of multi-tasking, the desired output is produced at coarse time steps (called **main-steps**) and the actuator command is needed at fine time steps (called **sub-steps**). Therefore, the algorithms used to extrapolate the desired output forward at main-steps are also used, then, as interpolation schemes to produce the smooth actuator command at sub-steps.

Note also that, unlike in much of the previously published work, amplitude compensation is used throughout. After initial testing, it is found that, even for the well tuned actuation system used, the inclusion of amplitude compensation has a positive effect on the accuracy comparable to that obtained thanks to the addition of a good delay update scheme. Amplitude compensation is therefore an important part of the solution to the problem posed.

## 5.2.2- Forward prediction schemes

### 5.2.2.1- Exact polynomial fitting extrapolation

This method is the most widely known in the field. It is described in Horiuchi *et al.* (1996). The idea is based on the exact mathematical fitting of a polynomial over the last few data points of the desired output. The polynomial equation obtained is then used for a forward extrapolation by an amount believed to be equal to the actuator delay. Note that due to the exact nature of the polynomial fitting, the number of data points required is equal to the chosen polynomial order plus one.

Following the analytical work published originally as well as simulation work conducted by the same authors, a third order polynomial fitting is used. The scheme used here is slightly evolved from the published one, by going back to the Lagrange formula (Dantal & Rondeau 2004) and reformulating a more general expression of the polynomial extrapolation. Equation (5.1) ensures the value by which the polynomial is extrapolated forward is fully independent from the time step describing the desired output data points:

$$d_{com}^{n+1} = d_{des}^{n+1+\delta} = d_{des}^{n+1} + \left(\frac{\delta}{T}\right).\left(\frac{-1}{3}d_{des}^{n-2} + \frac{3}{2}d_{des}^{n-1} - 3d_{des}^{n} + \frac{11}{6}d_{des}^{n+1}\right)$$
$$+\left(\frac{\delta}{T}\right)^2.\left(\frac{-1}{2}d_{des}^{n-2} + 2d_{des}^{n-1} - \frac{5}{2}d_{des}^{n} + d_{des}^{n+1}\right) + \left(\frac{\delta}{T}\right)^3.\left(\frac{-1}{6}d_{des}^{n-2} + \frac{1}{2}d_{des}^{n-1} - \frac{1}{2}d_{des}^{n} + \frac{1}{6}d_{des}^{n+1}\right) \qquad (5.1)$$

where $T$ is the main-step, $\delta$ is the amount of forward prediction and the ($n$-2) to ($n$+1) superscripts represent the main-steps at which the desired or command outputs are considered.

Although this expression seems a lot more complex than the scheme originally presented by Horiuchi, it still requires very little computational time and represents an important improvement over the original scheme if the delay estimate is to be updated in real-time during the experiment.

### 5.2.2.2- Least squares polynomial fitting extrapolation

This method is presented in Wallace *et al.* (2005*a*) and will not be extensively presented here. It uses a polynomial fitting on the last data points too, but takes into account a larger number of points and conducts a least squares approximation rather than an exact fit. The general formulation of the scheme is:

$$d_{com}^{n+1} = \left\{P_{O,p,T}[d_{des}]\right\}\left(t^{n+1} + \delta\right) \qquad (5.2)$$

where $P_{O,p,T}$ is the least squares fit polynomial of $O^{th}$ order through the $p$ points of desired output and $t^{n+1}$ expresses the time at the ($n$+1)$^{th}$ main-step.

Two parameters therefore need to be chosen: the order of the polynomial and the number of points to use. Following the original publication, several configurations have been tested in simulations and experiments, with the order varying between 2 and 4 and the number of points between 4 and 16. The simulation results showed that the runs with fewer data points are more sensitive to noise. This work resulted in the selection of a 4th order polynomial fitted to the last 12 data points.

The idea is appealing in order to remove some of the influence of noise and experimental errors. However, a potential problem of continuity may be introduced with this scheme. Since each polynomial is a best fit through a series of points, no point actually lies on it. Therefore, when operating the change from a polynomial to the next one at each main-step, slight discontinuity may result.

5.2.2.3- Extrapolation based on linearly predicted acceleration

This scheme, published in Horiuchi & Konno (2001), is not based on the fitting of a polynomial. Instead, the acceleration of the degree of freedom at the interface is assumed to vary linearly, and the displacement at the same point is then deduced by integration. To conduct the linear approximation and the subsequent integration, this scheme is based on the knowledge of the acceleration for the current step and its predecessor, as well as on the velocity and displacement values for the current step. However, most explicit time integration methods do not provide all this information for the last computed step. The solution proposed by Horiuchi, and used in the present research, is to work with the data available from the previous step and to predict forward by one time step plus the value of the delay, resulting in the following equations:

$$
\begin{aligned}
a_{com}^{n+1} &= \frac{\delta + 2\cdot T}{T}\cdot a_{des}^{n} - \frac{\delta + T}{T}\cdot a_{des}^{n-1} \\
v_{com}^{n+1} &= v_{des}^{n} + \frac{\delta + T}{2}.\left(a_{des}^{n} + a_{com}^{n+1}\right) \\
d_{com}^{n+1} &= d_{des}^{n} + \left(\delta + T\right)\cdot v_{des}^{n} + \frac{(\delta + T)^2}{3}\cdot a_{des}^{n} + \frac{(\delta + T)^2}{6}\cdot a_{com}^{n+1}
\end{aligned}
\tag{5.3}
$$

where $a$ and $v$ are the acceleration and velocity signals, with the subscripts and superscripts defined as above. Note that the second equality in Equation (5.3), although not directly used to compute the actuator command at main-steps, is necessary to compute the sub-step interpolation points with the same technique.

Horiuchi has shown this method to be theoretically superior in terms of stability to the exact polynomial fitting method with respect to mass and stiffness criteria. But no experimental results have yet been published showing that its implementation improves the RTS method. As for the previous schemes reviewed, more information can be found from the original publication.

5.2.2.4- The Laguerre extrapolator: a fast end-of-line process

Finally, a different type of extrapolation is considered. This algorithm, based on the Laguerre polynomials, can be described as an end-of line filter, directly working on the sub-step output just before it is sent to the actuator controller. It only requires the current data point as its input and effectively applies an exponential weighting to the recent history of the signal. The scheme is implemented by:

$$
d_{com}^{n+1} = \sum_{k=0}^{p} m_k(t^{n+1})\cdot L_k\left(-\alpha\cdot\delta\right) \tag{5.4}
$$

where $\alpha$ is a scaling factor, the $m_k(t^n)$ coefficients are defined in state-space form by:

$$\begin{Bmatrix} \dot{m}_0 \\ \dot{m}_1 \\ \vdots \\ \dot{m}_p \end{Bmatrix} = \begin{bmatrix} -\alpha & 0 & \cdots & 0 \\ -\alpha & -\alpha & \cdots & 0 \\ \vdots & \vdots & \ddots & 0 \\ -\alpha & -\alpha & \cdots & -\alpha \end{bmatrix} \begin{Bmatrix} m_0 \\ m_1 \\ \vdots \\ m_p \end{Bmatrix} + \begin{Bmatrix} 1 \\ 1 \\ \vdots \\ 1 \end{Bmatrix} \alpha \cdot d_{des}^{n} \tag{5.5}$$

and the Laguerre polynomials $L_k(x)$ are defined by:

$$\begin{aligned} L_0(x) &= 1 \\ L_1(x) &= 1 - x \\ L_k(x) &= \frac{2 \cdot k - 1 - x}{k} L_{k-1}(x) - \frac{k-1}{k} L_{k-2}(x) \end{aligned} \tag{5.6}$$

The sub-step sampling required before the signal can be extrapolated forward by the Laguerre filter may be obtained thanks to one of the three methods described above, used as interpolations rather than extrapolations. In the experiments presented in this chapter, the third order exact polynomial fitting is used to perform the interpolation.

The real-time implementation is fairly simple and efficient enough for a computation at every sub-step. Following simulations and trial experiments, a typical fourth order can be set, meaning that the first five polynomials are used.

### 5.2.3- Performance estimation algorithms

#### 5.2.3.1- The Darby estimator

To reduce the chance of instability when a live delay estimate is computed, the delay between the desired output and the actual output is used to update the previous delay estimate. The alternative, consisting in measuring the delay between the actuator command and the actual output as the delay that needs to be compensated for, has an inherent risk of winding-up. For example, if a higher delay is detected, the compensation becomes more important and results in an "earlier" command signal which will then be used again to recalculate a new delay. Such a circular strategy could naturally be prone to instability. Using the desired output to produce a delay update should largely attenuate this potential circular dependency.

The scheme proposed by Darby *et al.* (2002) produces delay update estimates from a measurement of the real-time error and a coefficient of proportionality, $C_p$, set empirically. An additional term, based on the characteristic of the hyperbolic tangent function, allows discriminating local peak areas from the calculation, where the real-time error is typically non-representative of the delay. This term also uses a velocity estimate and a second gain, $C_v$, set empirically. The following expression results:

$$\delta^{n+1} = \delta^{n} + C_p \cdot \left( d_{des}^{n} - d_{act}^{n} \right) \tanh\left( C_v \cdot \frac{d_{des}^{n+1} - d_{des}^{n}}{T} \right) \tag{5.7}$$

Although not proposed originally, the same discrimination principle can also be applied for the amplitude factor estimation, where the local peak, this time, is the best place to measure the amplitude error. Again, an update of the previous amplitude factor is calculated. More details about the scheme, as well as the typical procedure to follow to obtain good settings of the empirical gains, can be found in the original publication.

When implementing this scheme, the value chosen for $C_p$ depends on the time-step used, as well as on the units chosen for the displacement and velocity data. The value for $C_v$ does not depend on the time-step used. The use of limiting values of delay and amplitude factor to be compensated for is advised, especially during the $C_p$ and $C_v$ optimisation procedure, when the maximum gains before instability are searched.

5.2.3.2- The modified Darby estimator

Darby's method can be modified according to the precept that the real-time error is the product of the actuator velocity and the delay, as shown in Figure 5.1. This being a good assumption only when the velocity is close to being constant over the step considered, the same hyperbolic tangent term, with its associated $C_v$ gain, is used to discard the measurements conducted near a local peak. The resulting delay estimate is expressed by:

$$\delta^{n+1} = \delta^n + \left(d_{des}^n - d_{act}^n\right)\left(\frac{T}{d_{des}^{n+1} - d_{des}^n}\right).\tanh\left(C_v.\frac{abs(d_{des}^{n+1} - d_{des}^n)}{T}\right) \qquad (5.8)$$

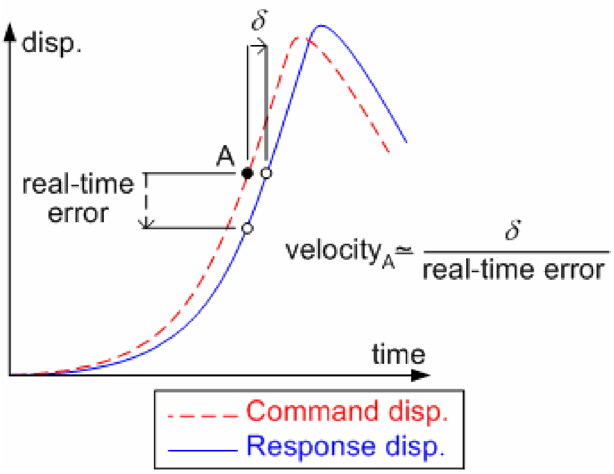

Figure 5.1: Delay approximation for the modified Darby scheme

Note that the $C_p$ gain is not required anymore, since the proportional coefficient between the real-time error and the delay update is now adequately addressed by the inverse of the velocity. Also, since the sign of the delay update is already affected by the direct velocity gain, the sign of the hyperbolic tangent argument is constrained to be positive.

With the incorporation of the amplitude correction, the delay expression becomes:

$$\delta^{n+1} = \delta^n + \left(\frac{d_{des}^n}{A_{fac}} - d_{act}^n\right)\left(\frac{A_{fac}.T}{d_{des}^{n+1} - d_{des}^n}\right).\tanh\left(C_v.\frac{abs(d_{des}^{n+1} - d_{des}^n)}{T}\right) \qquad (5.9)$$

where $A_{fac}$ is the amplitude factor as defined earlier. Note that the inclusion of the amplitude factor correction in the hyperbolic tangent term is not necessary as the $C_v$ gain multiplication is superseding.

The implementation of this equation is simple too. Due to the presence of a denominator term that can approach zero in the inverted velocity gain, it is useful to artificially limit the delay update produced to realistic values.

5.2.3.3- The zero-crossing estimations

This method, developed during this research, also produces delay updates from the desired and actual outputs. The approach is very pragmatic and consists in using a “stopwatch” to determine the time difference between the desired and actual outputs crossing a pre-defined threshold, by default chosen to be the initial zero displacement point. The crossings are detected with the values logged at sub-steps and finer interpolations are conducted on the assumption that the variation is linear between consecutive sub-steps. The amplitude factor calculation is also conducted with the zero crossings triggers and the detection of the local peaks of desired and actual outputs.

A limitation of the applicability of this method lies in the fact that a given threshold needs to be crossed often enough during the test for the updated delay and amplitude factor signals to describe the actuator performance well enough. This is not thought to be a problem for most earthquake engineering applications. Another limitation is that no update is computed between crossings, which can be problematic when important situations occur around local peaks, like for example high loads or non-linear behaviours.

The implementation in real-time is simple, as Simulink provides many options for programming algorithms with logic.

#### 5.2.3.4- The pre-recorded estimations

For this compensation method, also developed in this research, records of both the delay and the amplitude factor, post-processed from previously run test data, are used in real-time to compensate more accurately for the amplitude and delay errors.

Since the test first needs to be successfully run, for example with constant delay and amplitude factor inputs, the excitation amplitude may need scaling down. From the results of this initial test, the delay and amplitude factor records are worked out by comparison of the actuator command with the actual output. The records are then used in a new test, in place of the constant inputs. If the test amplitude had to be decreased to conduct the initial run, it can be increased, either to its nominal value or to another intermediate value. Once the nominal amplitude value has been reached, a final iteration is carried out to ensure valid records are used in subsequent tests. Even if no alteration of the nominal test procedure is needed to conduct the initial run, a final iteration is useful to check the stability of the test with the records obtained.

Due to the iterative process described above, the main disadvantage of this method is that it is restricted to experiments where failure does not occur. On the other hand, once the post-processing of the records is coded, the method is very simple to use. It is also trivial to code in real-time (only a look-up table with time input is required for each record) and is the least computationally demanding of all the schemes tested. Finally, of all the methods tested, it is the one capable of the best delay variation description within the oscillations of the structure.

Note, however, that filtering is necessary when post-processing the delay and amplitude factor records. Unfiltered data is too noisy and quickly results in unstable tests. For the filter not to introduce any lag in the data, the use of zero-phase-forward filters is crucial. The chosen filter is a four-pole 5Hz zero-phase-forward Butterworth.

### 5.2.4- MCS family of outer-loop control algorithms

The MCS family of outer-loop controllers (Stoten 1993) has been the subject of a lot of work. It has been used for the outer-loop control of the Bristol shaking table (Stoten & Gomez

2001) and has recently been considered as a potential solution to the real-time substructure control problem. Several types of formulation have been analysed and tested, from the simple adaptation of the MCS algorithm with the numerical substructure taking the place of the reference model and a force feedback introduced between the plant and the numerical model (Neild *et al.* 2005) to a more evolved error based formulation with integral action (Stoten *et al.* 2002).

More recently still, the minimal control synthesis algorithm with modified demand (MCSmd) has been proposed for conducting RTS testing (Lim *et al.* 2005). The implementation of the MCSmd significantly reduces the real-time error and allows controlling systems with low damping which could not be controlled by previous versions of the MCS controller. The rate of update of the gains in real-time, $\alpha$, is defined by the user. The highest value of $\alpha$ before instability of the command signal is recommended.

The implementation of the MCSmd algorithm in real-time programming does not pose specific issues and the algorithm is particularly computationally efficient. The MCSmd re-introduces a reference model in the algorithm, as well as a reference model compensator applied to the demand signal (Lim *et al.* 2005). The controller is adaptive but the initial values for the gains have to be set accurately to the Erzberger gains, which represent asymptotic values reached by the gains when the adaptive tuning is complete. The Erzberger values are deduced from the knowledge of the actuator performance and accordingly to the reference model used. They could also be estimated through the use of the MCSid system identification process (Stoten & Benchoubane 1993). This initial setting can be seen as equivalent to the initial delay estimate used for a direct compensation scheme.

Regarding the choice of the solver used in Simulink for the real-time algorithm, the MCSmd scheme is found to perform equally well with an ODE1 or an ODE4 solver, both also allowing to reach the same $\alpha$. The ODE1 is therefore chosen for consistency.

## 5.2.5- Other types of schemes researched that proved unsuccessful

In the interest of completeness, a brief account of some research conducted on other types of compensation schemes that proved unsuccessful is given here.

### 5.2.5.1- Live feedback signal correction

The idea behind this method is the following: "as the delay can be seen as equivalent to negative damping, its effect can be corrected by adding positive damping in the numerical substructure at the interface degree of freedom." One has to note that with this precept, a correction in the numerical model can be attempted but no direct compensation on the physical substructure would be done, meaning that the excitation would indeed be delayed and nothing would be done to eliminate the delay. So this method would not require any artificial extrapolation algorithm but it would also let some inaccuracy affect the physical substructure test. However, this inaccuracy in itself would remain very small, provided that its propagation is stopped by the numerical model correction – and of course that the actuation system is well tuned.

But another major point to note regarding this correction method concerns the equivalence between the delay and a negative damping effect. Horiuchi *et al.* (1996) have indeed only presented this equivalence in the case of a single mass-spring system where the spring only is considered as the physical substructure. In a more general case, it can be seen that the effect of the delay is not only equivalent to a simple damping effect but may also include other types of energy conservation, dissipation or introduction effects. Thus, a more natural way considered to correct the effects of the delay is by modifying the load feedback signal before it is used in the numerical substructure.

However still, such a correction implies some knowledge of the real-time properties of the physical substructure, in terms of damping, stiffness and inertia – those properties being by definition unknown and/or difficult to model. Some analytical and simulation work conducted on several methods for the real-time system identification and the load feedback correction shows that the method is not viable for testing. This route is therefore abandoned and not discussed further at the moment.

#### 5.2.5.2- Live delay update

By extension of the zero-crossing delay measurement method presented earlier, a live delay measurement algorithm has also been envisaged. This scheme would continuously evaluate an estimate of the delay, primarily based on the real-time knowledge of the actuator command and of the actual output. It would also take into account an estimate of the amplitude error, as one is needed for a correct measurement of the delay. Delay variations with loads and non-linear behaviours would therefore be captured, unlike in the zero-crossing scheme.

Several methods have been tested but all have posed the same problem. Even if a good delay prediction can be obtained, the forward prediction scheme used to apply it and the closed-loop environment characterising an RTS test mean that only fairly “slow and smooth” delay descriptions can be tolerated for a stable experiment to be realised. A noisy delay time history, typically obtained by a real-time measurement procedure such as that proposed here, would require filtering which would of course defeat the objective by introducing lag on the signal. Following this conclusion, work on this method was stopped.

#### 5.2.5.3- FFT method

Another method was investigated using fast Fourier transform functions on the actuator command and response to obtain a measurement of the delay. From real-time history data, the actuator transfer function can be obtained and the slope on the second Bode plot (phase angle in the frequency domain) is a measure of the delay introduced.

This technique, tested in a post-processing manner on saved data, shows good coherence and the delay measurement obtained is totally backed by more direct methods. However, the amount of data necessary to produce a result is too large and prevents its use in real-time for the type of application that is considered here.

## 5.3- EXPERIMENTAL RESULTS

### 5.3.1- Real-time implementation, simulation work & optimisation

All the selected delay compensation methods, coded for real-time application, show in simulations their merits towards reducing the synchronisation error. All of the simulation results are not shown here because it is thought real RTS experimental results, obtained with the presence of, notably, instrumentation noise and real actuator dynamics, are more valuable.

However, some simulation results are occasionally used in what follows to explain and/or put in perspective some of the experimental results.

The tests presented below are conducted with a "proof of concept" rig, consisting of a reconfigurable three degree of freedom (DOF) system in series. Such a rig easily allows addressing the modelling issues mentioned in the introduction. Three basic tests are carried out, with different and increasing challenges posed to conducting stable RTS experiments. For these tests, every scheme is first optimised, using both simulations and experiments. Finally, evaluation runs are conducted for which the results are presented and can be compared.

The actuators used are two 10kN dynamically rated Instron actuators, using Moog servo-valves. The controller is an Instron 8800 series digital unit operating at 5kHz.

## 5.3.2- Test A

The emulated system considered for the first test is a linear two DOF system in series with one outside input as shown in Figure 5.2.

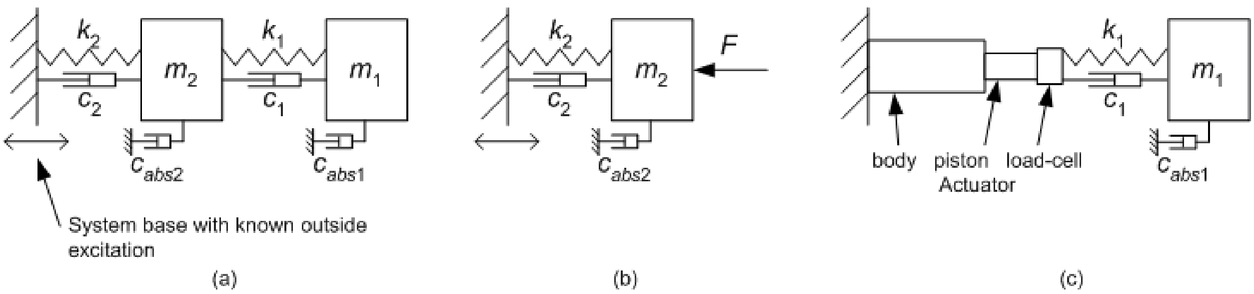


Figure 5.2: (a) Emulated system, (b) numerical substructure and (c) physical substructure for test A

The outside input, together with the adjacent spring/mass system constitutes the numerical substructure. The second spring/mass system constitutes the physical substructure and is modelled by the rig. This test can therefore be described as a single-axis RTS experiment with linear SDOF substructures. Aside from the mass and stiffness terms, some viscous damping is considered both as relative (i.e. from the springs) and absolute (i.e. from the linear bearings on the masses), even though the damping level is low (damping ratio of about 2%). This choice is made following a series of physical measurements conducted on the rig. All characteristics are linear and the mass and stiffness properties are adjusted so that both natural frequencies are below 10Hz with a low level of specimen stiffness.

With an outside excitation consisting of a 2mm sinusoid with a frequency sweeping from 0 to 10Hz in 40s, both resonances are hit while the actuator load level always remains fairly low (below 20% of the dynamic rating). The maximum physical displacements are around ±35mm. Given that the inner-loop actuator control system is optimised for a good level of actuation performance, this test therefore only poses a small challenge to conducting a stable RTS experiment, as the actuator should operate with a fairly consistent performance, with only slight variations around each resonance. The sub-step and main-step sizes chosen are respectively 0.5 and 5ms.

Once all the algorithms are implemented and optimised, the tests are carried out successively in the same conditions and in the order presented in the results tables. The main interest being the effectiveness of the actuation compensation schemes, observations should focus on the difference between the desired output and the actual output, rather than focus on the accuracy of the emulated system reproduction by the RTS test. Nonetheless, to check the validity of the RTS emulation, Figure 5.3 below presents typical experimental results in comparison to the output of a computational simulation of the system (solved with an explicit Newmark scheme). The data presented are obtained with a standard third order polynomial compensation, with constant delay and amplitude factor inputs. The other compensation methods tested produced similar results in test A.

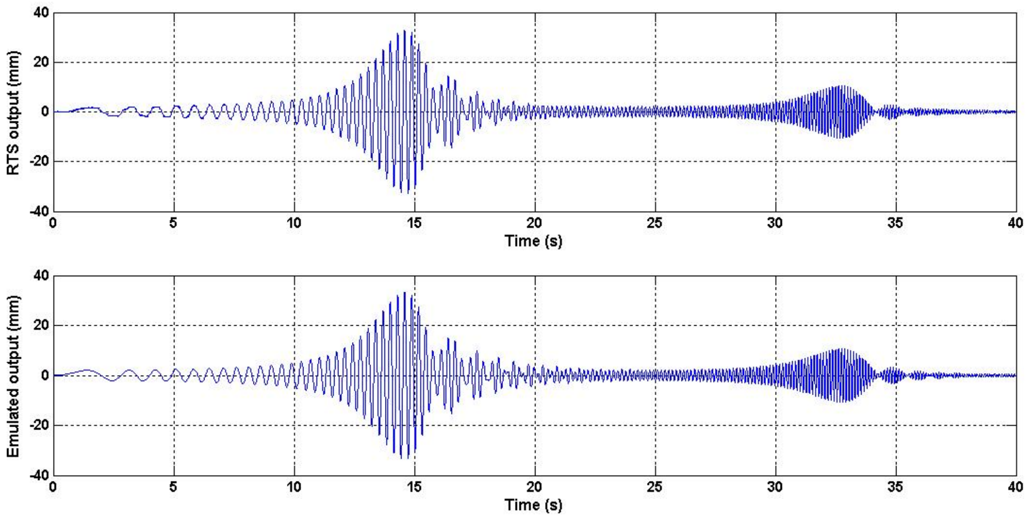


Figure 5.3: Real-time substructure emulation validity check for test A

To observe better the effectiveness of the compensation scheme, three XY plots can be produced as in Figure 5.4. The first one shows the actuator output against the actuator command and is characterised by an elliptic shape due to the delay introduced by the actuation. The second one, showing the command against the desired output, has the same overall shape because the command is predicted ahead of the desired output. The third one, the aggregate of the first two, shows the actual output against the desired output. The curve almost constantly overlaps a 45° line, proving the delay has been mostly corrected. These synchronisation plots have also been used by other researchers to assess the accuracy of RTS simulations (Wallace *et al.* 2004). However, such graphical evidence does not allow an accurate enough measurement of the delay compensation effectiveness when it comes to comparing several schemes. Analysing numerically the real-time error history can provide more information, and processing the residual delay and amplitude error information can give indications as to the performance of the compensation schemes. A potential residual delay between the desired output and the actual output means that the experimental error is of a systematic type and therefore implies a regular addition or dissipation of energy and a risk of error propagation (Shing & Mahin 1987*a*).

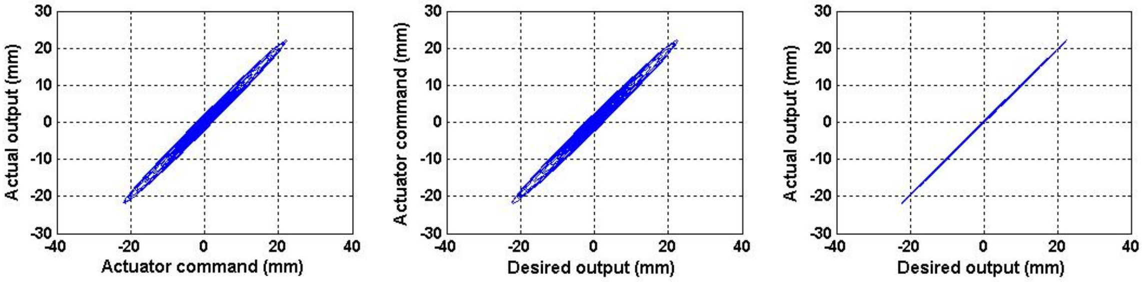


Figure 5.4: Synchronisation plots of desired output, actuator command and actual output.

Firstly, the forward prediction schemes are all compared with the use of constant delay and amplitude factor inputs. For each scheme, the synchronisation error time history is treated and two criteria – mean_crit & rms_crit – are post-processed over the 40s test history as defined by Equation (5.10).

$$mean\_crit = 100 \times \frac{mean\left(\left|d_{act} - d_{des}\right|\right)^{scheme-considered}}{mean\left(\left|d_{des}\right|\right)^{reference-scheme}} = 100 \times \frac{\sum_{i=1}^{N}\left|d_{act}^{i} - d_{des}^{i}\right|^{scheme-considered}}{\sum_{i=1}^{N}\left|d_{des}^{i}\right|^{reference-scheme}}$$

$$rms\_crit = 100 \times \frac{rms\left(d_{act} - d_{des}\right)^{scheme-considered}}{rms\left(d_{des}\right)^{reference-scheme}} = 100 \times \sqrt{\frac{\sum_{i=1}^{N}\left(d_{act}^{i} - d_{des}^{i}\right)^{2\ scheme-considered}}{\sum_{i=1}^{N}\left(d_{des}^{i}\right)^{2\ reference-scheme}}} \quad (5.10)$$

where $N$ is the number of data points over the test history and $i$ is the indexing variable sweeping through the data points. These two criteria are essentially similar except that the second one squares the error and desired values, thereby penalising large errors more. Note that absolute values are used in the first criterion to avoid artificially finding near-zero means due to the nature of the test. Note, also, that the denominators and the 100 factors are introduced to make the two criteria relative to the desired output and expressed as percentages. For better comparisons between the various schemes, the denominators are always calculated from the data obtained with the chosen reference scheme, namely the standard third order polynomial extrapolation using constant performance inputs. Table 5.1 presents these results for test A.

| | Relative command error (%) mean_crit | Relative command error (%) rms_crit |
|---|---|---|
| No compensation | instability | instability |
| Standard 3rd order polynomial extrapolation | 1.8 | 1.8 |
| Least squares polynomial fitting extrapolation | 2.0 | 1.9 |
| Linearly predicted acceleration extrapolation | 1.8 | 1.9 |
| Laguerre extrapolation with standard 3rd order polynomial interpolation | 1.7 | 1.8 |

Table 5.1: Comparison of the forward prediction schemes with constant performance inputs in test A

As can be seen from Table 5.1, no significant difference between the four schemes appears from these runs. All allow running an otherwise unstable experiment.

The performance estimation methods are then tested, along with the adaptive MCSmd controller. Given the results above, the standard third order exact polynomial fitting scheme is used for these runs. The results for the two criteria are presented in Table 5.2.

| | Relative command error (%) | |
|---|---|---|
| | mean_crit | rms_crit |
| No update | 1.8 | 1.8 |
| MCSmd outer-loop controller | 1.6 | 1.3 |
| Darby updates | 0.9 | 0.8 |
| Modified Darby updates | 0.9 | 0.7 |
| Zero crossing updates | 0.9 | 0.7 |
| Pre-recorded updates | 0.9 | 0.7 |

Table 5.2: Comparison of the performance estimation methods and the outer-loop controller in test A

All the adaptive techniques tested are viable and allow reaching better results than when using constant estimates. Moreover, even if the actuator performance does not vary much during a test, an adaptive scheme offers the advantage to be less sensitive to the user estimates, as they are only used at the start. Obviously, the advances provided by the use of an estimation scheme are at the expense of a little added optimisation work and computational time demand. The four direct estimation schemes produce very similar results.

The MCSmd is run with the adaptivity factor of $\alpha$=10 (setting $\alpha$=50 is unstable). The error produced is larger than for the other four schemes. Also, a positive residual delay is detected after the test, indicating the algorithm does not fully compensate for the actuator dynamics. Finally, when comparing the delay estimation histories of the four direct compensation schemes with the gain histories of the MCSmd run, it seems that the MCSmd is not responsive enough, with the gains only seen to adapt significantly during the resonance periods.

The computational demands for the algorithms tested above and whose results are presented in Tables 5.1 and 5.2 are presented in Tables 5.3 and 5.4. The demand for each task is presented separately. Note that each main-step task includes one simultaneous sub-step task and is therefore always more demanding.

| | Computational time (micro-sec) | |
|---|---|---|
| | sub-step | main-step |
| Standard 3rd order polynomial extrapolation | 41 | 61 |
| Least squares polynomial fitting extrapolation | 33 | 281 |
| Linearly predicted acceleration extrapolation | 33 | 53 |
| Laguerre extrapolation with standard 3rd order polynomial interpolation | 76 | 91 |

Table 5.3: Comparison of the forward prediction scheme computational demands with constant performance inputs in test A

| | Computational time (micro-sec) | |
|---|---|---|
| | sub-step | main-step |
| MCSmd outer-loop controller | 48 | 61 |
| Darby updates | 49 | 89 |
| Modified Darby updates | 51 | 90 |
| Zero crossing updates | 54 | 94 |
| Pre-recorded updates | 43 | 64 |

Table 5.4: Comparison of the performance estimation and outer-loop controller computational demands in test A

The main point to note from these tables is that the least squares polynomial fitting algorithm is found to be very computationally demanding.

**5.3.3- Test B**

For the second series of tests, the rig is configured as follows. A two DOF system is considered as the emulated system, where two masses are attached in series to a moving base, through two springs. Additionally, the mass that is not adjacent to the moving base is also linked to a stationary platform through a gapped spring. Depending on the oscillations of this mass, the gap closes and the spring opposes any further displacement. The initial configuration is such that the mass is just contacting the gapped spring, without preloading it. The gapped spring arrangement therefore offers zero stiffness in extension and the spring's stiffness in compression.

The RTS test devised aims at placing the non-linearity featured by the gapped mass-spring within the physical substructure, so as to induce a less consistent actuator performance (Bonnet *et al.* 2005) and therefore a more challenging situation for the actuator control algorithm. Similarly to test A, test B is a single-axis RTS experiment with SDOF substructures, but this time the physical substructure is non-linear (see Figure 5.5). Note that higher loads, achieved thanks to stiffer springs, and system resonance will also add to the challenge posed by this test. The intermediate spring is also placed in the physical substructure. The numerical substructure contains the rest, i.e. the moving base and the adjacent spring and mass. The numerical substructure is therefore of the same type as in the previous test – a linear SDOF system. Note that, as for the previous test, each spring and each mass also features a damping term, respectively relative and absolute. The level of damping is also similar to that of the previous test. The spring stiffnesses are nominally 300N/mm for the gapped spring and the intermediate spring, while the numerical substructure spring is set to 200N/mm. In terms of hardware, a slider is installed to prevent buckling of the gapped spring when coming into contact.

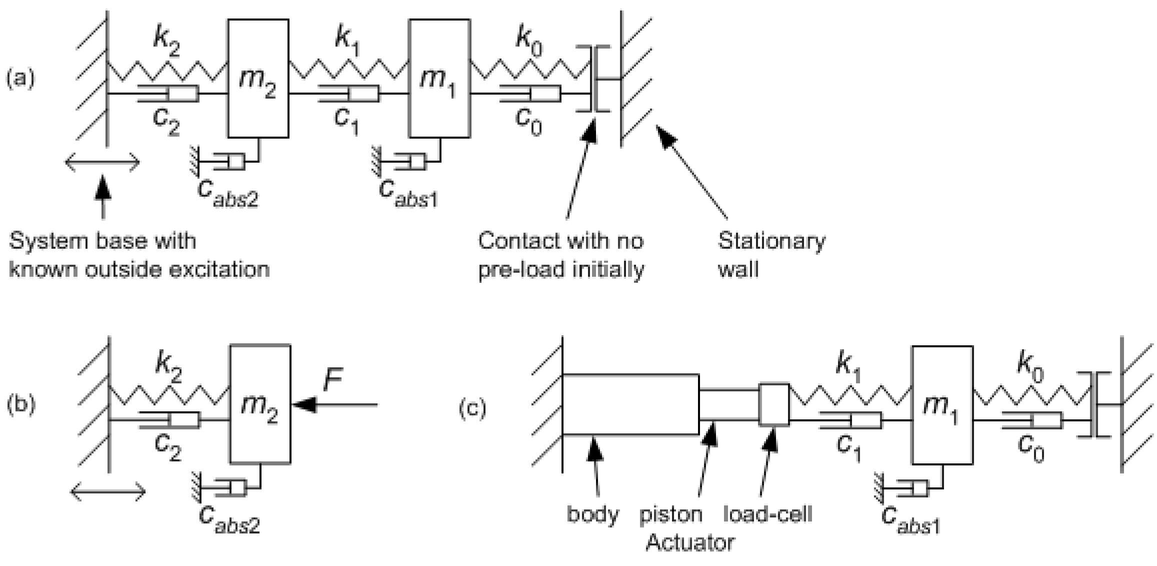


Figure 5.5: (a) Emulated system, (b) numerical substructure and (c) physical substructure for test B

The moving base excitation is chosen to be a 2.1mm sinusoidal signal whose frequency sweeps the range 0 to 10Hz. This makes the displacement experienced on the rig reach about 30mm and the load at the substructure interface reach about 9kN, which is 90% of the actuator dynamic rating, adding to the challenge posed by this experiment. The step sizes for this test are the same as for test A: 0.5ms sub-steps and 5ms main-steps.

To check the relevance of the RTS emulation, the experimental output is compared with a simulation output of the emulated system, using a Newmark scheme. The gap is modelled by a dead-zone and an additional Coulomb force for the slider. Some Coulomb friction terms were also introduced to better model the masses' non-linear friction. Note that the values of the viscous damping and Coulomb friction terms were previously measured through a series of bespoke tests, as well as the viscous damping and stiffness terms of the springs.

It must also be noted that with the Newmark explicit numerical scheme, at each time step, the displacement is predicted for the next step while the velocity and acceleration are predicted for the current step. Consequently, any behaviour that is non-linear with displacement can easily be taken into account, as is the case for the gapped spring. However, a behaviour that is non-linear with velocity and/or acceleration implies added complexity, for example requiring an iterative scheme to be used. To artificially avoid this, at the expense of slight mis-modelling, the Coulomb terms, necessary to achieve a good level of model accuracy, were operated on the previous step velocity. This model was successfully verified with an open-loop test of the physical substructure. Again, as the aim of this work is not to produce accurate RTS tests in the sense of output but in the sense of its interface boundary conditions, the mis-modelling proposed, only used for the emulated system simulation, is valid as it will not influence the results. The overall validity of the emulation can still be checked in Figure 5.6. Even though amplitude errors can be seen, broad agreement validates the model.

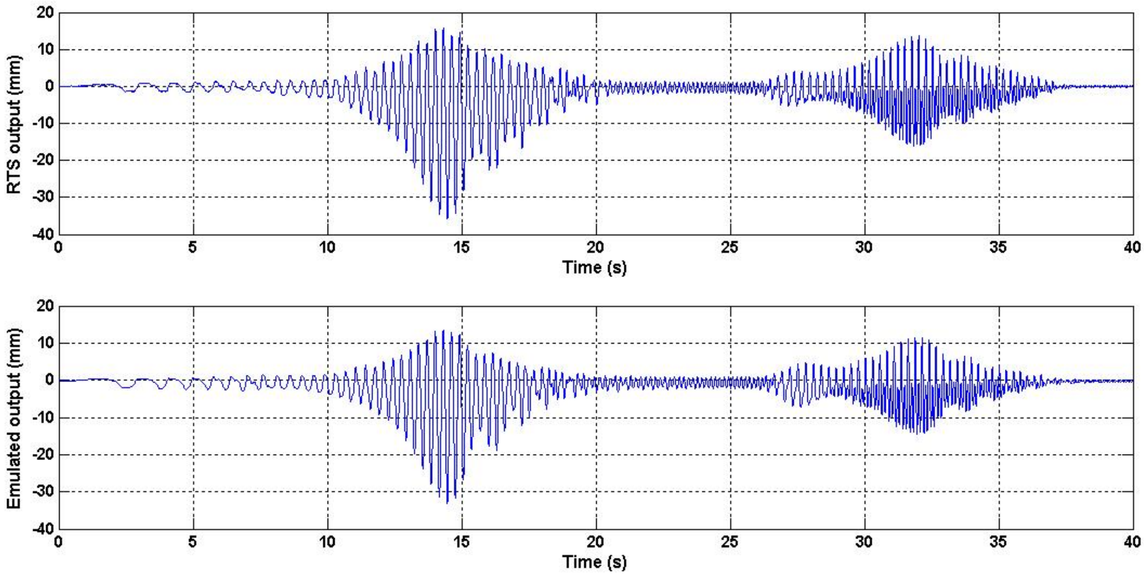


Figure 5.6: Real-time substructure emulation validity check for test B

As conducted for test A, the first runs assume constant actuator performance inputs and allow comparing the forward prediction schemes, as well as the Laguerre extrapolator. The two criteria presented for test A are post-processed in the same way and the results are shown in Table 5.5.

| | Relative command error (%) mean_crit | rms_crit |
|---|---|---|
| No compensation | instability | instability |
| Standard 3rd order polynomial extrapolation | 1.6 | 1.5 |
| Least squares polynomial fitting extrapolation | 2.0 | 2.0 |
| Linearly predicted acceleration extrapolation | 1.6 | 1.6 |
| Laguerre extrapolation with standard 3rd order polynomial interpolation | 1.7 | 1.7 |

Table 5.5: Comparison of the forward prediction schemes with constant performance inputs in test B

Again, all four schemes allow conducting an otherwise unstable test. The results are closely comparable for three of them, but the least squares polynomial fitting method yields slightly poorer results. It is believed that the non-linear nature of the physical substructure in this test makes it counterproductive for the extrapolation routine to work from data older than necessary. Moreover, the lack of continuity in the scheme may also affect the results.

The second series of tests intends to compare the four delay and amplitude factor estimation algorithms, together with the adaptive MCSmd algorithm. Again, all are implemented in conjunction with the third degree exact polynomial fitting extrapolation routine for the necessary interpolation and/or extrapolation computations. The results appear in Table 5.6.

| | Relative command error (%) mean_crit | rms_crit |
|---|---|---|
| No update | 1.6 | 1.5 |
| MCSmd outer-loop controller | instability | instability |
| MCSmd outer-loop controller - sub-steps reduced to 0.2ms | 2.2 | 2.3 |
| Darby updates | 1.3 | 1.5 |
| Modified Darby updates | 1.1 | 1.1 |
| Zero crossing updates | 1.5 | 1.6 |
| Pre-recorded updates | 1.1 | 1.1 |

Table 5.6: Comparison of the performance estimation methods and the outer-loop controller in test B

The MCSmd run could not be operated to successfully control the test with stability. The value of $\alpha$ was tested within the range 10 to 0.001, as well as with the 0 value. A decrease in amplitude was then tried to see if the MCSmd could complete a less demanding version of the test. This showed that the control signal was apparently unstable, with its oscillations steadily increasing instead of being damped out by the structural damping. This tends to confirm the results found from test A where it seems the MCSmd is not fully effective in compensating the actuation delay. Another test was conducted with MCSmd with a reduction in the sub-step size from 0.5ms to 0.2ms. This allows the algorithm to complete test B. The maximum $\alpha$ before instability is found at 15. However, the synchronisation error is quite high and, again, the delay compensation is not total. As observed in the first test, apart from resonance periods, the gains are not seen to adapt significantly.

After optimisation, it is found that the parameters for the Darby schemes and for the zero crossing scheme can not be set as high as they were for test A. In all cases, this confirms that test B is more demanding and that the update signals produced need to remain smooth. The pre-recorded method was performed through a series of test with increasing excitation amplitude and by finally repeating the full amplitude test to ensure convergence of the procedure. The modified Darby scheme and the pre-recorded scheme produce slightly better results than the rest.

The pre-recorded updates method is selected for the next series of tests in order to compare the interpolation / extrapolation schemes when the actuation performance input is not constant. The pre-recorded method is particularly suited to this purpose as it allows using the exact same delay and amplitude factor information in several tests. The results are presented in Table 5.7. As seen with Table 5.5, the results are very comparable for the exact polynomial extrapolation, the linearly predicted acceleration and the Laguerre polynomial schemes. Again, the least squares fitting scheme appears a little worse.

| | Relative command error (%) | |
|---|---|---|
| | mean_crit | rms_crit |
| Standard 3rd order polynomial extrapolation | 1.1 | 1.1 |
| Least squares polynomial fitting extrapolation | 1.4 | 1.6 |
| Linearly predicted acceleration extrapolation | 1.1 | 1.2 |
| Laguerre extrapolation with standard 3rd order polynomial interpolation | 1.1 | 1.2 |

Table 5.7: Comparison of the forward prediction schemes with pre-recorded performance inputs in test B

Also, four tests are conducted to compare the forward prediction schemes when used with the modified Darby updates. This time, because the performance updates are produced in real-time during the test, a feedback loop between the prediction scheme and the update scheme is possible. The results are presented in Table 5.8.

| | Relative command error (%) | |
|---|---|---|
| | mean_crit | rms_crit |
| Standard 3rd order polynomial extrapolation | 1.1 | 1.1 |
| Least squares polynomial fitting extrapolation | 1.6 | 1.5 |
| Linearly predicted acceleration extrapolation | 1.3 | 1.3 |
| Laguerre extrapolation with standard 3rd order polynomial interpolation | 1.3 | 1.4 |

Table 5.8: Comparison of the forward prediction schemes with modified Darby performance inputs in test B

The same indications are given, although the error achieved with the least squares fitting is this time a little closer to that obtained with the other schemes.

### 5.3.4- Test C

The challenge for the third test is brought by the active interaction between two actuators, both representing substructuring interfaces. This type of experiment is therefore described as a multi-axis RTS test, because the interface contains more than one degree of freedom. A co-axial setup with stiff springs is purposely chosen to make the coupling between the two actuators predominant, thereby challenging the ability of the compensation algorithms to adapt quickly. The physical substructure, as well as each numerical substructure, can be represented by SDOF systems. The emulated system therefore has three DOF linked together and to two external moving bases with four springs. A schematic of the emulated system and of the substructures is shown in Figure 5.7.

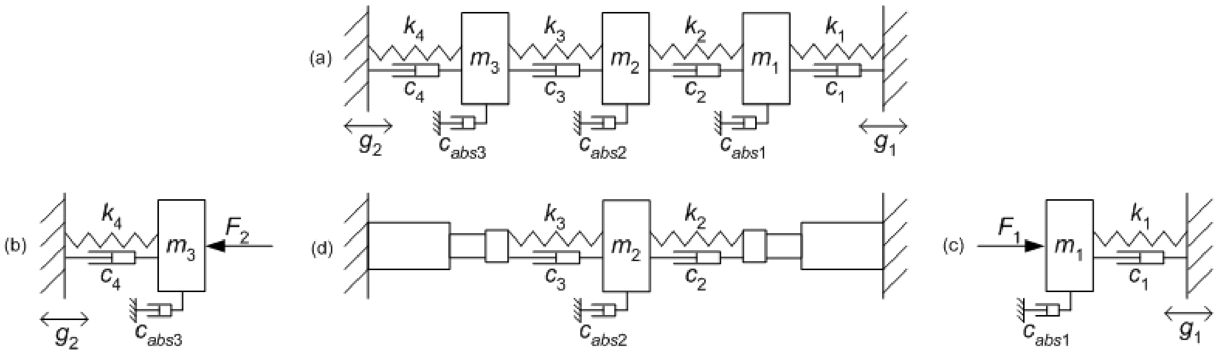


Figure 5.7: (a) Emulated system, (b) and (c) numerical substructures and (d) physical substructure for test C

The system is regarded as linear. The spring stiffnesses from $k_1$ to $k_4$ are respectively 0.8, 2.0, 2.1 and 1.3kN/mm and the resulting natural frequencies are 10.3, 19.5 and 27.2Hz. The viscous damping values of the numerical substructures are adjusted for the modal damping matrix of the emulated system to be predominantly diagonal. The modal damping coefficients are calculated at 1.4%, 1.0% and 0.7% respectively. The two external excitations are 3mm sinusoidal frequency sweeps, with $g_1$ sweeping from 0 to 3Hz and $g_2$ from 0 to 4Hz. This ensures that the system oscillates in a fashion where the two interfacing actuators have to deal with conflicting situations. This conflict is meaningful because of the high stiffness of the physical substructure – coupling stiffness of 1.02kN/mm from actuator to actuator – compared to the load capacity of the actuator used (10kN actuators). In other words, the movement of one actuator by just 1mm while the other stays stationary requires each actuator to resist to 10% of its capacity. Such coupling has been shown to render the actuator control less consistent (Bonnet *et al.* 2005) and potentially lead to unstable RTS experiments (Darby *et al.* 2002).

A similar test program to that conducted for test A is repeated, with the exception that the least squares polynomial fitting prediction algorithm is omitted, since it was found slightly less accurate and noticeably more computationally demanding than the other schemes and the value of the sub-step had to be kept to a certain level (0.5ms) for it to have enough computation time. This means that all schemes tested can now operate within a 0.2ms sub-step, i.e. to the same sampling frequency as the actuation inner-loop control system. The main-step size is also reduced to 1ms, to increase the accuracy of the explicit numerical scheme used. The overall validity of the substructure emulation can be checked in Figure 5.8.

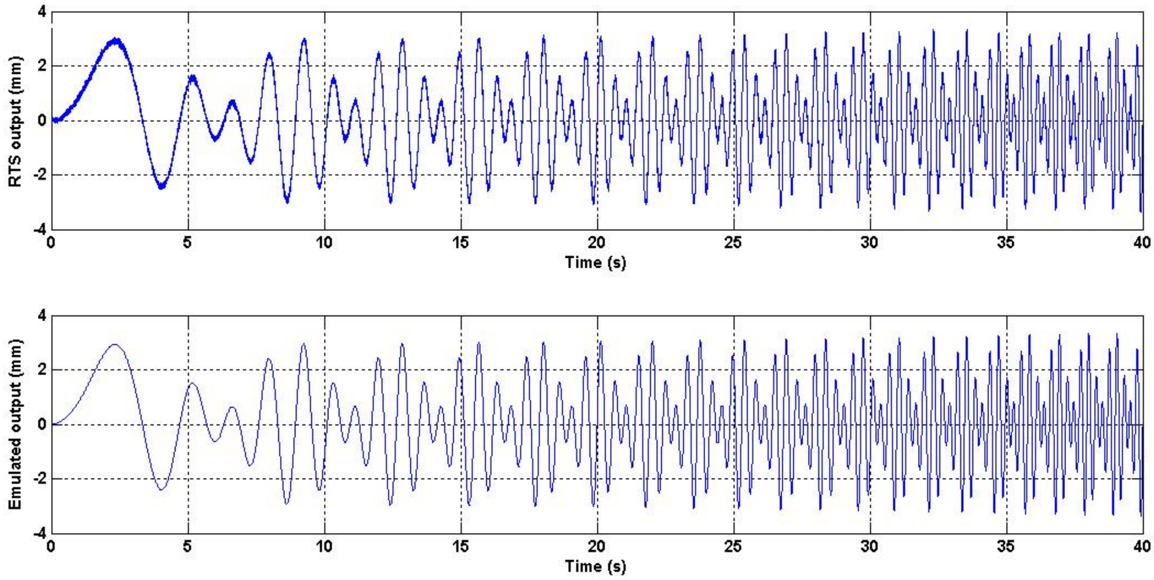


Figure 5.8: Real-time substructure emulation validity check for test C

The general behaviour is well reproduced. However, low amplitude 20Hz oscillations are present in the RTS experiment, resulting in what appears as a thicker line in Figure 5.8. These unwanted oscillations, affecting the early part of the test especially, are due to experimental errors exciting the second mode of the emulated structure. Note that the numerical scheme used possesses no numerical damping.

The results obtained with constant performance inputs and the forward prediction schemes are presented in Table 5.9. Again, the data obtained with the third order polynomial extrapolation with constant inputs is chosen as the reference for calculating the denominators of the criteria. For each run, the criteria values obtained at each actuator are provided.

| | | Relative command error (%) | |
|---|---|---|---|
| | | mean_crit | rms_crit |
| No compensation | act #1 | instability | instability |
| | act #2 | instability | instability |
| Standard 3rd order polynomial extrapolation | act #1 | 2.8 | 2.9 |
| | act #2 | 2.5 | 2.5 |
| Linearly predicted acceleration extrapolation | act #1 | 3.2 | 3.4 |
| | act #2 | 2.7 | 2.7 |
| Laguerre extrapolation with standard 3rd order polynomial interpolation | act #1 | instability | instability |
| | act #2 | instability | instability |

Table 5.9: Comparison of the forward prediction schemes with constant performance inputs in test C

The results can be described as acceptable, even though the relative error values are higher than those obtained in tests A and B, because of the coupling between the actuators. This increase is also partly due to the required actuator movements being of lower amplitudes (around ±4mm instead of ±30mm for tests A and B), resulting in poorer actuation performance (Bonnet *et al.* 2005). No stable test could be run with the Laguerre scheme, despite trying several order and scaling values. The adaptive schemes are then run and the results are presented in Table 5.10.

| | | Relative command error (%) mean_crit | rms_crit |
|---|---|---|---|
| No update | act #1 | 2.8 | 2.9 |
| | act #2 | 2.5 | 2.5 |
| MCSmd outer-loop controller | act #1 | instability | instability |
| | act #2 | instability | instability |
| Darby updates | act #1 | 2.3 | 2.6 |
| | act #2 | 1.9 | 1.9 |
| Modified Darby updates | act #1 | 2.1 | 2.3 |
| | act #2 | 1.7 | 1.8 |
| Zero crossing updates | act #1 | 3.1 | 3.4 |
| | act #2 | 2.5 | 2.6 |
| Pre-recorded updates | act #1 | instability | instability |
| | act #2 | instability | instability |

Table 5.10: Comparison of the performance estimation methods and the outer-loop controller in test C

In these experiments, the MCSmd fails to control the test with stability. The Erzberger gains are set according to the knowledge of the actuator performance and to the reference model used, and the $\alpha$ parameter is tested at various values, including 0. However, instability is witnessed within the first few seconds of testing. When examining the data more closely, it seems the command signal produced at the start of the test mainly consists of growing oscillations with a frequency close to that of the 3$^{rd}$ mode. This suggests the experimental errors are not well enough corrected and are amplified into the higher mode excitations.

The pre-recorded scheme also leads to an unstable experiment that needs to be stopped after about 5s of testing. Looking in detail at the actuator command generated, it seems that the 20Hz oscillations mentioned earlier grow out of control, instead of being damped out when the frequency increases. The high level of detail in the delay information may participate in creating a command signal that lacks continuity, provoking in turn experimental errors and, more importantly, second mode excitation.

Of the three other schemes, the modified Darby updates algorithm performs the best. The error criteria are good for both actuators, and its accuracy also manifests itself by a better control of the higher mode excitations. The delay information produced and used for each actuator by the modified Darby scheme is shown in Figure 5.9.

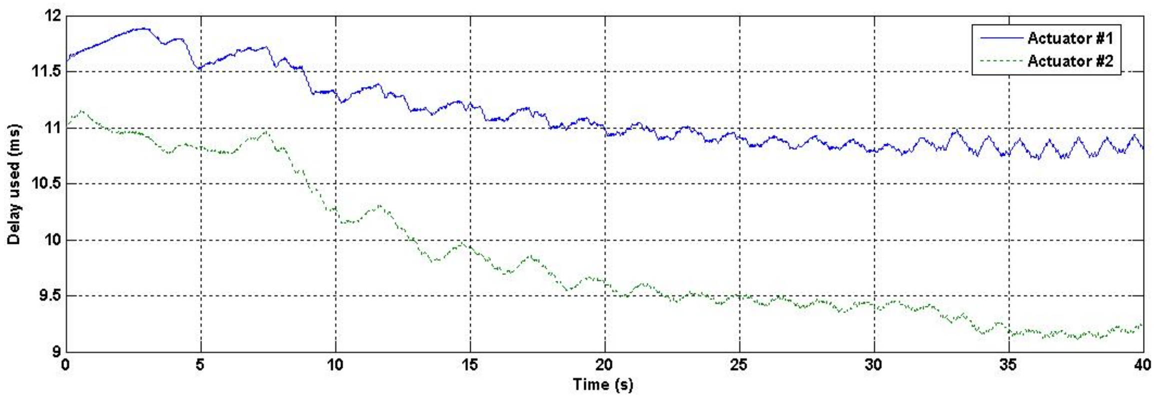


Figure 5.9: Delay signals produced by the modified Darby scheme in test C

The level of relative error reached by the zero-crossing adaptive scheme is higher than what is achieved with constant inputs. The reason for this is that updating at zero-crossing only, in the case of test C, does not allow detecting the worst of the actuator performance. In test C, the actuators' response delays are at their worst when the pistons are either the closest to or the furthest away from each other. This clearly means that relying on zero-crossings only leads to a somewhat underestimated actuator response delay, approximated to its lower bound. This hence results in poorer results than in the constant input case where the delay is approximated to its average.

## 5.4- DISCUSSION

Having a rough estimate of the actuator performance is recommended before conducting RTS experiments, especially if the adaptivity of the scheme used is low. If constant performance inputs are used, they need to be quite accurate, particularly if the physical substructure has low damping. Ideally, the delay and amplitude error inherent to the actuation would be measured as the test progresses and compensated for instantaneously. However, the delay and amplitude error cannot be identified from each other in real-time without additional assumptions. Moreover, the delay can vary quite rapidly even within individual oscillations and the forward prediction techniques used show that even if the delay is known at all times, it is difficult to compensate for it and still obtain a reliable command signal. Notably, some techniques seem to be more sensitive to higher mode excitation than others. The performance information therefore needs to be smooth enough for the output of the prediction scheme to provide a signal ensuring a stable operation of the RTS closed loop.

The scheme proposed in Darby *et al.* (2002) fulfils some of the requirements described above. By discarding the local peak areas, the fastest delay variations are not taken into account. Moreover, with the use of the gains, the smoothness of the delay output is controlled by the user. However, the original scheme has some drawbacks and a simple modification has been tested, based on the use of the inverse of the velocity as the proportional gain between the real-time error and the delay. The modification makes the new scheme simpler to optimise because there is only one gain to set. Moreover, it was found to be more effective in all the tests conducted in this programme of research. The use of this modified performance estimation scheme is recommended for conducting similar experiments, while further validation on different types of tests is required to extend its applicability.

Regarding the forward prediction schemes, three sensibly different approaches have been used:

- the exact third order polynomial extrapolation produces a prediction from the knowledge of the last four data point displacements,
- the linearly predicted acceleration extrapolation requires acceleration, velocity and displacement from the last two points,
- the Laguerre polynomials extrapolation works from the latest displacement input only, as would a filter.

In all tests conducted, the error was post-processed and analysed through an average criterion and a root-mean-square criterion. The results for the three schemes are close to each other. The linearly predicted acceleration scheme is the least computationally demanding. It is also the one whose assumptions are the closest to those of time integration schemes. Should an implicit time integration scheme be employed to solve the numerical substructure, the linearly predicted acceleration scheme could be applied to the latest computed step and would, then, be recommended. If an explicit scheme is used, as is the case for the tests presented here, the exact polynomial extrapolation scheme may be preferred. Finally, the Laguerre extrapolator is prone to higher mode excitation for the third experiment performed.

However, it may be used successfully for less demanding systems and can be particularly advantageous if the numerical integration time-step is large, as it can efficiently extrapolate the sub-step sampled signal.

## 5.5- CONCLUSIONS

Various actuation compensation schemes have been presented, discussed and tested through a series of real-time substructure experiments. It was found that all schemes do not have the same exact purpose and a classification was drafted according to their original aim: some only intend to produce accurate forward predictions, others try to quantify the actuator performance itself and yet others produce a command signal purely based on the control error history. Detailed presentations followed, including optimisation and implementation details. Presently unsuccessful research ideas have also been mentioned. Then, the compensation schemes considered have been subjected to RTS experimental testing. All the schemes tested have allowed conducting experiments which would have been unstable without any compensation. More complex tests have consequently been carried out and limitations to the application of multi-axis real-time hybrid testing were identified. Overall, it was found that the use of a non-adaptive scheme such as the third order exact polynomial extrapolation can be a good solution for some experiments but it requires that the actuator performance is accurately known in advance. If this prerequisite is not fulfilled, if the experiment intended is more challenging, or even simply by default, an adaptive scheme such as the modified Darby estimator can be included into the algorithm to provide, at little computational cost, a fast and accurate real-time update of the compensation operated.

# CHAPTER 6

# COMPARATIVE EVALUATION OF NUMERICAL TIME INTEGRATION SCHEMES FOR REAL-TIME HYBRID TESTING

## 6.1- INTRODUCTION

Although much work has been published on the application of numerical integration schemes to pseudo-dynamic testing, comparatively much less has been published on their applications to the RTS method. In an RTS experiment the numerical substructure needs to be solved in a minimal amount of time after the interface force is measured. No halt in the actuator can be tolerated. An iterative numerical scheme is not desirable either, as it disturbs the physical substructure dynamics. Furthermore, the user would lose control over the number of iterations required, possibly leading to an incompatibility with the amount of time available.

The work carried out by Hakuno in 1969 (see Takanashi & Nakashima 1987), recognised as the origin of hybrid testing, was realised with an analogue computer and the equation of motion was not discretised. Later, Nakashima *et al.* (1992) conducted real-time hybrid experiments with the staggered central difference method. This method was chosen for its simplicity at a time when computing equipment was a harsh limiting factor. Bayer *et al.* (2000) have presented the application to real-time testing of the implicit constant average acceleration method. However, this was only applied to a linear numerical substructure and the time steps used were too small to prove stability beyond the common limit of explicit schemes. To work around the stability problem of explicit schemes for MDOF systems, Blakeborough *et al.* (2001) presented a reduced basis method with which the unused modes are discarded, thereby raising the stability limit while also reducing the need for numerical damping of the higher modes. A method of accounting for non-linear modes into the reduced modal basis has also been described by Blakeborough *et al.*. Darby *et al.* (2001) have produced work on using the first order hold equivalent for a linear numerical model and showed its efficiency compared to the central difference method for time-steps close to but below the CDM stability limit. More recently, Wu *et al.* (2004, 2005, 2006) have proposed developments on two methods – the CDM and the operator splitting method – for their possible applications to the real-time substructure scheme. In this work, Wu is primarily concerned with the implications of non-linear velocity dependent forces in the numerical substructure model on the stability characteristics of the scheme considered.

This chapter attempts to further this knowledge, by investigating which schemes can be used for RTS testing and what relative success is likely to occur. There are many possible criteria to consider. Some critical points of concern are the accuracy, the stability condition, the amplification of higher structural modes, the computational cost, the ease of implementation in real-time, and the possibility of application to elements featuring non-linear load-displacement curves.

One major aspect of real-time hybrid experiments concerns the sampling rate of the various software tasks required. Roughly, two families of tasks can be drawn within the real-time algorithm: the tasks related to the solving of the numerical substructure and those related to the outer-loop control of the experiment. Although they rely on each other during a hybrid simulation, it is important to note that the frequency of operation of each of these tasks cannot necessarily be the same. Therefore, a bespoke multi-tasking strategy is necessary to ensure compatibility. This issue is developed in the following section.

## 6.2- MULTI-TASKING STRATEGY FOR COMPLEX NUMERICAL SUBSTRUCTURE MODELS

In a real-time substructure simulation, the computational routines must be able to solve complex non-linear numerical substructures, consisting of numerous degrees of freedom, possibly even requiring access through a network to data stored on a remote computer, for example operating a bespoke finite element code. For all these reasons, the numerical substructure may require a long time to be solved, and thus the integration time step may have to be set to a fairly large value in order to achieve a real-time simulation. The numerical substructure time step will be called the main-step.

Another principal aspect of real-time substructure testing lies in the outer-loop control, ensuring the boundary conditions are correctly applied at the interface of both substructures. Notably, this means the actuator control needs to follow the desired motion. This motion could for instance be defined by a continuous time history of displacement, velocity or acceleration. However, as developed above, the time-integration routine only produces discrete data points, possibly sampled at relatively large intervals. For a good actuator control, notably between the data points provided by the numerical substructure, it is necessary to produce a control signal at finer time steps (called sub-steps). Note here that the delay compensation can be either part of the main-step task (e.g. if an exact 3$^{rd}$ order polynomial extrapolation is used) or of the sub-step task (e.g. if a Laguerre extrapolator is used).

The following approach was used in this research for the value of the sub-step. Given that the digital controller carries out the actuator inner-loop control at a sampling rate of 5kHz, it is pointless for the outer-loop control to provide a signal any more frequently – this would only result in creating data points that would end up not being used by the digital controller. To ensure that the actuator motion follows the displacement, velocity and acceleration profiles required by the numerical substructure output, the outer-loop control task provides a new signal at every control cycle of the inner-loop. In other words, the outer-loop control task is also made to operate at 5kHz, which corresponds to a sub-step value of 0.2ms. This way, the inner-loop control error can remain as constant as possible loop after loop and the effects of the actuator dynamics are minimised. This strategy helps ensuring that the actuator velocity and acceleration are also controlled, although only a displacement command is emitted. Throughout the whole of this chapter, the value of the sub-step is kept at $t$=0.2ms.

From the diverse computational time requirements exposed above, the multi-tasking strategy provides, with two different time steps, the necessary flexibility. The Simulink® and compatible dSpace® software and hardware real-time multi-tasking functionalities are used. To make the computation possible and optimise the available computational time, the two tasks are assigned a priority system: the control task, operating on the sub-step, always has priority over the numerical integration task. In the event of the low priority task running when the high priority task should be carried out, an interrupt halts the low priority task and lets the higher priority task be executed. Once the higher priority task is completed, the lower priority task resumes its execution, as shown in Figure 6.1. Note that the task switching time of the digital signal processing board used for this work is under 5μs.

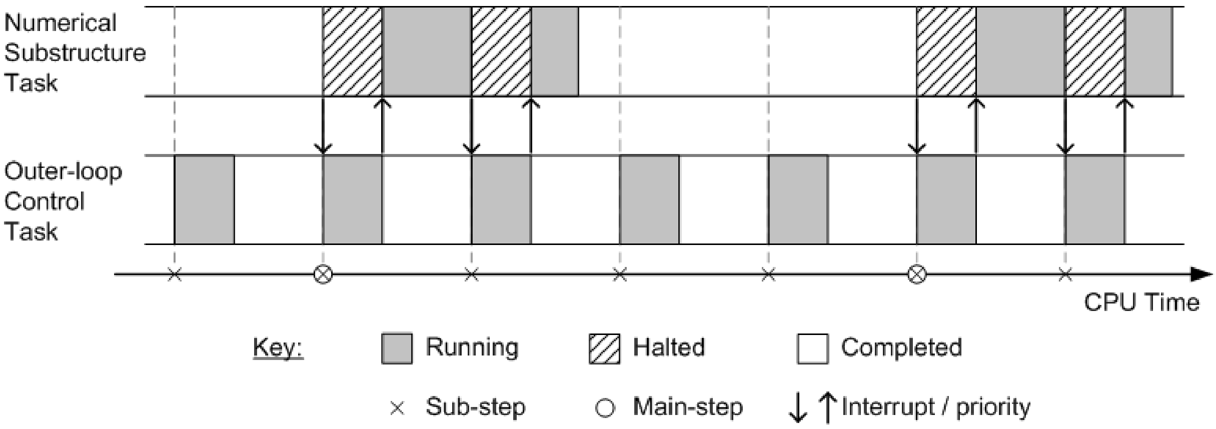

Figure 6.1: Schematic of the task switching logic

The idea behind the multi-tasking strategy described here is very similar to that already described by Nakashima & Masaoka (1999). However, a significant continuity problem presented below is introduced with such a strategy. To the knowledge of the author, no algorithmic details on possible solutions to this problem have previously been published.

## 6.2.1- Presentation of the problem introduced with the multi-tasking strategy

From the previous chapter, it was found that three algorithms could be used as good forward prediction schemes for the critical delay compensation issue: the exact third order polynomial scheme, the linearly predicted acceleration scheme or the Laguerre extrapolation method.

In the first instance, it is assumed that the exact third order polynomial scheme is used. At the end of a series of sub-steps, the actuator command reaches the value of $d_{com}^{n}$. However, if the numerical substructure is complex and/or requires substantial computational communication time, the numerical time integration is not yet completed, so $d_{des}^{n+1}$ is not yet known and, in turn, $d_{com}^{n+1}$ cannot be output by the polynomial extrapolator. This is the first part of the problem exposed here.

For the actuator not to stop, the only possibility at this stage is to extrapolate the next sub-step points from the last few main steps obtained. The exact third order polynomial method can be used here too, basing itself on the last four data points (up to and including $d_{com}^{n}$).

After a certain number of extrapolated sub-steps, $d_{des}^{n+1}$ is finally known and the desired command can be extrapolated to produce $d_{com}^{n+1}$. So the new interpolation polynomial through the last four $d_{com}$ points can be calculated too. However, the last extrapolated sub-step does not lie on this newly calculated polynomial but, instead, lies on the polynomial obtained from the previous four point series. Therefore, if no careful transition is adopted, an irregular step is bound to happen between the last extrapolated sub-step and the consecutive interpolated one. This transition is the second aspect of the issue arising from the multi-tasking strategy. This situation is illustrated in Figure 6.2. This problem is of course fully avoided if the numerical substructure can always be solved within the first sub-step – in which case a single-tasking strategy could actually be used. However, this would make the real-time substructure method less versatile for cases where a complex numerical substructure is necessary for good representation purposes.

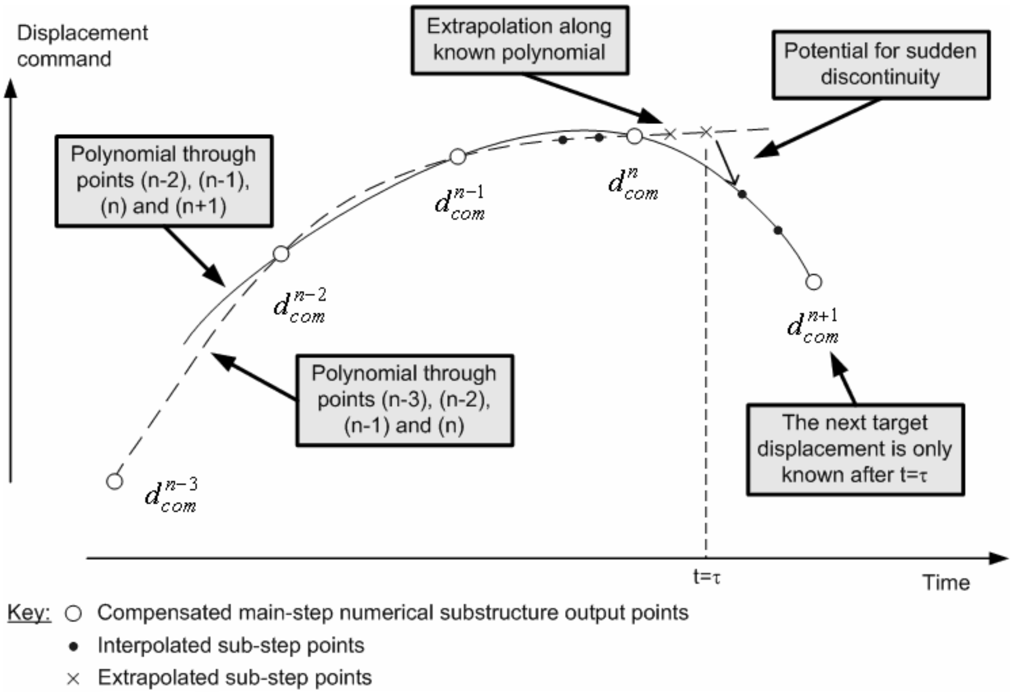


Figure 6.2: Illustration of the task switching transition problem

If it is now considered that the linearly predicted acceleration scheme is used, the same basic problem arises from the fact that $d_{com}^{n+1}$, $v_{com}^{n+1}$ and $a_{com}^{n+1}$ are not yet known at the time of the first sub-step. To ensure the physical substructure dynamics remain satisfactory, the actuator cannot stop and the only possibility is to extrapolate the sub-step points by remaining on the same linear acceleration variation. After a certain number of extrapolated sub-steps $d_{des}^{n+1}$, $v_{des}^{n}$ and $a_{des}^{n}$ are finally known and the new interpolation equation using $d_{com}^{n+1}$ with $v_{com}^{n+1}$ and $a_{com}^{n+1}$ is worked out. But the last extrapolated sub-step does not lie on this newly calculated equation, since it lies on an equation obtained from a different acceleration variation line. An irregular step will occur in this situation too between the last extrapolated sub-step and the first consecutive interpolated one.

Finally, the problem is similar too when considering the Laguerre sub-step extrapolation method, combined with the exact third order interpolation. The $d_{des}$ compilation cannot be updated in time and the only possibility is to extrapolate at sub-steps and to send the extrapolated sub-steps through the Laguerre forward prediction. When $d_{des}^{n+1}$ is finally known and the new polynomial is computed, the last extrapolated sub-step only lies on the polynomial obtained from the previous four-point series and, again, an irregular step happens between the last extrapolated sub-step and the consecutive first interpolated one.

## 6.2.2- Potential way to solve the problem

For the case where the exact third order polynomial is used, a simple solution can be conceived where the last extrapolated sub-step is taken into account in the new four-point compilation for the interpolation procedure to use. To keep the total number of data points used to four, the last main-step point obtained, $d_{com}^{n}$, is dropped. So, typically, instead of the interpolation being done on $d_{com}^{n+1}$, $d_{com}^{n}$, $d_{com}^{n-1}$ and $d_{com}^{n-2}$, it is done on $d_{com}^{n+1}$, $d_{com}^{n+x.sub-steps}$, $d_{com}^{n-1}$ and $d_{com}^{n-2}$, where $d_{com}^{n+x.sub-steps}$ is the last extrapolated sub-step command. This ensures that the newly computed interpolation polynomial crosses the last extrapolated point.

If the Laguerre scheme is used, the same correction can still be envisaged, except it is carried out before the forward prediction compensation. So instead of performing the interpolation on $d_{des}^{n+1}$, $d_{des}^{n}$, $d_{des}^{n-1}$ and $d_{des}^{n-2}$, it is done on $d_{des}^{n+1}$, $d_{des}^{n+x.sub-steps}$, $d_{des}^{n-1}$ and $d_{des}^{n-2}$ in order to account for the last extrapolated sub-step.

Solving the problem for the case when the linearly predicted acceleration scheme is used is not as straightforward, but a similar fix can be envisaged. In this case, the important information to take into account from the last extrapolated point is not its displacement value but its acceleration value, since the founding equation of the scheme is the linear variation of the acceleration. However, the application of this scheme is fundamentally different depending on the type of numerical integration scheme used – explicit or implicit – since not all schemes can provide target displacement, velocity and acceleration data at the current step. Therefore, it may not be a suitable scheme when one intends to compare several integration schemes fairly, which is the main aim in this chapter.

## 6.2.3- Choice of forward prediction algorithm

For the reasons mentioned in the section above, the linearly predicted acceleration scheme is not used in the consequent numerical scheme evaluation programme. Also, the Laguerre scheme is not initially retained, primarily because of the added parameter optimisation work associated, clearly not the point of interest here. The simple and proven exact third order polynomial scheme is therefore chosen for the following work.

## 6.2.4- The sub-step continuity problem

The potential solution mentioned above, where the last extrapolated sub-step point is taken into account for the subsequent interpolation, is considered here. A still untouched issue is that of the real-time implementation of this approach, including details on how the algorithm can provide the polynomial equation and apply it to the data points appropriately. Potentially complex logic may be required.

An important point can be observed concerning the four data point compilation used in the sub-step interpolation task: all four points used as well as any sub-step point produced by the process will always exactly lie on the polynomial. Consequently, exchanging any one of the four data points with any sub-step point produced will not affect the mathematical definition of the polynomial. So, if, at each sub-step, the chronologically third definition point is replaced by the last produced sub-step, the following effects are achieved:

- In normal operation, the polynomial definition remains unchanged and the sub-step interpolation is carried out as standard.
- After the end of the interpolation phase at the main-step value, if an extrapolation phase is required, the extrapolation polynomial is only deduced from main-step values as produced by the numerical substructure and compensation algorithm. Therefore, the extrapolation phase from a given main-step does not directly influence that of the following main-step, and yet the displacement continuity through the main-step point is realised.
- When the numerical substructure is solved, the last extrapolated sub-step automatically replaces the previous main-step point in the new four data point compilation, in order to retain continuity between the end of the extrapolation phase and the beginning of the interpolation one.

The implementation of this strategy ensures one part of the solution proposed.

Another important part remains: the production and application of the polynomial equation itself. The process used thus far was based on the assumption that the four data points provided in the compilation were all spaced in time by the value of one main-step. However, in the new compilation used for the interpolation phase, only three of the points are at main-steps (numbers 1, 2 & 4) while the added point is located in time at the sub-step just previous to the current one. To express mathematically the value of the desired interpolated point from this data compilation, it is necessary to start from the general Lagrange formula for a third degree polynomial $P(x)$ through four points $y_1=f(x_1)$, $y_2=f(x_2)$, $y_3=f(x_3)$ and $y_4=f(x_4)$:

$$\begin{aligned}P(x)=&\frac{(x-x_2)\cdot(x-x_3)\cdot(x-x_4)}{(x_1-x_2)\cdot(x_1-x_3)\cdot(x_1-x_4)}\cdot y_1+\frac{(x-x_1)\cdot(x-x_3)\cdot(x-x_4)}{(x_2-x_1)\cdot(x_2-x_3)\cdot(x_2-x_4)}\cdot y_2\\&+\frac{(x-x_1)\cdot(x-x_2)\cdot(x-x_4)}{(x_3-x_1)\cdot(x_3-x_2)\cdot(x_3-x_4)}\cdot y_3+\frac{(x-x_1)\cdot(x-x_2)\cdot(x-x_3)}{(x_4-x_1)\cdot(x_4-x_2)\cdot(x_4-x_3)}\cdot y_4\end{aligned}\tag{6.1}$$

In the case of interest, as defined above, and setting $x_1$ to be the local origin, the following applies:

$$\begin{array}{ll}x_1=0 & y_1=d_{com}^{n-2}\\ x_2=T & y_2=d_{com}^{n-1}\\ x_3=3.T+h-t & y_3=c_{com}^{n+1+h-t}\\ x_4=3.T & y_4=d_{com}^{n+1}\\ x=3.T+h & P(x)=c_{com}^{n+1+h}\end{array}\tag{6.2}$$

where $T$ is the value of the main-step, $t$ the value of the sub-step, $d_{com}$ is the actuator command signal produced at main-steps by the numerical integration and delay compensation algorithm, $c_{com}$ is the actuator command signal produced at sub-steps by the interpolation/extrapolation routine, the superscripts represent the steps considered, and finally $h$ is varied linearly from ($-T+t$) to 0 by sub-step increments to define the current interpolation point. If the interpolation is to be extended into extrapolation while the numerical substructure calculation is still being carried out, $h$ goes into positive values. Consecutively, when the numerical integration finishes, $h$ starts again from a value somewhat higher than ($-T+t$).

Introducing (6.2) into (6.1):

$$\begin{aligned}c_{com}^{n+1+h}=&\frac{(2.T+h)\cdot t\cdot h}{-T\cdot(-3.T-h+t)\cdot(-3.T)}\cdot d_{com}^{n-2}+\frac{(3.T+h)\cdot t\cdot h}{T\cdot(-2.T-h+t)\cdot(-2.T)}\cdot d_{com}^{n-1}\\&+\frac{(3.T+h)\cdot(2.T+h)\cdot h}{(3.T+h-t)\cdot(2.T+h-t)\cdot(h-t)}\cdot c_{com}^{n+1+h-t}+\frac{(3.T+h)\cdot(2.T+h)\cdot t}{3.T\cdot(2.T)\cdot(-h+t)}\cdot d_{com}^{n+1}\end{aligned}\tag{6.3}$$

Equation (6.3) can then easily be implemented into real-time code, together with an adequate update scheme for the variable $h$, as stipulated above.

Verification RTS tests are conducted with a linear SDOF numerical substructure and a SDOF physical substructure. The multiplication of random matrices is introduced as part of the main-step task in order to increase artificially the duration needed by the DSP hardware to complete the task. The test is setup with each main-step containing 25 sub-steps. The size of the random matrices is increased in order to force the algorithm to operate extrapolation tasks and the outer-loop control error is monitored statistically to measure the quality of the real-time synchronisation. With one extrapolation step conducted at the start of each main-step, no measurable difference on the quality of the RTS output can be seen. When four to nine consecutive extrapolation steps are necessary at each main-step, the output of the RTS experiment is still good, although control error differences can be observed with the case where no extrapolation is needed. Tests intended with more than nine extrapolations proved difficult, especially at high frequency (near 10Hz) where actuator control became difficult. But on the whole, the strategy developed in this section is shown capable of ensuring first order continuity when the hardware requires more than a sub-step to solve the numerical substructure.

### 6.2.5- Alternative strategy tested

A second way of solving the problem described above, potentially more stable when the number of extrapolated sub-steps increases, is now examined. It is based on measuring the error produced at the last extrapolated point and gradually eliminating its influence. The error itself can only be measured once the numerical substructure has been solved. Then the difference between the last extrapolated point and what would have been the interpolated point at the same time, had the numerical substructure response been known in time, is the value of the error due to the extrapolation stage. According to the number of sub-steps remaining to the end of the current main-step, the output of the interpolation routine produced once the true solution is known can be augmented by a declining proportion of this error. The proportion is the highest, just below 100%, at the first interpolated sub-step and reduces to 0% at the end of the main-step. The proportion considered can also be chosen to decline more rapidly and reach zero before the end of the main-step, so that the correct dynamics of the system are stabilised to more correct values when the step ends.

The implementation of such a strategy is somewhat conceptually simpler than that of the solution proposed in the previous paragraphs. However, it involves more logic and turns out to be just as computationally demanding. The evaluation tests described in the previous section were repeated for this strategy but did not prove quite as successful. Although completing the error correction before the end of the main-step was helpful, the final result was not as good as for the first presented strategy.

Other strategies could also be envisaged using an integrated form of the equation of motion in the numerical time integration. However, no integral form was used in the present research for reasons exposed in the next section.

## 6.3- NUMERICAL TIME INTEGRATION SCHEMES

This section presents numerical time integration schemes for use in real-time hybrid testing. A selection is made based on conclusions drawn from previous research and implementation details for the selected schemes are provided.

### 6.3.1- General presentation and selection

The discussion of various schemes, their nature and their characteristics, is based on the following framework. The numerical substructure type considered is based on linear inertial forces and linear damping forces (i.e. with a known constant viscous damping matrix). The forces due to the nodal displacement vector, however, may either be linear or non-linear (e.g. with a bi-linear hysteretic behaviour). This is the only potential source of non-linearity in the numerical substructure considered in the following work. The effects of non-constant mass that could potentially occur with damage can therefore not be modelled. Another subsequent limitation of this framework is the potential presence of non-linear damping devices in the numerical substructure. This limitation is precisely the specialisation of the work undertaken by Wu *et al.* (2004, 2005, 2006). It is however believed that, for civil engineering structures, damping is typically low enough for a linear approximation to be valid. Moreover, should special devices be studied with non-linear velocity dependent forces, they could be placed in the physical substructure for their exact contribution to be accounted for.

Apart from the suitability for real-time computation of a non-linear numerical substructure of the type described in the previous paragraph, the main two issues a numerical scheme needs to address are the accuracy and the stability. The accuracy can be measured by the minimisation of both the frequency distortion and the numerical damping. On the other hand, the stability is characterised by the existence and the value of a critical time-step value above which stability cannot be obtained. Some schemes, described as unconditionally stable, do not possess any such time-step restriction. Stability is also related to the potential accumulation and amplification into higher mode response of systematic experimental errors that can occur during an RTS experiment. It was shown for PsD testing (Shing & Mahin 1987*b*), however, that the presence of numerical dissipation in the time integration scheme can be beneficial by damping out the artificial higher mode contribution. For some algorithms, the numerical damping rises with the frequency considered, making it even more attractive: good accuracy in the lower modes and good dissipation of the higher mode contribution. However, in a real-time hybrid simulation, an effective delay compensation algorithm is often necessary to carry out a stable experiment and numerical damping may not be needed since the systematic character of the experimental errors should have already been corrected.

Within this framework, and with the analysis criterion mentioned above, a formal comparison of several numerical time-integration schemes is presented in Table 6.1 in the light of their application to RTS simulations.

The application of a numerical scheme to RTS testing is not as straightforward as for PsD testing. Indeed, the real-time constraint imposes a minimum computation speed. Moreover, an iterative approach of the type used by some researchers in PsD testing in conjunction with an implicit time integration scheme is not an option in an RTS simulation since iterations would involve the contamination of the physical substructure dynamics. Therefore, the available strategies for the use of a numerical time integration scheme for RTS testing can be classified in three types:

- The use of a fully explicit numerical scheme.
- The implementation of an implicit scheme through an explicit predictor target.
- The implementation of an implicit scheme through a direct sub-step feedback.

| Scheme designation | Explicit / Implicit | Stability condition for linear system | Suitability for non-linear force/displacement law | Order of accuracy | Numerical dissipation | Frequency distorsion | Some references & application considered |
|---|---|---|---|---|---|---|---|
| Central difference method (CDM) | E | $T < \tau_{min} / \pi$ | Y | 2nd | N | very low<br>lower than CAAM when $T < 0.3\ \tau_{min}$<br>(period shrinkage) | Shing & Mahin 1985 - PsD<br>Nakashima et al. 1992 - RTS |
| Newmark explicit | E | $T < \tau_{min} / \pi$ | Y | 2nd | N | same as CDM | Shing & Mahin 1985 - PsD<br>Chang 2002*b* - PsD |
| Newmark explicit with $\gamma$ damping ($\gamma$>0.5) | E | $T < \tau_{min} / \pi$<br>at best<br>but harsher condition when $\gamma$ increases | Y | 1st | Y<br>slightly favourable but lower modes are affected strongly | slightly higher than Newmark explicit with numerical dissipation Chang 1997<br>(period shrinkage) | Shing & Mahin 1985 - PsD<br>Chang 1997 - PsD |
| Newmark explicit with $\alpha$ & $\rho$ dissipation | E | $T < \tau_{min} / \pi$<br>for $\alpha$=0 & $\rho$>=0<br>but harsher condition when $\alpha$ increases | Y | 1st | Y<br>slightly favourable can be 0 for chosen mode but affects all other modes | higher than CDM especially for higher modes<br>(period shrinkage) | Shing & Mahin 1985 - PsD<br>Shing & Mahin 1987*b* - PsD |
| Newmark explicit with numerical disspation Chang 1997 | E | $T < \tau_{min} / \pi$<br>at best<br>but harsher condition if numerical damping is present | Y | 2nd | Y<br>favourable | slightly higher than CDM<br>(period shrinkage) | Chang 1997 - PsD |
| Newmark explicit with integral form | I | $T < \tau_{min} / \pi$ | not easy to introduce non-linearity method approximation is poorer for non-linear structures | 2nd | N | same as CDM | Chang et al. 1998 - PsD<br>Algaard et al. 2001 - PsD |
| Newmark explicit unconditionally stable Chang 2002*b* | E | None | Y | 2nd | N | same as CAAM | Chang 2002*b* - PsD |
| Constant average acceleration method (CAAM)<br>= Newmark implicit with $\gamma$=0.5 & $\beta$=0.25<br>= Trapezoidal rule | I | None | Y<br>with iterations or direct feedback | 2nd | N | very low<br>lowest of unconditionally stable schemes<br>(period elongation) | Newmark 1959 - Analysis<br>Thewalt & Mahin 1995 - PsD<br>Shing et al. 1996 - PsD<br>Bursi & Shing 1996 - PsD |
| Newmark implcit scheme with $\gamma$ damping (0.5<$\gamma$≤2.$\beta$) | I | None | Y<br>with iterations or direct feedback | 1st | Y<br>slightly favourable but lower modes are affected strongly | slightly higher than CAAM<br>(period elongation) | Newmark 1959 - Analysis<br>Hughes 1987 - Analysis<br>Garcia de Jalon & Bayo 1994 - Analysis |
| Newmark implicit $\alpha$−method (-1/3≤$\alpha$<0) | I | None | Y<br>with iterations or direct feedback | 2nd | Y<br>favourable<br>lower modes little affected | slightly higher than CAAM<br>(period elongation) | Hilber et al. 1977 - Analysis<br>Hughes 1987 - Analysis |
| Operator splitting method (OSM) | I | None | Y<br>high non-linearity shows limits | 2nd | N | same as CAAM for linear system<br>slightly worse than CAAM for non-linear system<br>(period elongation) | Bursi & Shing 1996 - PsD<br>Shing et al. 1996 - PsD<br>Combescure & Pegon 1997 - PsD |
| $\alpha$-Operator spliting method ($\alpha$-OSM) | I | None | Y<br>high non-linearity shows limits | 2nd | Y<br>favourable | slightly higher than OSM<br>(period elongation) | Buchet & Pegon 1994 - PsD<br>Bursi & Shing 1996 - PsD<br>Combescure & Pegon 1997 - PsD |
| Reduced basis method with Newmark explicit time integration scheme | E | $T < \tau_{min} / \pi$ | Y<br>with pre-empted "non-linear modes" | 2nd | N | same as CDM | Blakeborough et al. 2001 - RTS<br>Williams 2000 - RTS |

Table 6.1: Comparative presentation of numerical time integration schemes

From Table 6.1, not all schemes satisfy these requirements. The following schemes have been selected for implementation and real-time hybrid testing:

- The Newmark explicit scheme
- The Newmark explicit unconditionally stable (Chang 2002*b*)

- The operator splitting method
- The $\alpha$-shifted operator splitting method
- The constant average acceleration method
- The Newmark implicit $\alpha$-method

It is worth noting here that the CDM and the Newmark explicit methods possess the same characteristics for the aspects presented in Table 6.1. However, Shing & Mahin (1990) have shown that the error amplification properties of the CDM are poorer than those of the Newmark explicit scheme for small time steps. Other schemes could also have been selected, but the author was keen to find a compromise in establishing a list of work that could actually be achieved within the time available.

## 6.3.2- Newmark explicit scheme

Newmark (1959) presented a numerical time integration method that has since become a classic reference in computational structural dynamics. This method can be chosen to be explicit. Applied to real-time substructure testing, it is then based on Equation (6.4) as follows:

$$\begin{aligned}
&\mathbf{d}_{n+1} = \mathbf{d}_n + T \cdot \mathbf{v}_n + \frac{T^2}{2} \cdot \mathbf{a}_n \\
&\mathbf{v}_{n+1} = \mathbf{v}_n + \frac{T}{2} \cdot (\mathbf{a}_n + \mathbf{a}_{n+1}) \\
&\mathbf{M} \cdot \mathbf{a}_{n+1} + \mathbf{C} \cdot \mathbf{v}_{n+1} + \mathbf{R}_{n+1} = \mathbf{f}_{n+1} + \mathbf{F}_{n+1}
\end{aligned} \tag{6.4}$$

where **R** is the vector of numerical substructure restoring force due to the considered displacement. Note that for a fully linear system, the vector **R** could be written as the product **K**.**d**.

Thanks to the explicit character of the displacement difference equation in Equation (6.4), the target displacement vector $\mathbf{d}_{n+1}$ is easily computed without needing iterations or complex mathematical procedures. The displacement at the interface can then be applied on the physical substructure in real-time and the force feedback vector $\mathbf{f}_{n+1}$ formed. Following this, the second and third equations in (6.4) are solved for $\mathbf{v}_{n+1}$ and $\mathbf{a}_{n+1}$ in order to carry on the time integration for step ($n$+2). Since these calculations should be completed quickly enough for the dynamics of the physical susbstructure to be excited in real-time without stopping between steps, the simplicity of this scheme is a major advantage.

This scheme is also very accurate, with no numerical damping and only small amounts of period shrinkage. Its major drawback, however, is the stability limit proportional to the smallest natural period of the numerical substructure. For complex MDOF systems, a crucial problem can arise where the required time-step is too small for the computing hardware to solve the model in real-time. This drawback is very important for the development of real-time hybrid testing, since the method must be able to cope with complex numerical substructure models.

## 6.3.3- Newmark explicit unconditionally stable Chang 2002

Chang (2002*b*) devised a modification to the Newmark explicit scheme described by Equation (6.5):

$$\begin{aligned}
&\mathbf{d}_{n+1} = \mathbf{d}_n + \boldsymbol{\beta}_1 \cdot T \cdot \mathbf{v}_n + \boldsymbol{\beta}_2 \cdot T^2 \cdot \mathbf{a}_n \\
&\mathbf{v}_{n+1} = \mathbf{v}_n + \frac{T}{2} \cdot (\mathbf{a}_n + \mathbf{a}_{n+1}) \\
&\mathbf{M} \cdot \mathbf{a}_{n+1} + \mathbf{C} \cdot \mathbf{v}_{n+1} + \mathbf{R}_{n+1} = \mathbf{f}_{n+1} + \mathbf{F}_{n+1} \\
&\boldsymbol{\beta}_1 = \left[ \mathbf{I} + \frac{1}{2} \cdot T \cdot \mathbf{M}^{-1} \cdot \mathbf{C} + \frac{1}{4} \cdot T^2 \cdot \mathbf{M}^{-1} \cdot \mathbf{K}_0 \right]^{-1} \times \left[ \mathbf{I} + \frac{1}{2} \cdot T \cdot \mathbf{M}^{-1} \cdot \mathbf{C} \right] \\
&\boldsymbol{\beta}_2 = \frac{1}{2} \cdot \left[ \mathbf{I} + \frac{1}{2} \cdot T \cdot \mathbf{M}^{-1} \cdot \mathbf{C} + \frac{1}{4} \cdot T^2 \cdot \mathbf{M}^{-1} \cdot \mathbf{K}_0 \right]^{-1}
\end{aligned} \tag{6.5}$$

where $\mathbf{K}_0$ is defined as the initial stiffness matrix of the numerical substructure.

Two weighing parameters $\boldsymbol{\beta}_1$ and $\boldsymbol{\beta}_2$ are introduced into the displacement difference equation and are defined by the 4th and 5th equalities in (6.5). Note that $\boldsymbol{\beta}_1$ and $\boldsymbol{\beta}_2$ are matrices themselves. The implementation of this scheme is the same as that of the standard Newmark explicit scheme. The matrices $\boldsymbol{\beta}_1$ and $\boldsymbol{\beta}_2$ are computed before the test.

This derivation produces a scheme with numerical properties equivalent to those of the CAAM. It therefore has good accuracy (no numerical damping and low period elongation). More importantly perhaps, unlike most other explicit schemes, it is unconditionally stable for linear systems. Following the remarks made regarding the ease of application of the standard Newmark explicit scheme to RTS testing, Chang's development confers a high potential to the method.

### 6.3.4- Operator splitting method and $\alpha$-shifted operator splitting method

The operator splitting method can be combined with an $\alpha$-shifted equilibrium equation of motion in order to introduce numerical damping into the algorithm (Combescure & Pegon 1997). The scheme is defined by the following equations:

$$\begin{aligned}
&\tilde{\mathbf{d}}_{n+1} = \mathbf{d}_n + T \cdot \mathbf{v}_n + \left(\tfrac{1}{2} - \beta\right) \cdot T^2 \cdot \mathbf{a}_n \\
&\mathbf{d}_n = \tilde{\mathbf{d}}_n + \beta \cdot T^2 \cdot \mathbf{a}_n \\
&\mathbf{v}_n = \mathbf{v}_{n-1} + (1-\gamma) \cdot T \cdot \mathbf{a}_{n-1} + \gamma \cdot T \cdot \mathbf{a}_n \\
&\mathbf{M} \cdot \mathbf{a}_n + (1+\alpha) \cdot \mathbf{C} \cdot \mathbf{v}_n - \alpha \cdot \mathbf{C} \cdot \mathbf{v}_{n-1} + (1+\alpha) \cdot \mathbf{R}(\mathbf{d}_n) - \alpha \cdot \mathbf{R}(\mathbf{d}_{n-1}) \\
&= (1+\alpha) \cdot \mathbf{f}_n\left(\tilde{\mathbf{d}}_n^e, \tilde{\mathbf{v}}_n^e\right) + (1+\alpha) \cdot \mathbf{K}_{phys} \cdot \left(\mathbf{d}_n - \tilde{\mathbf{d}}_n^e\right) + (1+\alpha) \cdot \mathbf{C}_{phys} \cdot \left(\mathbf{v}_n - \tilde{\mathbf{v}}_n^e\right) + (1+\alpha) \cdot \mathbf{F}_n \\
&- \alpha \cdot \mathbf{f}_{n-1}\left(\tilde{\mathbf{d}}_{n-1}^e, \tilde{\mathbf{v}}_{n-1}^e\right) - \alpha \cdot \mathbf{K}_{phys} \cdot \left(\mathbf{d}_{n-1} - \tilde{\mathbf{d}}_{n-1}^e\right) - \alpha \cdot \mathbf{C}_{phys} \cdot \left(\mathbf{v}_{n-1} - \tilde{\mathbf{v}}_{n-1}^e\right) - \alpha \cdot \mathbf{F}_{n-1} \\
&\beta = \tfrac{1}{4} \cdot (1-\alpha)^2 \\
&\gamma = \tfrac{1}{2} - \alpha
\end{aligned} \tag{6.6}$$

where $\mathbf{K}_{phys}$ and $\mathbf{C}_{phys}$ are predetermined linear stiffness and damping properties of the physical substructure interface applied to the matrix form of the numerical substructure, $\tilde{\mathbf{d}}_n^e$ is the vector of effective predictor displacements containing the values applied on the physical substructure and measured experimentally, and $\tilde{\mathbf{v}}_n^e$ is the vector of effective velocity of application of the predictor displacement, approximated at sub-step points by:

$$\tilde{\mathbf{v}}_n^e = \frac{1}{t}\left(\tilde{\mathbf{d}}_n^e - \tilde{\mathbf{d}}_{n-sub-step}^e\right) \tag{6.7}$$

where $\tilde{\mathbf{d}}_{n-sub-step}^e$ is the vector of the values of the last interpolated sub-step predictor displacement applied before $\tilde{\mathbf{d}}_n^e$. The difference equations are the same as for the general Newmark implicit scheme, except that an explicit displacement predictor term is formulated.

The $\alpha$-OSM applied to structural testing implies that the actual specimen loading reaches the predictor displacement $\tilde{\mathbf{d}}$ rather than the corrector displacement $\mathbf{d}$ at the predictor velocity $\tilde{\mathbf{v}}$ instead of $\mathbf{v}$. For this reason, the interface force vector $\mathbf{f}$ is described in (6.6) as $\mathbf{f}\left(\tilde{\mathbf{d}}, \tilde{\mathbf{v}}\right)$. Therefore, in an RTS experiment, the physical substructure feedback load vector $\mathbf{f}$ is corrected, as expressed on the right hand side of the fourth equality in (6.6) with the $\mathbf{K}_{phys}$ and $\mathbf{C}_{phys}$ terms. Note that taking into account the effective displacement and velocity values as stipulated in this equation introduces a form of experimental error correction, comparable to the I-modification scheme proposed by Combescure & Pegon (1997) for the application to PsD testing. Such a correction aims at reducing the propagation and amplification of the control errors during a hybrid test.

When the numerical substructure has non-linear displacement driven behaviour (i.e. non-constant stiffness), a further approximation is necessary for the scheme to remain explicit for RTS testing (Combescure & Pegon 1997). The approximation introduced can be formulated as:

$$\mathbf{R}(d_n) = \mathbf{K}_0 \cdot \left(\mathbf{d}_n - \tilde{\mathbf{d}}_n\right) + \mathbf{R}\left(\tilde{\mathbf{d}}_n\right) \tag{6.8}$$

where $\mathbf{K}_0$ is a predetermined linear stiffness matrix for the numerical substructure. For the PsD application of the $\alpha$-OSM, it has been shown that the predictor stiffness matrix minus the tangent stiffness matrix of the non-linear system needs to remain at all times positive definite for the scheme to remain unconditionally stable.

The numerical damping is governed by the user-chosen $\alpha$ term, dictating the shift in the equilibrium point as well as the values for the $\beta$ and $\gamma$ parameters. For unconditional stability when linear systems are considered, the available range of $\alpha$ is [-1/3 ; 0]. Note that when $\alpha$ is chosen to be 0, no numerical damping is produced and the scheme's theoretical formulation becomes equivalent to that of the constant average acceleration method. When $\alpha$ is selected to be strictly negative, the scheme features a combination of $\gamma$ damping and negative $\alpha$ damping that produces good characteristics because it has little effect on the lower modes and a damping effect on higher mode vibrations. Moreover, the possibility for the researcher to easily tune the amount of numerical damping produced through the $\alpha$ parameter – and in particular to set the numerical damping to a zero value – is considered in this application to be a significant advantage.

Based on the explicit property of the predictor displacement, the implementation process for the $\alpha$-OSM is somewhat similar to that used for the Newmark explicit scheme. The predictor displacement is computed explicitly for the step ($n$+1) and applied to the physical substructure and the second, third and fourth equations from (6.6) can then be solved at the step ($n$+1) for $\mathbf{d}_{n+1}$, $\mathbf{v}_{n+1}$ and $\mathbf{a}_{n+1}$ to compute the next predictor displacement for the step ($n$+2). Equations (6.6) and (6.7) therefore provide the material for the algorithm's implementation, with the discretised equation of motion in (6.6) rearranged and solved for $\mathbf{a}_n$ as follows:

$$\begin{aligned}\mathbf{a}_n = \mathbf{D}\cdot\Big\{&\mathbf{B}\cdot\mathbf{v}_{n-1} + (1+\alpha)\cdot\Big(\mathbf{A}\cdot\mathbf{a}_{n-1} - \mathbf{R}\big(\tilde{\mathbf{d}}_n\big) - \mathbf{K}_{phys}\cdot\big(\tilde{\mathbf{d}}_n^e - \tilde{\mathbf{d}}_n\big) - \mathbf{C}_{phys}\cdot\tilde{\mathbf{v}}_n^e + \mathbf{f}_n + \mathbf{F}_n\Big)\\ &-\alpha\cdot\Big(\mathbf{G}\cdot\mathbf{a}_{n-1} - \mathbf{R}\big(\tilde{\mathbf{d}}_{n-1}\big) - \mathbf{K}_{phys}\cdot\big(\tilde{\mathbf{d}}_{n-1}^e - \tilde{\mathbf{d}}_{n-1}\big) - \mathbf{C}_{phys}\cdot\tilde{\mathbf{v}}_{n-1}^e + \mathbf{f}_{n-1} + \mathbf{F}_{n-1}\Big)\Big\}\end{aligned} \tag{6.9}$$

where the constant matrices **A**, **B**, **D** and **G** are defined and evaluated prior to the start of the test according to:

$$\begin{aligned}\mathbf{D} &= \left[\mathbf{M} + (1+\alpha)\cdot\gamma\cdot T\cdot\left(\mathbf{C} - \mathbf{C}_{phys}\right) + (1+\alpha)\cdot\beta\cdot T^2\cdot\left(\mathbf{K}_0 - \mathbf{K}_{phys}\right)\right]^{-1}\\ \mathbf{A} &= (1-\gamma)\cdot T\cdot\left(\mathbf{C}_{phys} - \mathbf{C}\right)\\ \mathbf{B} &= \mathbf{C}_{phys} - \mathbf{C}\\ \mathbf{G} &= \beta\cdot T^2\cdot\left(\mathbf{K}_{phys} - \mathbf{K}_0\right)\end{aligned} \tag{6.10}$$

By setting $\alpha = 0$, the scheme reduces to the OSM. Both the OSM and the $\alpha$-OSM are unconditionally stable for linear systems. Thanks to the explicit predictor formulation, their implementation for RTS simulations is kept simple, even though they are theoretically implicit schemes. The OSM has no numerical damping while the amount of dissipation for the $\alpha$-OSM can be controlled by the user up to a certain limit. The frequency distortion is kept to a good level for linear systems but, due to the approximations used, can reach higher values for non-linear systems if the stiffness varies greatly.

### 6.3.5- Constant average acceleration method with digital sub-step feedback algorithm

The CAAM is a fully implicit scheme. An additional strategy for its implementation is therefore necessary. The sub-step feedback algorithm was initially presented as an analogue solution by Thewalt & Mahin (1995) for the application to PsD testing. Later, it was also used by Bayer *et al.* (2000) in a digital version and applied to the RTS testing of a linear numerical substructure. The following material is mainly derived from that found in these two publications but also significantly adapted for its application to RTS testing with a non-linear numerical model.

The general formulation of the CAAM is as follows:

$$\begin{aligned}\mathbf{d}_{n+1} &= \mathbf{d}_n + T\cdot\mathbf{v}_n + \tfrac{1}{4}\cdot T^2\cdot\mathbf{a}_n + \tfrac{1}{4}\cdot T^2\cdot\mathbf{a}_{n+1}\\ \mathbf{v}_{n+1} &= \mathbf{v}_n + \tfrac{1}{2}\cdot T\cdot\mathbf{a}_n + \tfrac{1}{2}\cdot T\cdot\mathbf{a}_{n+1}\\ \mathbf{M}\cdot\mathbf{a}_{n+1} + \mathbf{C}\cdot\mathbf{v}_{n+1} + \mathbf{R}_{n+1} &= \mathbf{F}_{n+1} + \mathbf{f}_{n+1}\end{aligned} \tag{6.11}$$

where $\mathbf{R}_{n+1}$ is the restoring force vector of the numerical substructure according to the $\mathbf{d}_{n+1}$ displacements only (i.e. it does not contain the effects of velocity or acceleration). According to Dahlquist's theorem (Hughes 1987), this scheme is the most accurate unconditionally stable linear multi-step scheme. It features second order accuracy, no numerical damping and a small amount of frequency distortion (period elongation).

Re-arranging the first equation of (6.11) and replacing the resulting acceleration terms into the second provides:

$$\mathbf{a}_{n+1} = \frac{4}{T^2}\cdot\mathbf{d}_{n+1} - \frac{4}{T^2}\mathbf{d}_n - \frac{4}{T}\cdot\mathbf{v}_n - \mathbf{a}_n$$
$$\mathbf{v}_{n+1} = \frac{2}{T}\cdot\mathbf{d}_{n+1} - \frac{2}{T}\cdot\mathbf{d}_n - \mathbf{v}_n \tag{6.12}$$
$$\mathbf{M}\cdot\mathbf{a}_{n+1} + \mathbf{C}\cdot\mathbf{v}_{n+1} + \mathbf{R}_{n+1} = \mathbf{F}_{n+1} + \mathbf{f}_{n+1}$$

Then, introducing the acceleration and velocity terms into the third equation leads to:

$$\mathbf{a}_{n+1} = \frac{4}{T^2}\cdot\left(\mathbf{d}_{n+1} - \mathbf{d}_n - T\cdot\mathbf{v}_n\right) - \mathbf{a}_n$$
$$\mathbf{v}_{n+1} = \frac{2}{T}\cdot\left(\mathbf{d}_{n+1} - \mathbf{d}_n\right) - \mathbf{v}_n \tag{6.13}$$
$$\left(\frac{4}{T^2}\cdot\mathbf{M} + \frac{2}{T}\cdot\mathbf{C}\right)\cdot\mathbf{d}_{n+1} = \mathbf{f}_{n+1} - \mathbf{R}_{n+1} + \mathbf{F}_{n+1} + \left(\frac{4}{T^2}\cdot\mathbf{M} + \frac{2}{T}\cdot\mathbf{C}\right)\cdot\mathbf{d}_n + \left(\frac{4}{T}\cdot\mathbf{M} + \mathbf{C}\right)\cdot\mathbf{v}_n + \mathbf{M}\cdot\mathbf{a}_n$$

From the knowledge that implicit schemes of the Newmark family are typically only unconditionally stable when a predictor stiffness $\mathbf{K}_0$ is used and kept higher than or equal to the tangent stiffness of the system considered, the restoring force vector is split into two terms according to $\mathbf{R}_{n+1} = \mathbf{K}_0\cdot\mathbf{d}_{n+1} + \Delta\mathbf{R}_{n+1}$, leading to:

$$\mathbf{a}_{n+1} = \frac{4}{T^2}\cdot\left(\mathbf{d}_{n+1} - \mathbf{d}_n - T\cdot\mathbf{v}_n\right) - \mathbf{a}_n$$
$$\mathbf{v}_{n+1} = \frac{2}{T}\cdot\left(\mathbf{d}_{n+1} - \mathbf{d}_n\right) - \mathbf{v}_n$$
$$\left(\frac{4}{T^2}\cdot\mathbf{M} + \frac{2}{T}\cdot\mathbf{C} + \mathbf{K}_0\right)\cdot\mathbf{d}_{n+1} = \mathbf{f}_{n+1} - \Delta\mathbf{R}_{n+1} + \mathbf{F}_{n+1} + \left(\frac{4}{T^2}\cdot\mathbf{M} + \frac{2}{T}\cdot\mathbf{C}\right)\cdot\mathbf{d}_n + \left(\frac{4}{T}\cdot\mathbf{M} + \mathbf{C}\right)\cdot\mathbf{v}_n + \mathbf{M}\cdot\mathbf{a}_n \tag{6.14}$$

Equations (6.14) present the formulation of the constant average acceleration method applied to the non-linear RTS test proposed. Its implicit character means a direct solution cannot be obtained. Its implementation using a digital sub-step feedback algorithm is therefore presented as follows.

In the third equation of (6.14), the matrices within brackets are constant throughout the experiment. They can therefore be evaluated before the start of the test. The first one is inverted in anticipation of solving for the target displacement:

$$\mathbf{A} = \frac{4}{T^2}\cdot\mathbf{M} + \frac{2}{T}\cdot\mathbf{C}$$
$$\mathbf{B} = \frac{4}{T}\cdot\mathbf{M} + \mathbf{C} \tag{6.15}$$
$$\mathbf{D} = \left(\frac{4}{T^2}\cdot\mathbf{M} + \frac{2}{T}\cdot\mathbf{C} + \mathbf{K}_0\right)^{-1}$$

Let us now consider the particular main-step in which the target displacement vector $\mathbf{d}_{n+1}$ is to be computed. In the third equation of (6.14), the last four terms on the right hand side are explicitly known. Therefore, at each main-step, a vector $\mathbf{S}$ is formulated as follows from these terms:

$$\mathbf{S}_{n+1} = \mathbf{D}\cdot\left(\mathbf{F}_{n+1} + \mathbf{A}\cdot\mathbf{d}_n + \mathbf{B}\cdot\mathbf{v}_n + \mathbf{M}\cdot\mathbf{a}_n\right) \tag{6.16}$$

On the other hand, the two terms left out, namely $\mathbf{f}_{n+1}$ and $-\Delta\mathbf{R}_{n+1}$, are not explicitly known. The sub-step feedback algorithm proposes the following sub-step target displacement formulation to solve this problem:

$$\mathbf{d}_{n+1}^{k} = \mathbf{P}\left(\mathbf{S}_{n+1}, \mathbf{S}_{n}, \mathbf{S}_{n-1}, k\right) + \mathbf{D} \cdot \left(\mathbf{f}_{n+1}^{k-1} - \Delta\mathbf{R}_{n+1}^{k-1}\right) \tag{6.17}$$

where $k$ represents the sub-step index, varying from 1 to the number of sub-steps in each main-step, $p$, within the main-step indicated by the subscripts and where **P** is a second order polynomial interpolation operator. The second order was found to be the most adequate from simulation results, although a linear interpolation was originally proposed by Bayer *et al.* (2000).

The interface force and numerical substructure restoring force update terms used in (6.17) are considered with one sub-step delay. At main-step, for $k$=1, the initial values used are those retained from the end of the previous main-step: $\mathbf{f}_{n+1}^{0} = \mathbf{f}_{n}^{p}$ & $\mathbf{R}_{n+1}^{0} = \mathbf{R}_{n}^{p}$ .

At the end of a main-step, the quantity $\mathbf{D} \cdot \left(\mathbf{f}_{n+1}^{p-1} - \mathbf{f}_{n+1}^{p} - \Delta\mathbf{R}_{n+1}^{p-1} + \Delta\mathbf{R}_{n+1}^{p}\right)$ can be estimated and regarded as the remaining error due to the finite number of sub-steps. This error is subtracted from the final sub-step target displacement to produce the end of step displacement vector $\mathbf{d}^{eos}$ that will be used for the following main-step integration:

$$\mathbf{d}_{n+1}^{eos} = \mathbf{d}_{n+1}^{p} - \mathbf{D} \cdot \left(\mathbf{f}_{n+1}^{p-1} - \mathbf{f}_{n+1}^{p} - \Delta\mathbf{R}_{n+1}^{p-1} + \Delta\mathbf{R}_{n+1}^{p}\right) \tag{6.18}$$

The correction of the final sub-step error before a new main time integration step is computed limits the associated error amplification.

At this point, the index $n$ is incremented, and a new set of main-step calculations start. Note that the acceleration and velocity terms are explicitly expressed at the start of each main-step by using the known $\mathbf{d}_{n}^{eos}$ vector from the latest sub-step, which is also used for the calculation of the vector $\mathbf{S}_{n+1}$:

$$\begin{aligned}
\mathbf{a}_{n} &= \frac{4}{T^{2}} \cdot \left(\mathbf{d}_{n}^{eos} - \mathbf{d}_{n-1}^{eos} - T \cdot \mathbf{v}_{n-1}\right) - \mathbf{a}_{n-1} \\
\mathbf{v}_{n} &= \frac{2}{T} \cdot \left(\mathbf{d}_{n}^{eos} - \mathbf{d}_{n-1}^{eos}\right) - \mathbf{v}_{n-1} \\
\mathbf{S}_{n+1} &= \mathbf{D} \cdot \left(\mathbf{F}_{n+1} + \mathbf{A} \cdot \mathbf{d}_{n}^{eos} + \mathbf{B} \cdot \mathbf{v}_{n} + \mathbf{M} \cdot \mathbf{a}_{n}\right)
\end{aligned} \tag{6.19}$$

Equations (6.15), (6.17), (6.18) and (6.19) constitute the scheme used to implement, explicitly, the fundamentally implicit constant average acceleration method for the non-linear RTS experiment proposed. The general idea behind the digital sub-step feedback strategy is that the discretisation can be fine enough to produce a smooth route converging to the end-of-step solution without involving unnecessary unloading stages, to which a standard iterative technique would lead. An infinite number of sub-steps would indeed reproduce the exact CAAM results. This algorithm is in concept equivalent to the iterative scheme with reduction factor proposed by Shing *et al.* (1991) for PsD testing of non-linear systems, where the convergence is obtained by small incremental steps.

Note that the final sub-step error correction can be voluntarily tuned by a gain kept close to but not exactly equal to unity in order to stabilise the closed-loop RTS algorithm.

The above procedure fulfils the purpose of the sub-step signal generation task. However, the delay compensation is still necessary and, in this case, needs to be applied to the sub-step outputs. The standard third order polynomial extrapolation applied to four sub-step values, spaced by main-steps, including the latest one is easily implemented to carry out this necessary compensation. The amplitude compensation factor can also be implemented at this stage.

### 6.3.6- $\alpha$-Method with digital sub-step feedback

The Newmark implicit scheme can be applied to an $\alpha$-shifted equilibrium in order to introduce some numerical dissipation into the integration algorithm (Hilber *et al.* 1977). This modification produces the scheme generally known as the $\alpha$-method. The difference equation parameters are also defined as functions of $\alpha$ in order for the scheme to obtain remarkable properties:

$$\begin{aligned}
&\mathbf{d}_{n+1} = \mathbf{d}_n + T\cdot\mathbf{v}_n + \left(\tfrac{1}{2}-\beta\right)\cdot T^2\cdot\mathbf{a}_n + \beta\cdot T^2\cdot\mathbf{a}_{n+1}\\
&\mathbf{v}_{n+1} = \mathbf{v}_n + (1-\gamma)\cdot T\cdot\mathbf{a}_n + \gamma\cdot T\cdot\mathbf{a}_{n+1}\\
&\mathbf{M}\cdot\mathbf{a}_{n+1} + (1+\alpha)\cdot\mathbf{C}\cdot\mathbf{v}_{n+1} - \alpha\cdot\mathbf{C}\cdot\mathbf{v}_n + (1+\alpha)\cdot\mathbf{R}_{n+1} - \alpha\cdot\mathbf{R}_n =\\
&(1+\alpha)\cdot\mathbf{f}_{n+1} - \alpha\cdot\mathbf{f}_n + (1+\alpha)\cdot\mathbf{F}_{n+1} - \alpha\cdot\mathbf{F}_n\\
&\beta = \tfrac{1}{4}\cdot(1-\alpha)^2\\
&\gamma = \tfrac{1}{2}-\alpha
\end{aligned} \tag{6.20}$$

If -1/3≤$\alpha$<0, the scheme is unconditionally stable and possesses favourable numerical damping, increasing with the square of the frequency considered. If $\alpha$=0, the scheme reduces to the unconditionally stable CAAM possessing no numerical damping.

Conducting the same permutations as presented above for the CAAM, the scheme can be implemented using a digital sub-step feedback algorithm:

$$\begin{aligned}
&\mathbf{A} = \frac{1}{\beta\cdot T^2}\cdot\mathbf{M} + (1+\alpha)\cdot\frac{\gamma}{\beta\cdot T}\cdot\mathbf{C} + \alpha\cdot\mathbf{K}_0\\
&\mathbf{B} = \frac{1}{\beta\cdot T}\cdot\mathbf{M} + \left((1+\alpha)\cdot\frac{\gamma}{\beta}-1\right)\cdot\mathbf{C}\\
&\mathbf{D} = \left(\frac{1}{\beta\cdot T^2}\cdot\mathbf{M} + (1+\alpha)\cdot\frac{\gamma}{\beta\cdot T}\cdot\mathbf{C} + (1+\alpha)\cdot\mathbf{K}_0\right)^{-1}\\
&\mathbf{G} = \left(\frac{1}{2\cdot\beta}-1\right)\cdot\mathbf{M} + (1+\alpha)\cdot\left(\frac{\gamma}{2\cdot\beta}-1\right)\cdot T\cdot\mathbf{C}\\
&\mathbf{d}_{n+1}^{k} = \mathbf{P}(\mathbf{S}_{n+1},\mathbf{S}_n,\mathbf{S}_{n-1},k) + (1+\alpha)\cdot\mathbf{D}\cdot\left(\mathbf{f}_{n+1}^{k-1} - \Delta\mathbf{R}_{n+1}^{k-1}\right)\\
&\mathbf{d}_{n+1}^{eos} = \mathbf{d}_{n+1}^{p} - (1+\alpha)\cdot\mathbf{D}\cdot\left(\mathbf{f}_{n+1}^{p-1} - \mathbf{f}_{n+1}^{p} - \Delta\mathbf{R}_{n+1}^{p-1} + \Delta\mathbf{R}_{n+1}^{p}\right)\\
&\mathbf{a}_n = \frac{1}{\beta\cdot T^2}\cdot\left(\mathbf{d}_n^{eos} - \mathbf{d}_{n-1}^{eos} - T\cdot\mathbf{v}_{n-1}\right) - \left(\frac{1}{2\cdot\beta}-1\right)\cdot\mathbf{a}_{n-1}\\
&\mathbf{v}_n = \frac{\gamma}{\beta\cdot T}\cdot\left(\mathbf{d}_n^{eos} - \mathbf{d}_{n-1}^{eos}\right) - \left(\frac{\gamma}{\beta}-1\right)\cdot\mathbf{v}_{n-1} - \left(\frac{\gamma}{2\cdot\beta}-1\right)\cdot T\cdot\mathbf{a}_{n-1}\\
&\mathbf{S}_{n+1} = \mathbf{D}\cdot\left((1+\alpha)\cdot\mathbf{F}_{n+1} - \alpha\cdot\left(\mathbf{f}_n - \Delta\mathbf{R}_n + \mathbf{F}_n\right) + \mathbf{A}\cdot\mathbf{d}_n^{eos} + \mathbf{B}\cdot\mathbf{v}_n + \mathbf{G}\cdot\mathbf{a}_n\right)
\end{aligned} \tag{6.21}$$

Equations (6.21) allow an explicit implementation of the $\alpha$-method to an RTS simulation containing a non-linear numerical substructure. In these equations, the choice of the parameter

$\alpha$ between -1/3 and 0 governs the amount of dissipation introduced numerically. For instance, $\alpha$=-0.1 implies $\beta$=0.3025, $\gamma$=0.6, and provides just over 4% numerical damping for oscillations with a period equal to twice the value of the time step used (Hilber *et al.* 1977). Regardless of the value chosen, the scheme developed possesses second order accuracy, unconditional stability and small amounts of frequency distortion in the form of period elongation.

## 6.4- IMPLEMENTATION OF NON-LINEAR FORCE-DEFLECTION IN THE NUMERICAL SUBSTRUCTURE

In this section, the non-linear character of the force-displacement relationship used in the following experiments is described. This is essentially a bi-linear characteristic with hysteresis, as shown in Figure 6.3(a). This type of behaviour is typical of ductile structural engineering members, and the hysteresis description is particularly important in earthquake engineering and structural dynamics as it introduces substantial energy dissipation potential. It is important that all numerical schemes tested for real-time hybrid simulations can accommodate such non-linear characteristics.

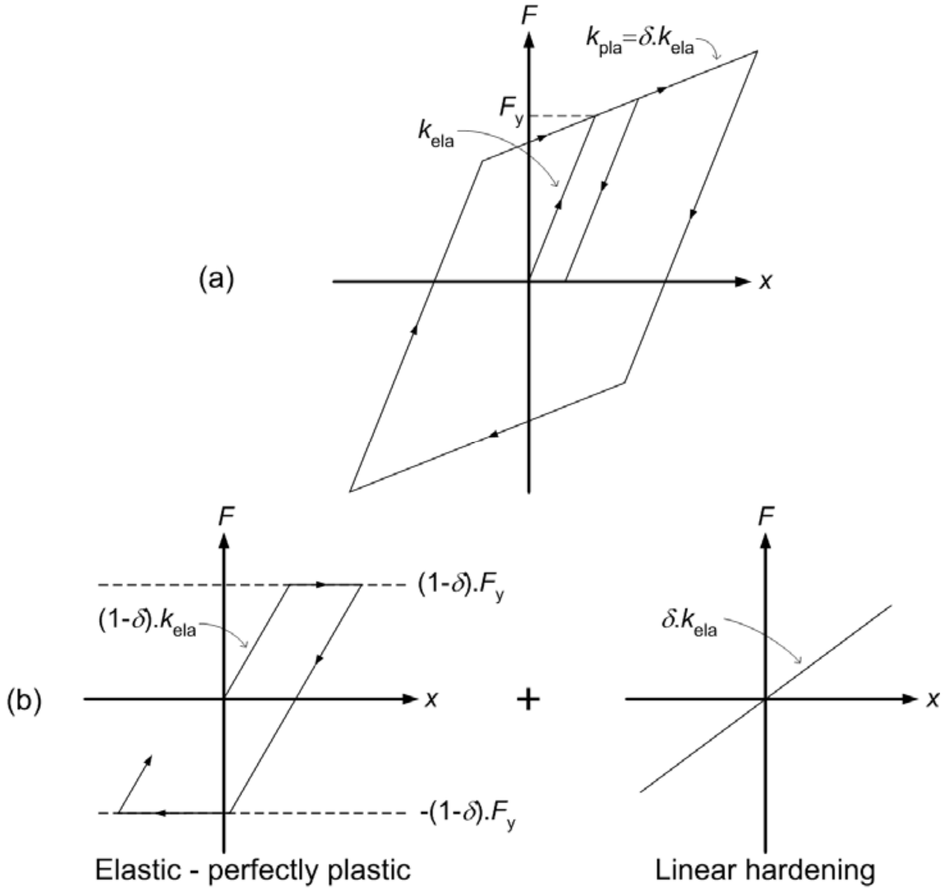


Figure 6.3: Non-linear force-deflection implementation – (a) characteristic model, (b) implementation as summation of two simpler models

This "elastic-plastic-hysteresis" model is based on two linear equations. The first one, representing elasticity, is only defined by the slope $k_{ela}$. Any point on an elastic part of the model can be obtained from the slope, the previous point values and the deflection from the previous point. The intercepts of all elastic lines are not the same but depend on the starting point of the line. This also results in the definition of residual deflection under no load. The second linear equation represents the plasticity law and is defined by the slope $k_{pla}$ and the initial yielding point. In the case considered, symmetry between tension and compression is assumed, so the two resulting plastic laws have exactly opposite intercept values. The plastic stiffness is typically smaller than the elastic stiffness, and a strain hardening ratio is defined as $\delta = k_{pla} / k_{ela}$. The model is fully defined by the values of $k_{ela}$, $F_y$ and $\delta$.

To obtain better computational efficiency, this model can be programmed as the summation of an "elastic-perfectly plastic" model and a supplementary elastic hardening model, as defined by Figure 6.3(b). The perfectly plastic laws are implemented as dynamic saturation curves. When the saturation limit stops being a constraint, travel along the elastic law resumes at the point considered. The hysteresis is therefore automatically created by crossing the X axis at points with various residual displacement values. In Simulink, the model obtained is shown in Figure 6.4. For MDOF systems, this model can accept as its input a vector of deflections that are individually treated to return a vector of restoring forces. The extreme simplicity of the model obtained is of course a great advantage for the real-time applications considered.

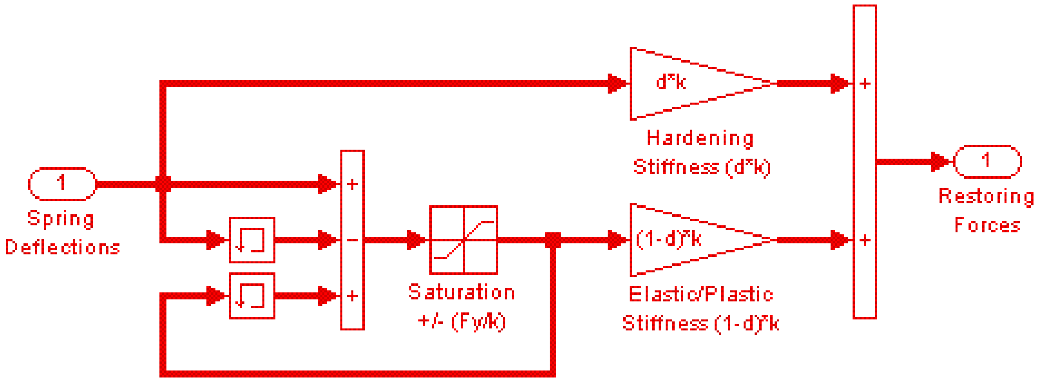


Figure 6.4: Implementation in Simulink of the bi-linear hysteretic spring

The model described here is easy to use with all the schemes presented in details in the previous section, since they are either fully explicit or based on the implementation of an explicit term. In the case of the implicit schemes, the error produced between the explicit term and the exact implicit value obviously also leads to a restoring force error.

## 6.5- COMPUTATIONAL VERIFICATION & INITIAL HYBRID EXPERIMENTS

The six schemes presented in detail in the above sections were implemented in real-time code. All possible computations were conducted prior to the start of the actual experiment in order to keep as much computational power for the real-time process as possible. A series of verification experiments was then carried out to check the implementation and build up the modelling complexity.

The first verification was conducted through a purely computational simulation based on a non-existent physical substructure (i.e. the physical substructure force feedback equals 0 throughout) and a linear SDOF numerical substructure. This simulation was executed in Matlab® and not in real-time. The main-step stability conditions were checked at this stage and found to be as expected: the first method is conditionally stable while the other five are unconditionally stable.

A further computational simulation was conducted in real-time for each scheme where the force feedback was artificially produced from the actuator command, an estimate of the actuator delay and the SDOF physical substructure response (produced from a transfer function model). The integrity of the response was checked, as well as its apparent matching with that of a standard computational simulation of the emulated system.

In the next step, a hybrid real-time simulation was conducted with the same linear SDOF numerical substructure and a SDOF experimental substructure. In this experiment, the physical substructure had no direct contact with the outside excitation of the emulated system (e.g. earthquake motion). The numerical substructure received the external excitation and transmitted it to the physical specimen. This experiment therefore required the use of only one actuator.

This situation was then reversed in the following stage, where a hybrid real-time simulation was conducted with the physical substructure receiving the external excitation directly and the numerical substructure being excited by the interface force feedback only. Note that this simulation type required two actuators for a single-axis RTS simulation: one for the known external excitation and one for the boundary condition interface.

Finally, the numerical substructure system was rendered non-linear using the element described in section 6.4. To this end, an additional degree of freedom was included in the numerical substructure, finally consisting of two masses and a non-linear spring between them, as well as a damper element. The physical substructure consisted of one mass between two spring-damper units. The resulting emulated structure was therefore a 3DOF system in series attached to the moving base through spring-damper units, with the spring element between the top two masses possessing a non-linear characteristic. The main-step value ($T$=5ms) was well inside the stability limit of the Newmark explicit scheme.

For fairer comparison of the numerical schemes, the actuator delay compensation necessary for stability of the RTS tests presented here is executed with a standard third order exact polynomial extrapolation scheme. Also, unless otherwise stated, the delay estimate is kept constant throughout the tests.

All the schemes studied allow successful real-time hybrid simulations to be conducted with this system and all produce very similar structural response. Their general suitability for the RTS method with a non-linear numerical substructure and delay compensation was therefore proved at this stage.

An important point of the work described in this chapter is to look at increasing the number of degrees of freedom present in the numerical substructure and to compare the relative abilities of the proposed schemes. Increasing the integration time step is also an important issue investigated later in this chapter.

## 6.6- EVALUATION TEST WITH 10 DOF NUMERICAL SUBSTRUCTURE

In the first instance, the number of degrees of freedom of the numerical substructure is increased to ten. Nine non-linear spring elements link the lumped masses in series. Strain hardening ratios of $\delta$=0.5 were used to simulate that parts of the structural elements would be yielding. The physical substructure remains the same as before and simulates the base of the emulated structure. A schematic of the emulated system is shown in Figure 6.5 and its structural properties are presented in Table 6.2. The physical substructure parameters are estimates obtained from bespoke identification experiments. For instance, the absolute damping terms offer a good linear approximation of the friction in the bearings guiding the masses in their linear motion.

The external input is a constant 3mm amplitude sinusoidal wave sweeping in frequency from 0 to 10Hz, exciting the physical substructure end of the system via an actuator as shown in Figure 6.5. A second actuator, not shown on Figure 6.5, is placed at the substructure interface and controlled in real-time during the experiment.

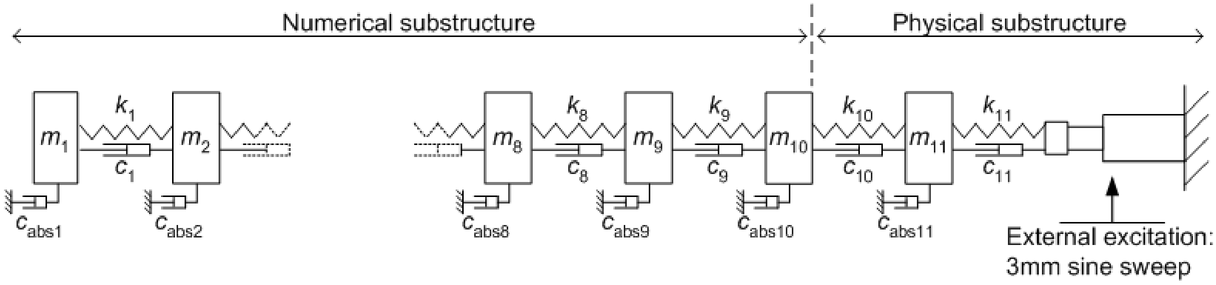


Figure 6.5: Schematic of the emulated system tested in the 10DOF simulations

| DOF index (-) | 1 | 2 | 3 | 4 | 5 | 6 | 7 | 8 | 9 | 10 | 11 |
|---|---|---|---|---|---|---|---|---|---|---|---|
| Mass $m$ (kg) | 150 | 150 | 150 | 150 | 150 | 150 | 150 | 150 | 150 | 150 | 151 |
| Absolute damping $c_{abs}$ (N.s/m) | 180 | 180 | 180 | 180 | 180 | 180 | 180 | 180 | 180 | 180 | 180 |
| Relative damping $c$ (N.s/m) | 10 | 10 | 10 | 10 | 10 | 10 | 10 | 10 | 10 | 10 | 10 |
| Spring stiffness $k$ (N/mm) | 250 | 250 | 250 | 250 | 250 | 250 | 250 | 250 | 250 | 290 | 317 |
| Spring yield load $F_y$ (kN) | 2 | 2 | 2 | 2 | 2 | 2 | 2 | 2 | 2 | - | - |
| Spring strain hardening raito $\delta$ (-) | 0.5 | 0.5 | 0.5 | 0.5 | 0.5 | 0.5 | 0.5 | 0.5 | 0.5 | - | - |
| Natural frequencies of linear system (Hz) | 0.9 | 2.7 | 4.4 | 6.1 | 7.6 | 9.0 | 10.2 | 11.3 | 12.1 | 12.7 | 13.0 |
| Modal damping ratios (%) | 10.5 | 3.6 | 2.2 | 1.7 | 1.4 | 1.2 | 1.1 | 1.0 | 0.9 | 0.9 | 0.9 |

Table 6.2: Structural properties of the emulated system for the 10DOF tests

All six numerical schemes are tested with integration time steps of $T$=5ms. The response time history of the numerical substructure interface point (i.e. the displacement of $m_{10}$ as shown on Figure 6.5) is shown in Figure 6.6 for each scheme, plotted against the results of a full computational simulation of the systems' vibrations. This computational simulation result, regarded here as a reference, was produced using the Newmark explicit scheme with an integration time step of 1ms. It is represented by the red line in each graph of Figure 6.6. For clarity reasons, offsets have been introduced to shift the response plots in different parts of the plotting window, and a close-up view is provided on the right-hand side. Figure 6.7 shows the numerical substructure response in the frequency domain. Again, the simulation is plotted as a red line and absolute offsets have been introduced for clarity.

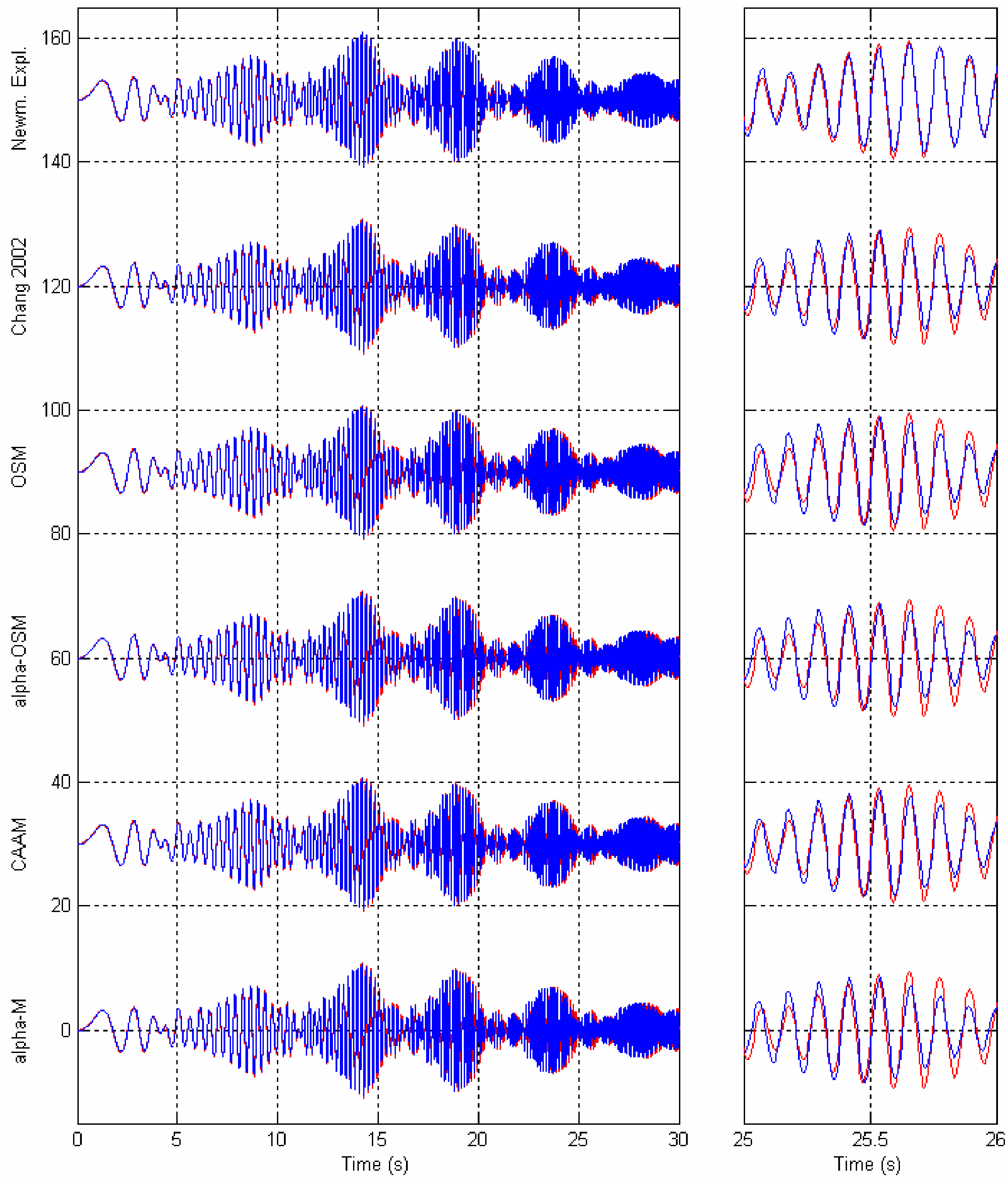


Figure 6.6: Time history plots of numerical substructure interface response (mm) of the real-time experiments for each integration scheme (blue) against computational simulation result (red) – offsets have been introduced for clarity

The results presented for the $\alpha$-OSM and $\alpha$-M were obtained with $\alpha$ values of -0.1 and -0.3 respectively. The effect of $\alpha$ relative to the results from the OSM and CAAM on numerical dissipation and frequency distortion can just be seen in both the time and the frequency domains.

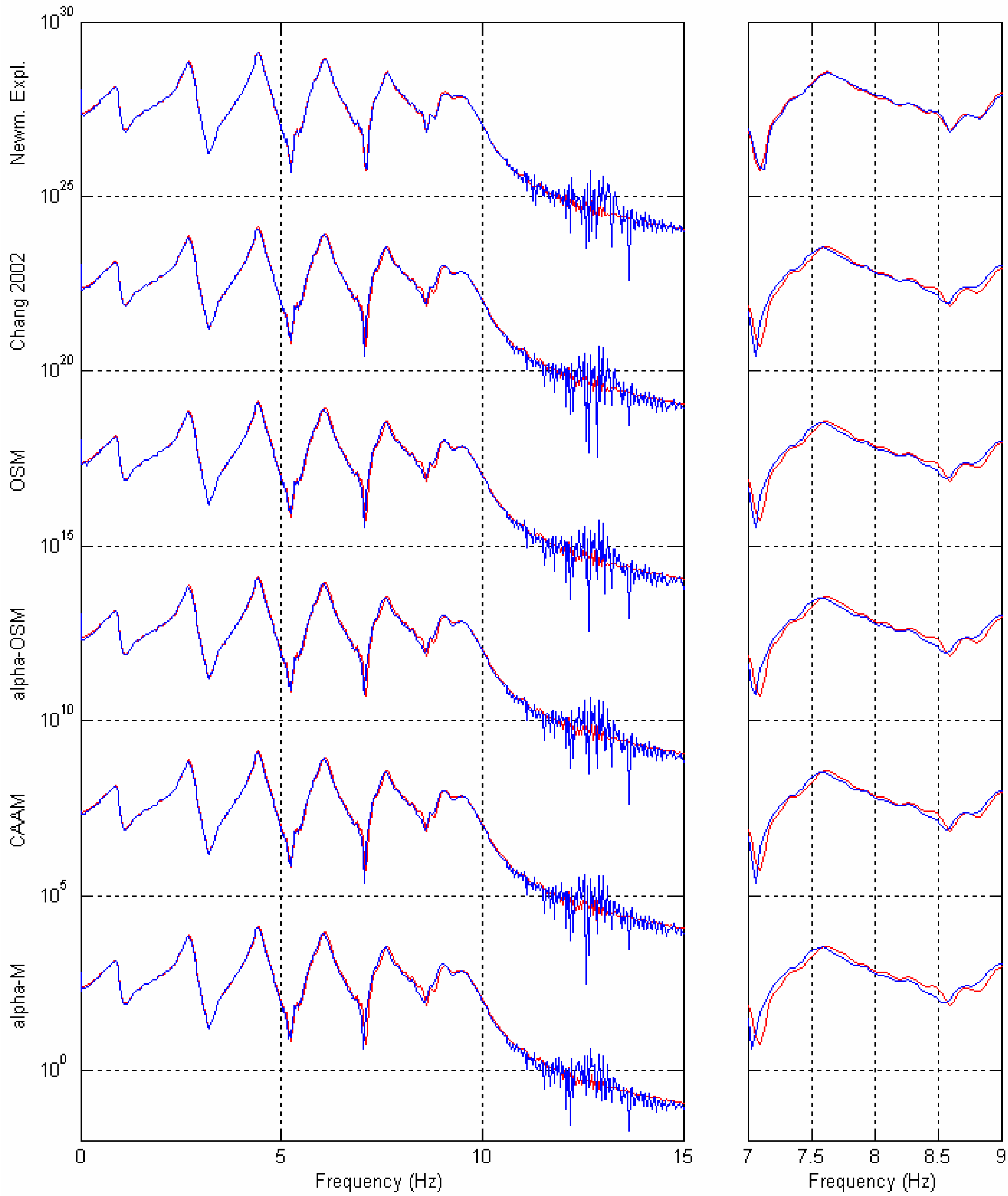


Figure 6.7: Frequency domain plots of numerical substructure interface response for each integration scheme (blue) against computational simulation result (red) for the 10DOF test – offsets have been introduced for clarity

It is clear from Figures 6.6 and 6.7 that all methods produce broadly similar results. The level of matching with the computational solution is also very good. This is a particularly useful result, indicating that the noise and experimental errors are well repeatable and therefore quite likely limited to small amounts.

Also, the analytical results obtained previously by other researchers regarding the accuracy of the schemes – and summarised in Table 6.1 – appear to be confirmed by these experiments. The most accurate solution – if one considers the computational simulation output as an exact trace – is that obtained from the Newmark explicit experiment. With the

5ms step used – for a stability limit of 24ms for the 10DOF numerical system tested – the Newmark explicit scheme is that producing the smallest frequency distortion, while also featuring no numerical dissipation. It can also be checked that it is the only scheme producing a period shrinkage while all others tend to elongate periods, as shown on the close-up in Figure 6.7.

From the frequency plots more specifically, it can be seen that the first six modal frequencies of the complete system are excited in the experiment in the range 0-10Hz. In the 12-13Hz area, which contains the highest three modes of vibration, it can be seen that all methods produce increased higher mode amplification over the exact solution. This erroneous response in the high modes is the result of experimental errors, measurement noise and numerical inaccuracies (Shing & Mahin 1987*a*). In these experiments, the higher mode amplification observed is fairly low and apparently well controlled by the structural damping. In the PsD applications, the presence of numerical damping has been stated as a major tool to reduce the high-mode amplification significantly. However, for this experiment, judging by the results from the $\alpha$-OSM and $\alpha$-M, with respectively $\alpha$=-0.1 and $\alpha$=-0.3, the amplification obtained is not significantly reduced, mostly because the integration time step is kept to a low value. More on this will be shown with the next experiment.

Putting accuracy results aside, the relative computational efficiency of the numerical schemes is now considered, as measured by the hardware CPU time needed for the DSP board to compute each task. The results are presented in Table 6.3. Note that the CPU time necessary at each main-step is always superior to that for the sub-step, as each main-step task includes a sub-step task within it. The times are obtained for the implementation using Simulink® block programming and bespoke compilation for the DSP hardware.

| | Computational time (μs) | |
|---|---|---|
| | sub-step | main-step |
| Newmark Explicit | 35 | 72 |
| Newmark - Chang 2002 | 36 | 83 |
| OSM | 38 | 99 |
| $\alpha$-OSM | 40 | 100 |
| CAAM | 91 | 146 |
| $\alpha$-M | 96 | 160 |

Table 6.3: Computational time for executing the 10DOF real-time code

It is worth noting here that all the CPU times are smaller than the sub-step value used (0.2ms). This means that in this experiment, all tasks can have their execution completed without requiring any extrapolation of the sub-step actuator command.

As could have been expected from their implementation details, the schemes are tested in an order of increasing computational cost. The increase is relatively more important for the sub-step task as it is for the main-step task, especially for the two schemes that use the digital sub-step mechanism. This is not a good result, since the sub-step task has a harsher real-time constraint (0.2ms) and is repeated many times during each main-step. This is discussed further in the following section.

## 6.7- LIMITATIONS IN NUMBER OF DEGREES OF FREEDOM

For the real-time computational constraint, three potential limiting factors exist:

1) If the sub-step task needs more CPU time than available, the sub-step task has to be optimised and/or downgraded and/or the sub-step increased.
2) If the main-step task needs more CPU time than available, the main-step task has to be optimised and/or downgraded and/or the main-step increased.
3) If the sub-step task requires a large part of the sub-step, little CPU time is left for the main-step task so a better compromise between the two tasks is needed.

In the third case, one has to bear in mind that a reduction of the sub-step task will pay off better than the same reduction in the main-step task, since the sub-step task is repeated many times within each main-step.

Following the results presented in Table 6.3, some real-time implementation tests were carried out with the various methods with an increasing number of degrees of freedom in the numerical substructure – starting with just 2 and increasing to 5, 10, 15, 20, 30, 40 and finally 50. The time steps for these experiments were also $t$=0.2ms and $T$=5ms. This was a purely computational hardware exercise, in which the physical substructure feedback was set to zero throughout. The CPU times required on the DSP board for each task are presented in Table 6.4 and graphically in Figure 6.8.

| | Number of DOFs in numerical substructure | | | | | | | |
|---|---|---|---|---|---|---|---|---|
| | 2 | 5 | 10 | 15 | 20 | 30 | 40 | 50 |
| **Newmark Explicit** | | | | | | | | |
| CPU time for sub-step task | 35 | 36 | 35 | 37 | 35 | 36 | 34 | 35 |
| CPU time for main-step task | 56 | 64 | 72 | 94 | 133 | 316 | 507 | 713 |
| Number of extrapolated sub-steps | 0 | 0 | 0 | 0 | 0 | 1 | 2 | 3 |
| **Newmark - Chang 2002** | | | | | | | | |
| CPU time for sub-step task | 34 | 34 | 36 | 38 | 37 | 38 | 38 | 37 |
| CPU time for main-step task | 57 | 65 | 83 | 139 | 283 | 498 | 867 | 1247 |
| Number of extrapolated sub-steps | 0 | 0 | 0 | 0 | 1 | 2 | 4 | 6 |
| **OSM** | | | | | | | | |
| CPU time for sub-step task | 40 | 38 | 38 | 38 | 37 | 39 | 39 | 39 |
| CPU time for main-step task | 61 | 74 | 99 | 173 | 328 | 646 | 1059 | 1523 |
| Number of extrapolated sub-steps | 0 | 0 | 0 | 0 | 1 | 3 | 5 | 7 |
| **$\alpha$-OSM** | | | | | | | | |
| CPU time for sub-step task | 39 | 41 | 40 | 39 | 37 | 39 | 37 | 36 |
| CPU time for main-step task | 65 | 77 | 100 | 183 | 334 | 659 | 1066 | 1518 |
| Number of extrapolated sub-steps | 0 | 0 | 0 | 0 | 1 | 3 | 5 | 7 |
| **CAAM** | | | | | | | | |
| CPU time for sub-step task | 66 | 76 | 91 | 121 | N/A | N/A | N/A | N/A |
| CPU time for main-step task | 79 | 101 | 146 | 537 | task | task | task | task |
| Number of extrapolated sub-steps | 0 | 0 | 0 | 2 | overrun | overrun | overrun | overrun |
| **$\alpha$-M** | | | | | | | | |
| CPU time for sub-step task | 69 | 77 | 96 | 124 | N/A | N/A | N/A | N/A |
| CPU time for main-step task | 83 | 106 | 160 | 557 | task | task | task | task |
| Number of extrapolated sub-steps | 0 | 0 | 0 | 2 | overrun | overrun | overrun | overrun |

Table 6.4: Computational times (μs) and number of necessary extrapolated sub-steps for various sizes of the numerical substructure

The relative computational cost of the digital sub-step feedback algorithm, used for both the CAAM and $\alpha$-M, mentioned in the previous section is here more obvious. Although the sub-step task of the first four schemes always requires around 40μs regardless of the number of degrees of freedom, the sub-step task of the two schemes using the digital sub-step feedback algorithm requires substantially more time, and, more importantly, this time grows with an increasing number of degrees of freedom. For a 20DOF numerical structure, the sub-step task would require more than 0.2ms to complete and the code can therefore not be executed in real-time (this situation is called an over-run). With the sub-step chosen and with the hardware used, the digital sub-step feedback algorithm is computationally too demanding to compute twenty DOFs.

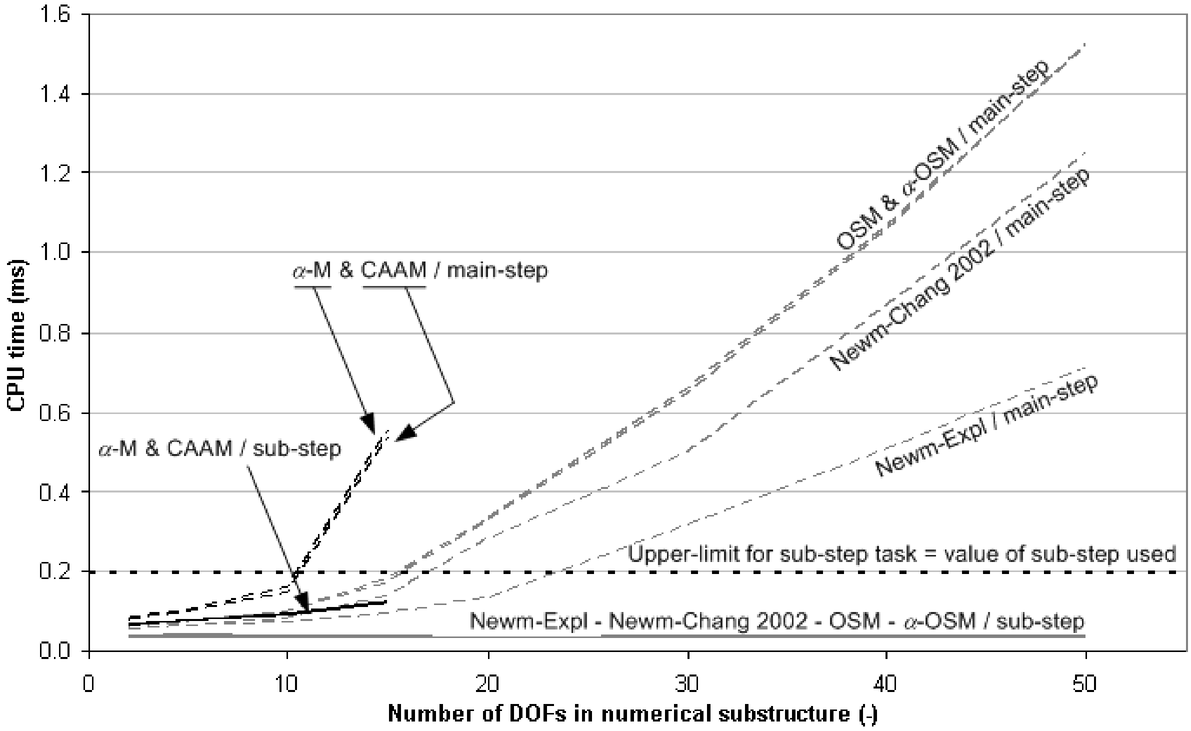


Figure 6.8: Graphical view of CPU times for various sizes of the numerical substructure

In the digital sub-step feedback algorithm, the vector and matrix calculations required at each sub-step are too important and the computational demand grows too quickly with the number of DOFs. This problem is obviously not related to the numerical formulation of the CAAM or $\alpha$-M themselves, but rather to their fully implicit nature which led to the implementation using the sub-step feedback strategy. Due to high computational demand, the CAAM and the $\alpha$-M cannot be used in the following section with a 50DOF numerical substructure.

## 6.8- REAL-TIME HYBRID EXPERIMENT WITH 50DOF NUMERICAL SUBSTRUCTURE

### 6.8.1- RTS simulations with small time integration step

Using the same experimental format as for the 10DOF simulations, the size of the numerical problem is increased and the remaining four methods are tested. The structure is the same as that presented in Figure 6.5 except that the number of DOFs in the numerical substructure is increased to 50. The mass $m_1$ at the top of the structure is set to 10kg instead of 150kg for all other masses. This ensures the highest natural frequency of the 50DOF numerical substructure to increase from 13Hz to 26Hz, imposing a much more drastic constraint on the numerical stability of the integration schemes – from 24ms to 12ms (assuming linear structural behaviour). However, because of the non-linearity in the model, the stability limit increases. From pure simulations, it is found to be close to 17ms. Table 6.5 gives the first ten natural frequencies of the full system tested, obtained computationally assuming linear structural behaviour.

| DOF index (-) | 1 | 2 | 3 | 4 | 5 | 6 | 7 | 8 | 9 | 10 |
|---|---|---|---|---|---|---|---|---|---|---|
| Natural frequencies of linear system (Hz) | 0.2 | 0.6 | 1.0 | 1.4 | 1.8 | 2.2 | 2.6 | 3.0 | 3.4 | 3.8 |

Table 6.5: First 10 modes for the 50DOF tests

The models are solved with the same integration time step of $T$=5ms with the Newmark explicit, Newmark-Chang 2002, OSM and $\alpha$-OSM schemes. These experiments check that the higher computational demand is handled properly by the real-time software and that the extrapolation/interpolation routine implemented with the multi-tasking strategy works effectively, as described at the start of this chapter.

Note that the experiments presented in this section use a different delay compensation algorithm. The reason for this change is detailed in the next section regarding higher time-steps. Comparisons between the results obtained with the different schemes are of course still legitimate.

Figures 6.9 and 6.10 present the response at the substructure interface in the time and frequency domains respectively. All the modes above 15Hz do not participate significantly to the response and are not included on Figure 6.10 for clarity.

In Figure 6.9, all four responses obtained are very similar, with again the Newmark explicit scheme producing the most accurate solution when a small integration time step can be employed.

The accuracy of the schemes is generally confirmed in the frequency domain too. Note that the natural frequencies indicated in Table 6.5 match with the high content peaks seen on Figure 6.10. Finally, none of the experiments is subject to erroneous higher mode response.

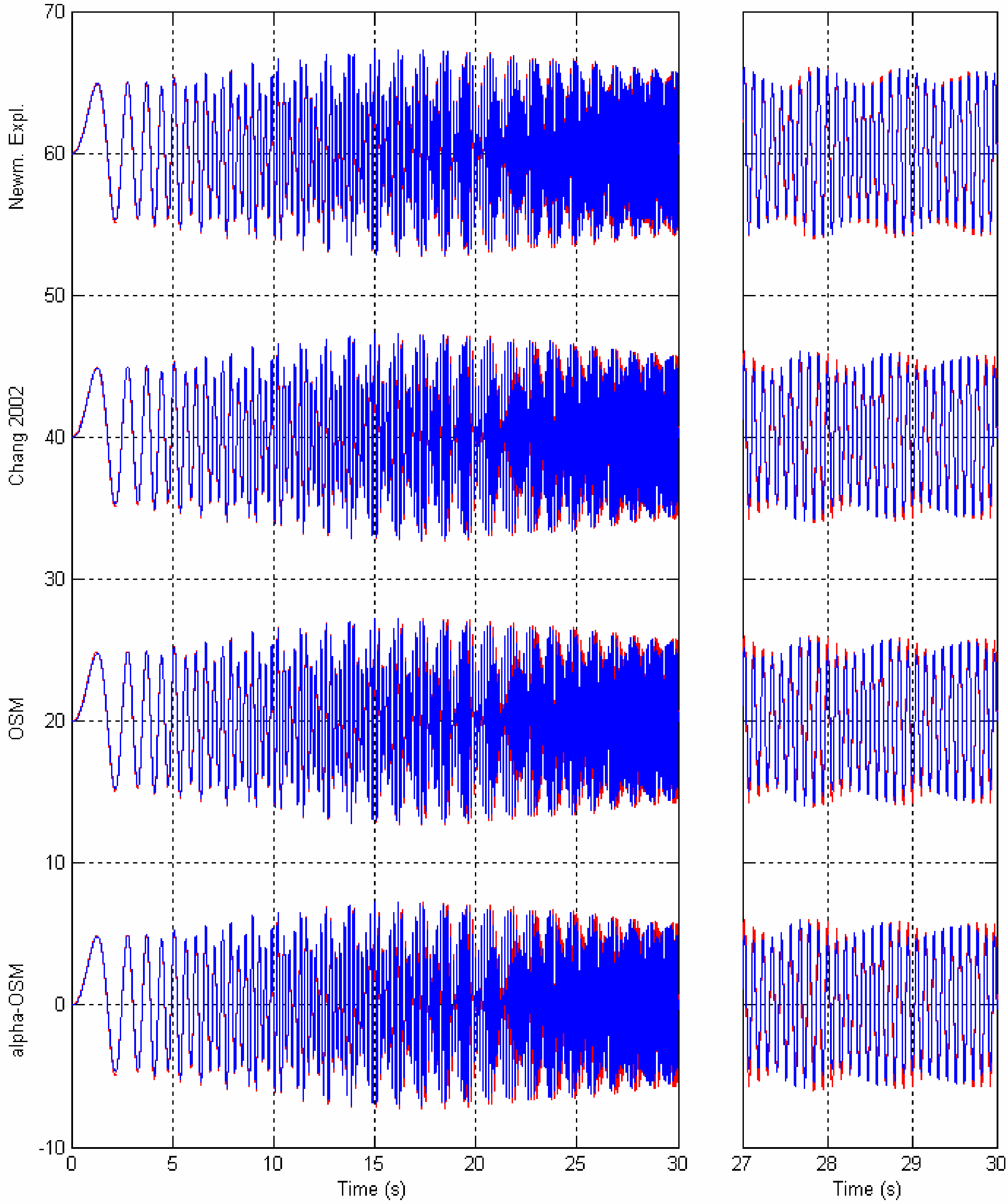


Figure 6.9: Time history plots of numerical substructure interface response (mm) for each integration scheme (blue) against computational simulation result (red) for the 50DOF test with 5ms time steps – offsets have been introduced for clarity

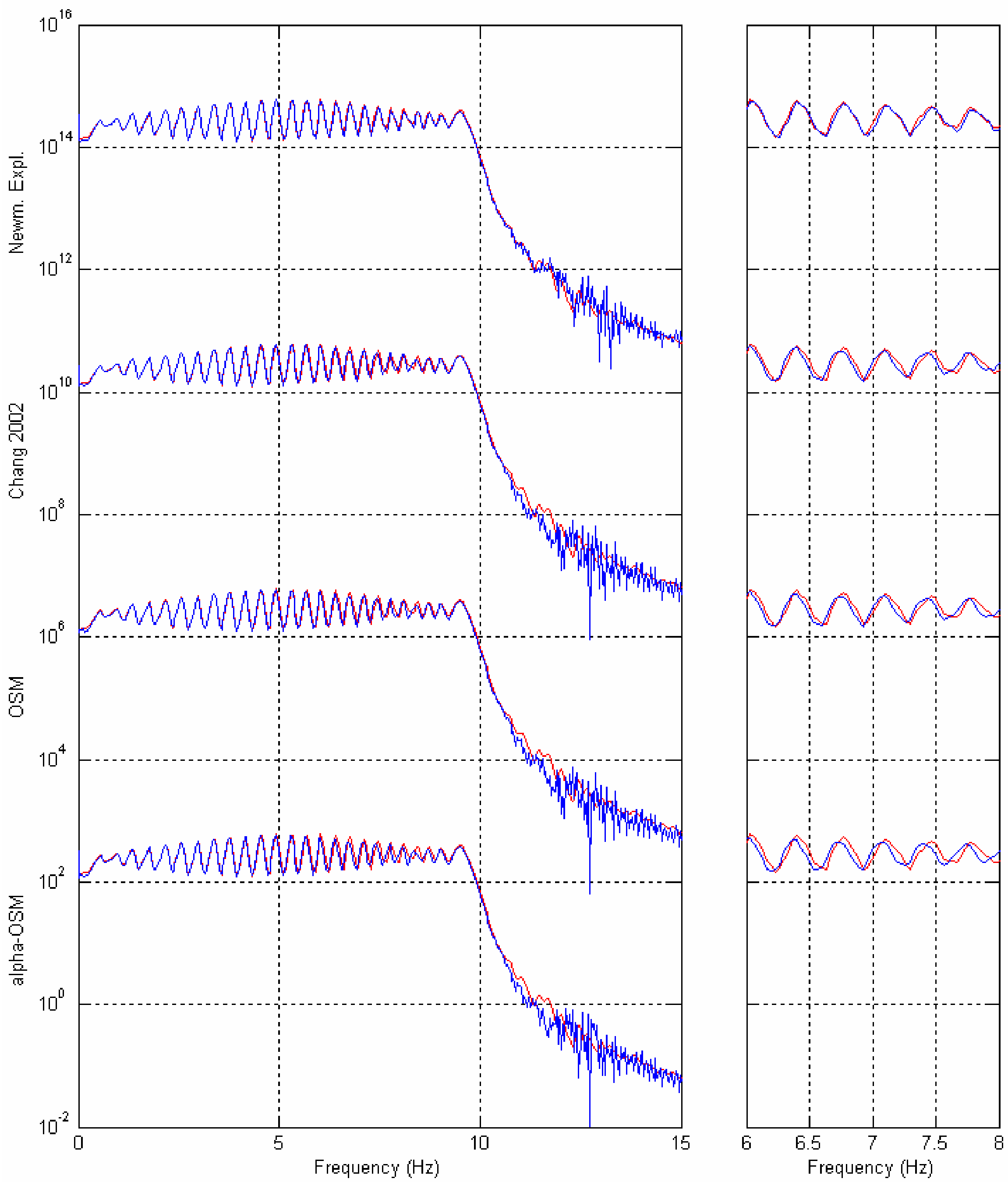


Figure 6.10: Frequency domain plots of numerical substructure interface response for each integration scheme (blue) against computational simulation result (red) for the 50DOF test with 5ms time steps – offsets have been introduced for clarity

## 6.8.2- RTS simulations with higher time integration step

It is now interesting to increase the integration time step and more specifically to prove the stability advantage of the Newmark-Chang 2002, OSM and $\alpha$-OSM schemes over the Newmark explicit method.

However, for higher time steps, the delay compensation algorithm employed so far shows limits. Typically, for the standard 3rd order polynomial extrapolation technique, this meant that the delay value used is not applied accurately when the time-step becomes significantly larger than the compensation time applied (problems were observed with time-steps greater than about four times the amount of forward prediction applied). This issue was slightly improved by introducing the modified Darby adaptive delay update algorithm (see previous chapter for details on this adaptive method). However, when increasing the numerical time-step to larger values, problems also arise due to the extrapolation polynomial not providing as smooth a signal as necessary because it is based on points further apart from each other. This then leads to a less consistent actuator performance which aggravates the problem and can affect the stability of the experimental simulation.

To address this problem, using the extrapolation algorithm proposed by Horiuchi & Konno (2001) is not advised as the numerical schemes tested here do not provide the displacement, velocity and acceleration information necessary at the current step. So the prediction scheme would need to be based on the previous step values which would only provide approximate data.

The Laguerre scheme, however, is a good candidate to address this issue. Because it is based on the interpolated sub-step values, it is not directly affected by an increase in numerical time-step (see previous chapter for details of the Laguerre prediction scheme). Moreover, it possesses some filtering properties, capable of smoothing out unwanted oscillations. As a consequence, the delay compensation algorithm used for the 50DOF experiments presented in this section is based on the modified Darby update scheme and the Laguerre forward predictor.

The numerical integration time-steps can be successfully increased to $T$=25ms for the Newmark-Chang 2002, OSM and $\alpha$-OSM schemes, therefore proving their unconditional stability in a MDOF RTS simulation. However, it is confirmed that the original explicit scheme from Newmark cannot be used with a main-step of 25ms, or even 20ms. An experiment with $T$=15ms, though, is successful. Figures 6.11 and 6.12 present the response results obtained in these RTS tests.

For a 25ms numerical step, the OSM and $\alpha$-OSM induce smaller participation of the higher modes than for the Newmark-Chang 2002 algorithm. This is of course particularly visible for the $\alpha$-OSM because of the extra numerical damping ($\alpha$=-1/3). It can be seen that even the modes in the 5-10Hz range are significantly reduced although they are actually part of the experiment. This can be observed in both the time and frequency domains. However, these higher modes do not typically participate in most structural dynamics and earthquake engineering applications, so their participation reduction is likely to not affect the response to real-life loading conditions.

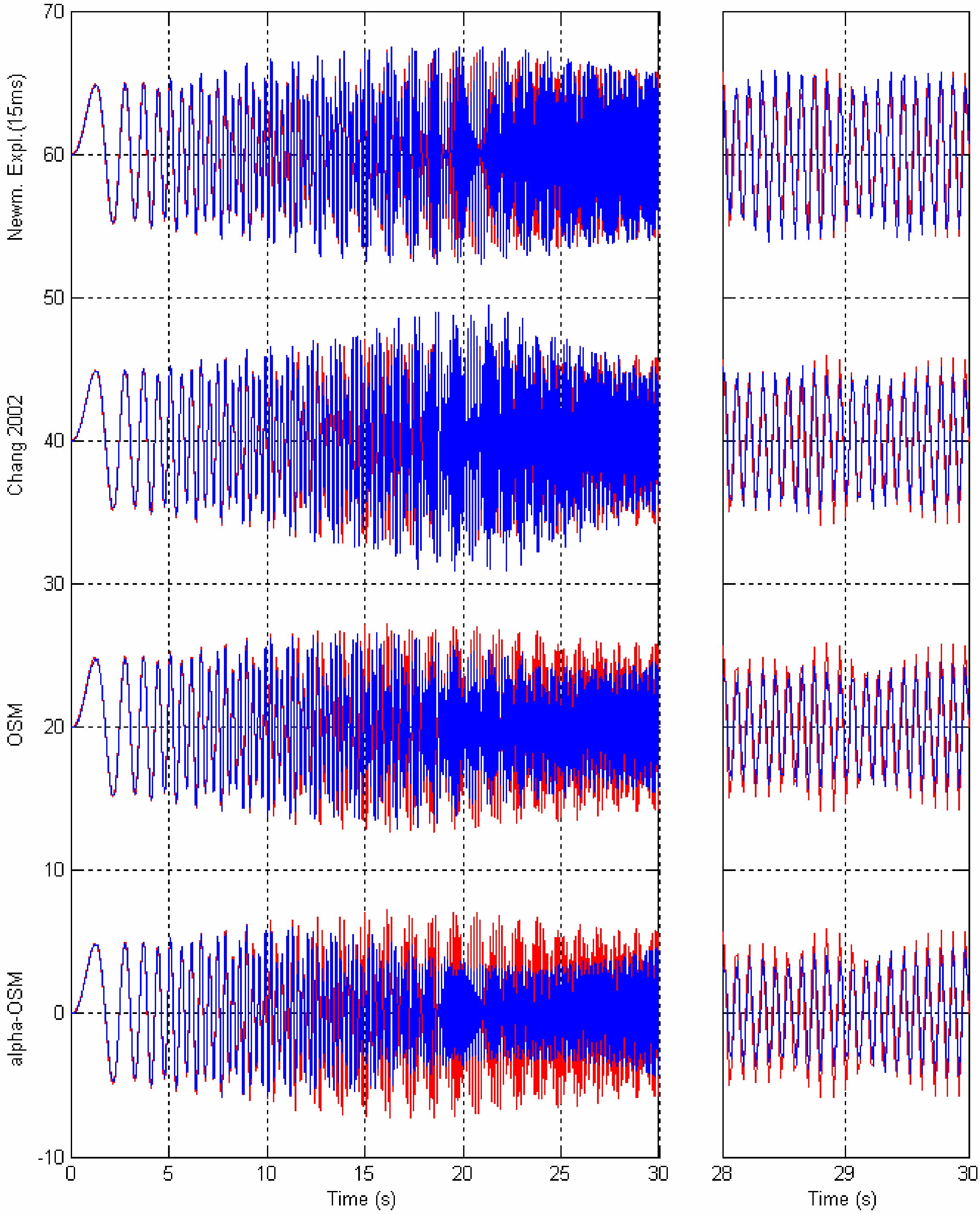


Figure 6.11: Time history plots of numerical substructure interface response (mm) for each integration scheme (blue) against computational simulation result (red) for the 50DOF test with 25ms time steps (except 15ms for Newmark explicit) – offsets have been introduced for clarity

Comparing the Newmark-Chang 2002 to the OSM, Figure 6.12 shows that the OSM does not significantly modify the amplification up to around 5Hz. At this frequency however, the method developed by Chang is seen to slightly amplify the response.

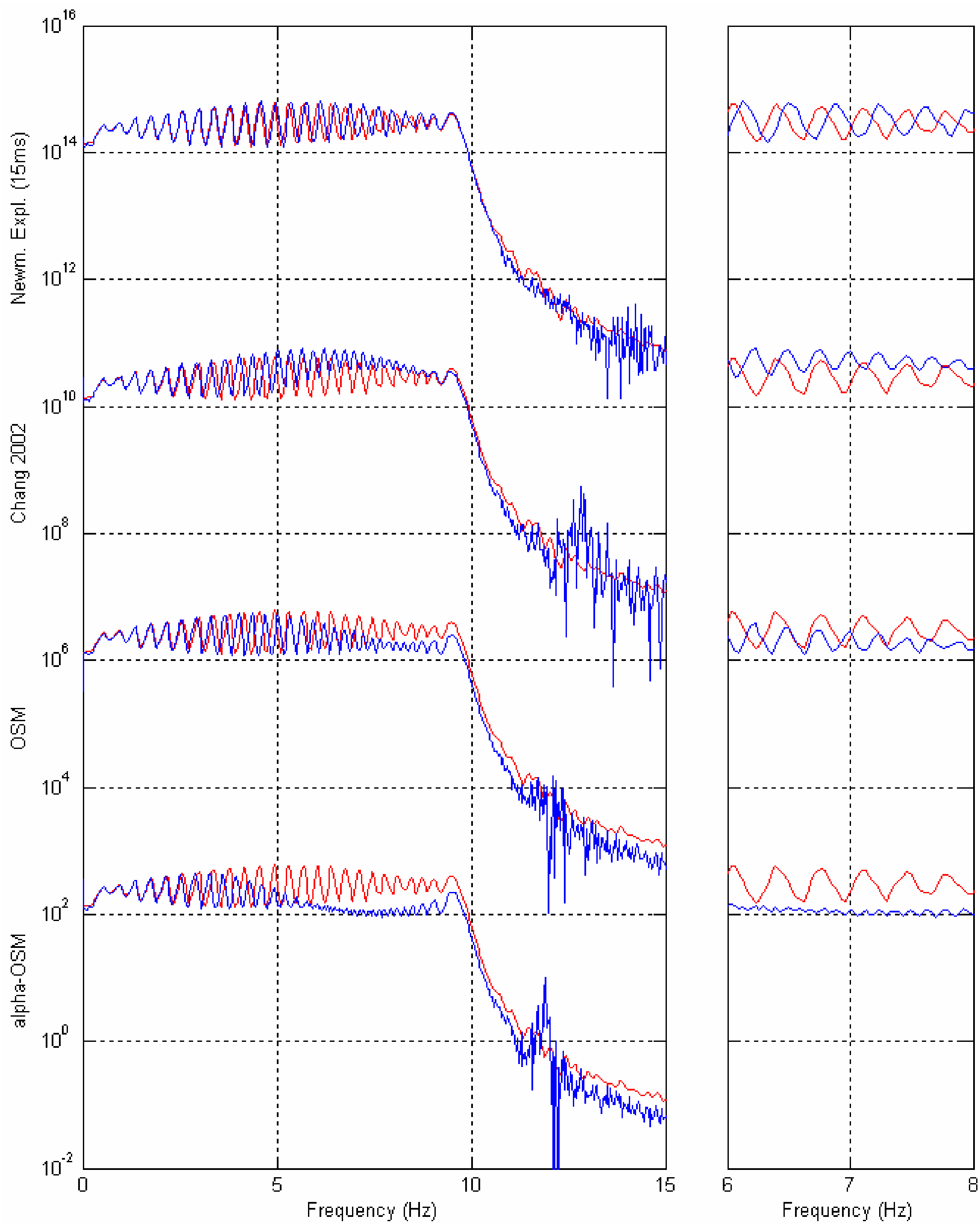


Figure 6.12: Frequency domain plots of numerical substructure interface response for each integration scheme (blue) against computational simulation result (red) for the 50DOF test with 25ms time steps (except 15ms for Newmark explicit) – offsets have been introduced for clarity

Looking now at the output of the Newmark explicit method, it can be seen that both the frequency distortion and the amplification are smaller. Remember however that this scheme could only be used for a main-step of 15ms at the most, explaining partly the accuracy observed.

In terms of the real-time control of the actuator, the results can be summarised by the mean relative command error value, as defined in the previous chapter. This number is presented in Table 6.6 for each scheme. Table 6.6 also presents statistical results on the zero-crossing synchronisation delay – between the desired actuator output and the actual one – in terms of its mean and standard deviation values across the whole RTS tests.

| | Newmark Explicit | | | Newmark - Chang 2002 | | | | |
|---|---|---|---|---|---|---|---|---|
| Main-step used (ms) | 5 | 10 | 15 | 5 | 10 | 15 | 20 | 25 |
| Relative control error - mean_crit (%) | 0.5 | 0.5 | 0.7 | 0.5 | 0.8 | 1.0 | 0.7 | 1.5 |
| Control error 0-Xing delay - mean value (ms) | -0.01 | 0.00 | -0.05 | -0.03 | 0.01 | -0.06 | -0.01 | -0.13 |
| Control error 0-Xing delay - std value (ms) | 0.09 | 0.12 | 0.14 | 0.11 | 0.13 | 0.15 | 0.11 | 0.18 |

| | OSM | | | | | $\alpha$-OSM ($\alpha$=-0.33) | | | | |
|---|---|---|---|---|---|---|---|---|---|---|
| Main-step used (ms) | 5 | 10 | 15 | 20 | 25 | 5 | 10 | 15 | 20 | 25 |
| Relative control error - mean_crit (%) | 0.5 | 0.9 | 1.0 | 0.7 | 1.3 | 0.5 | 0.8 | 1.1 | 0.7 | 1.1 |
| Control error 0-Xing delay - mean value (ms) | -0.02 | 0.02 | -0.04 | -0.02 | -0.08 | -0.02 | 0.03 | -0.07 | 0.00 | -0.07 |
| Control error 0-Xing delay - std value (ms) | 0.11 | 0.15 | 0.14 | 0.18 | 0.16 | 0.08 | 0.14 | 0.19 | 0.13 | 0.20 |

Table 6.6: Relative actuator command error for the 50DOF experiments

The control error is very low, always below 2% and below 1% in most cases. It can also be noted that the resulting control delay is very close to zero in all cases (two decimal places are used to express it meaningfully in milliseconds). Moreover, the standard deviation values are substantially larger than their corresponding mean values (sometimes even by an order of magnitude), confirming that the control delay changes sign and thus that the experimental errors are not of a systematic type during the whole experiment. These are important results regarding the adaptive delay compensation scheme employed here. The amount of delay compensated for is accurate enough for the control error to remain minimal and over-compensation can be avoided, thereby ensuring a higher level of accuracy for the experiment.

Because of the use of the Laguerre predictor instead of the exact third order polynomial extrapolation the computational demands are slightly different from those shown in Table 6.4 and Figure 6.8 for 50DOFs. The turnaround times and the numbers of necessary extrapolated sub-steps are presented in Table 6.7.

| Newmark Explicit | |
|---|---|
| CPU time for sub-step task | 48 |
| CPU time for main-step task | 771 |
| Number of extrapolated sub-steps | 3 |

| Newmark - Chang 2002 | |
|---|---|
| CPU time for sub-step task | 46 |
| CPU time for main-step task | 1333 |
| Number of extrapolated sub-steps | 6 |

| OSM | |
|---|---|
| CPU time for sub-step task | 49 |
| CPU time for main-step task | 1667 |
| Number of extrapolated sub-steps | 8 |

| $\alpha$-OSM | |
|---|---|
| CPU time for sub-step task | 49 |
| CPU time for main-step task | 1687 |
| Number of extrapolated sub-steps | 8 |

Table 6.7: Computational times (μs) and number of necessary extrapolated sub-steps

The computational advantage of the Newmark explicit is very clear with the 50DOF numerical problem. The main-step task can be fully solved within less than four sub-steps, against seven sub-steps for the Newmark-Chang 2002 and nine for the OSM and $\alpha$-OSM. The maximum size of the problem, in terms of number of DOFs in the numerical substructure, not only has constraints in terms of stability but also in terms of computational demand for the real-time implementation.

## 6.9- CONCLUSIONS

In this chapter, the problem of numerical time integration for real-time hybrid simulations of dynamic systems was studied in detail. A general multi-tasking strategy was devised around the various control and numerical requirements and mathematical developments were provided to meet these requirements. A selection of time integration schemes of different types was then presented together with implementation solutions applicable to non-linear force-displacement elements. One is explicit and conditionally stable, another is explicit and unconditionally stable, two are based on an implicit formulation and an explicit implementation and are unconditionally stable and finally two are fully implicit and unconditionally stable.

Conditional stability was proven for the first scheme and the other five were shown to work beyond this stability condition. The two fully implicit schemes were implemented thanks to the digital sub-step feedback technique but this implementation requires too much computation in the sub-step task, making it overrun for a relatively small number of DOFs. All the schemes were tested on MDOF systems, but only the four explicitly implemented schemes could manage a 50DOF system and were therefore found better suited to the multi-tasking technique.

For real-time hybrid applications, the stability and computational efficiency requirements of time integration schemes are somewhat more important than for purely computational applications. Consequently, the accuracy requirements should be regarded as relatively less important.

In cases where the numerical substructure poses no harsh stability condition, the results above show that the Newmark explicit method should be employed. It is very computationally efficient and also very accurate within its stability range. Provided an accurate actuation performance compensation algorithm is used, the higher modes of vibration are not overly amplified.

In many of the results, the Newmark-Chang 2002 and the OSM turn out to produce very similar results. However, the Newmark-Chang method is more computationally efficient than the OSM and is therefore recommended if numerical stability cannot be obtained with the Newmark explicit scheme. The unconditional stability of this relatively unknown scheme makes the Newmark-Chang method very appealing for real-time hybrid testing and researchers can safely choose to use it if unsure about the stability requirements of their particular system.

Finally, if numerical dissipation of the higher modes is necessary, the $\alpha$-OSM can be chosen. This may be necessary, for instance, if the actuator performance varies a lot during an experiment and the compensation scheme is not able to keep track and correct accurately. This situation can notably be found in cases of high actuator coupling and/or high non-linearity in the physical substructure. Note that the modified Darby compensation scheme, described in the previous chapter and used in this chapter, was particularly developed to cope with this phenomenon and extends the workable limit of the algorithms, independently of the use of numerical damping.

# CHAPTER 7

# REAL-TIME HYBRID EARTHQUAKE SIMULATION OF A STEEL COLUMN IN A 20-STOREY BUILDING

## 7.1- INTRODUCTION

Each of the previous three chapters have dealt with particular issues related to the realisation of successful real-time hybrid simulations. The importance of actuation quality was shown and measured, compensation algorithms were devised and implemented and comparisons were conducted regarding the use of numerical time integration schemes. This work was entirely validated experimentally through the use of a versatile development test rig (see Chapter 3), which was not meant to represent any particular application.

The main purpose of the present chapter is to show that the real-time hybrid earthquake simulation can now be applied to study the structural behaviour of a civil engineering component in its real-life environment. The work contained in this chapter is regarded as a final validation of the development work conducted during this research.

Unlike in the previous chapters, the emulated system considered here purposely represents a building structure. Moreover, it is subject to a true earthquake acceleration loading as opposed to a sinusoidal input. Finally, the actuators are used at the maximum of their nominal dynamic capacity. After initial experiments, an earthquake engineering dissipative device is designed, integrated into the substructure setup and its effect on the system is measured through a real-time hybrid experiment.

The system studied is a single-bay 4-column 20-storey building structure under a mono-directional earthquake acceleration input (the N-S component of the 1940 El Centro earthquake). The component isolated as the physical substructure is the lower part of the column, from the ground level to the bottom of the 2$^{nd}$ floor. The structure is tested at 40% of full scale.

The structural capacity of columns is one of the critical subjects in earthquake engineering. A lot of research has already concentrated on this subject and experimental testing still has a lot to contribute (Nakashima & Liu 2005). Although open-loop experiments can provide a lot of useful data, real-time hybrid simulations can also be used to analyse column resistance and provide a better understanding of complex structural system behaviour during true earthquake situations.

For reasons of actuator unavailability, the axial buckling load on the column, due to the building weight, could not be applied during the experiment. This would have influenced the test results, but it is believed it would not have made the experiment either easier or more difficult to conduct. In this respect, the lack of buckling load is not a limitation for the main aim which is here to show the application of the RTS method to a civil engineering problem.

# 7.2- EXPERIMENTAL SETUP

## 7.2.1- General setup overview

The resulting substructuring and experimental setup is presented in Figure 7.1, with the actuator loading as shown. The earthquake loading is applied at the base of the building and the columns are excited in their minor axis of bending.

Since, in this idealised building, each floor mass is assumed to be infinitely stiff compared to the columns, all the columns of a particular storey undergo the same deflection shape at any time. It is therefore valid to isolate one column as the physical substructure and assume the other three provide the same response. However, the substructure load feedback measured at each actuator needs to be multiplied by a factor of four before being applied to the relevant node in the numerical substructure.

The bracing used to apply the loading onto the physical substructure consists of a beam connected to each actuator by a pin joint and to the specimen by a moment resisting connection. These beams are further constrained relatively to the reaction floor by two pinned bars. This arrangement ensures that the correct moment reactions are applied to the specimen at each floor connection without requiring any moment loading of the actuators. The system works as a parallelogram arrangement so that the two beams representing the floors always remain parallel to the reaction floor, as rigid floors would do if all four columns were present. The symmetry constraints of the full system are therefore preserved even though only one column is tested physically in isolation.

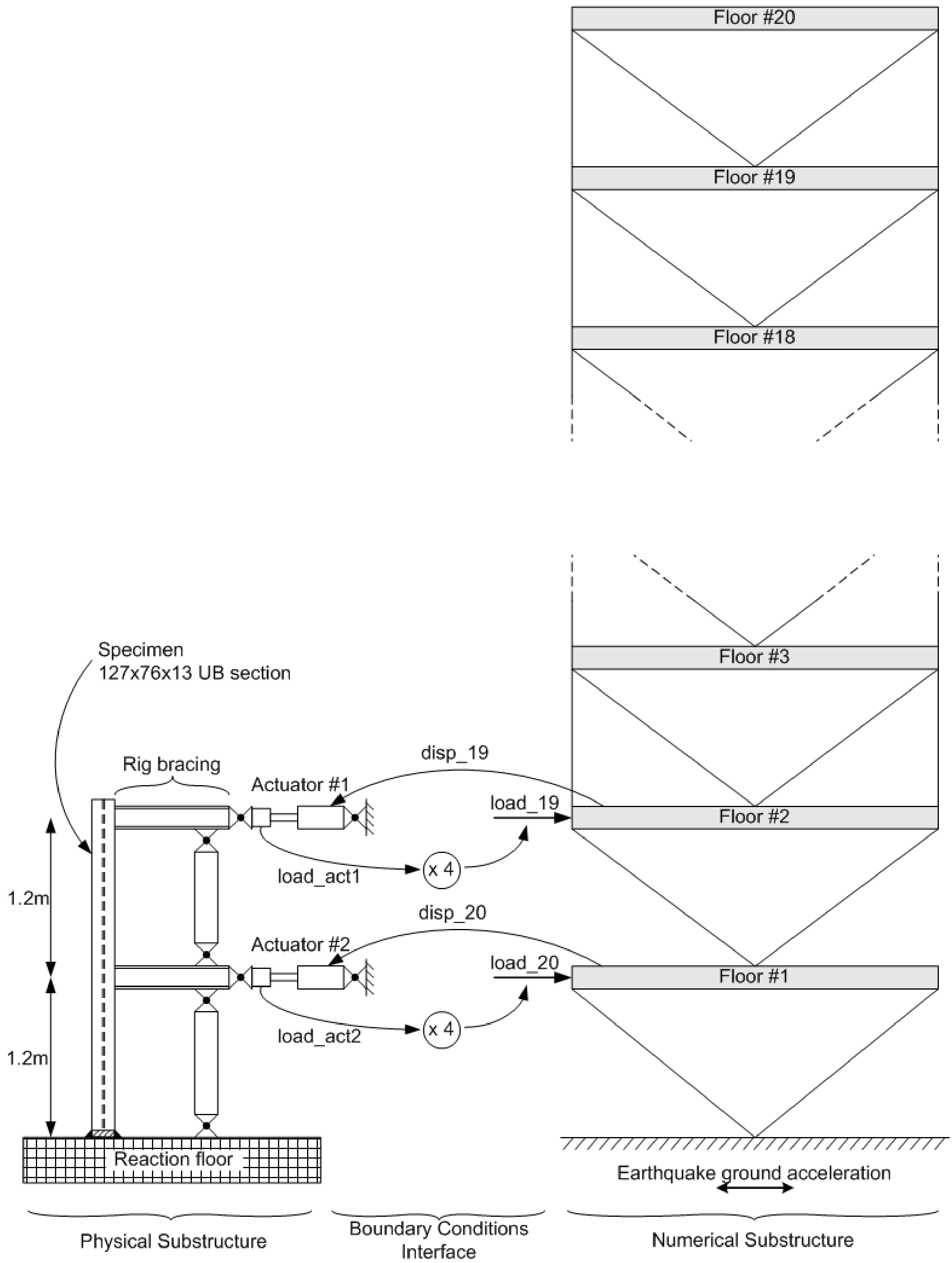

Figure 7.1: Schematic view of the system analysed and its substructuring

## 7.2.2- Structural properties of the 20-storey building

The structural properties of a full scale 20 storey building are first calculated. The following assumptions are used:

- The building mass is approximated as being lumped at each floor and each floor is considered to have the same mass.
- The full-scale building section is chosen to be square with 12m sides. Given typical values of floor density, flooring weight and additional loading, the floor weights are calculated and the columns are then chosen for the buckling resistance of the building, with a safety factor of 3.
- For the lateral stiffness of the building, a typical value of 0.1s per storey is assumed for the fundamental mode period, leading, for the 20 storey structure, to a 0.5Hz first natural frequency. The sway stiffness is assumed to be the same for each storey.
- The column section is assumed to remain the same all the way up and the lateral stiffness provided by the column is calculated. The remainder of the lateral stiffness required by the first mode natural frequency is provided by cross braces at each storey.
- In the numerical substructure, the cross braces are assumed to behave linearly in tension and have no stiffness in compression (assuming low buckling stiffness). Pure tension stresses are assumed, all bending is neglected.
- The damping coefficients are assumed to be the same at each storey and the first mode damping ratio is assumed to be 2%. The damping matrix is calculated accordingly and is therefore proportional to the stiffness matrix, although this is not a requirement of the numerical scheme used.

Following this procedure, a spreadsheet is designed. The numerical results for the full-scale building are presented in Figure 7.2. The yellow cells contain user input values and the green cells contain calculated outputs. Note that the "Stiffness needed per storey" input in the 3rd stage was worked out separately from an eigen-analysis, based on the first natural frequency requirement.

**1- Storey Mass**

| | | |
|---|---|---|
| Reinforced concrete density | 2600 | kg/m3 |
| Flooring density | 250 | kg/m2 |
| Extra loading | 440 | kg/m2 |
| Floor thickness | 0.35 | m |
| Floor side | 12 | m |
| Floor volume | 50 | m3 |
| Concrete mass | 131040 | kg |
| Flooring mass | 36000 | kg |
| Extra mass | 63360 | kg |
| Total storey mass | **230400** | kg |

**2- Buckling requirement for columns**

| | | |
|---|---|---|
| Number of storeys | 20 | - |
| Number of columns per storey | 4 | - |
| Building mass per column | 1152000 | kg |
| Buckling load safety factor | 3 | - |
| Column Young modulus | 207000 | N/mm2 |
| Storey height | 3 | m |
| 2nd moment required | **3734** | cm4 |

**(e.g. a 254x254x73 UC)**

**3- Lateral stiffness provided by this**

| | | |
|---|---|---|
| Stiffness per column | 3435 | N/mm |
| Stiffness per storey | 13741 | N/mm |
| Stiffness needed per storey | 350000 | N/mm |
| Stiffness provided by columns | **3.9** | % |

**4- Cross bracing necessary (based on 2 pairs)**

| | | |
|---|---|---|
| Stiffness required | 336259 | N/mm |
| Brace Young modulus | 207000 | N/mm2 |
| Brace angle | 27 | deg |
| Extension/displacement ratio | 0.89 | - |
| Cross brace length | 6.7 | m |
| Cross section surface area needed | 12183 | mm2 |

**(e.g. 305x127x48 UB)**

Figure 7.2: Full-scale building structural properties

Following these results, the same procedure is conducted for the scaled building. The properties are worked out based on floor sides, floor thicknesses and storey heights reduced to

40% of the full-scale values. The scaled structure has the same natural frequencies as the full-scale structure. The main properties of both the full-scale and 40% scaled buildings are summarised in Table 7.1.

| | Full scale structure | 40% model |
|---|---|---|
| Storey mass (T) | 230 | 21 |
| Lateral stiffness (kN/mm) | 350 | 32 |
| Lateral viscous damping (kN.s/m) | 4700 | 434 |

Table 7.1: Properties of the 20-storey full-scale and 40% structures – values are per storey

The column size required for this building is then the type tested as the physical substructure in the following experiments: UB 127x76x13 oriented in its minor axis. The experiment reproduces the lower two storeys physically. The columns of the 18 remaining floors are modelled in the numerical substructure as linear beams with moment connections at all floors. The sway stiffness provided by the braces is also part of the numerical substructure model. Note that, since a large proportion of sway stiffness of the lower two storeys is provided by the braces in the numerical model, the stability of the experiment is likely to be less problematic.

## 7.2.3- Finite element model

To obtain a better idea of the loading the specimen will be subject to during the experiments, a finite element analysis (FEA) model was constructed. It also provided useful data for the design of the bracing system (see next section).

For the problem considered, a 2-D wireframe static linear analysis suffices. The SAP2000® software package was used since it is especially tailored for civil engineering structural analysis applications. The proper beam and bar sections are applied, as well as the loading mechanism, consisting of the bracing system, the actuators and the right constraints, allowing free degrees of freedom where required. The pin-joints are idealised and the length of the actuators is used as the loading input for the analysis. In terms of the choice of the sections for the bracing system elements, iterations were conducted between the modelling and the detailed design, presented in the next section. For clarity, the results presented in Figure 7.3 are the final ones.

The loading is applied in terms of actuator displacements according to the first mode shape of the 20 storey building. The amplitude chosen is that producing a maximum bending moment of 8.0kN.m in the specimen.

The results of this analysis show very small deflections from the bracing system, which should therefore ensure the proper loading of the specimen, provided the stress levels do not exceed the material limits. This last point will be checked in the following section. Another point discovered from the FEA results is the extent by which the 1$^{st}$ mode shape loading introduces loads mainly on the second storey actuator. In other words, if the whole specimen was purely loaded through the second storey actuator only, the deflection shape obtained would be close to that of the first mode of the whole structure.

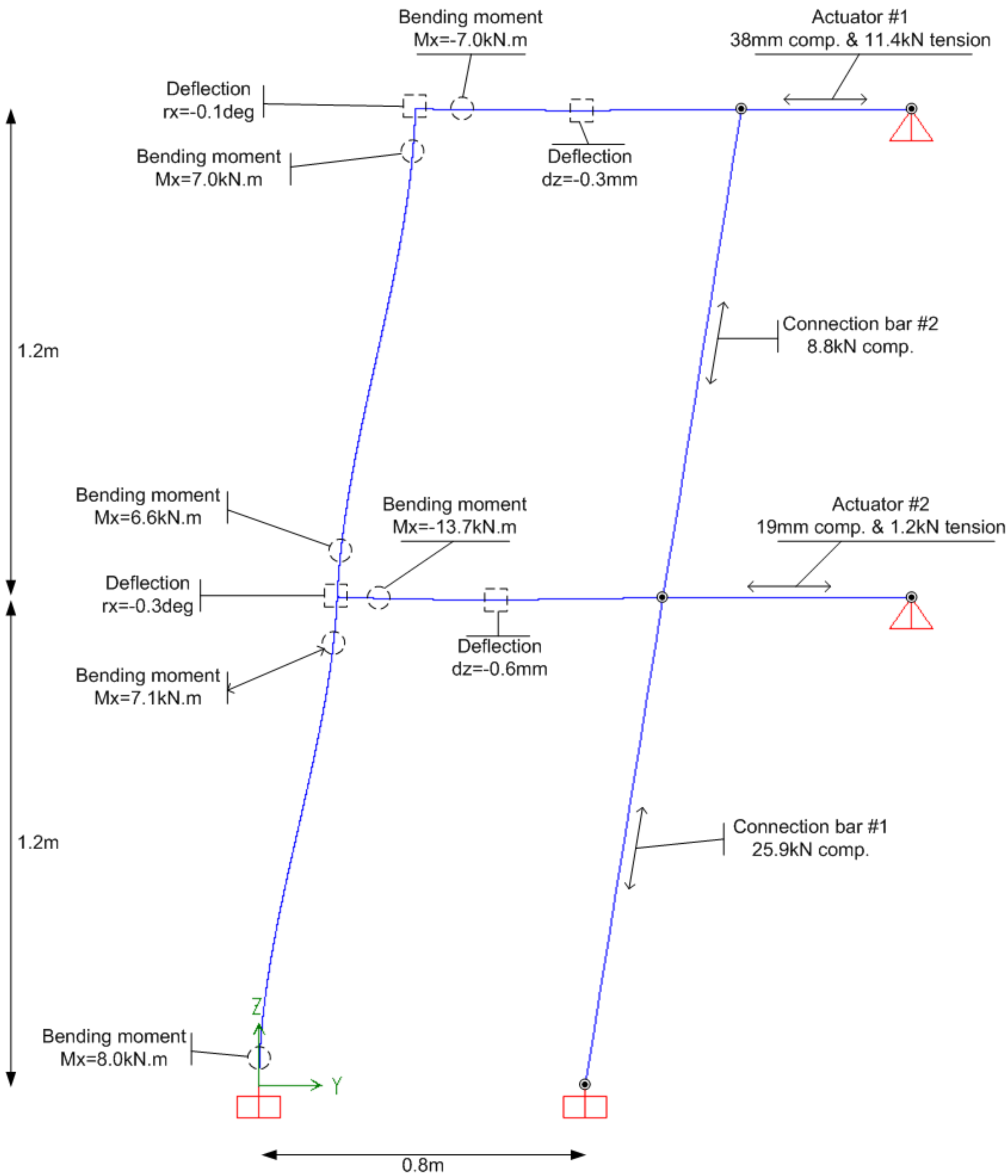

Figure 7.3: FEA model results

## 7.2.4- Actuator coupling stiffness

As already pointed out in Chapters 4 and 5, when intending to run a multi-axis RTS experiment, one of the key features of the physical substructure laboratory installation is the amount of coupling between the various actuators. The coupling stiffness is a measure of the importance of conflicting situations that may arise in the test. In the experimental setup, as shown in Figure 7.1, substantial coupling is obviously present due to the specimen through the moment connections between the column and the bracing. Assuming perfect moment connections and using linear beam theory for the specimen, the coupling stiffness between the two actuators is given by Equation (7.1):

$$K_{coupling} = \frac{96 \cdot E \cdot I_{yy}}{l^3} \tag{7.1}$$

where $E$ is the Young modulus of the material, $I_{yy}$ is the second moment of area in the direction considered (i.e. 55.7cm$^4$ in the case considered) and $l$ is the length of the beam. A value of $K_{coupling}$=801N/mm is obtained from Equation (7.1) for the setup proposed. This value is fairly high for the actuators used since only 6mm displacements in opposing directions of the actuators would imply reaching their 10kN nominal dynamic load limit.

The coupling stiffness can also be estimated from the FEA results. In this model, the moment capacity of the braces is not fully idealised and the coupling stiffness is found to be around 600N/mm. However, this measurement may prove to be an underestimate of the true value, as point connections are used, thereby providing slightly overestimated beam lengths. The true coupling stiffness value will therefore be obtained from the experiment, but it is expected to be between 600 and 800N/mm in the linear range of the specimen.

## 7.3- DETAILED RIG DESIGN

Along with the work described in the previous section, the following hand calculations were conducted to design the main components of the rig. Since components were already available which could be used for the reaction floor mountings of the specimen and actuators, the rig design mainly concentrated on the bracing required for the specimen loading.

### 7.3.1- Floor beam moment capacity VS specimen moment capacity

For the short beams used as the floor connections onto the specimen, it is proposed to use the same structural element as the specimen (UB 127x76x13) oriented in its major axis. It is therefore required that, in the experiment, the elastic capacity in the major axis (for the brace) should not be reached before the plastic capacity in the minor axis (for the specimen).

The elastic modulus of the section in the major axis is 74.6cm$^3$. The plastic modulus in the minor axis is 22.6cm$^3$. Assuming that the steel yield stress is a maximum of 355N/mm$^2$ (since a S275 grade is ordered and S355 material is stipulated as not suitable), the brace elastic capacity is 26.5kN.m and the specimen plastic capacity is 8.0kN.m.

When the SAP model is loaded accordingly to the first mode shape and so that the maximum specimen bending moment reaches 8.0kN.m, the highest bending moment in the braces is 13.7kN.m. This condition is that shown on Figure 7.3. Using the same section in its major axis therefore ensures with a safety factor of 1.9 that the brace will not undergo any plastic deformation.

### 7.3.2- Buckling capacity of the inter-floor connection bars

As shown in Figure 7.1, two bars, articulated by pin-joints, introduce the additional constraint required for the floor connections to react properly. These two bars will be subjected to substantial tension and compression loads when the actuators displace the rig away from its static equilibrium position. The buckling capacity therefore needs to be checked.

For practical reasons, it is proposed to use 80x80x3mm mild steel box section bars. The Euler buckling load for a pinned-pinned setup is given by:

$$F_{buckling} = \frac{\pi^2 \cdot E \cdot I}{4 \cdot l^2} \tag{7.2}$$

where $l$ is the length of the section subject to buckling. Neglecting the radii of the box section and over-estimating the length of the bars to 1.2m (the height of each floor), the buckling load calculated is 313kN. By comparison, the load obtained in the SAP model when reaching the moment capacity of the specimen is 26kN. The section chosen is therefore validated.

### 7.3.3- Pin joint design and calculation

Previous experience of structural dynamics testing in the OUSDL has shown that relying on fully articulated pin-joints to transmit high loads and accurate restraints was difficult. Instead, purpose-made flexible elements have been developed to allow the required degrees of freedom without compromising the level of restraint in others.

In this application, the pin-joints shown in Figure 7.1 are realised by sections of I-beams, where the flanges are used as mounting faces and the web is used to provide the DOF, through its low bending stiffness in one direction only. The buckling load capacity of this device has to be checked.

For the actuator articulation, it is proposed to use existing elements made from 64mm-wide sections of the 127x76x13 UB section. Using Equation (7.2), a buckling capacity of 13.4kN is obtained. This number is suitable for the proposed use as actuator pin-joints. However, the other pin-joints needed for the inter-floor connection bars need higher capacity.

For the inter-floor connections, it is therefore proposed to manufacture similar joints, using 76x50x5mm plates as the flexible elements, where the section width is 76mm and the buckling length is 50mm. The shortening of the buckling length from 127mm increases the buckling load capacity to 156kN. This design is validated since the maximum load from the SAP model when the moment capacity of the specimen is reached is 26kN.

## 7.4- INITIAL EXPERIMENT, ALGORITHMS USED AND RESULTS

The test rig is assembled in the OUSDL, as shown on Figure 7.4 with the specimen along the left hand side. Since no major gravity load will affect the behaviour of the physical substructure, the experiment is set up horizontally, at a centreline height of 180mm above the laboratory floor. Note however that a 45mm ball bearing is placed underneath the second storey floor connection beam, rolling onto a platform that can be seen on Figure 7.4. This bearing takes some of the dead weight without introducing any additional kinematic restraint to the setup.

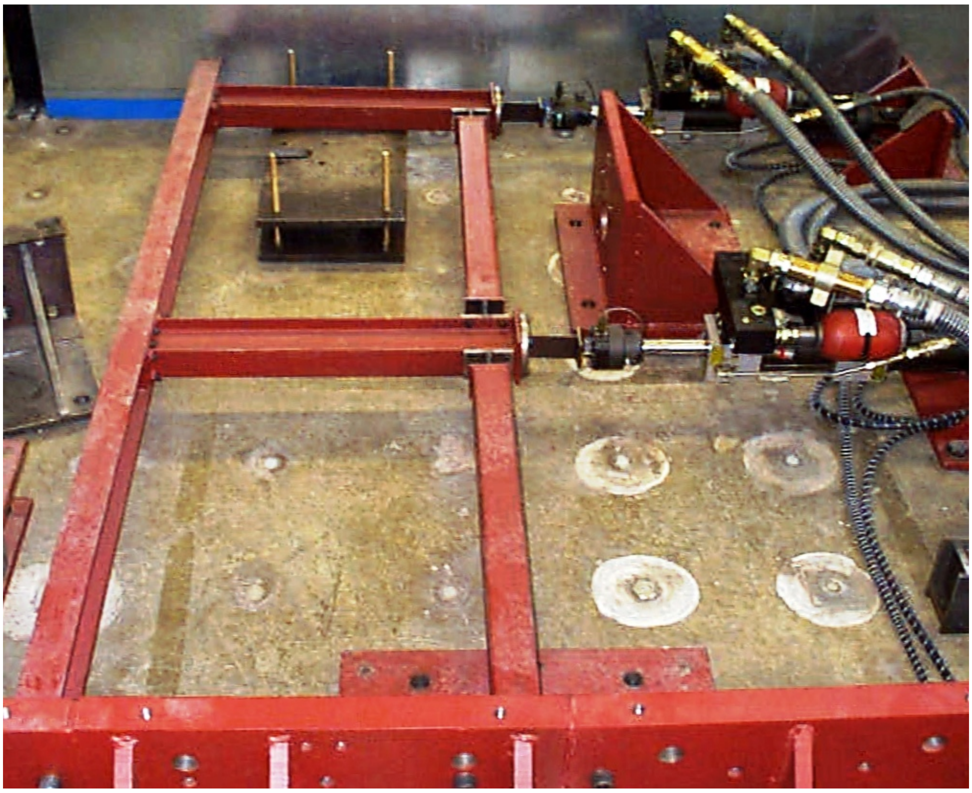

Figure 7.4: Physical substructure laboratory assembly

The loading used in this test is the acceleration record of the El Centro earthquake North-South component. This record is well-known by the earthquake engineering community and its use here provides consistency with many experiments conducted in the past by other researchers. It was measured and recorded in Southern California on the 18th of May 1940. It will be used with a duration of 40s although the highest values are concentrated in the first 6s. The peak acceleration measured was 3.2m/s$^2$. The acceleration data are shown in Figure 7.5, in both the time and frequency domains. Initially, this record is scaled by a factor of 40% to reflect the model scale.

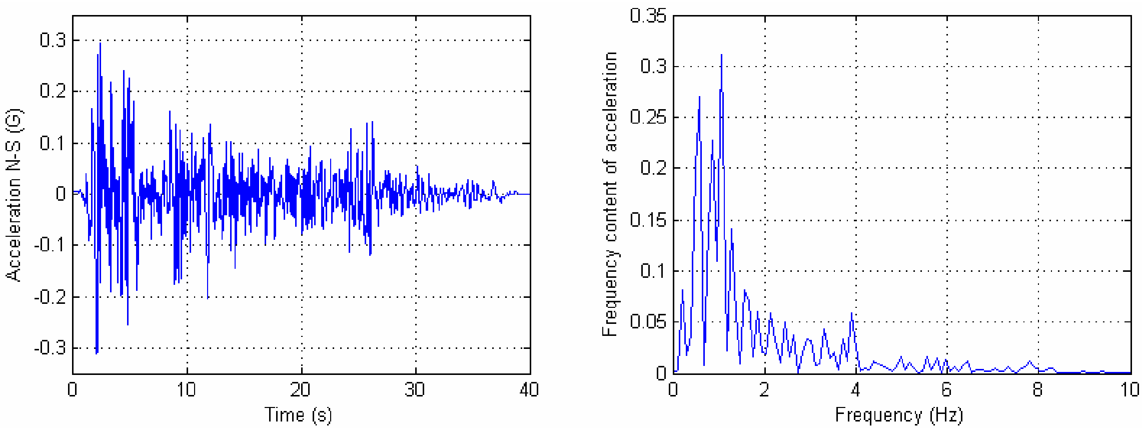


Figure 7.5: El Centro N-S component record

Due to the relatively high number of degrees of freedom in the numerical substructure for this experiment, a numerical time integration scheme that puts a harsh time-step constraint for stability reasons is not desired. Due to its simplicity and numerical stability, as presented in Chapter 6, it is proposed to use the Newmark-Chang 2002 explicit scheme (Chang 2002*b*).

The only potential downside of this scheme is its lack of numerical dissipation. Therefore, the $\alpha$-OSM (Combescure & Pegon 1997) has also been tested with a setting of $\alpha$=-1/3 in an attempt to check if this would enhance the response, in particular in eliminating any unwanted higher mode contribution. However, since no measurable difference could be found between the two schemes, the $\alpha$-OSM scheme was not used further due to its lower theoretical accuracy and its requirement for some of the physical substructure properties, for a similar stability condition.

Initially, the integration time-step chosen was 10ms. From earlier RTS test results, as presented in the previous chapters, the modified Darby delay update scheme is chosen as the adaptive actuator outer-loop control scheme. It is used in conjunction with a third order exact polynomial algorithm (Horiuchi *et al.* 1996) to conduct the necessary forward extrapolation. This combination produced good results for the 10ms time-step.

The conflicting situations arising because of the high actuator coupling stiffness make the inner loop control of the actuator more difficult. The discrepancies between the actuator command and the actual displacement obtained are more complex than those due to a near constant delay. Oscillations between undershoot and overshoot situations of the actuator can even occur. To eliminate, or at least reduce, this behaviour, which can otherwise quickly amplify, the inner loop PID controller can be tuned differently (typically, by reducing the proportional gain value). This reduces the chance of any overshoot happening. The downside is of course a slightly poorer actuator performance, but this can easily be compensated by the adaptivity of the delay correction scheme.

However, when the time-step is increased to 20 and 30ms, the polynomial extrapolation scheme shows stability issues in producing a reliable prediction. This is observed, during the experiment, by a command signal oscillating around the desired signal rather than being purely shifted forward in time. This quickly leads to experimental errors, carried from step to step by the substructuring feedback and amplified faster than the adaptive control scheme can correct.

To resolve the difficulty observed for higher time steps, the Laguerre predictor can be used to conduct the extrapolation from the sub-step data. Experiments with 30ms numerical steps were run successfully, thereby proving once more the stability of the numerical scheme proposed by Chang (2002*b*) over the usual limit of the original Newmark explicit scheme. In this experiment, the shortest natural period of the numerical substructure is 80ms, implying a stability limit on the integration time-step of $T_{max}$=25ms for the standard Newmark explicit scheme.

The control errors obtained in this experiment are respectively 0.45% and 2.6% for actuators #1 and #2. It should be noted that actuator #1 transmits most of the substructuring interface constraint and it therefore should be focussed on. The control plot for actuator #1 is shown on Figure 7.6. It can be seen that, throughout the test time history, the desired and achieved actuator signals match very well. This confirms the validity of the boundary conditions applied at the interface and therefore the validity of the experiment.

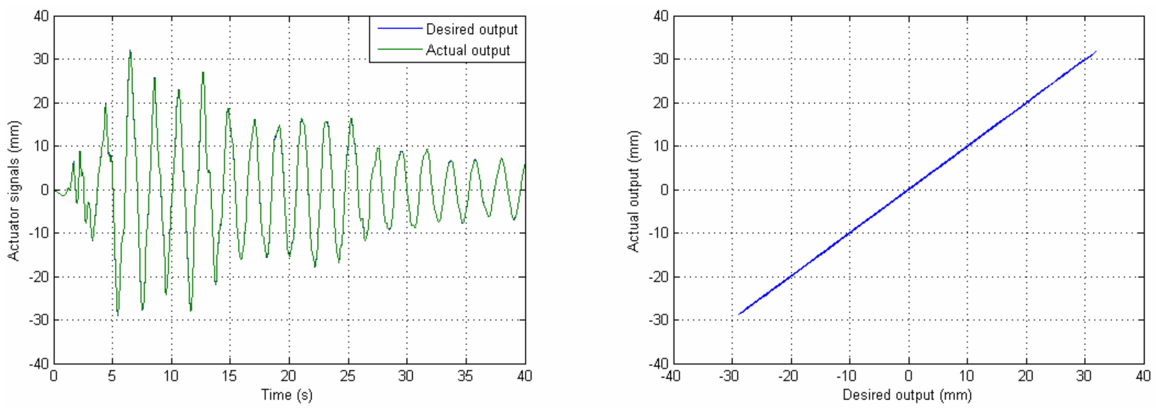


Figure 7.6: Control plot for actuator #1

The response of the scaled structure to the earthquake is shown in Figure 7.7. The time-history responses of the $1^{st}$, $2^{nd}$, $11^{th}$ and $20^{th}$ storeys are produced – the former two were measured from the physical substructure and the latter two were produced as part of the numerical substructure computation. The similarity between the various traces for most of the 40s history points out the importance of the first mode of vibration in the overall response of the structure. It is noted that the top storey deflects by about ±180mm around the static position.

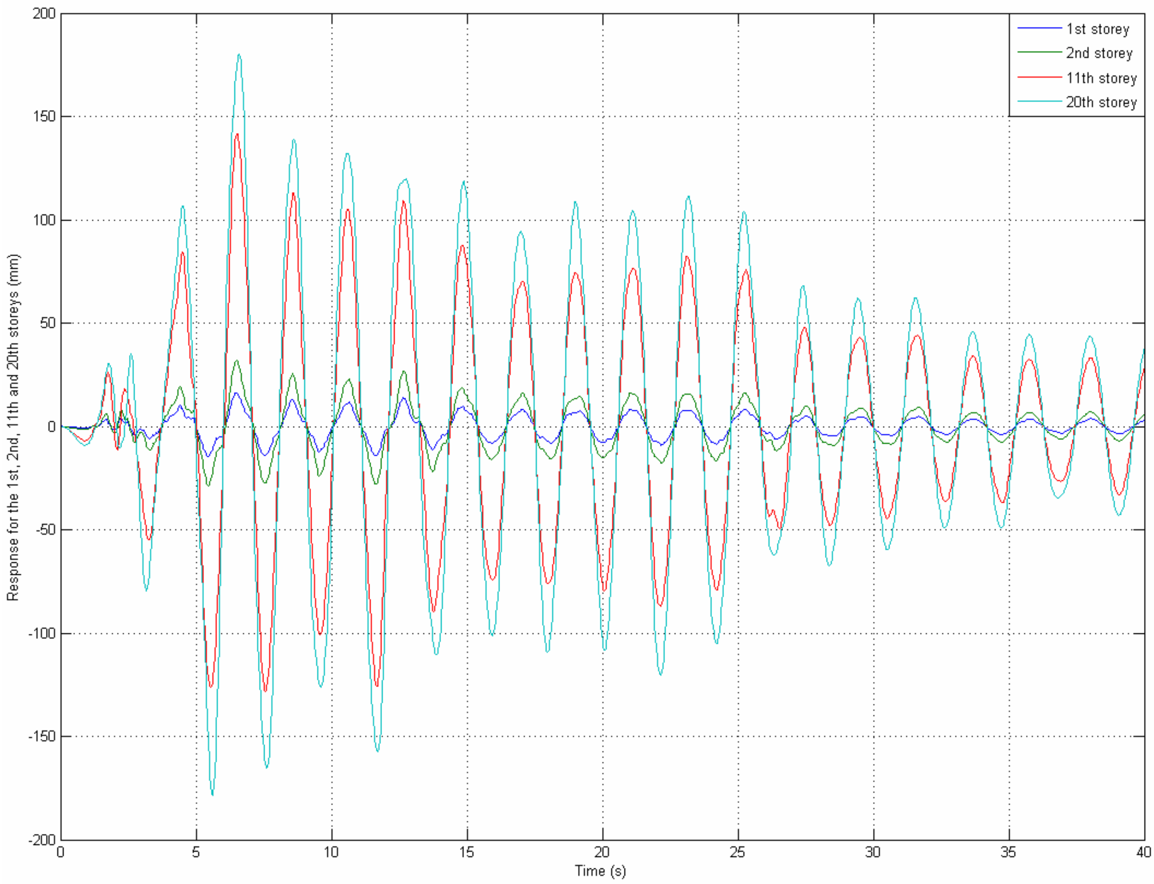


Figure 7.7: Earthquake response plot for several storeys

Next, the scaling factor was increased from 40% to 60%. This ensures the substructure interface loads generated reach the top of the actuator dynamic range (10kN), where non-linearity in the actuator behaviour is at its highest. The test system is still stable in these conditions. Moreover, this means the steel column selected just enters its non-linear deformation regime. Note that, thanks to the reciprocal boundary condition application on the two substructures in real-time, the energy dissipation through the hysteresis behaviour of the specimen is actively taken into account in the experiment and affects the overall response accordingly.

The specimen hardly undergoes any significant deformation in the non-linear regime. With the 60% earthquake scaling, the maximum load at actuator #1 is 11kN, which is 110% of the nominal actuator dynamic range (note that the load cell used has a higher capacity). Under this load, it is clear that the specimen starts to undergo slight yielding and hysteresis, even though the loops are very narrow. Evidence of the hysteresis is shown in Figure 7.8 by comparing the load/displacement curves for the first storey column for both 40% and 60% earthquake inputs.

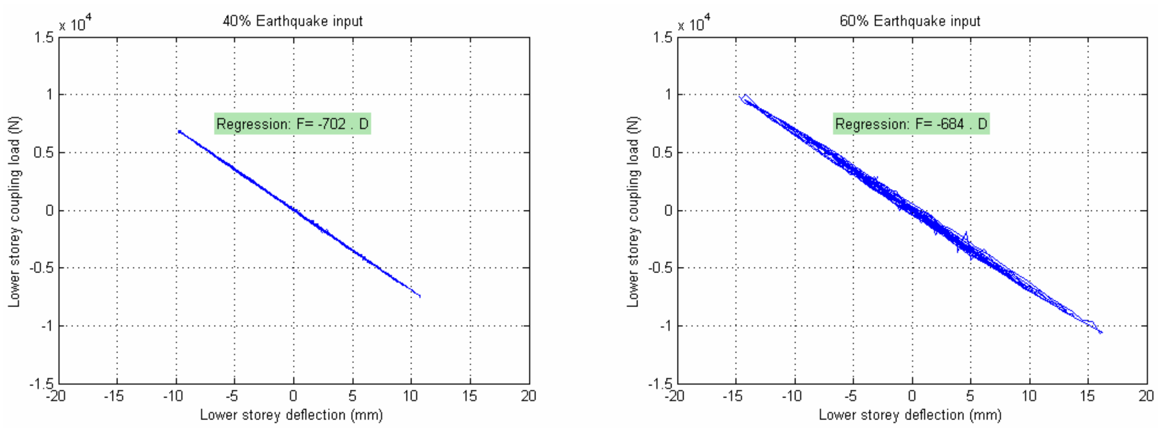


Figure 7.8: Load displacement plots for the first storey – 40% and 60% earthquake inputs

Assuming from Figure 7.8 a yielding load of about 8kN, equating to a maximum bending moment of 5kN.m at the moment resisting connections according to the FEA results, the maximum bending stress induced is 340N/mm$^2$. This result confirms the S275 material grade ordered. But since the bending occurs about the minor axis of the I-section, only the material present at the tips of the flanges is subject to plastic deformations when yielding first occurs. It is therefore understandable that only a small loss of stiffness is observed and a substantial increase in load can still take place. When bending about the major axis is considered, the whole width of the flanges is subject to yielding simultaneously and non-linearity is likely to be more important.

Finally, from Figure 7.8 it can also be seen that the first storey stiffness is found to be 702N/mm in the linear regime. Conducting a similar calculation for the 2$^{nd}$ storey leads to a result of 693N/mm. These numbers fit very well with the estimates of the actuator coupling stiffness presented previously in this Chapter.

## 7.5- EFFECT OF A TUNED-MASS-DAMPER ON THE BUILDING RESPONSE

To illustrate the versatility of the RTS simulation, the impact of a tuned-mass-damper (TMD) device on the structural control during the earthquake is now studied. The same experiment will be repeated with the addition of the TMD fitted at the top of the building structure and accounted for in the numerical substructure. The substructuring setup is therefore slightly modified from that presented in Figure 7.1, with the numerical substructure augmented with a TMD degree of freedom as shown in Figure 7.9.

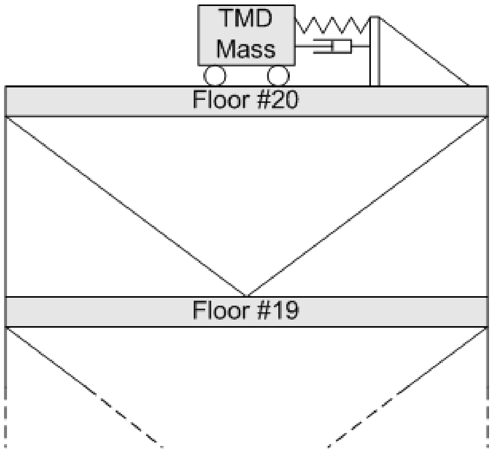


Figure 7.9: Numerical substructure update for TMD experiments

## 7.5.1- Tuned-mass damper design

The overall TMD properties are calculated using the simplified TMD design guidelines provided by Rana & Soong (1998). The calculations for both the full-scale and 40% scale buildings are shown in Figure 7.10.

Referring to the full-scale case, the first mode modal mass is calculated at 2365t using the normalised first mode shape. With a TMD mass assumed to be 1.5% of the building mass (i.e. 69t), a first mode modal mass ratio of 2.9% is obtained. Knowing the first mode damping ratio for the structure without TMD (2%), the design tables produced by Rana & Soong are then used to provide the optimal frequency ratio and the optimal TMD damping ratio. Finally, accounting for the first mode natural frequency, the stiffness and damping values for the TMD are worked out.

| | Full scale building | | 40% scale building | |
|---|---|---|---|---|
| **Initial property calculations** | | | | |
| Storey mass | 230400 | kg | 20828 | kg |
| 1st mode modal mass | 2365035 | kg | 213803 | kg |
| TMD mass % of building mass | 1.5 | % | 1.5 | % |
| TMD mass | **69120** | kg | **6248** | kg |
| 1st mode modal mass ratio | 2.9 | % | 2.9 | % |
| **Optimal TMD parameters** | | | | |
| (from Design Table in Rana et al. 1998) | | | | |
| 1st mode damping ratio | 2.0 | % | 2.0 | % |
| Optimal frequency ratio | 0.957 | - | 0.957 | - |
| Optimal TMD damping ratio | 10.5 | % | 10.5 | % |
| **Final TMD parameter calculations** | | | | |
| 1st mode frequency (from Matlab) | 0.5 | Hz | 0.5 | Hz |
| TMD stiffness | **565** | N/mm | **51** | N/mm |
| TMD damping | **41643** | N.s/m | **3765** | N.s/m |

| | Full scale building | 40% scale building |
|---|---|---|
| **Building first mode shape** (from Eigen analysis in Matlab) | -6.51E-04 | -2.14E-03 |
| | -6.47E-04 | -2.13E-03 |
| | -6.39E-04 | -2.10E-03 |
| | -6.28E-04 | -2.07E-03 |
| | -6.13E-04 | -2.02E-03 |
| | -5.94E-04 | -1.96E-03 |
| | -5.72E-04 | -1.88E-03 |
| | -5.47E-04 | -1.80E-03 |
| | -5.18E-04 | -1.70E-03 |
| | -4.86E-04 | -1.60E-03 |
| | -4.52E-04 | -1.49E-03 |
| | -4.14E-04 | -1.36E-03 |
| | -3.75E-04 | -1.23E-03 |
| | -3.33E-04 | -1.09E-03 |
| | -2.89E-04 | -9.51E-04 |
| | -2.43E-04 | -8.01E-04 |
| | -1.96E-04 | -6.46E-04 |
| | -1.48E-04 | -4.88E-04 |
| | -9.94E-05 | -3.27E-04 |
| | -4.99E-05 | -1.64E-04 |
| **Normalised first mode shape** | 1.000 | 1.000 |
| | 0.994 | 0.994 |
| | 0.982 | 0.982 |
| | 0.965 | 0.965 |
| | 0.942 | 0.942 |
| | 0.913 | 0.913 |
| | 0.879 | 0.879 |
| | 0.840 | 0.840 |
| | 0.796 | 0.796 |
| | 0.747 | 0.747 |
| | 0.694 | 0.694 |
| | 0.637 | 0.637 |
| | 0.576 | 0.576 |
| | 0.511 | 0.511 |
| | 0.444 | 0.444 |
| | 0.374 | 0.374 |
| | 0.302 | 0.302 |
| | 0.228 | 0.228 |
| | 0.153 | 0.153 |
| | 0.077 | 0.077 |

Figure 7.10: Calculation procedure for TMD design

## 7.5.2- Experiment and results

The TMD is introduced in the numerical substructure, consisting of an additional DOF as shown in Figure 7.9. The same algorithms are used and an experiment with an integration time step of 30ms and the earthquake scaling of 60% is conducted. The control of the experiment is validated and the response of the structure equipped with the TMD can be directly compared to the response of the unprotected structure. This is presented in Figure 7.11 for the 1$^{st}$, 2$^{nd}$, 11$^{th}$ and 20$^{th}$ storeys. The displacement of the TMD itself is also shown.

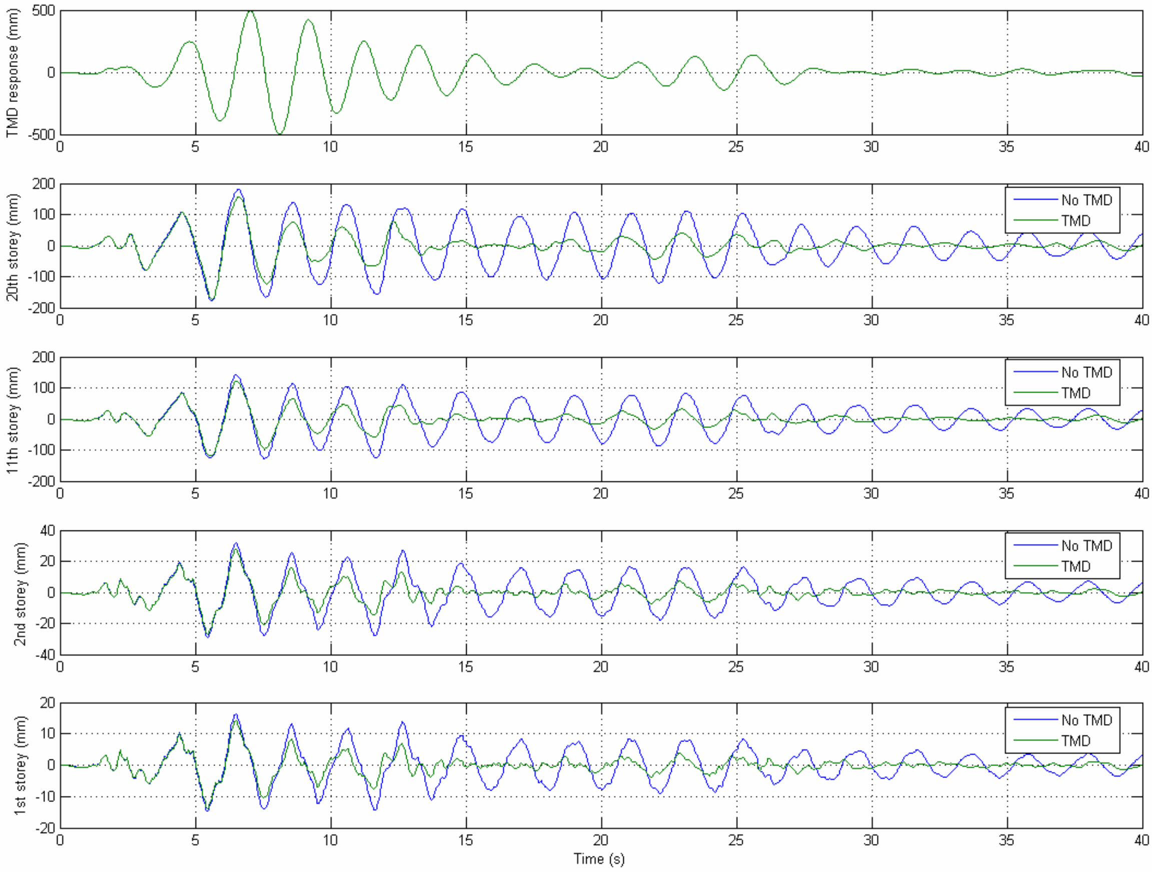

Figure 7.11: Effect of the TMD device on the structural response

The direct impact of the TMD on the maximum deflection can be observed. It amounts to a reduction of about 5% when measured at the 20$^{th}$ floor. The impact on the oscillations' decay is much higher. It can be seen that the specimen undergoes noticeably fewer cycles of large deformation: only two peaks above 100mm at the 20$^{th}$ storey instead of ten when the TMD is not present. The TMD device is therefore shown to improve both the ultimate resistance and the fatigue life of the structure.

The drawback of the TMD device, as exposed in this experiment, is its reaction time. This is particularly true for an earthquake record that features its highest levels of acceleration in the first few seconds of the event. For the TMD to become most effective, its oscillations need to be in phase opposition with those of the top storey. This does not naturally happen straight away and only small amounts of energy can be dissipated (see for example t=6s on Figure 7.11). Once in phase opposition, the energy dissipation is high and the structural displacements are drastically reduced (t=16s), then leading to the oscillations decay of the TMD (t=20s). New in phase oscillations appear where the TMD is not able to dissipate much energy (t=22s) and the same cyclic behaviour takes place.

## 7.6- CONCLUSIONS

In this chapter, the real-time substructure computational/experimental method has been applied to study the structural behaviour of a steel column as part of a 40% scaled 20-storey structure under realistic earthquake loading. The general layout of the test was presented and the modelling approximations were laid out. From these, the main structural properties of the building models were obtained. The loading rig was then designed, with the aid of a finite element model of the experiment and a series of hand calculations. The actuator coupling stiffness for this experiment was also estimated.

Earthquake hybrid simulations were then conducted to reproduce the structural response of the entire building. The numerical time-integration and actuator delay compensation schemes used were directly applied from the results developed in Chapters 5 and 6. Tests were conducted with the Newmark-Chang 2002 explicit scheme, for which numerical stability was proved beyond the common limit for explicit schemes. Regarding actuator delay compensation, large time-steps showed the limits of the main-step polynomial extrapolation. However, the sub-step Laguerre extrapolation was used successfully instead.

As a further display of the usefulness of the RTS test method for earthquake engineering applications, a tuned-mass-damper device was integrated into the numerical substructure and comparative experiments were carried out. The effect of the TMD in reducing the structural response was easily measured and reported.

# CHAPTER 8

# CONCLUSIONS AND FUTURE PROSPECTS

## 8.1- CONCLUSIONS

The multi-axis real-time hybrid testing method was developed in this research in relation to its applications to earthquake engineering. A methodical literature review was presented in Chapter 2. Initially, its place and role within the experimental methods of structural dynamics were analysed. The possibilities offered by the RTS method are unique and attractive, and this is illustrated by the fact that other experimental techniques such as shaking table or pseudo-dynamic testing currently evolve towards it.

The challenges posed by RTS were also thoroughly reviewed. The crucial subject of time-integration of the numerical substructure was first assessed. Numerous schemes were presented, some of which had not previously been applied to RTS testing. Their characteristics and relative merits were discussed, as well as their potential suitability for the application to real-time testing of non-linear multi-degree of freedom numerical substructures. This review formed the basis of the comparative analysis carried out in Chapter 6.

The issue of actuator dynamics was then explored and findings from previous literature were summarised. This then led to the presentation of the various compensation algorithms that had typically been used for RTS simulations, based on forward extrapolation and delay estimation techniques. This problem was also analysed more generally with control engineering methods and bespoke adaptive algorithms for substructure testing were presented.

In Chapter 3, the main elements of the hardware installation necessary to conduct real-time hybrid experiments were described in detail. The configuration options were also given in order to optimise the behaviour of the actuator control and minimise the influence of its dynamics. To complement the actuation and computational hardware used in this research, a development rig was designed and constructed. Finally, some preliminary RTS experiments were conducted to display the performance of the overall system.

The issue of real-time synchronisation was consequently analysed. It is critically linked to the response of the actuation equipment, and a step back is taken in Chapter 4 to analyse how this can be best quantified. Experimental evidence was then gathered about the exact response of servo-hydraulic actuators in various types of circumstances. Beside the settings of the proprietary controller, it was found that the actuator response is linked to a variety of environmental factors affecting its performance and consistency. The implementation and application of compensation algorithms was then considered in Chapter 5. A classification of the previously published – including direct compensation and MCS-based algorithms – schemes was given and augmented by newly developed schemes. Extensive experimental comparisons followed, based on accuracy and computational efficiency results for three tests of varied complexity with the last one representing a demanding multi-axis test with high actuator coupling. This analysis resulted in the formulation of some recommendations. It was found that the direct compensation methods could potentially be more responsive and effective than the MCS-based adaptive controllers. More specifically, the modified Darby scheme was found to be the most adequate performance estimate algorithm overall.

Regarding the forward prediction schemes, three schemes showed good results and can be used according to the time-step and the properties of the time-integration scheme used for the numerical substructure.

Chapter 6 was then devoted to the solution of the numerical substructure model through time-integration software. A multi-tasking strategy was first presented in order to decouple the incompatible time-step requirements of the numerical substructure problem with those of the actuation continuity. Within this framework, the time-integration schemes reviewed in Chapter 2 were re-considered for their suitability for application to RTS testing with non-linear MDOF models. Six schemes were chosen and detailed implementation equations for RTS were developed. Experiments with an increasing number of DOFs were then carried out and this showed the limitations of some of the schemes. Finally, the integration time-step was increased to prove the unconditional stability of the schemes concerned. Of all the algorithms studied, three were considered as a suitable portfolio of methods to be chosen from for most applications. The Newmark explicit scheme, in its standard form, is very accurate and requires very little computational power. Provided its stability can be ensured, it should be considered as the first choice. If stability issues become dominant, the modified Newmark explicit algorithm proposed by Chang was shown to be very efficient. The unconditional stability was also proved for this system, using the Laguerre extrapolation routine for the delay compensation. The $\alpha$-OSM scheme was also shown to be unconditionally stable in this application and found to be a possible choice, due to the introduction of numerical damping. These three schemes have all permitted the successful completion of RTS experiments with fifty non-linear DOFs in the numerical substructure.

The algorithms developed in Chapters 4, 5 and 6 and presented in the recommendations above have permitted the conduct on a simple proof of concept rig of more complex and more advanced real-time substructure experiments than had previously been published. To exhibit the relevance of real-time hybrid testing on a pertinent application, a typical earthquake engineering experiment was conducted on a different test rig in Chapter 7. A 20-storey building was considered and the steel column for the lower two storeys was tested physically. Due to the available hardware and laboratory space, a 40% model was analysed. The response of the building structure to the 1940 El Centro earthquake (North-South component) was produced through real-time hybrid simulations. Additionally, a dissipative device was included into the numerical substructure in the form of a tuned-mass-damper fitted on top of the 20$^{th}$ storey. Subsequent experiments were conducted and showed the expected response reduction obtained from the TMD. According to the findings of the previous chapters, these experiments were realised thanks to the successful use of the Newmark-Chang explicit unconditionally stable numerical method and the modified Darby actuator performance update scheme. In terms of forward prediction, the third order exact polynomial extrapolation scheme proved successful for the conduct of experiments with small main time steps and the Laguerre extrapolator was effectively applied for the conduct of experiments with larger time steps, thereby enabling tests with potentially more complex numerical substructures.

## 8.2- FUTURE PROSPECTS

As presented in the previous section, the main fundamental aspects of multi-axis real-time substructure testing have been researched and, as shown by the results obtained, this experimental technique is becoming mature. Recommendations were expressed regarding laboratory installations, actuator compensation algorithms, multi-tasking strategies and numerical integration routines.

Regarding the hardware used for RTS simulations more specifically, a lot of progress has of course been made in the previous years and decades. The capabilities of the DSP boards and actuator digital controllers are obviously at the heart of these improvements. However, now that the precise requirements for these two entities are better understood, their fusion into one controller/calculator would make the realisation of RTS tests simpler and more efficient and would constitute an important incentive for dynamic actuator owners to realise such experiments. To a lesser extent, purely digital communications between the DSP board and the controller would be a step in the right direction. Although the two units are typically fully digital ones, only analogue signal communications are usually available between the two, implying the unnecessary use of A/D and D/A converters and the introduction of electrical noise.

In terms of the algorithms used, there are also many improvements that could still be produced. For the forward prediction of the desired actuator signal, the original third order exact polynomial extrapolation has shown its adequacy but the new Laguerre extrapolator scheme clearly has some benefits and more research should be conducted on its development. Regarding performance updating, the complete discrimination of the local peaks and troughs of the modified Darby scheme is a drawback and the introduction of developments in this area, perhaps with a more accurate description of the amplitude error, would improve accuracy and also drive the stability limit back. The alternative choice of using a bespoke outer-loop control scheme such as the MCS family also has advantages and research should also be continued on this front, probably concentrating on increasing the speed of adaptation, even if some more knowledge of the test equipment is required. Concerning numerical time integration methods, the Newmark-Chang scheme has shown its unique advantages but is not capable of accommodating explicitly non-linear velocity dependent forces. Developments in this area would be beneficial for the versatility of the RTS method.

More realistic applications in the field of earthquake engineering and in others should now be considered. There are indeed programmes underway in Oxford for the applications of real-time testing to earthquake engineering dissipative devices, cantilever grandstands with crowd-structure interaction and foundation systems for offshore wind turbines. Potential applications can also be envisaged in numerous areas of mechanical engineering, especially where the loading type remains local or at least can be applied with a fairly small number of actuators. In contrast, applications with complex loading such as structural compliance coupled with aerodynamic loads would be difficult to reproduce experimentally in real-time and this is probably the type of study where purely computational modelling is more adequate. As the application of real-time substructure testing becomes more widespread, new challenges will undoubtedly appear but the experience already accumulated and the continuous hardware improvements should help resolving them.

Independently of the particular field of application considered, a related relevance of some of the methods developed as part of this research lies in the field of geographically distributed hybrid testing where, typically, a substructure pseudo-dynamic test may be realised with the various substructures being modelled in different laboratories, based in different cities or countries. This field has already been substantially researched in Japan (Pan *et al.* 2005*b*, 2006; Takahashi & Fenves 2006) and in the USA under the NEES program (Mosqueda *et al.* 2005). A similar collaborative approach is also currently under investigation in the UK.

# REFERENCES

Algaard W. H. (2001) Integrated implementation system for pseudodynamic testing (DPhil thesis), University of Glasgow, UK - Department of Civil Eng.

Algaard W. H., Agar A., Bicanic N. (2001) Enhanced integral form of the Newmark time stepping scheme for pseudodynamic testing, Eng. Computations, Vol. 18, 2001, 3/4, 676-689.

Bajer C. (2002) Time integration methods: still questions, Proc. Theoretical Foundations of Civil Engineering, W. Szczeniak Ed., Warsaw, Vol. 1, 2002, 45-54.

Battini J. M. (2003) Structural dynamics, www2.mech.kth.se/~jean/dynamics.html

Bayer V., Dorka U. E., Füllerkrug U. (2000) A new algorithm for real-time sub-structure pseudo-dynamic tests, Proc. 12th World Conf. Earthquake Eng., Auckland, New Zealand, 30 January 2000, paper 0401.

Bayer V., Dorka U. E., Füllerkrug U., Gschwilm J. (2002) Realisation of real-time pseudo-dynamic sub-structure testing, Proc. Int. Conf. on Noise & Vibration Eng., Leuven, Belgium, 16-18 September 2002.

Bayer V., Dorka U. E., Füllerkrug U., Gschwilm J. (2005) On real-time pseudo-dynamic sub-structure testing: algorithm, numerical and experimental results, Aerospace Science and Technology, Vol. 9, 2005, 3, 223-232.

Blakeborough A., Williams M. S., Darby A. P., Williams D. M. (2001) The development of real-time substructure testing, Phil. Trans. Royal Soc. London, Series A, 359, 1869-1891.

Bonelli A., Bursi O. (2004) Generalized -a methods for seismic structural testing, Earthquake Eng. & Struct. Dyn., Vol. 33, 2004, 1067-1102.

Bonnet P. A. (2005) Developing real-time substructure dynamic testing, Proc. Soc. for Earthquake and Civil Eng. Dyn. (SECED) Young Eng. Conf., Bath, UK, 21-22 March 2005.

Bonnet P. A., Williams M. S., Blakeborough A. (2005) Actuator performance in real time hybrid tests, Proc. 1st Int. Conf. on Advances in Exp. Struct. Eng., Nagoya, Japan, 19-21 July 2005.

Booth E. D. (1998) Earthquake engineering in the 1990s: achievements, concerns and future directions, Proc. Inst. Civ. Engrs, 128, 154-166.

Buchet P., Pegon P. (1994) PSD testing with substructuring - implementation and use, Joint Research Centre, ELSA, European Commission, Special Publication # I.94.25.

Bursi O. S., Shing P. B. (1996) Evaluation of some implicit time-stepping algorithms for pseudodynamic tests, Earthquake Eng. & Struct. Dyn., Vol. 25, 1996, 333-355.

Chang S. Y. (1997) Improved numerical dissipation for explicit methods in pseudodynamic tests, Earthquake Eng. & Struct. Dyn., Vol. 26, 1997, 917-929.

Chang S. Y. (1998) A time integration pseudodynamic algorithm, Proc. 11th Europ. Conf. on Earthquake Eng., 1998, Rotterdam.

Chang S. Y. (2001) Application of the momentum equations of motion to pseudo-dynamic testing, Phil. Trans. Royal Soc. London, Series A, 359, 1801-1827.

Chang S. Y. (2002*a*) An improved on-line dynamic testing method, Eng. Structures, Vol. 24, 2002, 5, 587-596.

Chang S. Y. (2002*b*) Explicit pseudodynamic algorithm with unconditional stability, Journal of Eng. Mech., Vol. 128, 2002, 9, 935-947.

Chang S. Y. (2003) Nonlinear error propagation analysis for explicit pseudodynamic algorithm, Journal of Eng. Mech., Vol. 129, 2003, 8, 841-850.

Chang S. Y. (2005) Error propagation in implicit pseudodynamic testing of nonlinear systems, Journal of Eng. Mech., Vol. 131, 2005, 12, 1257-1269.

Chang S. Y., Tsai K. C., Chen K. C. (1998) Improved time integration for pseudo-dynamic tests, Earthquake Eng. & Struct. Dyn., Vol. 27, 1998, 711-730.

Clarke D. W., Hinton C. J. (1997) Adaptive control of materials-testing machines, Automatica, Vol. 33, 1997, 1119-1131.

Clough R. W., Penzien J. (1995) Dynamics of structures - 2nd edition revised (book), Computers and Structures, Inc.

Combescure D., Pegon P. (1997) $\alpha$-Operator splitting time integration technique for pseudodynamic testing error propagation analysis, Soil Dyn. & Earthquake Eng., Vol. 16, 1997, 427-443.

Craig R. R., Bampton M.C.C. (1968) Coupling of substructures for dynamic analysis, American Institute of Aeronautics and Astronautics Journal, Vol. 6, 1968, 1313-1319.

Dantal Y., Rondeau M. (2004) Librairie Algorithmique, Soluscience, 2004 (in French).

Darby A. P., Blakeborough A., Williams M. S. (1999) Real-time substructure tests using hydraulic actuator, Journal Eng. Mech., Vol. 125, 1999, 10, 1133-1139.

Darby A. P., Blakeborough A., Williams M. S. (2001) Improved control algorithm for real-time substructure testing, Earthquake Eng. & Struct. Dyn., Vol. 30, 2001, 431-448.

Darby A. P., Williams M. S., Blakeborough A. (2002) Stability and delay compensation for real-time substructure testing, Journal Eng. Mech., Vol. 128, 2002, 12, 1276-1284.

Dimig J., Shield C., French C., Bailey F., Clark A. (1999) Effective force testing: a method of seismic simulation for structural testing, Journal Struct. Eng., Vol. 125, 1999, 9, 1028-1037.

Drury D., Stoten D. P., Wagg D. J., Gomez E. G., Crewe A. J. (2002) Advances in numerical experimental substructuring techniques using MCS control, Proc. 12th Europ. Conf. on Earthquake Eng., 9-13 September 2002, London, paper 277, 1-10.

dSpace Ltd. (2002) dSPACE - Solutions for control - User guide, dSPACE Ltd.

Franklin G. F., Powell J. D., Workman M. (1998) Digital control of dynamic systems - 3rd edition (book), Addison-Wesley.

Garcia de Jalon J., Bayo E. (1994) Kinematic and dynamic simulation of multibody systems: the real-time challenge, Springer-Verlag, http://mat21.etsii.upm.es/mbs

Gawthrop P. J., Wallace M. I., Wagg D. J. (2005) Bond-graph based substructuring of dynamical systems, Earthquake Eng. & Struct. Dyn., Vol. 34, 2005, 687-703.

Hilber H. M. (1976) Analysis and design of numerical integration methods in structural dynamics, Earthquake Eng. Research Center, University of California, Berkeley, 1976, EERC Report No. 76-29.

Hilber H. M., Hughes T. J. R., Taylor R. L. (1977) Improved numerical dissipation for time integration algorithms in structural dynamics, Earthquake Eng. & Struct. Dyn., Vol. 6, 1977, 283-292.

Horiuchi T., Nakagawa M., Sugano M., Konno T. (1996) Development of real-time hybrid experimental system with actuator delay compensation, Proc. 11th World Conf. on Earthquake Eng., Acapulco, paper 660.

Horiuchi T., Inoue M., Konno T., Namita Y. (1999) Real-time hybrid experimental system with actuator delay compensation and its application to a piping system with energy absorber, Earthquake Eng. & Struct. Dyn., Vol. 28, 1999, 1121-1141.

Horiuchi T., Inoue M., Konno T. (2000) Development of a real-time hybrid experimental system using a shaking table, Proc. 12th World Conf. Earthquake Eng., Auckland, New Zealand, 30 January 2000, paper 0843.

Horiuchi T., Konno T. (2001) A new method for compensating actuator delay in real-time hybrid experiments, Phil. Trans. Royal Soc. London, Series A, 359, 1893-1909.

Hughes T. J. R. (1983) Analysis of transient algorithms with particular reference to stability behavior, Computational methods for transient analysis, edited by Belytschko & Hughes, 1983, 67-155.

Hughes T. J. R. (1987) The finite element method: linear static and dynamic finite element analysis, Prentice-Hall International Editions.

Iemura H., Igarashi A., Aoki T., Yamamoto Y. (2005) Real-time substructure hybrid earthquake loading system for super high damping rubber bearings, Proc. 1st Int. Conf. on Advances in Exp. Struct. Eng., Nagoya, Japan, 19-21 July 2005.

Igarashi A., Iemura H., Tanaka H. (2002) Development of substructure hybrid shake table test method and application to verification tests of vibration control devices, Proc. China-Japan workshop on vib. cont. & health monitoring of struct., Shanghai, China, 2002, paper C007.

Instron (1998) Labtronic 8800 structural test control system computer interface: reference manual, IST Systems Limited, 1998.

Kobayashi H., Tamura K. (2000) Experimental study on the validity of real-time hybrid vibration experiments with a 2-dimensional and 3-degree-of-freedom model, Proc. 12th World Conf. Earthquake Eng., Auckland, New Zealand, 30 January 2000, paper 0965.

Kyrychko Y. N., Blyuss K. B., Gonzalez-Buelga A., Hogan S. J., Wagg D. J. (2006) Real-time dynamic substructuring in a coupled oscillator-pendulum system, Proc. Royal Soc. A, 2006, 462, 1271-1294.

Léger P., Wilson E. L. (1987) Generation of load dependent Ritz transformation vectors in structural dynamics, Eng. Computations, Vol. 4, December, 309-318.

Lim C. N., Neild S. A., Stoten D. P., Drury D. (2005) Real-time dynamic substructure testing via an adaptive control strategy, Proc. 1st Int. Conf. on Advances in Exp. Struct. Eng., Nagoya, Japan, 19-21 July 2005.

Magonette G. (2001) Development and application of large-scale continuous pseudo-dynamic testing techniques, Phil. Trans. Royal Soc. London, Series A, 359, 1771-1799.

Mahin S. A., Shing P. B., Thewalt C. R., Hanson R. D. (1989) Pseudo dynamic test method: current status and future directions, Journal Struct. Eng., Vol. 115, 1989, 8, 2113-2128.

Molina F. J., Verzeletti G., Magonette G., Buchet P., Renda V., Geradin M., Parducci A., Mezzi M., Pacchiarotti A., Federici L., Mascelloni S. (2002) Pseudodynamic tests on rubber base isolators with numerical substructuring of the superstructure and strain-rate effect compensation, Earthquake Eng. & Struct. Dyn., Vol. 31, 2002, 1563-1582.

Molina F. J., Bairrao R., Blakeborough A., Bursi O., Tirelli D., Magonette G. E., Mouzakis H., Williams M. S. (2006) Testing performance benchmark for shaking tables and reaction walls within the Neforeee project, Proc. 1st Eur. Conf. on Earthquake Eng. And Seismology, Geneva, Switzerland, 3-8 September 2006, paper 303.

Nakashima M. (2001) Development, potential and limitations of real-time online (pseudo-dynamic) test, Phil. Trans. Royal Soc. London, Series A, 359, 1851-1867.

Nakashima M., Kato H., Takaoka E. (1992) Development of real-time pseudo dynamic testing, Earthquake Eng. & Struct. Dyn., Vol. 21, 1992, 79-92.

Nakashima M., Masaoka N. (1999) Real-time on-line tests for MDOF systems, Earthquake Eng. & Struct. Dyn., Vol. 28, 1999, 393-420.

Nakashima M., Liu D. (2005) Instability and complete failure of steel columns subjected to cyclic loading, Journal Eng. Mech., Vol. 131, 2005, 6, 559-567.

Neild S. A., Drury D., Wagg D. J., Stoten D. P., Crewe A. J. (2002) Implementing real-time adaptive control methods for substructuring of large structures, Proc. 3rd World Conf. on Structural Control, Como, Italy, 7-12 April 2002, Vol 2, 811-817.

Neild S. A., Stoten D. P., Drury D., Wagg D. J. (2005) Control issues relating to real-time substructuring experiments using a shaking table, Earthquake Eng. & Struct. Dyn., Vol. 34, 2005, 1171-1192.

Newmark N. M. (1959) A method of computation for structural dynamics, Journal Eng. Mech., Vol. 85, 1959, EM3 July, 67-94.

Pan P., Nakashima M., Tomofuji H. (2005*a*) Online test using displacement-force mixed control, Earthquake Eng. & Struct. Dyn., Vol. 34, 2005, 869-888.

Pan P., Tada M., Nakashima M. (2005*b*) Online hybrid test by internet linkage of distributed test-analysis domains, Earthquake Eng. & Struct. Dyn., Vol. 34, 2005, 1407-1425.

Pan P., Tomofuji H., Wang T., Nakashima M., Ohsaki M., Mosalam K. M. (2006) Development of peer-to-peer (P2P) internet online hybrid test system, Earthquake Eng. & Struct. Dyn., Vol. 35, 2006, 867-890.

Pegon P., Pinto A. V. (2000) Pseudo-dynamic testing with substructuring at the ELSA laboratory, Earthquake Eng. & Struct. Dyn., Vol. 29, 2000, 905-925.

Plummer A. R. (2006) Model-in-the-loop testing, Proc. I Mech E, Part I, Journal of Systems & Control Eng., in press.

Rana R., Soong T. T. (1998) Parametric study and simplified design of tuned mass dampers, Eng. Struct., Vol. 20, 1998, 193-204.

Reinhorn A. M., Bruneau M., Whittaker A. S., Constantinou M. C., Thevanayagam S., Chu S., Pitman M. C., Winter K. (2002) A versatile high performance testing facility towards real-time dynamic hybrid testing, Proc. 7th Nat. Conf. on Earthquake Eng., Boston, July 2002, on CD-ROM (Paper Reference S-17/NS-1d).

Reinhorn A. M., Sivaselvan M. V., Liang Z., Shao X. (2004) Real-time dynamic hybrid testing of structural systems, Proc. 13th World Conf. Earthquake Eng., Vancouver, Canada, August 2004, paper 1644.

Shing P. B., Mahin S. A. (1987*a*) Cumulative experimental errors in pseudodynamic tests, Earthquake Eng. & Struct. Dyn., Vol. 15, 1987, 409-424.

Shing P. B., Mahin S. A. (1987*b*) Elimination of spurious higher-mode response in pseudodynamic tests, Earthquake Eng. & Struct. Dyn., Vol. 15, 1987, 425-445.

Shing P. B., Mahin S. A. (1990) Experimental error effects in pseudodynamic testing, Journal Eng. Mech., Vol. 116, 1990, 4, 805-821.

Shing P. B., Vannan M. T., Carter E. W. (1991) Implicit time integration for pseudo-dynamic tests, Earthquake Eng. & Struct. Dyn., Vol. 20, 1991, 551-576.

Shing P. B., Nakashima M., Bursi O. (1996) Application of pseudodynamic test method to structural research, Earthquake Spectra, Vol. 12, 1996, 1, 29-56.

Smith S. W. (1997) The scientist and engineer's guide to digital signal processing, ISBN 0-9660176-3-3, www.dspguide.com, 1997.

Spencer Jr. B. F., Nagarajaiah S. (2003) State of the art of structural control, Journal Struct. Eng,. Vol 129, 2003, 7, 845-856.

Stoten D. P. (1993) An overview of the minimal control synthesis algorithm, Proc. I Mech E Conf. on Aerospace Hydraulics and Systems, London, UK, paper C474-033.

Stoten D. P., Benchoubane H. (1993) The minimal control synthesis identification algorithm, Int. Journal Cont., Vol. 58, 3, 685-696.

Stoten D. P., Gomez E. G. (2001) Adaptive control of shaking tables using the minimal control synthesis algorithm, Phil. Trans. Royal Soc. London, Series A, 359, 1697-1723.

Stoten D. P., Neild S. A., Wagg D. J., Drury D. (2002) Dynamic substructuring via the adaptive MCS algorithm, Proc. 3rd World Conf. on Structural Control, Como, Italy, 7-12 April 2002, Vol 2, 819-825.

Stoten D. P., Neild S. A. (2003) The error-based minimal control synthesis algorithm with integral action, Proc. I Mech E, Part I, Journal of Systems & Control Eng., Vol 217, 2003, 187-201.

Takahashi Y., Fenves G. L. (2006) Software framework for distributed experimental-computational simulation of structural systems, Earthquake Eng. & Struct. Dyn., Vol. 35, 2006, 267-291.

Takanashi K., Nakashima M. (1987) Japanese activities on on-line testing, Journal Eng. Mech., Vol. 113, 1987, 7, 1014-1032.

Thewalt C. R., Mahin S. A. (1995) An unconditionally stable hybrid pseudodynamic algorithm, Earthquake Eng. & Struct. Dyn., Vol. 24, 1995, 723-731.

Wagg D. J., Stoten D. P. (2001) Substructuring of dynamical systems via the adaptive minimal control synthesis algorithm, Earthquake Eng. & Struct. Dyn., Vol. 30, 2001, 865-877

Wallace M. I., Wagg D. J., Neild S. A. (2004) Multi-actuator substructure testing with applications to earthquake engineering: how do we assess accuracy?, Proc. 13th World Conf. Earthquake Eng., Vancouver, Canada, August 2004, paper 3241.

Wallace M. I., Sieber J., Neild S. A., Wagg D. J., Krauskopf B. (2005*a*) Stability analysis of real-time dynamic substructuring using delay differential equation models, Earthquake Eng. & Struct. Dyn., Vol. 34, 2005, 1817-1832.

Wallace M. I., Wagg D. J., Neild S. A. (2005*b*) An adaptive polynomial based forward prediction algorithm for multi-actuator real-time dynamic substructuring, Proc. Royal Soc. A, 2005, 461, 3807-3826.

Williams D. M. (2000) Numerical modelling of real-time substructure testing (DPhil thesis), University of Oxford, UK - Department of Engineering Science.

Williams M. S., Blakeborough A., Houlsby G. T., Williams D. M. (1998) Development of a real-time hybrid dynamic testing system, Proc. Int. Conf. on Seismic Des. Practice into the Next Century (6th SECED Conf.), Oxford, UK, 1998, 373-379.

Williams D. M., Darby A. P., Williams M. S., Blakeborough A. (1999) Real-time dynamic testing system for structures with delay compensation, Proc. 8th Canadian Conf. on Earthquake Eng., Vancouver, Canada, 603-608.

Williams D. M., Williams M. S., Blakeborough A. (2001) Numerical modelling of a servohydraulic testing system for structures, Journal Eng. Mech., Vol. 127, 2001, 8, 816-827.

Williams M. S., Blakeborough A. (2001) Laboratory testing of structures under dynamic loads: an introductory review, Phil. Trans. Royal Soc. London, Series A, 359, 1651-1670.

Williams M. S., Blakeborough A. (2002) Development of a real-time test method for structures, Proc. 3rd World Conf. on Structural Control, Como, Italy, 7-12 April 2002.

Wu B., Wang Q., Bao H., Ou J. (2004) Analysis and preliminary experimental study on central difference method for real-time substructure testing, Proc. ANCER Annual Meeting Presentations, Honolulu, USA, 28-30 July 2004.

Wu B., Bao H., Ou J., Tian S. (2005) Stability and accuracy analysis of the central difference method for real-time substructure testing, Earthquake Eng. & Struct. Dyn., Vol. 34, 2005, 705-718.

Wu B., Xu G., Wang Q., Williams M. S. (2006) Operator-splitting method for real-time substructure testing, Earthquake Eng. & Struct. Dyn., Vol. 35, 2006, 293-314.

Yu E., Whang D. H., Conte J. P., Stewart J. P., Wallace J. W. (2005) Forced vibration testing of buildings using the linear shaker seismic simulation (LSSS) testing method, Earthquake Eng. & Struct. Dyn., Vol. 34, 2005, 737-761.

Zhang Y., Sause R., Ricles J. M., Naito C. J. (2005) Modified predictor-corrector numerical scheme for real-time pseudo dynamic tests using state-space formulation, Earthquake Eng. & Struct. Dyn., Vol. 34, 2005, 271-288.

Zhao J., French C., Shield C., Posbergh T. (2003) Considerations for the development of real-time dynamic testing using servo-hydraulic actuation, Earthquake Eng. & Struct. Dyn., Vol. 32, 2003, 1773-1794.

Zhao J., Shield C., French C., Posbergh T. (2004) Effect of servovalve/actuator dynamics on displacement controlled testing, Proc. 13th World Conf. Earthquake Eng., Vancouver, Canada, August 2004, paper 267.

Zhao J., Shield C., French C., Posbergh T. (2005) Nonlinear system modelling and velocity feedback compensation for effective force testing, Journal Eng. Mech., Vol. 131, 2005, 3, 244-253.